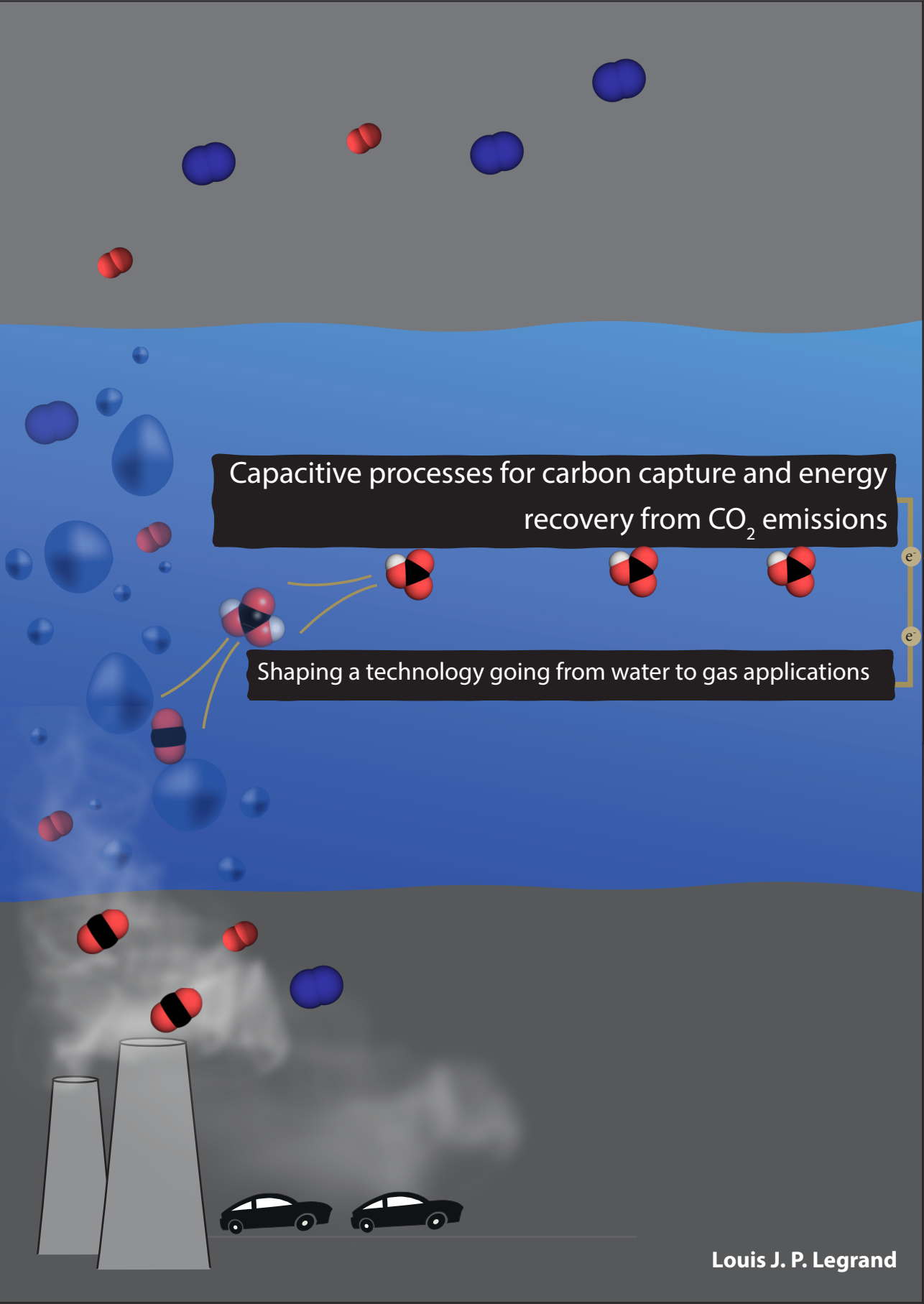

Louis J. P. Legrand

Propositions

1. The establishment of the electrical double layer influences the dissociation of weak acids in electrode micropores. (this thesis)

2. Unlike conventional Membrane Capacitive Deionization, low ionomer permselectivity is an advantage for Capacitive Deionization for CO_2 capture. (this thesis)

3. Scientific marketing is nowadays an essential skill for researchers.

4. In the future, artificial intelligence will be more suitable to handle scientific integrity than humans.

5. The popularization of science is a threat to the development of science.

6. To solve climate change, scientists must focus on education and social science rather than technology.

Proposition belonging to the thesis, entitled

Capacitive processes for carbon capture and energy recovery from CO_2 emissions.
Shaping a new technology going from water to gas applications.

Louis Legrand
Wageningen, 11 September 2020

Capacitive processes for carbon capture and energy recovery from CO_2 emissions

Shaping a new technology going from water to gas applications

Louis J.P. Legrand

Thesis committee

Promotor
Prof. Dr Cees J.N. Buisman
Professor of Biological Recovery and Re-use technology, Wageningen University & Research

Co-promotors
Dr Hubertus V.M. Hamelers
Program Director
Wetsus, European Centre of Excellence for Sustainable Water Technology, Leeuwarden

Dr Michele Tedesco
Scientific Project Manager
Wetsus, European Centre of Excellence for Sustainable Water Technology, Leeuwarden

Other members
Prof Dr Karel J. Keesman, Wageningen University & Research
Prof. Dr Matthew E. Suss, Technion, Haifa, Israel
Prof. Dr Angel V. Delgado-Mora, University of Granada, Spain
Dr Anca Anastasopol, TNO, Delft, the Netherlands

This research was conducted under the auspices of the Graduate School for Socio-Economic and Natural Sciences of the Environment (SENSE)

Capacitive processes for carbon capture and energy recovery from CO_2 emissions

Shaping a new technology going from water to gas applications

Louis J.P. Legrand

Thesis

Submitted in fulfilment of the requirements for the degree of doctor
at Wageningen University
by the authority of the Rector Magnificus,
Prof. Dr A.P.J. Mol,
In the presence of the
Thesis Committee appointed by the Academic board
to be defended in public
on Friday 11 September 2020
at 10.00 a.m. in de Harmonee, Leeuwarden

Louis J.P. Legrand
Capacitive processes for carbon capture and energy recovery from CO_2 emissions. Shaping a new technology going from water to gas applications,
217 pages.

PhD thesis, Wageningen University , Wageningen, the Netherlands (2020)
With references, with summary in English

ISBN 978-94-6395-489-1
DOI https://doi.org/10.18174/528554

To my family, my partner, and my daughter

Table of contents

Chapter 1

Introduction

1.1. Reducing Global warming challenge

Global warming is one of the biggest challenges that humanity is facing nowadays. The atmospheric temperature continually increases every year due to a constant increase of greenhouse gases (GHG) in the atmosphere, i.e., carbon dioxide (CO_2), methane (CH_4) and nitrogen dioxide (NO_2) and (Fig. 1.1a-b). Among these greenhouse gases, CO_2 gas contributes the most to the GHG emissions (up to 75% in 2015). CO_2 emissions caused by anthropogenic activities continuously increases[1], which induce a constant increase of the CO_2 level in the atmosphere[2] (Fig. 1.1c). The most significant contributor to CO_2 emissions is mainly industries (power industry and other industries) and the transport sector (Fig. 1.1d). To reduce global warming, industries should embrace innovative technologies to minimize CO_2 emissions.

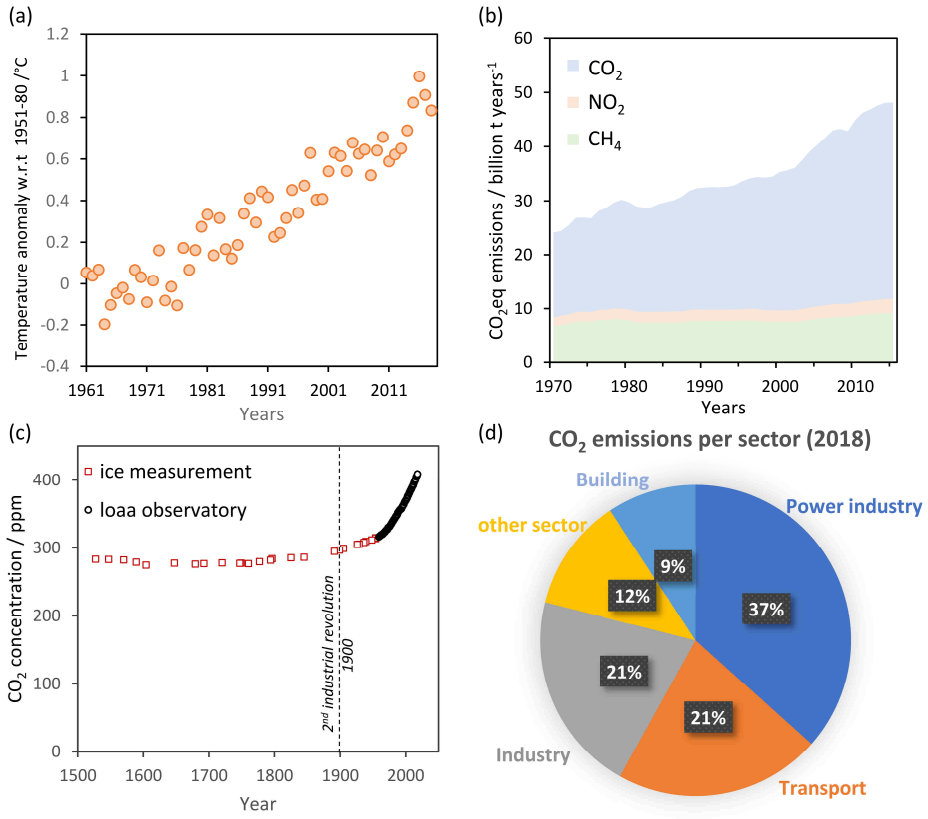

Fig. 1.1: (a) Temperature anomaly for the years 1970-2018 (Refs. [3,4]). (b) greenhouse gas emissions during the last 50 years (Ref. [5]). (c) CO_2 level measurement in the loaa observatory and air enclosed from ice cores (Refs [1,6]). (d) Global CO_2 emissions per sector in 2018 (Ref. [5]).

Global warming is the primary cause of many environmental problems, such as the deterioration of ecological systems worlwide[7] and the increase of the sea level[8–10], many effects of which are predicted to be irreversible[11]. Due to such an unprecedented negative impact on our environment, nations worldwide agreed to limit the temperature increase by 2°C before the end of this century (2100) while pursuing efforts to limit the increase by 1.5°C (COP21 in Paris in 2015[12]). To ensure the success of these ambitious goals, the Energy International Agency (IEA) designed a roadmap, the so-called "2-degree scenario" (2DS), i.e., a detailed plan in which a panel of different mitigations strategies are proposed to reduce CO_2 emissions [13,14]. These strategies mostly consist of (i) developing renewable energies, (ii) increasing carbon storage and capture (CCS), (iii) improving the energy efficiency of power plants and end-use, (iv) including the use of nuclear power and (v) switching end-use fuel. Though the development of renewable energies meets the prediction of the 2-degree scenario, the amount of CO_2 capture rate is falling behind [14], thus endangering the success of the objective set by the Paris Agreement (COP21). Up to now, large-scale deployment of CO_2 capture technologies is limited by the high operating costs of the commercially available technologies, i.e., mostly amine scrubbing. Part of their high costs is related to the high energy demand, which is up to 20 times higher than the minimum thermodynamic energy needed ($\approx$100 kJ $molCO_2^{-1}$ against $\approx$5 kJ $molCO_2^{-1}$ for capturing flue gas from power plants[15]). Therefore, technology development is still essential to reduce CO_2 emissions, for instance, to increase the energy efficiency of CO_2 capture technologies.

1.2. Novel capacitive technologies to contribute to the global warming challenge

The work done in this Ph.D. thesis aims to contribute to the global warming challenge by developing two innovative capacitive technologies to reduce CO_2 emissions. These two capacitive technologies have mainly been inspired by capacitive deionization (CDI) [16,17] and capacitive mixing (CAPMIX) [18–20], both of which are electrochemical technologies developed for water-related applications. CDI is a desalination technology that aims at removing salt ions from water by applying an electrical current. CAPMIX is an electrochemical technology, which aims at generating electrical energy from salinity gradients, e.g., when sea and river water streams are mixed (also known as "Blue energy") [18,19,21,22]. CDI and CAPMIX are complementary as they use the same technology principle but are operated in opposite ways. Fig. 1.2a shows the complementarity between CDI and CAPMIX.

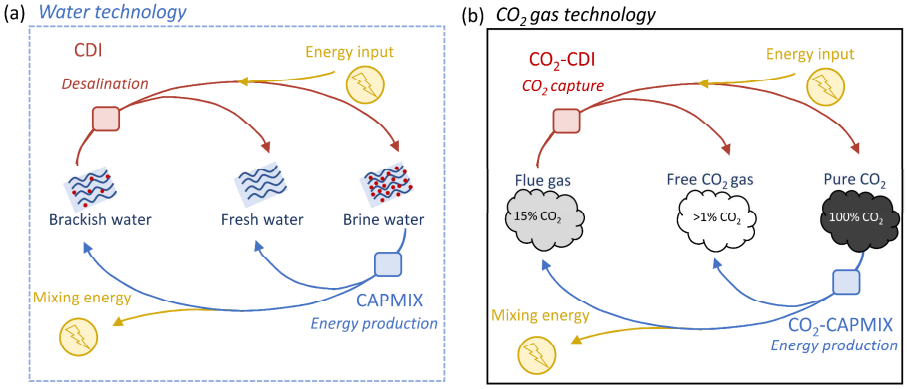

Fig. 1.2: Schematic representation of different capacitive technologies for water and CO_2 systems: a) CDI and CAPMIX, b) CO_2-CDI, and CO_2-CAPMIX.

In this Ph.D. work, we adapted CDI and CAPMIX from water-based technologies to gas-based technologies (Fig. 1.2b). In 2014, Hamelers et al. show that a CAPMIX cell can generate electrical energy from a CO_2 gas concentration difference, i.e., flue gas and atmospheric air (i.e., a "CO_2-CAPMIX" technology)[23]. As a result, CO_2-CAPMIX can generate electrical power from CO_2 emissions. Based on Ref.[23], a coal power plant could improve its energy efficiency by up to 5% by harvesting the electrical energy available from their CO_2 emissions with a CO_2-CAPMIX cell. This improvement of energy efficiency fits well with the 2DS scenario developed by the IEA shown in section 1.1. Moreover, a CDI cell could also be theoretically used to capture CO_2 (i.e., a "CO_2-CDI" technology), instead of desalinating water. In fact, CO_2-CDI represents a new electrochemical CO_2 capture technology, which can be promising in the field of sustainable CO_2 capture strategies.

Nonetheless, how can we convert a water technology into a gas technology? The first step is to identify a strategy to produce ions from CO_2 gas. As CO_2 gas is not an ion, the CDI and CAPMIX cells are not directly usable with gas streams. Nevertheless, ions can be generated from CO_2 by sparging CO_2 gas in water, a process in which bicarbonate ions are formed (see Box 1).

Box 1: Ionization process of CO_2 in water

CDI and CAPMIX are capacitive technologies that require the presence of ions in solution to be operated. The ions in salt streams (mainly Na^+ and Cl^- as shown in Fig. 1.3) are either desalinated (CDI operation) or use to generate electrical energy (CAPMIX operation). Although CO_2 is a neutral molecule, it can react with water via a hydration reaction to give $H_2CO_3^*$ (Eq. 1.1), and, by means of further acid-based reactions, into HCO_3^- and CO_3^{2-} (Eqs. 1.2-1.3). Fig. 1.3 illustrates the formation of ions from CO_2 gas.

$$\mathbf{CO_2(g) + H_2O \overset{H^{cc}}{\leftrightarrow} H_2CO_3^*} \quad \text{with } H^{cc}=0.83 \text{ from Refs.}[24,25] \quad 1.1$$

$$\mathbf{H_2CO_3^* \overset{K_1}{\leftrightarrow} HCO_3^- + H^+} \quad \text{with } K_1=10^{-6.35} \text{ M from Ref.}[26] \quad 1.2$$

$$\mathbf{HCO_3^- \overset{K_2}{\leftrightarrow} CO_3^- + H^+} \quad \text{with } K_2=10^{-10.33} \text{ M from Ref.}[26] \quad 1.3$$

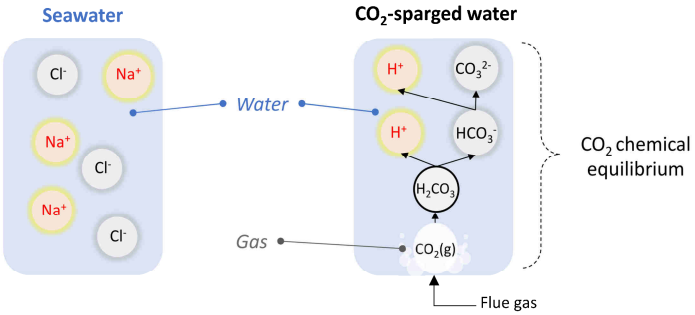

Fig. 1.3: Illustration of ions in seawater and CO_2-sparged solutions. CO_2 gas reacts into the formation of bicarbonate ions and protons through chemical reactions (shown in Eqs. 1.1-1.3).

Overall, two new capacitive technologies (CO_2-CAPMIX and CO_2-CDI) can potentially reduce CO_2 emissions. CO_2-CDI can be compared with other electrochemical systems developed for CO_2 capture (section 1.3), while regarding CO_2-CAPMIX, only one study has been reported so far showing another technology for harvesting electrical energy from CO_2 emissions[27]. Regarding CO_2-CAPMIX, only early works showing the proof of concept have been reported so far[23,28,29], thus leaving still many technological questions unsolved. Instead, on the CO_2-CDI concept, no studies have been reported prior to this Ph.D. research.

1.3. Development of electrochemical CO_2 capture technologies

Nowadays, amine scrubbing is currently the only CO_2 capture technology that has already reached a commercial development stage (TRL 9, see Fig. 1.4). Thus, most operating large-scale carbon capture and storage (CCS) plants are using amine scrubbing technology. In particular, among the total of 28 CCS plants that are currently under operation worldwide, 22 of them are using amine scrubbing as capture technology [30]. Nevertheless, despite its technological maturity, amine processes show several drawbacks, such as (i) high thermal energy consumption, and (ii) poor stability of the chemical solvent, leading to toxicity[31,32] and solvent degradation[32–34]. Driven by the search of solvent-free and more energy-efficient technologies, other alternative technologies have been investigated for CO_2 capture, e.g., adsorption [35–39] (TRL 7), calcium looping [35,40–43] (TRL 6), membrane absorption [35,44–47] (TRL 3-7), and electrochemical processes (TRL 3)[48]. Fig. 1.4 shows that these technologies currently have different stages of development, some of which are already at demonstration scales (TRL 7-8), but not yet at a commercial scale (TRL 9).

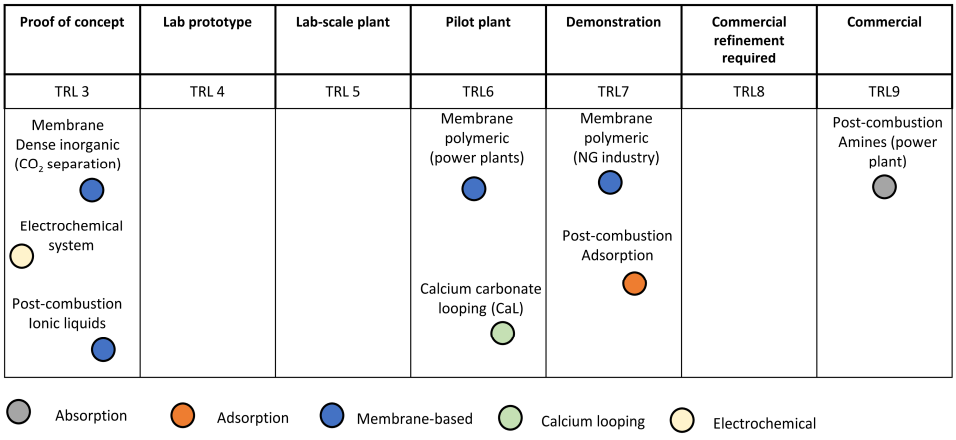

Fig. 1.4: Comparison of current technology readiness level (TRL) of different CO_2 capture technologies (adapted from Ref.[15]).

Although electrochemical technologies are on the earliest stage of development compared to other CCS solutions, their application recently attracts much interest due to their potential advantages compared to traditional amine systems. The main advantages of electrochemical capture technologies include (i) no use of toxic and corrosive chemical

solvents[49], (ii) better control and tuning of the strength of CO_2 binding[48], (iii) possibility to minimize side reactions, and (iv) potentially minimizing the energy consumption[48]. Beside CO_2-CDI, other electrochemical CO_2 capture technologies have been recently reported for CO_2 capture, e.g., molten carbonate CO_2 concentrator [50–52], pH swing [49,53–55], faradaic electro-swing [48,56,57] and supercapacitive swing adsorption [58–61].

1.3.1. Molten Carbonate CO_2 concentrator

Historically, the molten carbonate CO_2 concentrator (MCCC) has been the first developed electrochemical system for CO_2 separation[50]. This system was designed to remove CO_2 gas from breathing gas mixture of humans on space flight by adapting the molten carbonate fuel cell (MCFC) technology. Both technologies operate on the same principle: CO_2 gas is transported from the cathode to anode compartments, while H_2 is consumed in the anode compartment (see Fig. 1.5). The anode and cathode reactions are summarized in Table 1.1. When operated as an MCFC, the cell is a fuel cell that generates electrical energy from H_2. When operated as an MCCC, the cell remove CO_2 gas from the gas mixture in the cathode compartment (see Fig. 1.5). The concentrated CO_2 gas is recovered in the anode compartment.

Table 1.1: anode and cathode reactions in a Molten carbonate CO_2 concentrator (MCCC)

Anode compartment	$\frac{1}{2}\mathrm{O_2(g)} + \mathrm{CO_2(g), anode} + 2\mathrm{e^-} \rightarrow \mathrm{CO_3^{2-}(l)}$
Cathode compartment	$\mathrm{H_2(g)} + \mathrm{CO_3^{2-}(l)} \rightarrow \mathrm{H_2O(g)} + \mathrm{CO_2(g), cathode}$
Overall reaction	$\frac{1}{2}\mathrm{O_2(g)} + \mathrm{CO_2(g), anode} + \mathrm{H_2}(g) \rightarrow \mathrm{H_2}O + \mathrm{CO_2(g), cathode}$

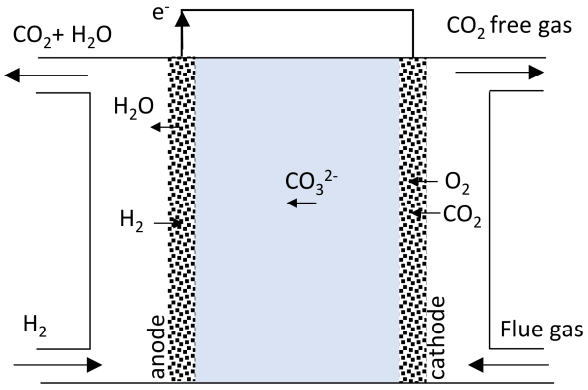

Fig. 1.5: Schematic principles of a molten carbonate CO_2 concentrator (MCCC).

Although the MCFC/MCCC are mature technologies developed for more than 40 years, the performances are mainly limited by two factors, i.e., the energy demand and the CO_2 purity of the concentrated gas. On the one hand, the energy requirement of the cell is mainly impacted by the high temperature required to achieve high transport of CO_3^{2-} (typically, 500 650 °C [51,52]). On the other hand, a gas mixture is recovered on the anode compartment, limiting the CO_2 purity of the concentrated gas (around 70-80% [51]).

1.3.2. Electrochemical pH swing

CO_2 capture can be achieved by generating a pH swing between two chambers in an electrochemical cell. The electrochemical pH swing has been mostly investigated in electrodialysis cell[62,63] and bipolar electrodialysis cell[49,53–55]. The CO_2 absorption takes place in the alkaline compartment (high pH) through the reaction of CO_2 with hydroxide ($CO_2 + OH^- \rightarrow HCO_3^-$), whereas the CO_2 desorption takes place in the acidic compartment ($HCO_3^- + H^+ \rightarrow CO_2$). Fig. 1.6 shows an example of CO_2 capture with bipolar electrodialysis.

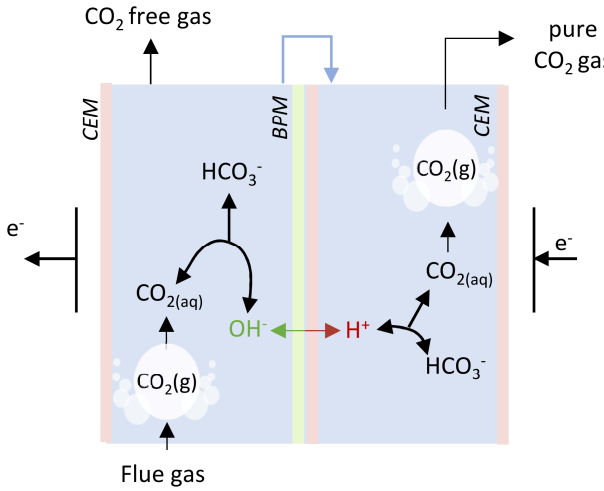

Fig. 1.6: Schematic principles of a pH swing electrochemical cell with bipolar membranes.

In electrodialysis, the pH gradient is generated through both the water oxidation (anode) and water reduction (cathode), as shown in Table 1.2. In bipolar electrodialysis, the pH gradient is produced by the bipolar membrane (as shown in Fig. 1.6). The major advantage of this system is the flexibility of operation. The pH gradient is directly controlled by the current density and can be adapted depending on the CO_2 content in the gas inflow. Therefore, bipolar electrodialysis can be used for a broad range of gas composition (e.g., flue gas [49] or direct air capture[55]). Although the energy requirement of the technology is still high (~100-500 kJ molCO_2^{-1})[49,54], its application is of particular interest for direct air capture[55].

Table 1.2: Water oxidation and reduction reactions

Anode compartment	$2H_2O \rightarrow 4H^+ + O_2(g) + 4e^-$
Cathode compartment	$4H_2O + 4e^- \rightarrow 2H_2(g) + 4OH^-$

Besides ion exchange membranes, pH swing can be obtained by electrosorption of proton by using proton-selective electrochemically active material. This approach has been adopted in a pseudo-capacitive cell using intercalation electrodes[64] and a proton-coupled electron transfer (quinones[65]).

1.3.3. Faradaic electro-swing CO_2 adsorption

Faradaic electro-swing consists of reversibly adsorb and desorb CO_2 on electrochemically active materials. CO_2 is then absorbed by applying a reductive potential (reduction reaction) and is desorbed by applying an oxidative potential (oxidation reaction). Fig. 1.7a shows an example of a faradaic electro-swing. Several electrochemically active materials have been tested for faradaic electro-swing, including, e.g., quinone-based nucleophile [48,66] and monoalkylated bipyridinium[67,68]. Moreover, the active material is either free in the electrolyte solution [48,56] (see Fig. 1.7b) or fixed in the electrode matrix[57]. This system shows promising low energy consumption values (~20-90 kJ molCO_2^{-1})[56,57].

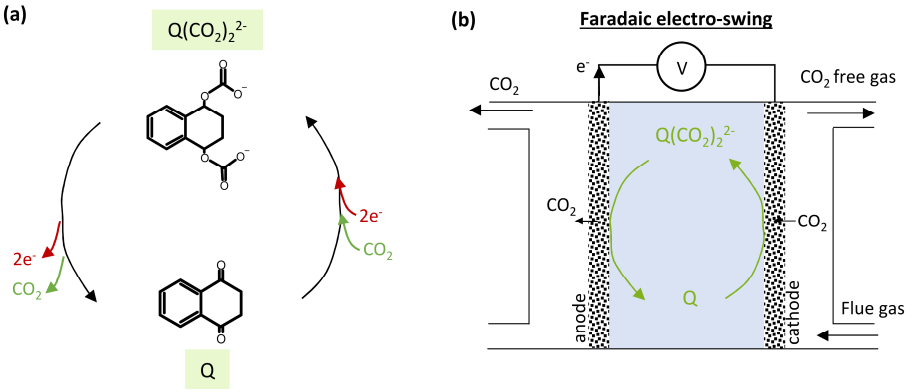

Fig. 1.7: (a) Example of CO_2 adsorption and desorption through the reaction with a quinone (1,4-naphthoquinone). Q stands for Quinone and $Q(CO_2)^{2-}$ stands for Quinone after CO_2 adsorption. (b) Electrochemical cell using a faradaic swing to capture CO_2 (based on Refs.[48,66]).

1.3.4. Supercapacitive swing adsorption

Supercapacitive swing adsorption (SAA) is an electrical double-layer capacitor (EDLC) for CO_2 capture[58–61]. The concept consists of adsorbing CO_2 on the cathode in a gas channel while charging the EDLC cell in a highly concentrated NaCl solution. Fig. 1.8 shows an illustration of the SAA concept. Three mechanisms have been suggested for the CO_2 gas adsorption in the electrodes, i.e. (a) adsorption of gas molecules at gas-solid interface, (b) adsorption of gas molecules at the gas-liquid interface, and (c) adsorption of ionized gas molecule[61]. Adsorption at the gas-solid interface would occur when CO_2 gas is adsorbed in non-filled electrode pores stimulated by a change of affinity between the pore wall and CO_2 during the charging step of the cell. Adsorption at the gas-liquid interface would occur due to an increased CO_2 solubility in the electrical double layer (EDL) by charging the capacitive cell. Finally, ionization adsorption occurs through the adsorption

of HCO_3^- and CO_3^{2-} in the EDL during charging (see Box 1). This latter mechanism is the same principle of a CO_2-CDI cell and will be discussed in more detail in the next section.

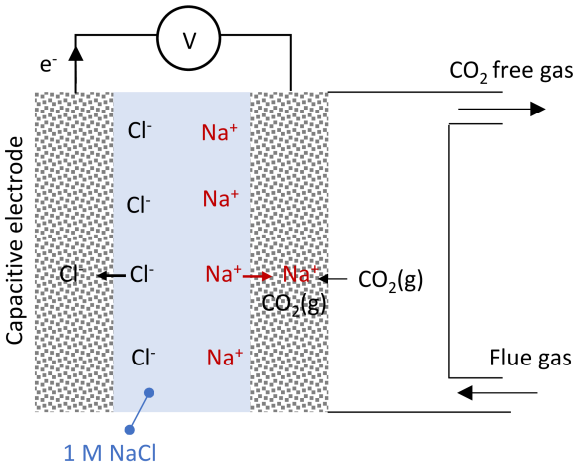

Fig. 1.8: Schematic principles of a supercapacitive swing adsorption for CO_2 capture.

1.4. Principles of Capacitive Deionization (CDI) and Capacitive mixing (CAPMIX) systems

CDI and CAPMIX technologies are EDLC-based technology. Both technologies have been widely investigated in the field of water technology in the past years, and several EDLC cell architectures have been proposed for both systems, e.g., flow-by CDI[69–73], Membrane CDI[72,74,75], flow-through electrode[76], flow-electrode CDI[77,78], and wire-shaped electrode[19,22,79]. Conventionally, a flow-by CDI is considered as the "conventional" design for CDI application, while the Membrane CDI is the conventional design for CAPMIX application.

1.4.1. Ion electrosorption mechanisms in CDI

Flow-by CDI cells are composed of two capacitive electrodes separated by a flow channel where an electrolyte solution is fed (Fig. 1.9). Upon applying a cell voltage, the capacitive electrodes are electronically charged, resulting in the ion adsorption from the electrolyte solution to the micropores of the electrodes. As a result, the micropores of the electrodes act as ion storage in the capacitive cell. This process is the basic underlying mechanism to desalinate water streams with an EDLC.

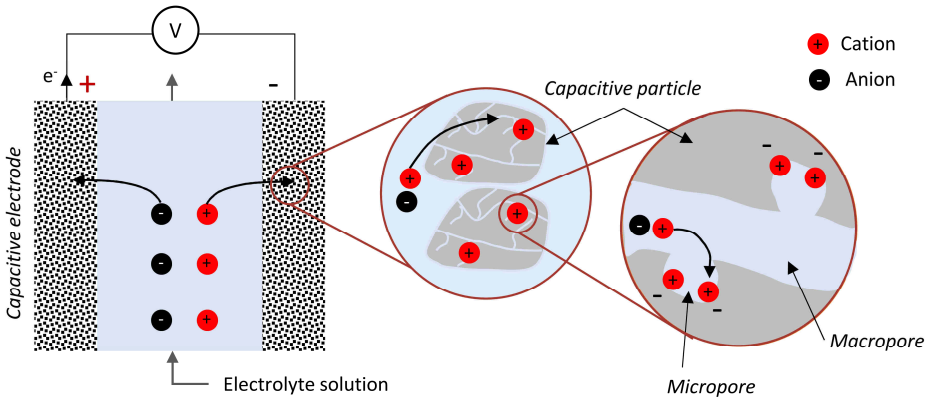

Fig. 1.9: Scheme of a flow-by CDI cell with an illustration of the ion electrosorption mechanism. In conventional CDI, Na^+ is the cation, and Cl^- is the anion. In CO_2-CDI, H^+ is the cation and HCO_3^- is the dominant anion.

To describe the ion electrosorption mechanisms, two theories have been applied in CDI, i.e., the Gouy-Chapman-Stern (GCS) theory 80–82 and the modified Donnan models83–85. The (GCS) theory describes the basic principles of ion adsorption in the electrode. According to the GCS theory, each electrode/solution interface can be separated into three regions, i.e., (i) carbon surface, (ii) the Stern layer, and (iii) the diffuse layer (see Fig. 1.10). During charging, the electronic charge is stored in the carbon, while the ionic charge is stored in the diffuse layer. The ionic charge concentration in the diffuse layer follows a Boltzmann distribution, i.e., changing exponentially with the highest ionic charge concentration close to the electrode surface, and the lowest close to the bulk solution. The ionic charge can vary by adsorbing or desorbing ions in the diffuse layer and must compensate the electronic charge to respect overall the electroneutrality. Note that the thickness of the diffuse layer, which is referred to as the Debye length, λ_D, is depending on the ion concentration of the bulk solution as

$$\lambda_D = \sqrt{\frac{\epsilon_r \cdot \epsilon_0 \cdot R \cdot T}{2 \cdot F^2 \cdot c_i}} \qquad 1.4$$

where ϵ_r is the dielectric constant, ϵ_0 is the permittivity of free space, R the gas constant, T the temperature, F the Faraday constant and c_i the ion concentration in the bulk solution. Finally, the Stern layer represents the layer of solution separating the diffuse layer, and the carbon matrix surface. In theory, ions are surrounded by a hydration shell, and therefore, the charged ions are not infinitely close to the electrode surface.

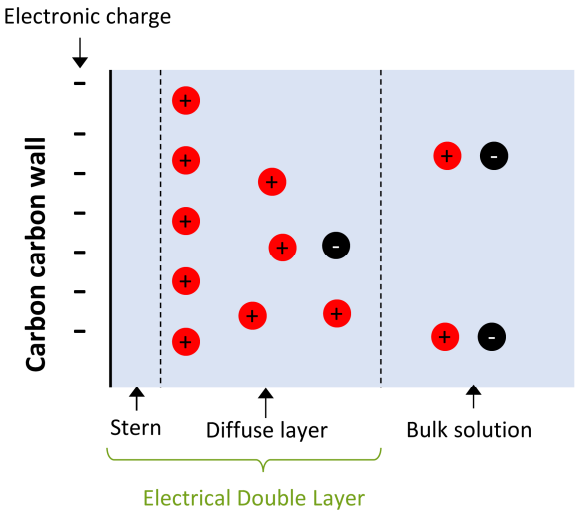

Fig. 1.10: Illustration of the electrical double layer at the wall of carbon electrodes according to the Gouy-Chapman-Stern theory.

Since the GCS theory describes the structure of the EDL for planar (metallic) electrodes, its validity is limited in the case of microporous electrodes. Inside microporous electrodes, the EDL formed on the surface of micropores are strongly overlapping, especially at low ion concentration[17,85,86]. The GCS model does not describe this situation. For instance, the Debye length of 1 mM monovalent electrolyte solution is ~ 9.6 nm (using Eq. 1.4), which is five times larger than the average pore diameter of electrode micropores (<2 nm). To describe the structure of EDL inside microporous electrodes, the GCS theory has been revisited to take into account overlapping EDLs in a different model, i.e., the modified Donnan model [17,70]. Compared to the GCS model, the Donnan model assumes a constant electrical potential (i.e., the Donnan potential, $\Delta\phi_D$) and ionic concentration in the micropores ($c_{mi,i}$), which can be estimated as[70]

$$c_{mi,i} = c_i e^{-\frac{z_i \cdot \Delta\phi_D \cdot F}{R \cdot T}} \qquad 1.5$$

where z_i is the valence of the ion.

Understanding the mechanisms of ion electrosorption in CDI is a crucial aspect of the technology. The ion adsorption mechanisms of the EDL has been studied by measuring the charge efficiency[87], Λ, defined as

$$\Lambda = \frac{n_{salt}}{n_{charge}} \qquad 1.6$$

where n_{salt} is the amount of salt ion removed and n_{charge} is the molar amount of electrical charge stored in the electrodes. Ideally, during charge, the electrical charge would be compensated by ion adsorption (i.e., counter-ion adsorption) in the electrodes, thus resulting in a charge efficiency of Λ=1. However, the electrical charge is partly compensated by the desorption of ions (or co-ion expulsion), leading to Λ<1. Co-ion expulsion is then the source of energy losses and loss of ion adsorption capacity of the electrodes. Co-ion expulsion is more critical at low cell voltages [16,87] and high ion concentrations[87].

1.4.2. Use of ion exchange membranes in CDI and CAPMIX

Another commonly used cell architecture for CDI (also representing the conventional design of CAPMIX cells) consists of porous electrodes covered by ion exchange membranes (IEM) (see Fig. 1.11). The anode is covered by an anion exchange membrane (AEM), and the cathode is covered by a cation exchange membrane (CEM).

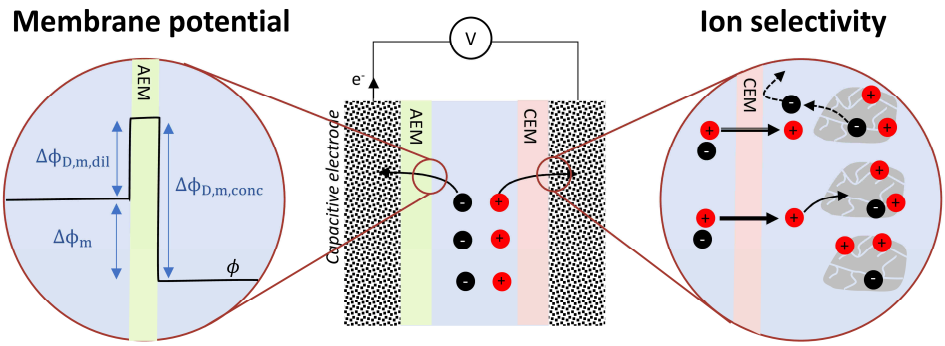

Fig. 1.11: Illustration of a flow-by MCDI combined with ion exchange membranes (MCDI)

IEMs are ionomer, i.e., charged polymer, which primarily act as selective charge barriers. Ideally, only anions can be transported through the AEM, and only cations can be transported through the CEM (counter-ion transport). IEMs are mainly used in CDI to improve the charge efficiency (in Membrane CDI or MCDI)[70,72] and are required in CAPMIX to generate an electrical potential.

Thanks to their charge selectivity, ion exchange membranes improve the charge efficiency in CDI by decreasing the effect of co-ion expulsion (see Fig. 1.11). Blocked by the IEM, co-ions are retained in the macropores of the electrodes, while counter-ions are transported across the IEM. Thus, in MCDI, the ion storage occurs both in the micropores and macropores of the electrodes.

In CAPMIX, IEMs represent the active cell element that allows the generation of an electric voltage. An electrical potential, or membrane potential, occurs when a concentration difference exists across an IEM. This concentration difference leads to a difference of Donnan potential on each membrane side, generating a membrane potential (see Fig. 1.11). The principle of the establishment of the Donnan potential for IEM is the same as capacitive electrodes (Eq. 1.5). As capacitive electrodes, the IEM is a charged material leading to the establishment of an EDL. Unlike capacitive electrodes, the IEM charge is constant, thus leading to a constant ionic concentration in the EDL ($C_{i,mi}$ in Eq. 1.5). Therefore, the Donnan potential of the IEM directly depends on the ion concentration of the bulk solution (C_i in Eq. 1.5). For IEM, Eq. 1.5 can be rewritten as:

$$\Delta\phi_{D,m,side} = \frac{\alpha \cdot R \cdot T}{z_i \cdot F} \cdot \ln\left(\frac{C_{i,side}}{C_m}\right) \qquad 1.7$$

where $\Delta\phi_{D,m,side}$ is the Donnan potential at one specific membrane/solution interface, C_m the ion concentration in the EDL of the IEM, $C_{i,side}$ the ion concentration of the bulk solution on one side of the membrane (right or left) and α the membrane apparent permselectivity. The membrane apparent permselectivity is a direct measurement of the charge selectivity of the membrane. For an ideal membrane, α=1, only counter-ions are transported through the membranes. Finally, the membrane potential is obtained from the difference of Donnan potentials on both membrane sides (see Fig. 1.11) as:

$$\Delta\phi_m = \Delta\phi_{m,conc} - \Delta\phi_{m,dil} = \frac{\alpha \cdot R \cdot T}{z_i \cdot F} \cdot \ln\left(\frac{C_{i,conc}}{C_{i,dil}}\right) \qquad 1.8$$

where $\Delta\phi_m$ is the membrane potential, $\Delta\phi_{m,conc}$ the Donnan potential at the membrane/solution interface on the concentrate side, $\Delta\phi_{m,dil}$ the Donnan potential at the interface on the dilute side, $C_{i,conc}$ the concentration of the concentrate, $C_{i,dil}$ the concentration of the dilute. Overall, Eq. 1.8 shows that the membrane potential directly depends on the ratio of concentration difference across the membrane. For instance, in the case of the CAPMIX process between seawater and river water, the ion concentration ratio is ~30, leading to a membrane potential of ~170 mV (α=1).

1.5. CO_2-CAPMIX and CO_2-CDI: from water to gas streams

1.5.1. Principle of CO_2-CAPMIX

Hamelers et al. demonstrated in 2014 the possibility to harvest electrical energy from the mixing of CO_2 emissions into atmospheric air using a CAPMIX cell (CO_2-CAPMIX)[23]. Fig. 1.12 shows the CO_2-CAPMIX process. The CO_2-CAPMIX and conventional CAPMIX share the same principle except for the feed solution. Firstly, ions in CO_2-sparged solution results from chemical reactions between CO_2 gas and water, unlike the case of true electrolyte solutions. Secondly, in the case of CAPMIX, feed solutions (i.e., natural waters) are mostly constituted by inorganic salts, fully dissociated electrolytes. Instead, in the case of CO_2-CAPMIX, the feed solution is a weak electrolyte composed of amphoteric ions (HCO_3^-). As the ion concentration of the gas-sparged solution directly depends on the CO_2 partial pressure, an ion concentration difference is obtained by flushing separately air (0.04% CO_2) and a concentrated CO_2 gas stream (100% CO_2). From the concentration ratio, a membrane potential arises, and electrical energy is generated.

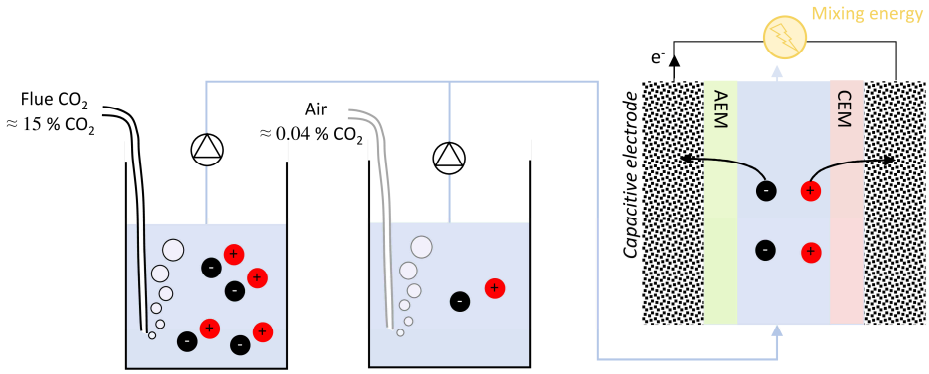

Fig. 1.12: Scheme of the CO_2-CAPMIX process. AEM and CEM stand for anions exchange membrane and cation exchange membrane, respectively.

Fig. 1.13a shows the solution pH as a function of CO_2 partial pressure, and the resulting theoretical membrane potential (calculated from Eq. 1.8). Theoretically, a concentration ratio of 20 can be obtained between air-sparged (0.04% CO_2) and flue gas-sparged (15% CO_2) solutions, thus resulting in a membrane potential of 162 mV. A concentration ratio of 60 can be obtained with pure CO_2 gas (100% CO_2), leading to a theoretical membrane potential of 210 mV[29].

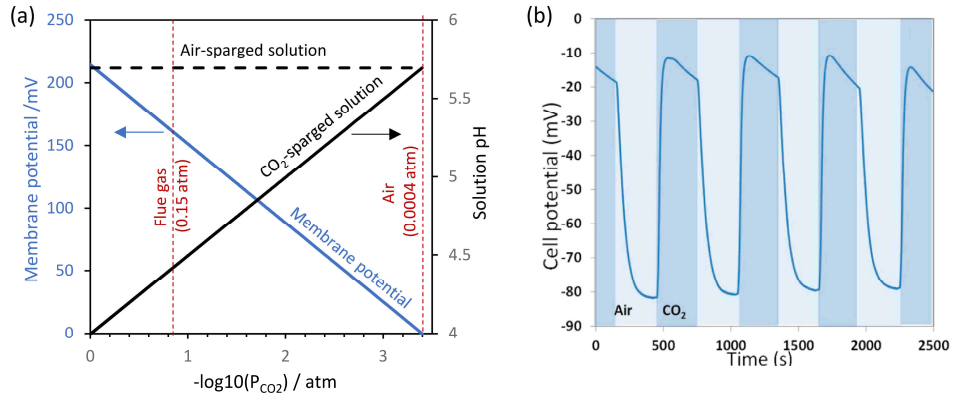

Fig. 1.13: (a) membrane potential for an air-sparged solution and a CO_2-sparged solution at different CO_2 partial pressures (calculations based on Eq.1.8) and the pH of the sparged solution at different CO_2 partial pressures. (b) Experimental Open cell voltage measurement by alternatively pumping CO_2-sparged and air-sparged solutions (OCV cycles) obtained in Ref.[23]. The difference in cell voltage by switching solutions is a measurement of the membrane potential.

1.5.2. Challenges of CO_2-CAPMIX and CO_2-CDI

Improving membrane selectivity

The highest membrane permselectivity reported so far in CO_2-CAPMIX is ~50%[23] (experimental results from Ref.[23] are shown in Fig. 1.13b). This apparent permselectivity value is low in comparison with conventional CAPMIX system (α >95%)[18] or similar systems using monovalent salt solutions[88–90]. The difference has been attributed to the specific CO_2 chemistry, i.e., (i) the diffusion of non-ionic species ($H_2CO_3^*$) and (ii) the high pH of the AEM[29,91]. The selectivity of IEMs is also an important parameter to consider in CO_2-CDI. An in-depth understanding of the CO_2 carbon species transport through IEM is essential to improve the membrane permselectivity. Moreover, investigating alternative cell designs is also of interest to reduce the diffusion of non-ionic species and increase the membrane permselectivity.

Switching from solution-feeding to gas-feeding operation

Sparging CO_2 and air gases in water is an energy-intensive operation. Hamelers et al. [23] predicted that the energy required for gas-sparging is higher than the theoretical electrical energy available. Thus, including gas sparging, the net energy generation is expected to be negative. To avoid the gas sparging step, we propose to feed the gas

directly in the cell (gas-feeding), instead of pumping a sparged-solution (solution-feeding). The gas ionization step is then taking place in the cell, where residual water is present.

Reducing the internal resistance

The major limitation of the CO_2-CAPMIX cell performance is the high internal resistance of the CAPMIX cell[23]. The same conclusion has been reported for conventional CAPMIX systems[18]. In general, energy losses occur in every resistive element of the CAPMIX cell (see an equivalent circuit of the CAPMIX cell in Fig. 1.14). Among these elements, the highest contribution in the internal resistance originates from the spacer channel due to the low ionic conductivity of the diluted solution. For instance, the solution conductivity of synthetic river water (1 g L^{-1} NaCl) is ~1880 µS cm^{-1}, which is 100 times lower than the conductivity of electrolyte solutions used in batteries[92] (typically in the range of 10^5 µS cm^{-1}). This low ionic conductivity is even more critical in CO_2-CAPMIX as the conductivity of the air-sparged solution is below 1 µS cm^{-1}, i.e., 1000 times lower than conventional CAPMIX. Strategies must be investigated to improve the ionic conductivity of the cell. Simply adding background electrolyte (e.g., NaCl) to the bulk solution is not feasible, as the IEMs are only charge-selective and not ion-selective. As a result, adding salt in the water would decrease the ion concentration ratio between the air and CO_2-sparged solutions, and thus reducing the membrane potential.

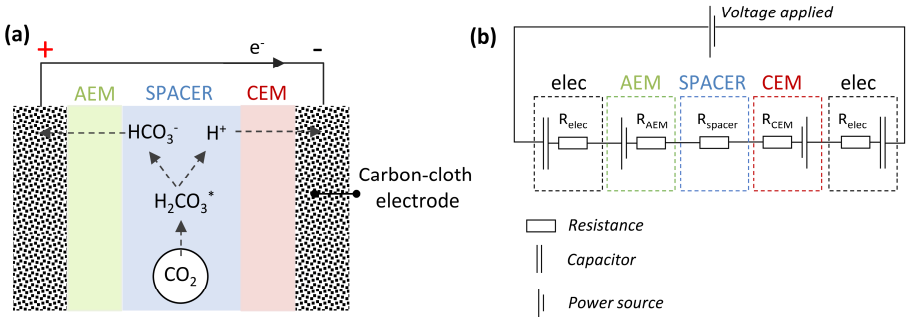

Fig. 1.14: (a) Scheme of a MCDI cell design and (b) its representation as an equivalent circuit

Furthermore, we expect an additional increase of internal resistance by switching from liquid to gas feeding in a conventional CAPMIX cell design (Fig. 1.14). Clearly, the conventional CAPMIX cell design is not suitable for CO_2-CAPMIX (as presented in Fig. 1.14). The same observation also applies to CO_2-CDI.

1.6. Key challenges

Up to now, only the proof-of-principle of the CO_2-CAPMIX process has been reported, demonstrating the possibility to harvest electrical energy by the controlled mixing of flue gas and air [23]. To further develop the CO_2-CAPMIX technology, many research efforts are still required, both focused on the scientific understanding of the process, as well as on technology development. Furthermore, at the beginning of this thesis, the CO_2-CDI process has never been investigated. Therefore, a proof-of-concept should be demonstrated for CO_2-CDI. Then, further studies should be done to improve the performance of the CO_2-CDI and CO_2-CAPMIX processes. Key challenges of this project can be summarized as:

i. Developing Proof of concepts

   Two concepts have to be demonstrated in this Ph.D. thesis, i.e., CO_2-CDI and direct gas feeding into capacitive cells. This first step is essential before optimizing the capacitive cell for CO_2 gas.

ii. Understanding the effect of CO_2-sparged solutions on capacitive cells

   CAPMIX and CDI have been mostly investigated for saline electrolyte solutions (i.e., NaCl), and very few studies have been made with CO_2-sparged solutions. Using CO_2-sparged solutions have a significant impact on the performance of the CAPMIX cell, due to the amphoteric nature of bicarbonate. For instance, the membrane apparent permselectivity of the CO_2-CAPMIX cell is below 50%[23], which is significantly lower than the expected membrane apparent permselectivity using saline solutions (≈90%).

iii. Developing innovative cell designs to reduce internal resistance

   The performance of the CO_2-CAPMIX cell is limited by the low cell internal resistance, due to the low ionic conductivity of the air-sparged and CO_2-sparged solutions. Different strategies should be investigated to decrease the internal resistance. Novel cell designs need to be developed to optimize the cell internal resistance.

iv. General assessment of the technology potential

After the first development stages of CO_2-CAPMIX and CO_2-MCDI technologies, the feasibility of both technologies should be discussed. This final assessment can give direction on refining the possible applications for CO_2-MCDI and CO_2-CAPMIX (e.g., post-combustion, pre-combustion, other), and provide future research direction to develop the technology.

1.7. Thesis outline

In this thesis, we investigate the use of EDLC capacitive cells for two different novel applications: (i) energy harvesting from CO_2 emissions (CO_2-CAPMIX) and (ii) CO_2 capture (CO_2-CDI). Chapters 2 and 3 focus on CO_2-CAPMIX, whereas chapters 4,5 and 6 focus on CO_2-CDI. Fig. 1.15 shows a scheme of all chapters presented in this thesis. Moreover, the research project presented in this Ph.D. thesis is divided into four different steps, i.e., (i) proof of concept, (ii) understanding, (iii) exploration of cell designs, and (iv) discussion (see Fig. 1.15).

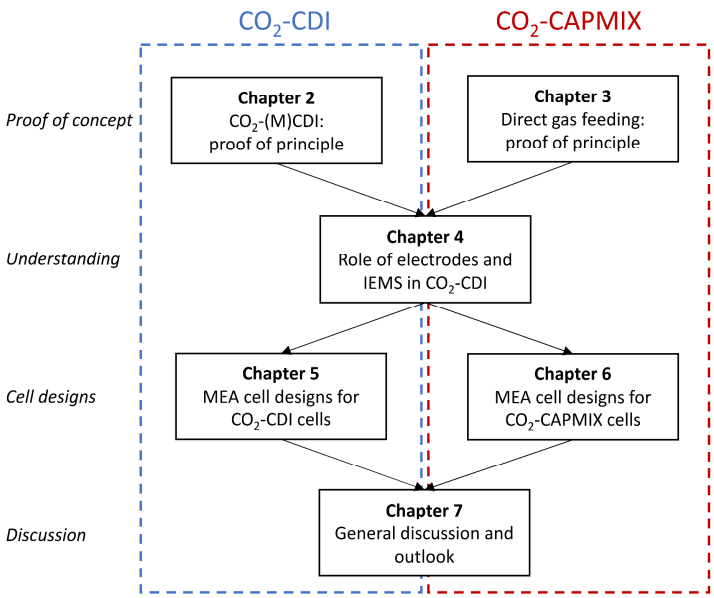

Fig. 1.15: Outline of this Ph.D. thesis, including connections between different chapters.

In the first part of this thesis, **Chapter 2** shows a proof of principle of CO_2-CDI, and **Chapter 3** shows a proof of principle of direct gas feeding in CO_2-CAPMIX. We report in Chapter 2 several performance parameters, such as energy consumption and absorption efficiency, which is similar to the charge efficiency in conventional MCDI. To further improve the system, we identify two major limiting factors, which are (i) the charge efficiency and (ii) the high internal resistance. In Chapter 3, Three different cell designs are investigated to optimize internal resistance and membrane potential. In particular, we investigate the use of a membrane electrode assembly (MEA) cell design and compare results in terms of membrane potential, internal resistance, and energy consumption.

In the second part, we investigate in **Chapter 4** the role of the electrodes and IEMs on ion selectivity in capacitive cells. Absorption efficiency was reported in a flow-by CO_2-CDI with and without membranes (flow-by CO_2-MCDI and flow-by CO_2-CDI, respectively). Furthermore, a theoretical model (amphoteric Donnan model) was adopted and tested in CO_2-CDI by comparing theoretical and experimental results. The main finding shows that the anion exchange membrane (AEM) is essential to obtain high absorption efficiencies (up to 70%). Furthermore, the electrode adsorption performance was unexpectedly lower than predicted by the model. Both the role of IEMs and electrode were discussed in more detail.

In the third step, we explore the possibility of reducing the internal cell resistance by testing different cell designs. **Chapter 5** shows a comparison between a flow-by MCDI design and membrane electrodes assembly (MEA) designs in CO_2-CDI. Our main finding shows that the internal resistance successfully decreased with MEA designs, resulting overall in lower energy consumption to capture CO_2. Moreover, we tested the same MEA designs with ionomer coated electrodes in **Chapter 6** for CO_2-CAPMIX. We highlight the benefits of using an ionic conductive material coating on both electrodes to reduce the internal resistance of a CO_2-CAPMIX cell.

Finally, in **Chapter 7,** we discussed the potential of both technologies and future research directions based on the results obtained from all other chapters.

Chapter 2

Solvent-Free CO_2 Capture Using Membrane Capacitive Deionization

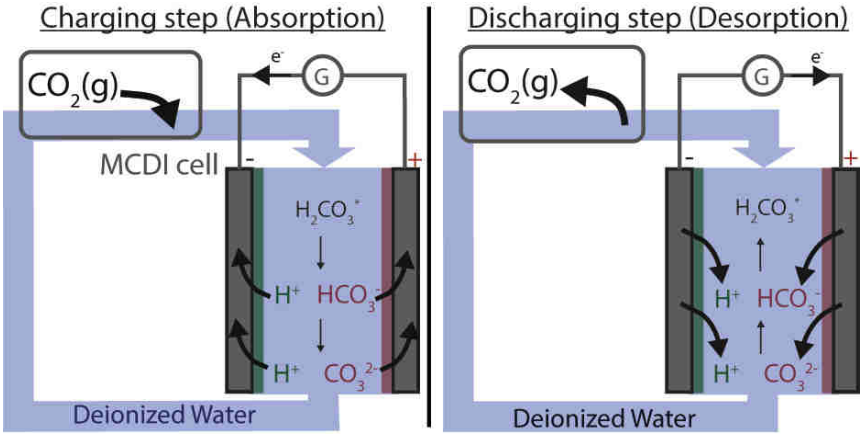

This Chapter has been published as:

L. Legrand, O. Schaetzle, R.C.F. de Kler, H.V.M. Hamelers, Solvent-Free CO_2 capture using Membrane Capacitive Deionization, *Environ. Sci. Technol.* 52(16) (**2018**) 9478-9485. https://doi.org/10.1021/acs.est.8b00980.

Abstract

The capture of CO_2, originating both from fossil fuels, such as coal combustion and from renewables, such as biogas, appears to be one of the most significant technological challenges of this century. In this study, we show that Membrane Capacitive Deionization (MCDI) can be used to capture CO_2 as bicarbonate and carbonate ions produced from the reaction of CO_2 with water. This novel approach allows capturing CO_2 at room temperature and atmospheric pressure without the use of chemicals. In this process, the adsorption and desorption of bicarbonate ions from the deionized water solution drives the CO_2(g) absorption/desorption from a gas phase. In this work, the effect of the current density and the CO_2 partial pressure were studied. We found that between 55-75% of the electrical charge of the capacitive electrodes can be directly used to absorb CO_2 gas. The energy requirement of such a system was found ≈40 kJ mol^{-1} at 15% CO_2 and could be further improved by reducing the ohmic and non-ohmic energy losses of the MCDI cell.

2.1. Introduction

Projections made by the International Energy Agency predict that achieving a net-zero CO_2 emission by the mid-century (≈2050) is critical to limit the temperature increase to 2°C[13]. While renewable energy sources like solar and wind already replaced fossil fuels for power production in part, the production of fuels and chemicals from renewable sources is slow. It seems that some form of CO_2 capture from different sources such as flue gas (coal, gas, or biomass power plants), biogas, or even from ambient air is required to achieve net-zero emissions in 2050. The captured CO_2 can be either stored or utilized as a chemical building block by electrochemical CO_2 reduction[93–95] or thermocatalytic CO_2 conversion[96,97].

To capture CO_2 from a gas mixture, various concepts have been developed, including adsorption[98–100], absorption[101–103], membrane separation[104,105], cryogenic separation[106], electrochemical methods[49,53,107], and biochemical methods[108,109]. Among these concepts, amine scrubbing (chemical absorption) is the most developed and applied technology. This technology is based on the chemical interaction between CO_2 and an amine group, which drives the absorption process of CO_2 into the amine solvent. Despite its wide usage, this process shows several disadvantages, such as high amount of heat energy needed to regenerate the solvent[110,111] and solvent degradation[34], which leads to high costs and some other toxic emissions[31], solvent loss[32] and corrosion effects[33]. Thus, more energy-efficient and environmentally friendly CO_2 capture methods are still of importance to investigate.

Alternative approaches based on electrochemistry attract more and more attention. This approach uses fewer chemicals and can potentially minimize energy consumption. Moreover, electrochemical systems, based on electrical power, are more suitable for CO_2 removal from emission points where insufficient waste heat is available for solvent regeneration. Various concepts have been explored, such as Molten carbonate fuel cell[50,112], pH swing with ion-exchange membranes[49,53], electrochemical generation of nucleophile[113,114], and supercapacitive swing adsorption[107]. In this study, we propose an alternative concept to capture CO_2 based on Membrane Capacitive Deionization (MCDI)[17,72,74].

MCDI cells are composed of activated carbon electrodes and ion-exchange membranes and are mainly used to desalinate water. By applying a current through the MCDI cell, ions are removed from the electrolyte into the pores of the electrodes and are stored in the electrical double layer (EDL). During this step, energy is temporarily stored in the electrodes due to its capacitive behavior. By reversing the current, the ions are

desorbed from the pores of the electrodes to the electrolyte, and the energy previously stored is released. An anion-exchange membrane covers one electrode, and a cation-exchange membrane covers the other electrode. Due to the selectivity of ion-exchange membranes, MCDI shows higher ions adsorption capacity[70] for monovalent salt (NaCl, KCl) compared to CDI.

In this study, we show that MCDI technology can be used to capture CO_2(g) in the form of HCO_3^- and CO_3^{2-}. These ions are produced by the reaction between CO_2(g) and deionized water, producing ions as described in Eqs. **2.1**-**2.3**. Here, $H_2CO_3^*$ stands for the combined concentrations of CO_2(aq) and H_2CO_3. These two species are usually added up as they are difficult to distinguish. The value for H^{cc} (defined as aqueous concentration over gaseous concentration) was calculated from Ref.[24,25], and the K_1 and K_2 values were taken from Ref.[26].

$$\mathbf{CO_2(g)} \overset{H^{cc}}{\leftrightarrow} \mathbf{H_2CO_3^*} \quad \text{with } H^{cc}=0.83 \qquad 2.1$$

$$\mathbf{H_2CO_3^*} \overset{K_1}{\leftrightarrow} \mathbf{HCO_3^-} + \mathbf{H^+} \quad \text{with } K_1=10\text{-}6.35 \text{ M} \qquad 2.2$$

$$\mathbf{HCO_3^-} \overset{K_2}{\leftrightarrow} \mathbf{CO_3^{2-}} + \mathbf{H^+} \quad \text{with } K_2=10\text{-}10.33 \text{ M} \qquad 2.3$$

Depending on the CO_2 content in the gas, the reactions between CO_2(g) and deionized water lead to an equilibrium composition. Fig. 2.1b shows the concentration of CO_2(g) and $H_2CO_3^*$ as well as the pH, based on the Eqs. 1-3 as a function of HCO_3^- concentration in deionized water. The concentration of CO_3^{2-} can be neglected as it is lower than 10-11 mM, due to the low pH of the electrolyte (pH<5). Applying a current would lead to the adsorption of HCO_3^- and H^+ into the porous electrodes. Fig. 2.1a shows that when HCO_3^- and H^+ are adsorbed into the porous electrodes, the chemical equilibrium is displaced, leading to CO_2(g) absorption in deionized water. Upon reversing the current direction, desorption of HCO_3^- and CO_3^{2-} ions from the carbon electrodes takes place, which drives the chemical equilibrium in the opposite direction toward CO_2(g) desorption into the gas phase. Overall, the CO_2(g) absorption or desorption can be controlled via the current direction, whereas the amount of CO_2(g) absorbed or desorbed is determined by the electrode charge, which is controlled by the current and charging time.

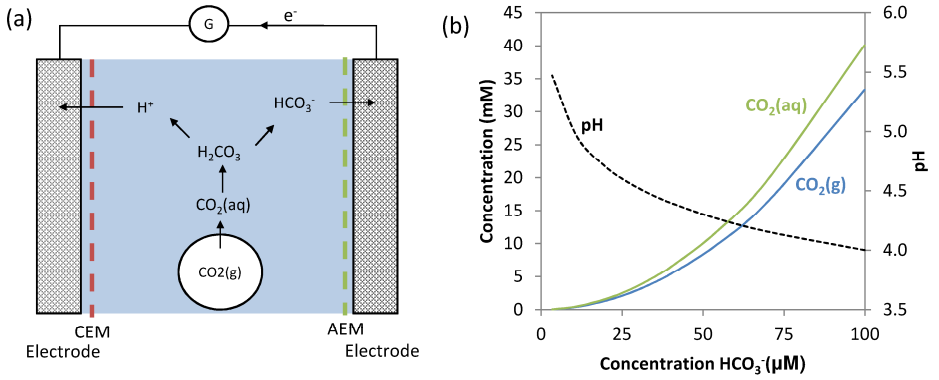

Fig. 2.1: (a) Scheme of an MCDI cell during charging. AEM stands for anion exchange membrane, and CEM stands for cation exchange membrane. (b) The concentration of $CO_2(g)$, $H_2CO_3^*$ and the pH depending on the HCO_3^- concentration in solution based on the Eqs. **2.1**-**2.3**.

To give a proof-of-concept using MCDI, CO_2 gas was alternately absorbed from and desorbed to a constant gas volume by applying a constant electrical current through an MCDI cell. Different CO_2:N_2 gas mixtures at different current densities were tested; 15% $CO_2(g)$ as artificial flue gas from coal-fired power plants, 30% $CO_2(g)$ as artificial biogas and 100% $CO_2(g)$, to further understand the effect of CO_2 pressure. The amount of energy required to absorb and desorb $CO_2(g)$ from the water phase was calculated at each applied current density and gas mixture used. This energy loss was split into the ohmic and non-ohmic losses. Directions for further improvement of the technology are proposed.

2.2. Materials and Methods

2.2.1. Experimental set-up

The activated carbon electrodes were prepared following a previously reported method[18,23]. In short, a slurry containing activated carbon powder (DLC, super 30, Norit, Amersfoort the Netherlands, BET=1600 $m^2\ g^{-1}$), polyvinylidene fluoride (KYNAR HSV 900, Arkema Inc., Philadelphia) and N-Methyl-2-pyrrolidone (NMP), was cast onto a graphite foil (300 µm) as a current collector. After evaporation of the NMP for 24 hours at room temperature, a resulting carbon layer made of 90 wt% of activated carbon and 10 wt% of PVDF was obtained. The final layer thickness, surface area, and weight of each activated carbon electrode were around 250 µm, 50 $cm^{2,}$ and 1 g. One electrode was covered by a cation-exchange membrane (CMX, Neosepta, Japan, 50 cm^2), and the other electrode was covered by an anion-exchange membrane (AMX, Neosepta, Japan, 50 cm^2). In the MCDI

cell, the electrodes were separated by a polymer spacer (PA 6.6 fabric, Nitex 03-300/51, Sefar, Heiden, Switzerland, 200 µm) to create a flow-channel between the electrodes.

The electrolyte solution fed to the MCDI cell was prepared by flushing a CO_2:N_2 gas mixture through deionized water in a tank. The composition of the gas mixture was controlled by two mass flow meters (mass view, MV-104, Bronkhorst). Three different CO_2 gas mixtures were prepared: 15% CO_2, 30% CO_2, and 100% CO_2.

The MCDI cell was operated in batch mode. A flow of the CO_2-flushed deionized water solution (33 ml ± 5 ml) was continuously re-circulated between the MCDI cell and a gas-liquid contactor at a flow-rate of 20 mL min^{-1}. The gas-liquid contactor ensures the CO_2 exchange between the solution and a gas volume, secures that the outgoing water is equilibrated with the gas phase. The gas-liquid contactor was made of a spiral-shaped glass tube, in which the effluent of the MCDI cell flowed from top to bottom in contact with a volume of gas contained in the headspace of the spiral-shaped tube. As the solution flows, the exchange of CO_2 occurs via the interphase between the gas and liquid phases all along the tube length. Fig. 2.2 depicts the research set-up during operation, and a photo of the research set-up is available in supporting information. The relative pressure (relative to atmospheric pressure) of the gas in the tube headspace was monitored with a manometer (Cerabar T PMP131, Endress+Hauser). The pressure measurement is a direct measurement of the CO_2 partial pressure as N_2 is considered an inert gas. The gas-liquid contactor contains 233 ml of CO_2:N_2 gas mixture, and the water residence time inside the gas-liquid contactor was around 45 seconds. The conductivity of the CO_2-dissolved solution was measured with a conductivity meter (pH/Cond 340i, Mettler Toledo). A Galvanostat (Ivium, the Netherlands) was used for Galvanostatic Charge and Discharge (GCD) experiments at three different current densities, 1 mA (0.2 A m^{-2}, 0.5 mA g^{-1}), 2 mA (0.4 A m^{-2}, 1 mA g^{-1}) and 3 mA (0.6 A m^{-2}, 1.5 mA g^{-1}). Multiple consecutive GCD cycles were applied between two different cell voltage limits, 0 V and 1 V. Simultaneously, an impedance measurement at 5 kHz with an amplitude of 1 mA was applied to the MCDI cell in order to estimate the ohmic resistance of the MCDI cell. Triplicates were obtained for each current and each gas mixture. At the 5 kHz frequency, the major contribution to the resistance is the ohmic resistance, mainly related to the solution resistivity in the spacer channel, the membranes resistivity, the electrodes ionic resistance, and the External Electronic Resistance (EER)[115]. EER is defined as the electronic resistances generated in the cables, current collectors, and current collector-electrode contacts. A study[116] showed that the current collector contact resistance can be observed at lower frequencies than 5 kHz and could represent up to 50% of the total internal resistance. Here, we consider the resistance of the current collector-electrode contacts negligible. By following the

procedure developed in Ref.[115], we estimate EER to be around 0.6 Ω in the MCDI cell, which is negligible compared to the ohmic resistance measured (≈20-50 Ω).

Before the experiment, the MCDI cell was short-circuited to reach 0 V cell voltage, while CO_2-flushed deionized water was fed continuously into the MCDI cell. After this first step, a volume of the equilibrated CO_2-flushed deionized water solution (33 ± 5 mL) was continuously recirculated between the MCDI cell and the gas-liquid contactor. Simultaneously, the CO_2:N_2 gas mixture was continuously flushed through the gas-liquid contactor (0.9 L min^{-1}). This step ensures that the liquid and the gas phases are equilibrated with the same CO_2 gas partial pressure. Afterward, gas valves were closed to contain a volume of gas into the gas-liquid contactor, and the batch experiment was started as described above, at 0 V.

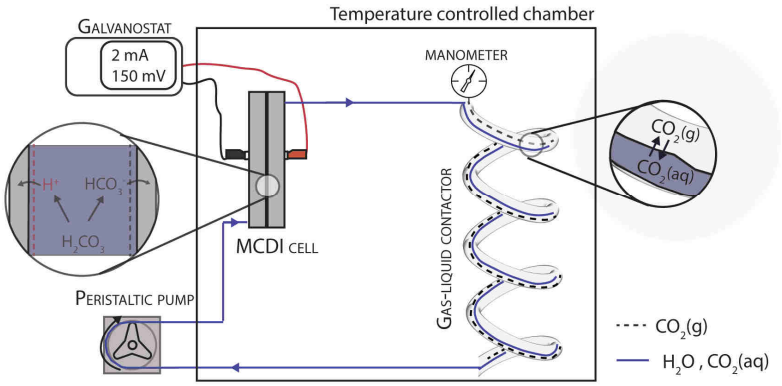

Fig. 2.2: Research set-up scheme. The blue line represents the CO_2-flushed deionized water, while the black dashed line represents the CO_2(g) volume.

2.2.2. Analysis

The molar amount of CO_2(g) either absorbed or desorbed ($n_{CO_2}(g)$) during the experiments was derived from the changes in the gas pressure using the ideal gas law ($n_{CO_2}(g)=(P\cdot V)/(R\cdot T)$). The gas is adsorbed from and desorbed to a fixed gas volume. As the amount of CO_2 exchanged is small compared to the amount of CO_2 present in the gas phase (<9%), the effect of the changing gas pressure can be neglected. The average between $n_{CO2(g)}$ obtained during the charging step, and the discharging step is reported as CO_2 exchanged. The difference between $n_{CO_2}(g)$ exchanged during the charge and discharge is on average 2.2% for most of the experiments. This difference might be caused by minor leakages in the system, especially in the gas phase and not yet fully equilibrated conditions in the system. For instance, the initial CO_2 partial pressure, the volume of water,

and the volume gas might differ between the different experiments. The values of $n_{CO_2(g)}$ during charge and discharge are reported in the supplementary information. The molar amount of charge exchanged during the experiments (n_{charge}) was calculated based on the Faraday number (F) and the electrical charge (Q), as n_{charge}=Q/F, where Q is the electrical charge expressed in Coulombs.

CDI and MCDI systems are commonly characterized by charge efficiency (Λ)[70,72,87], which for a 1:1 salt solution, such as NaCl, is defined as the ratio of the desired salt ions removed from the electrolyte, divided by the total charge transferred between the electrodes. In the case of CO_2-flushed deionized water, there are not only monovalent bicarbonate ions (HCO_3^-) but also divalent carbonate ions (CO_3^{2-}) present. The charge efficiency can, for such a situation, be evaluated as given in Eq. 2.4.

$$\Lambda = \frac{n_{HCO_3^-(ad)} + 2\, n_{CO_3^{2-}(ad)}}{n_{charge}} \qquad 2.4$$

Ideally, this metric has value $\Lambda=1$, but due to co-ion expulsion and faradaic reactions, Λ is lower. This parameter has been widely studied in (M)CDI[70,72,87].2.

However, in this study, we are specifically interested in how much CO_2 is adsorbed in the form of carbonate and bicarbonate, as this drives the CO_2(g) absorption. Thus, we define a related metric, the electrode carbon adsorption efficiency (Λ_c), which defines the amount of CO_2 adsorbed in the electrodes independently of its ionic form (HCO_3^- and CO_3^{2-}).

$$\Lambda_c = \frac{n_{HCO_3^-(ad)} + n_{CO_3^{2-}(ad)}}{n_{charge}} = \frac{n_{HCO_3^-(ad)} + n_{CO_3^{2-}(ad)}}{n_{HCO_3^-(ad)} + 2 * n_{CO_3^{2-}(ad)}} \cdot \Lambda \qquad 2.5$$

While Λ is determined by processes such as co-ion expulsion and faradaic reactions, Λ_c is also influenced by the distribution of CO_3^{2-} and HCO_3^- in the EDL. A shift in the distribution towards CO_3^{2-} will lead to a decreased Λ_c. The distribution of HCO_3^- and CO_3^{2-} in the EDL is determined by the pH in the EDL, as described by Eq. **2.3**. Different studies on (M)CDI showed pH effects in the EDL and electrolyte, due to faradaic reactions[73,77,117,118] or the presence of amphoteric groups[118,119]. This might leads to a shift in the carbonate ions distribution in the EDL. The effect of pH in the electrodes is discussed in more detail later in this study.

Λ_c describes the efficiency of the CO_2 adsorbed in the electrodes, in the form of HCO_3^- and CO_3^{2-}. For the proposed technology, the key parameter of interest is the amount of CO_2(g) removed from the gas phase $\Lambda_a = n_{CO_2}(g)/n_{charge}$. However, the source of CO_2 adsorbed in the electrodes can originate either from the gas phase, as CO_2(g), or from the liquid phase ($H_2CO_3^*$, HCO_3^- and CO_3^{2-}). The fraction of CO_2 adsorbed in the electrode, which is derived from the liquid phase, is denoted as f_w. Thus, to describe the efficiency of the CO_2(g) absorption process, the CO_2 absorption efficiency (Λ_a) is defined as:

$$\Lambda_a = (1 - f_w) \cdot \Lambda_c \qquad 2.6$$

The parameter f_w is mainly determined by the volume of gas (V_g) and liquid (V_w) in the system and the CO_2 solubility in deionized water at 298 K (H^{cc}). We estimated f_w=0.11 for our system. Calculations are shown in the supporting information.

$$f_w = \frac{Vw \cdot H^{cc}}{Vg + Vw \cdot H^{cc}} \qquad 2.7$$

Overall we can relate Λ_a and Λ_c in the following equation:

$$\Lambda_a = (1 - fw) \frac{n_{HCO_3^-(ad)} + n_{CO_3^{2-}(ad)}}{n_{HCO_3^-(ad)} + 2 * n_{CO_3^{2-}(ad)}} \cdot \Lambda \qquad 2.8$$

Eq. 2.7 shows that the absorption efficiency is determined by the fraction of CO_2 adsorbed from the aqueous phase (f_w), the distribution of bicarbonate/carbonate in the EDL, and the factors influencing the charge efficiency (faradaic reactions and co-ion expulsion).

The energy needed for gas separation has two components, the separation work (W_{min}) required to separate CO_2 gas to a higher concentration and the work lost as heat (irreversible loss) during the process due to mainly resistances. In the case of CO_2 gas, the separation work can be calculated based on Eq. 2.8, in which R represents the ideal gas constant, T the temperature, x_{N_2} the proportion of N_2 in the mixed gas and x_{CO_2} the proportion of CO_2 in the mixed gas

$$W_{min} = R \cdot T \cdot (x_{N_2} \cdot \ln(x_{N_2}) + x_{CO_2} \cdot \ln(x_{CO_2})) \qquad 2.9$$

Eq. 2.9 implies that the separation work needed is around 7 kJ molCO_2^{-1} for 15% CO_2 at 298K. This number is small compared to irreversible losses, which is generally true for all separation processes. In our experimental set-up, the CO_2 pressure only slightly changes, and thus the energy used up is the irreversible energy losses during the process. The key parameter in this respect is the specific energy per mole of CO_2(g) (W^*_{net}). This energy is defined as $W^*_{net}=W_{net}/n_{CO_2}(g)$ and is calculating from the amount of CO_2 absorbed ($n_{CO_2(g)}$) and the energy lost during a GCD cycle of the MCDI cell (W_{net}). The amount of CO_2(g) can be further expressed as $n_{CO_2(g)}=Q\cdot F/\Lambda_a$. Eq. 2.9 demonstrates that W^*_{net} is mainly depending on two key parameters, which are Λ_a and W_{net}.

$$W^*_{net} = \frac{W_{net} \cdot F}{\Lambda_a \cdot Q} \qquad 2.10$$

In MCDI, the energy losses (W_{net}) is derived as the difference between the energy input stored during the charge and the energy recovered during the discharge, which can be calculated by integrating the cell voltage (E_{cell}) by the electrical charge shown in Eq. 2.10. The superscript C stands for charging, and the superscript D stands for discharging.

$$W_{net} = \int_0^Q E^C_{cell}\, dQ - \int_0^Q E^D_{cell}\, dQ \qquad 2.11$$

In this study, the specific energy losses (W^*_{net}) is differentiated into two categories: (i) the specific ohmic losses (W^*_{ohmic}) and (ii) the specific non-ohmic losses ($W^*_{non-ohmic}$), which is defined in Eq. 2.12.

$$W^*_{net} = W^*_{non-ohmic} + W^*_{ohmic} = \frac{W_{ohmic} + W_{non-ohmic}}{n_{CO_2(g)}} \qquad 2.12$$

W^*_{ohmic} and $W^*_{non-ohmic}$ are calculated based on the ohmic energy losses of the MCDI cell (W_{ohmic}) and the remaining non-ohmic energy losses of the MCDI cell ($W_{non-ohmic}$). Values for W_{ohmic}, $W_{non-ohmic}$, W^*_{ohmic}, $W^*_{non-ohmic}$ are reported in the supplementary information. W^*_{ohmic} is defined as the specific energy losses related to the ohmic resistance (R_{ohmic}) of the MCDI cell over the electrical charge. The non-ohmic losses are defined as the remaining losses ($W^*_{non-ohmic}=W^*_{net}-W^*_{ohmic}$). The specific non-ohmic losses include different possible effects such as concentration polarization[50] and other phenomena such as faradaic reactions. We can write W_{ohmic} based on an averaged (constant) internal resistance, which can be written as:

$$W_{ohmic} = 2 \cdot I \cdot R_{ohmic} \cdot Q \quad 2.13$$

The current is defined as I, and R_{ohmic} is the ohmic resistance. We can write the specific ohmic energy losses in our system as:

$$W^*_{ohmic} = \frac{2 \cdot I \cdot R_{ohmic} \cdot F}{\Lambda_a} \quad 2.14$$

W^*_{ohmic} is determined by Λ_a and the internal resistance (R_{ohmic}). The study, therefore, aims at quantifying the effect of R_{ohmic} and Λ_a on W^*_{ohmic} and the specific energy losses due to other phenomena ($W^*_{non-ohmic}$).

2.3. Results and Discussion

Fig. 2.3a shows the measured gas pressure and the electrodes charge for several GCD cycles for an experiment at 0.4 A m^{-2} and 15% CO_2. During charging, the pressure decreases with increasing the electrode charge while during discharging, the pressure increases with decreasing the charge stored inside the electrodes. Data for different currents densities and CO_2 partial pressures (supporting information) show similar behavior. The gas pressure decrease can be explained as the absorption of CO_2(g) by the water, resulting from the HCO_3^-/CO_3^{2-} adsorption in the electrodes. In contrast, when the electrode charge decreases, the pressure increases due to the $H_2CO_3^*$ desorption into the gas phase, driven by the HCO_3^-/CO_3^{2-} desorption. The amount of CO_2 gas exchanged, electrode charge and Λ_a obtained for different current densities and different CO_2 partial pressures were stable for several GCD cycles, as shown for 0.4 A m^{-2} at 15% CO_2 in Fig. 2.3b. For instance, Λ_a at 0.4 A m^{-2} was between 65%-70% for several cycles during the charging and the discharging steps. This demonstrates for the first time that an MCDI cell can be operated to absorb CO_2 from a gas stream and that its performance is stable.

Surprisingly, Fig. 2.3c shows that Λ_a is depending on the current density. With increasing the current density, the electrical charge decreases (Fig. 2.3c). The upper charging voltage (1 V) is the same for all experiments. The ohmic voltage loss ($R_{ohmic} \cdot I$) is higher at higher current density, which reduces the voltage available to charge the MCDI cell. Consequently, the charge stored in the electrodes is lower at higher current density. Λ_a is higher at higher current densities, and reaches a maximum of 0.76 at 0.6 A m^{-2}. This value corresponds to Λ_c=0.86 (based on Eq. 2.5), which suggests that a minimum of 86% of the electrical charge has been used to adsorb some carbonate and bicarbonate ions.

Although the respective amount of HCO_3^- and CO_3^{2-} adsorbed in the electrode is not known, we can safely assume that $\Lambda \geq 0.86$ at 15% CO_2 and 0.6 A m^{-2}. This value of Λ is in good agreement with MCDI work using monovalent solutions, where high Λ values, around 0.9, are expected[72].

In contrast, lower Λ_a is obtained at lower current density, $\Lambda_a \approx 0.58$ ($\Lambda_c \approx 0.64$) for 0.2 A m^{-2} and $\Lambda_a \approx 0.70$ ($\Lambda_c \approx 0.78$) for 0.4 A m^{-2}, which was not expected. Based on MCDI research with NaCl, it is not expected that at lower current density Λ will decrease. In the case of NaCl, a lowering of Λ is attributed to two main phenomena, which are the co-ion expulsion and faradaic reactions. Co-ion expulsion is negligible in our system as the concentration of the ions is low, below 1 mM, and the ion-exchange membranes blocked the transport of co-ions from the electrodes to the spacer. Also, Λ could be affected by faradaic reactions inside the electrodes, as shown in many studies in MCDI and CDI[73,77,117,118]. However, most studies[73,117,118] suggested that the faradaic reactions involved in MCDI are associated with O_2 and Cl^-, which are both negligible in our electrolyte solution. Furthermore, charge leakages, determined as the difference between the electrode accumulated charge of the charging step and the discharging steps, were on average 4.4% in all our experiments. The charge leakages are reported in Supporting information. In (M)CDI, the charge leakages are expected to be caused by faradaic reactions. Thus, faradaic reactions are not expected to play a major role in the lowering of the adsorption process.

The lowering of Λ_a would thus point to a change in the distribution of HCO_3^- and CO_3^{2-} in the EDL, accompanied by a local high pH in the electrodes. With capacitive electrodes, preferential adsorption of divalent ions over monovalent has been shown to occur over time[120], which suggests the preferential adsorption of CO_3^{2-} rather than HCO_3^- into the pores of the electrode. The pH of the electrolyte cannot explain the preferential adsorption of CO_3^{2-} in the electrode as the pH of the electrolyte is acidic (pH≈3.9-4.4 between 15% and 100% CO_2) and thus CO_3^{2-} is not present at this condition. A higher local pH in the anode would favor the conversion of HCO_3^- into CO_3^{2-} (Eq. **2.3**). During our experiments, the local pH in the pores of both electrodes is unknown. Changes in pH in the electrodes or in the electrolyte in (M)CDI have been mostly related to faradaic reactions[77,118], consuming H^+ in the cathode (high pH) and producing H^+ in the anode (low pH). As described above, this seems unlikely under the condition employed in this experiment (no O_2 and Cl^- present). This leaves the question open on what causes a possible shift in HCO_3^-/CO_3^{2-} adsorption. A possible explanation might be related to the amphoteric property of HCO_3^-. Recent studies in (M)CDI suggest that amphoteric groups could have a significant effect on both the pH in the EDL and the electrolyte[119]. Amphoteric ions have potentially similar properties than amphoteric groups and could also influence

the pH of the electrodes. Thus, more efforts and studies are needed to characterize the pH inside the pores of the electrode with amphoteric ions in order to investigate Λ_c and Λ with a CO_2-flushed deionized water solution electrolyte in MCDI.

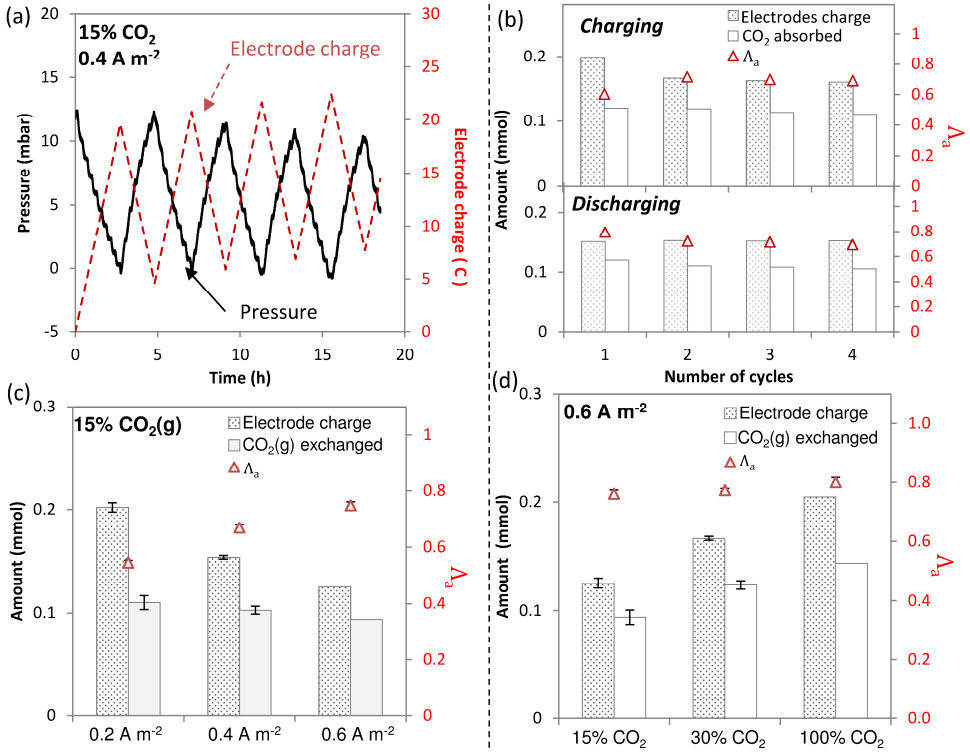

Fig. 2.3: (a) Gas pressure in the gas-liquid contactor and electrode charge at 0.4 A m^{-2} in 15% CO_2(g). Electrode charge, CO_2(g) absorbed and the absorption efficiency (Λ_a) (b) for 0.4 A m^{-2} and 15%, (c) for different current densities at 15% CO_2(g) and (d) for different CO_2 partial pressures at 0.6 A m^{-2}.

To estimate the minimum amount of energy needed to capture CO_2 using MCDI technology, the energy losses to separate the CO_2(g) from the gas phase was estimated. In MCDI, the amount of energy required to desalinate salty streams is obtained by subtracting from the energy input, during the charging step of the GCD, the amount of energy recovered during the discharging step of the GCD[74]. Following the same procedure, energy to capture CO_2(g) was estimated based on the energy input during the CO_2(g) absorption step and the energy recovered during the CO_2(g) desorption step during GCD cycles. The energies input and recovered are shown in supporting information. Two

different types of energy losses were differentiated in this study, which are (i) the ohmic losses (W^*_{ohmic}) related to the ohmic resistance (R_{ohmic}) and (ii) the non-ohmic losses ($W^*_{non-ohmic}$), which are not related to ohmic origins, such as concentration polarization[121] and other non-ideal cell behaviors, such as faradaic reactions.

At 15% CO_2, the total energy consumption to capture CO_2 was found to be between 39.5 and 49 kJ $molCO_2^{-1}$ (≈0.89-1.13 GJ TCO_2^{-1}) for all different current densities tested at 15% CO_2 (Fig. 2.4a). Fig. 2.4a shows that at higher current densities, the energy losses are mainly determined by W^*_{ohmic}. At 0.6 A m^{-2}, W^*_{ohmic} accounts for 70% of the energy losses, whereas at 0.2 A m^{-2}, W^*_{ohmic} accounts for 38% of the energy losses. W^*_{ohmic} is directly dependent on the R_{ohmic} of the capacitive cell and the current density applied. The higher the current, the higher is W^*_{ohmic}. R_{ohmic} is mainly determined by the low conductivity of the electrolyte separating both electrodes, measured around 1.7 mS m^{-1} at 15% CO_2. Reducing R_{ohmic}, e.g., via reducing the electrode distance, could significantly improve the energy efficiency and reduce W^*_{ohmic}. Lower current densities are mainly limited by $W^*_{non-ohmic}$. Further investigation studies are required to understand the cause of $W^*_{non-ohmic}$ to improve the energy efficiency of the MCDI cell. Fig. 2.4b shows that the energy needed to absorb CO_2 decreases at higher CO_2 partial pressures (from 49 kJ $molCO_2^{-1}$ at 15% CO_2 to 27 kJ $molCO_2^{-1}$ at 100% CO_2). This is mainly caused by a lower W^*_{ohmic} due to a decrease of R_{ohmic} at higher CO_2 partial pressure.

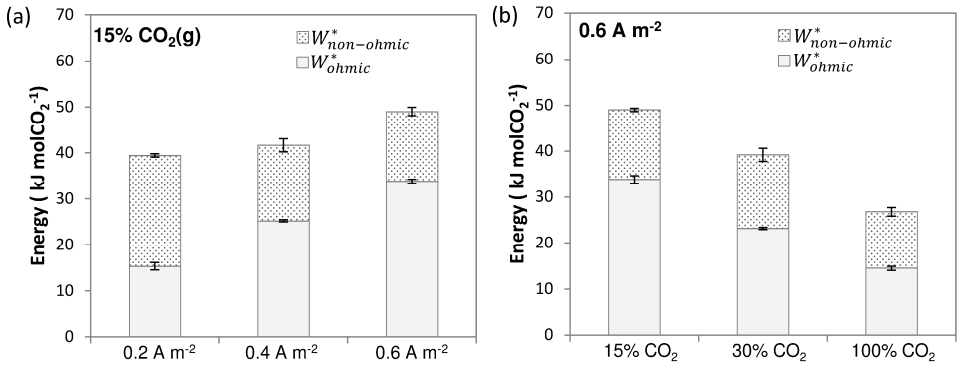

Fig. 2.4: Ohmic losses (W^*_{ohmic}) and non-ohmic losses ($W^*_{non-ohmic}$) for (a) different current densities tested at 15% CO_2(g) and (b) different CO_2 partial pressures tested at 0.6 A m^{-2}.

Meaningful comparison of this technology with conventional methods should be done in realistic and similar conditions i.e., gas composition, scale, design, and operations mode. This study shows a proof of principle, where data are lacking for such a comparison. Thus, we compare the energy performance of the MCDI cell with a similar technology,

which used similar conditions, the supercapacitive swing absorption (SAA)[107]. MCDI clearly shows a lower energy consumption than SAA (41-50 kJ molCO_2^{-1} against 103 kJ molCO_2^{-1})[107]. This difference is mainly due to the much lower Λ_a of SAA. We estimated, based on the data shown on SWA[107], Λ_a=0.2-0.3 at 2 mA, which is 3 times lower than Λ_a obtained in MCDI. The difference in Λ_a seems to point to a difference in adsorption mechanisms of both technologies. Both SWA and MCDI use capacitive electrodes to drive the sorption or desorption of CO_2(g) in an electrolyte. In SAA, however, a 1M NaCl electrolyte is used, while in MCDI deionized water is used containing only dissolved carbonate species. In SAA, the authors claim that the CO_2 gas is directly adsorbed as a neutral species inside the EDL made of Na^+ and Cl^-. In MCDI, we claim that the CO_2(g) is absorbed into the electrolyte due to the formation of an EDL consisting of carbonate species (HCO_3^- and CO_3^{2-}) as no other anions are present in the deionized water. Thus, SWA is expected to be dependent on both the CO_2 partial pressure, as adsorption process is knowns to be pressure dependent, and the electrode charge. In MCDI, the CO_2 sorption is expected to be only dependent on the electrical charge, since the CO_2 sorption is driven only by the adsorption of ions. The difference between both sorption principles is well demonstrated at different CO_2 partial pressures experiments. In SWA, the amount of CO_2 adsorbed in the electrolyte increases significantly (3.5 times) between 15% and 100% CO_2 gas mixtures (based on data in Ref.[107]), whereas, the amount of CO_2 absorbed was not significantly affected by the CO_2 partial pressure in MCDI. The small increase of CO_2 absorption observed in MCDI at higher CO_2 partial pressure was mainly caused by a higher amount of electrical charge stored in the electrodes.

In applications, CO_2(g) should be absorbed from a diluted gas mixture, for instance, 15% CO_2(g), when the MCDI is charged, and desorbed into a concentrated stream, ideally 100% CO_2(g), when the MCDI is discharged. A membrane contactor could be used to separate the gas from the liquid phase after the charging and the discharging steps, respectively. Experiments at different CO_2 gas mixtures show that the system can be operated with different gas mixtures. In this study, the CO_2 capture rate was still low ($6 \cdot 10^{-9}$ mol s^{-1} g_{carbon}^{-1}), which is 50 times lower than the state of the art of CO_2 capture based on adsorption materials like zeolite[122]. The lower capture rate is mainly caused by the low current densities used and the non-optimal Λ_a. In our experimental set-up, the current density is mainly limited by R_{ohmic}, as increasing the current density increases W^*_{ohmic}. Reducing the internal resistance is thus not only of paramount interest for the energetic performance but would be even more for improving the capture rate.

In conclusion, we proposed a new concept to capture CO_2 using capacitive electrodes and deionized water. This system could potentially capture CO_2 at lower energy consumption and without any addition of chemical solvent or heat. In this study, we

showed the first proof of principle of this concept and reported energy consumption comparable to or lower than similar technology, such as swing supercapacitive adsorption. This energy consumption can be potentially lowered by reducing ohmic losses and non-ohmic losses. This could be based on well-known strategies from the field of MCDI or new ones based on insight to be developed on the amphoteric behavior of bicarbonate in the double layer. Moreover, a continuous process to capture CO_2, including an MCDI should be developed and tested to compare this new concept to other electrochemical technologies.

2.4. Supporting information

2.4.1. Calculations

Estimation of the External Electronic Resistance (EER)

The resistance in an (M)CDI can be divided into the electronic resistance and the ionic resistance. The electronic resistance was previously described as the External Electronic Resistance (EER). It was defined as the resistance generated by the cable's wires connecting the galvanostat to the MCDI cell, the resistance of the current collector, and the different contact resistances (cables-current collector and current collector-electrodes). On the contrary, the ionic resistance is related to the ionic conductivity of the ions present in the electrodes, the membrane, and the spacer compartment.

Recently, Dykstra et al. proposed a simple method to estimate the EER[115] by measuring the internal resistance of the MCDI cell at different NaCl ionic conductivity solutions. By subtracting the contribution of the ionic resistivity of the solution on the total internal resistance measured, it is then possible to isolate the EER. We performed this test in our cell with different concentrations of NaCl (from 1 M NaCl to 1 mM NaCl), and CO_2 dissolved deionized water at different CO_2 partial pressures. Fig. S2.1 shows that EER was found around 0.6 Ω. This value is between 40 and 75 times lower than the resistance measured in all experiments. Since the resistance is dominated by the low ionic conductivity of CO_2-flushed deionized water, we assume EER negligible.

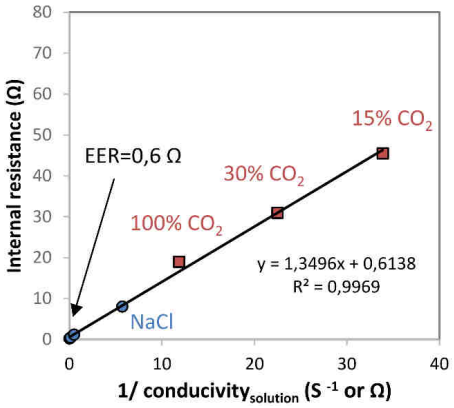

Fig. S2.1: Internal resistance measurement at different salt concentrations (NaCl) and CO_2-flushed deionized water at different CO_2 partial pressure. The intersection with the y-axis represents the external electronic resistance in our set-up.

Relationship between the absorption efficiency and the carbon adsorption efficiency

CDI and MCDI systems are commonly characterized by charge efficiency (Λ) for monovalent salt, which defined the ratio of salt ions removed from the electrolyte, divided by the total electrical charge transferred. In the case of CO_2-flushed deionized water, monovalent and divalent ions are in the electrolyte. Thus, the charge efficiency is defined as:

$$\Lambda = \frac{n_{HCO_3^-(ad)} + 2\, n_{CO_3^{2-}(ad)}}{n_{charge}} \qquad \text{S2.1}$$

In this study, we are interested in the removal of the total carbon (n_T), contained into two different phases: a liquid and gas phase. Thus, next to Λ, we define two related metrics named electrode carbon adsorption efficiency (Λ_c) and absorption efficiency (Λ_a). The different metrics are illustrated in Fig. S2.2.

Λ_c is defined as the ratio of total carbon ($H_2CO_3^*$ and $CO_2(g)$) exchanged from the system, caused by the adsorption of HCO_3^-/CO_3^{2-} by the molar electrode charge.

$$\Lambda_c = \frac{n_{HCO_{3(ad)}^-} + n_{CO_3^{2-}(ad)}}{n_{charge}} = \frac{dn_T}{dn_{charge}} \quad \text{S2.2}$$

Since H^+ is the only cation in the bulk solution, $[H^+]>>[OH^-]$, hence the acidic pH in solution. Given the high pKa of pK_2 (10.33 M) and the low pH of the bulk solution, we can assume that CO_3^{2-} is negligible. Moreover, pKa of pK1 and pK2 suggest that $H_2CO_3^*$ is the dominant carbon molecule in solution at low pH. Hence, $[H_2CO_3^*]>>[HCO_3^-]>>[CO_3^{2-}]$. Thus, we assume the amount of carbon in deionized water only depending on $[H_2CO_3^*]$.

$$H_2CO_3^* \overset{k_1}{\leftrightarrow} HCO_3^- + H^+ \quad \text{with } pK_1=6.35 \text{ M} \quad \text{S2.3}$$

$$HCO_3^- \overset{k_3}{\leftrightarrow} CO_3^{2-} + H^+ \quad \text{with } pK_2=10.33 \text{ M} \quad \text{S2.4}$$

Thus, Λ_c can be defined in Eq. S2.5.

$$\Lambda_c = \frac{dn_T}{dn_{charge}} \approx \frac{dn_{CO_2(g)} + dn_{H_2CO_3^*}}{dn_{charge}} \quad \text{S2.5}$$

Λ_a is defined as the ratio between the molar amount of CO_2 from the gas phase exchanged divided by the molar electrical charge.

$$\Lambda_a = \frac{dn_{CO_2(g)}}{dn_{charge}} \quad \text{S2.6}$$

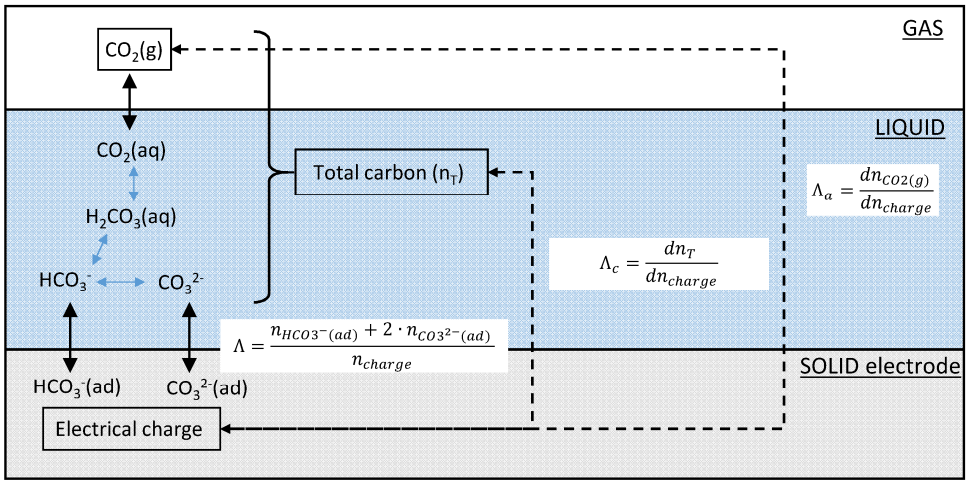

Fig. S2.2: illustration of the different metrics used in the system, which are Λ, Λ_c and Λ_a.

For low dilute solutions, the physical equilibrium for the dissolution of CO_2(g) into deionized water is given by the CO_2 solubility constant:

$$[H_2CO_3^*] = H^{cc} \cdot [CO_2(g)] \qquad \text{S2.7}$$

where H^{CC} represents the solubility constant for CO_2 in water at 298 K.

$$n_{H_2CO_3^*} = \frac{H^{cc} \cdot V_w}{V_g} \cdot n_{CO_2(g)} \qquad \text{S2.8}$$

V_w stands for the water volume in the system. From Eqs. S2.5 and S2.8, we can derive the absorption efficiency according to the carbon adsorption efficiency (Eq. S2.9).

$$\Lambda_c = (1 + \frac{H^{cc} \cdot V_w}{V_g}) \cdot \frac{dn_{CO_2(g)}}{dn_{electrons}} \qquad \text{S2.9}$$

By integrating Eqs. S2.6 and S2.9, we obtain:

$$\Lambda_a = (1 - f_w) \cdot \Lambda_c \qquad \text{with } f_w = \frac{Vw \cdot H^{cc}}{Vg + Vw \cdot H^{cc}} \qquad \text{S2.10}$$

By substituting V_W=0.033 L, V_g=0.233 L, H^{cc}=0.83, we obtain:

$$\Lambda_a \approx 0.89 \cdot \Lambda_c \qquad \text{S2.11}$$

2.4.2. Figures

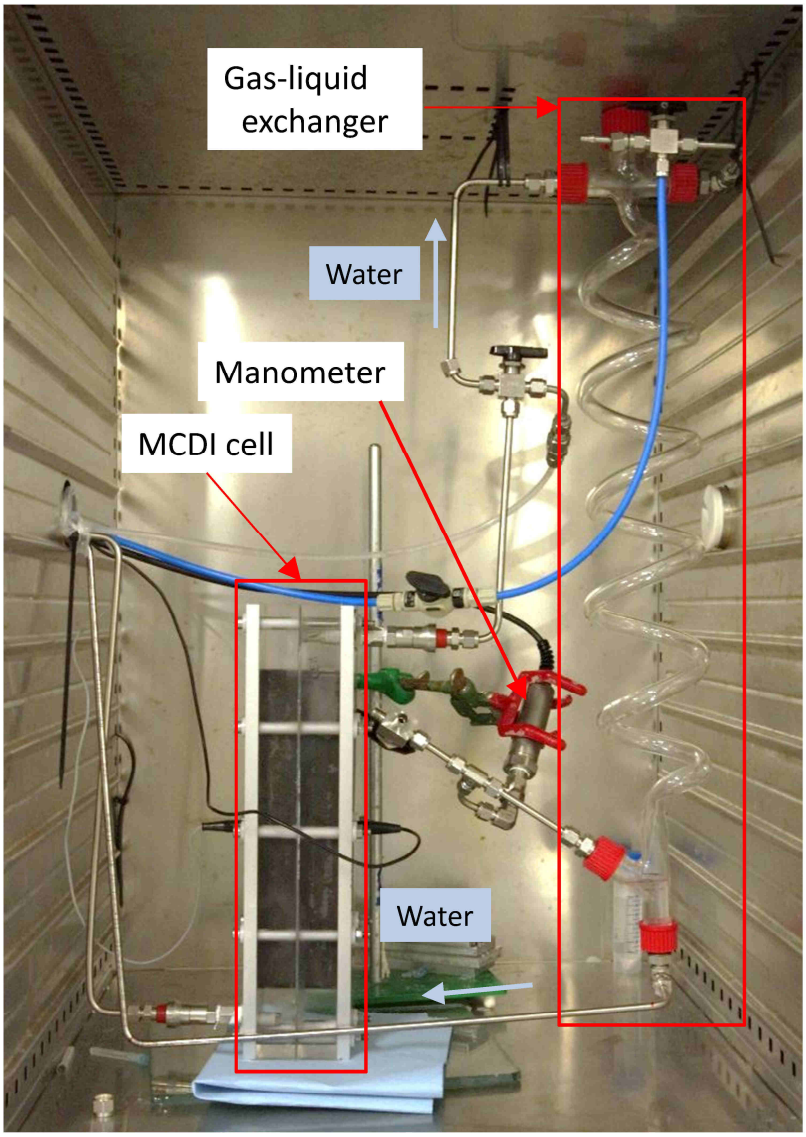

Fig. S2.3: Photo of the research set-up during operation. The peristaltic pump is located outside the temperature-controlled chamber

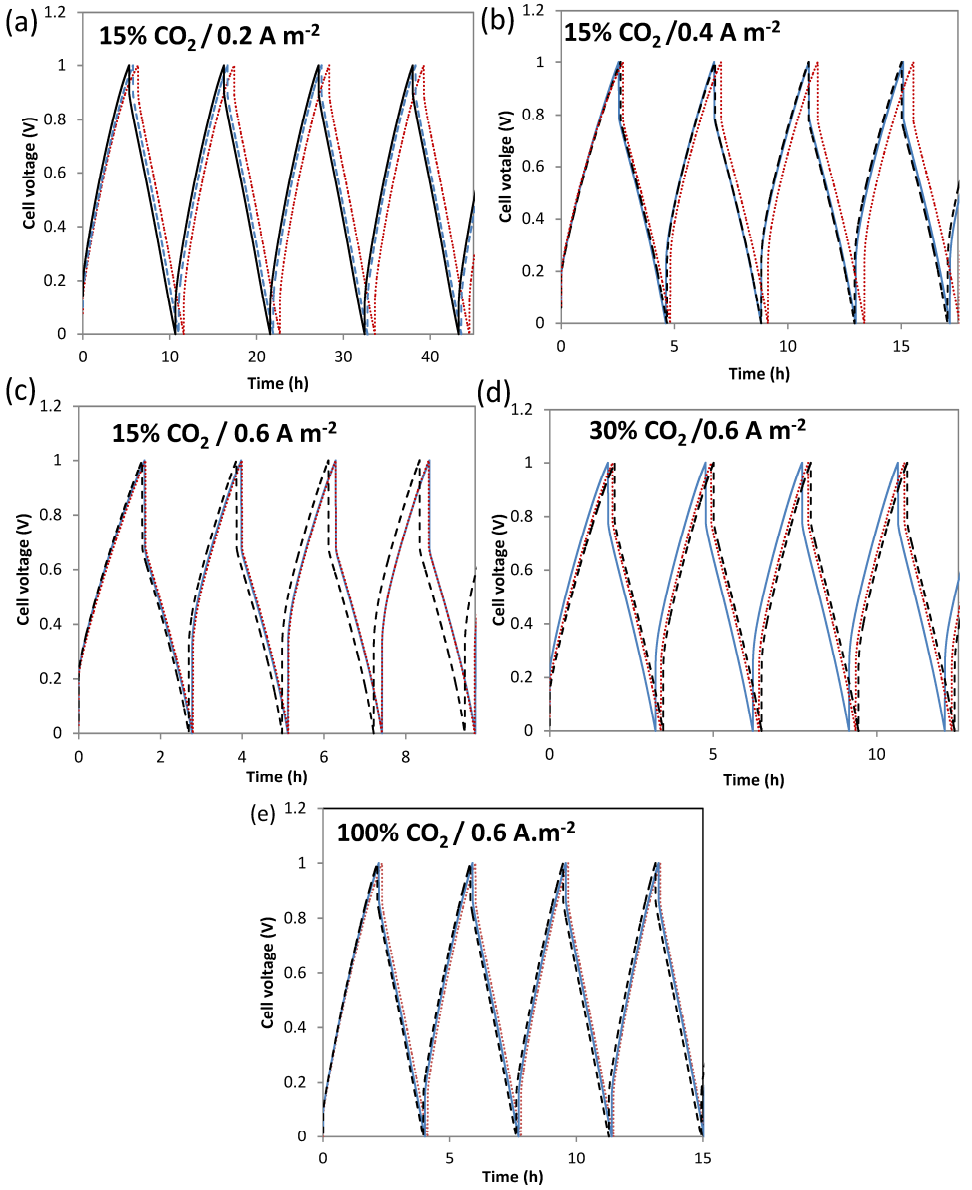

Fig. S2.4: Cell potential during Galvanostatic charge-discharge at different current densities with (a-c) 15% CO_2, (d) 30% CO_2 and (e) 100% CO_2-flushed deionized water. Three replicates are shown on each graph.

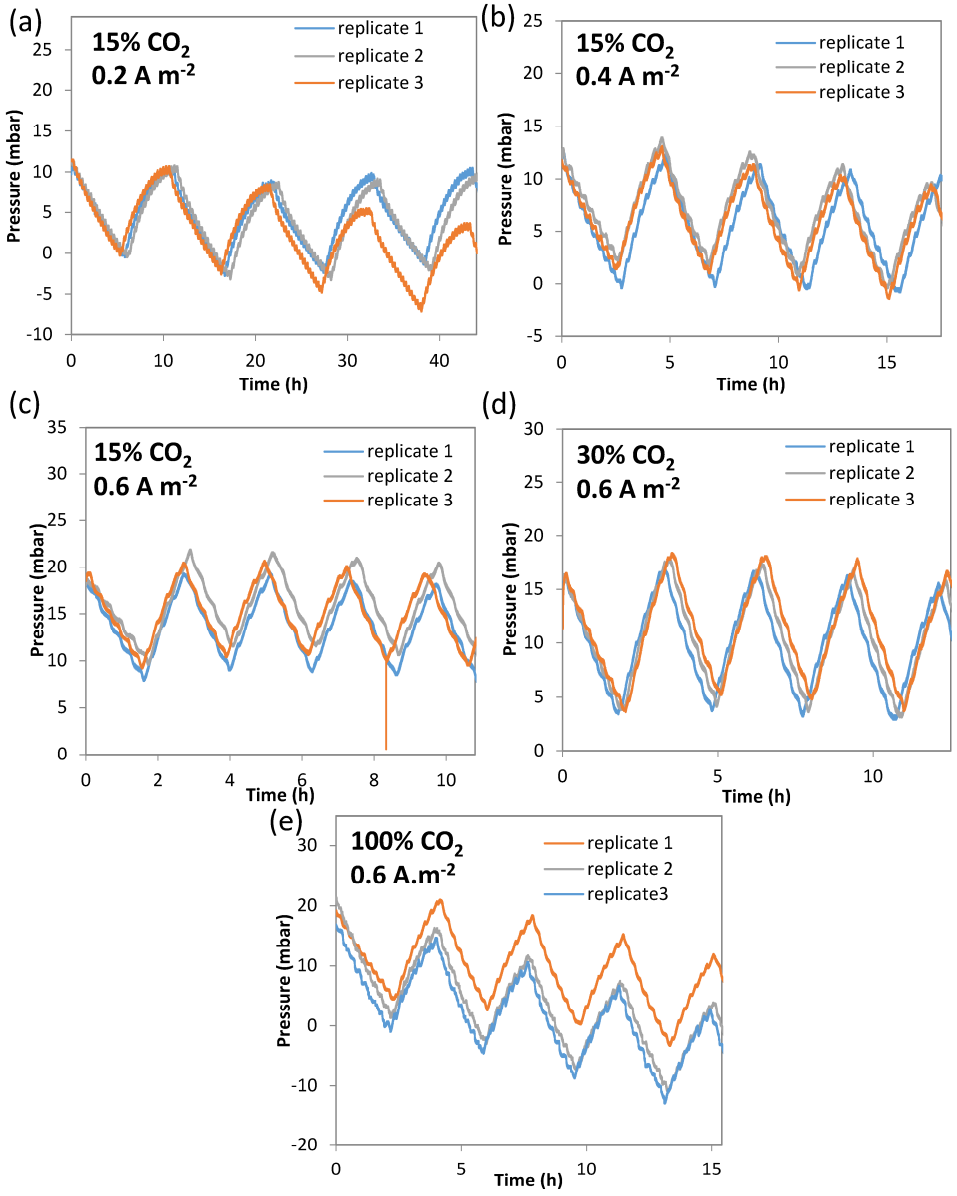

Fig. S2.5: Gas-liquid contactor pressure for (a-c) 15% CO_2 (d) 30% CO_2 and (e) 100% CO_2 for different current densities.

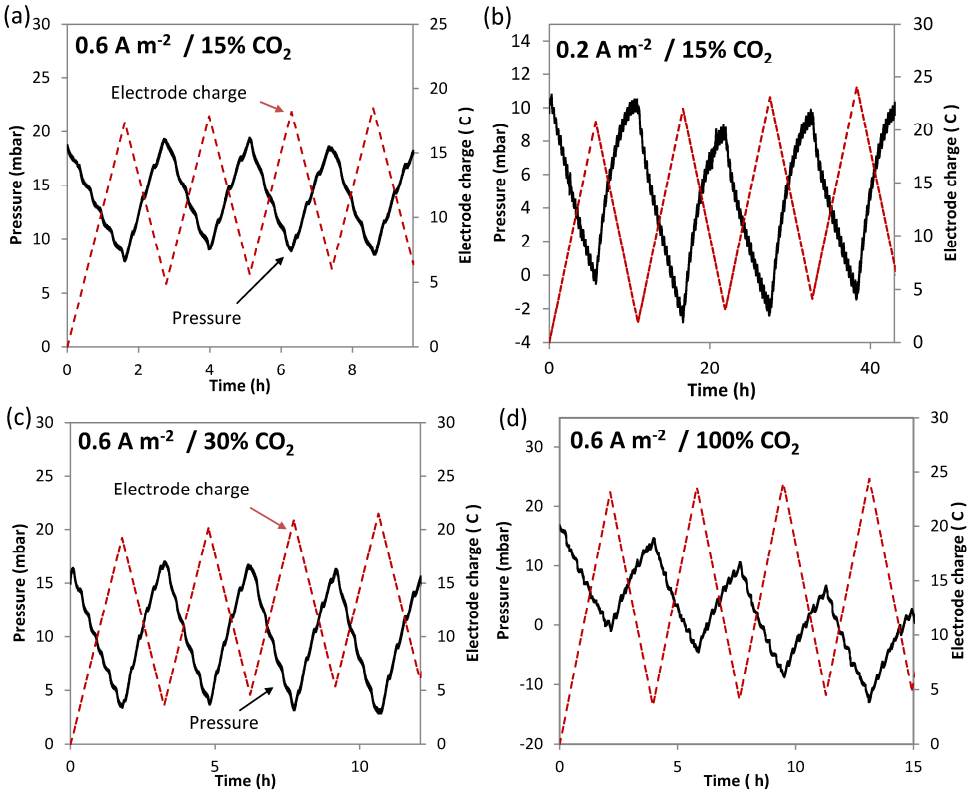

Fig. 2.6: Gas-liquid contactor pressures and electrodes charge at (a,b) 15% CO_2, (c) 30% CO_2 and (d) 100% CO_2 for different current densities.

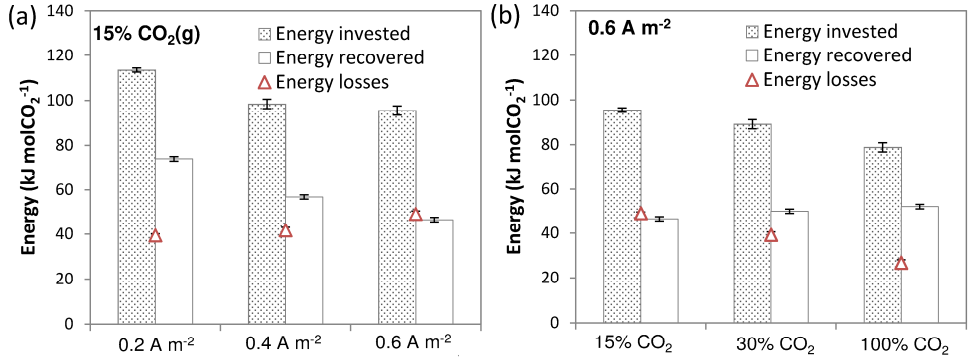

Fig. 2.7: Specific energy losses obtained during charge and discharge (a) for different current densities at 15% CO_2 and (b) for different CO_2 partial pressures at 0.6 A m^{-2}.

Table S2.1: Electrode charge, CO_2(g) absorbed, Λ_a, Λ_c, W_{net}, W^*_{net} , W^*_{ohmic} $W^*_{non-ohmic}$ for different current densities and different CO_2 partial pressures.

	Electrode charge (Coulomb)			CO_2(g) absorbed (µmol)		Λ_a		Λ_c
	Charging step	Discharging step	Charge leakage	Charging step	Discharging step	Charging step	Discharging step	Average
0.2 A m-2 15% CO2	20.1 (±0.3)	18.8 (±0.1)	1.26 (±0.4)	118 (±4.0)	110 (±6.8)	0.59 (±0.03)	0.55 (±0.04)	0.61 (±0.05)
0.4 A m-2 15% CO2	15.2 (±0.4)	14.6 (±0.2)	0.6 (±0.5)	112 (±1.6)	103 (±3.9)	0.72 (±0.02)	0.67 (±0.03)	0.75 (±0.04)
0.6 A m-2 15% CO2	12.3 (±0.3)	11.9 (±0.2)	0.4 (±0.1)	97 (±0.9)	94 (±0.9)	0.77 (±0.02)	0.75 (±0.01)	0.84 (±0.02)
0.6 A m-2 30% CO2	16.2 (±0.04)	15.5 (±0.1)	0.7 (±0.1)	129 (±1.6)	124 (±0.09)	0.80 (±0.01)	0.74 (±0.01)	0.83 (±0.01)
0.6 A m-2100% CO2	19.8 (±0.2)	19.2 (±0.2)	0.7 (±0.1)	178 (±5.1)	144 (±2.5)	0.89 (±0.02)	0.70 (±0.02)	0.78 (±0.02)

	Energy (J cycle^{-1})			Energy (kJ molCO_2^{-1})			Energy (kJ molCO_2^{-1})	
	Charging step	Discharging step	W_{net}	Charging step	Discharging step	W^*_{net}	W^*_{ohmic}	$W^*_{non-ohmic}$
0.2 A m^{-2} 15% CO_2	13.0 (±0.3)	8.4 (±0.1)	4.5 (±0.3)	113 (±0.2)	74.0 (±2.1)	39.42 (±2.1)	15.3 (±0.2)	24.1 (±2.0)
0.4 A m^{-2} 15% CO_2	10.6 (±0.3)	6.1 (±0.1)	4.5 (±0.3)	98.4 (±1.7)	56.7 (±1.4)	41.7 (±1.9)	25.2 (±0.3)	16.5 (±1.7)
0.6 A m^{-2} 15% CO_2	9.1 (±0.1)	4.4 (±0.03)	4.7 (±0.1)	95.5 (±0.7)	46.5 (±0.6)	49.0 (±1.0)	33.8 (±0.8)	15.18 (±0.4)
0.6 A m^{-2} 30% CO_2	11.3 (±0.1)	6.3 (±0.1)	4.9 (±0.2)	89.1 (±1.4)	49.9 (±0.4)	39.2 (±1.7)	23.2 (±0.2)	16.0 (±1.4)
0.6 A m^{-2} 100% CO_2	12.7 (±0.1)	8.4 (±0.1)	4.3 (±0.1)	78.8 (±2.0)	52.02 (±0.8)	26.7(±1.3)	14.5 (±0.4)	12.3 (±0.9)

Chapter 3

Electrical energy from CO_2 emissions by direct gas feeding in capacitive cells

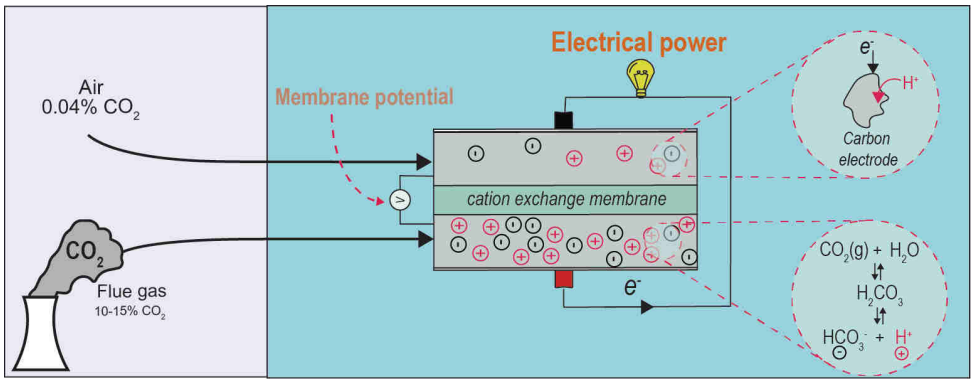

This Chapter has been published as:

L. Legrand, O. Schaetzle, M. Tedesco, H.V.M. Hamelers, Electrical Energy from CO_2 emissions by direct gas feeding in capacitive cells, *Electrochim. Acta.* 319 (**2019**) 264-276. doi:10.1016/j.electacta.2019.06.126.

Abstract

This work demonstrates the possibility of harvesting electrical power from CO_2 emissions by feeding CO_2 and air gas directly into a capacitive cell. Hamelers et al. previously showed that the available mixing energy of CO_2 emitted into the air could be converted into electricity but at high energy costs for gas-sparging in the process. In the present work, electrical power is generated by feeding the gas directly into the capacitive cell. We investigated three different cell designs (namely, "conventional," "flow-by(wire)," and "flow-by(flat)"), by changing both electrode and cell geometry. The flow-by(flat), inspired from fuel cell design, showed the best performance thanks to a high membrane potential (≈190 mV), which is the highest value so far reported from CO_2 and air. A maximum membrane apparent permselectivity between CO_2 and air of 90% was obtained, i.e., almost double of values reported in previous studies. On the contrary, the "conventional" cell design gave poor performance due to non-optimal gas flow in the cell. We highlight the importance of water management and internal electrical resistance, to indicate directions for future developments of the technology.

3.1. Introduction

It is widely accepted that the increase of the CO_2 concentration in the atmosphere is linked to climate change, leading to a global pledge to reduce carbon dioxide emissions[13]. To reach this objective, the international energy agency (IEA) suggested a panel of different mitigation strategies, including the increase of clean and renewable energy production and the improvement of energy efficiency of thermal power plants[13]. In close relation with these two strategies, Hamelers et al. demonstrated a concept to extract electrical energy from CO_2 emissions (from exhaust gases, combustion of biomass, cement, or steel industries) when mixed in the atmosphere[23]. This energy extraction process is based on the mixing energy available when two streams of different concentrations, such as CO_2 in the flue gas and atmospheric air, are mixed. This new technology uses a capacitive cell, but given the recentness of the concept, its designs have yet to be optimized, as we further explore in this article.

Up to now, the chemical mixing energy has been mostly exploited for salt streams of different salt concentrations, such as freshwater and seawater (i.e., "salinity gradient energy" processes). For that application, several technologies have been developed by using, e.g., semipermeable membranes in pressure-retarded osmosis (PRO)[123–125], ion exchange membranes in reverse electrodialysis (RED)[88,121,126–128], capacitive electrodes[129,130], capacitive electrodes covered by ion exchange membrane[18–20,131,132], and intercalation electrodes[133]. To the exception of pressure-retarded osmosis, these technologies are electrochemically-based, which rely on the presence of ions, i.e., mostly Na^+ and Cl^{-+} in case of salt, to generate electrical power. Therefore, the mixing energy between CO_2 and air gas streams can only be harvested into electrical power if the CO_2 concentration difference between both gases is converted into an ion concentration difference. The shift of concentration difference, from CO_2 gas to ions, was previously obtained from the chemical reaction between CO_2 and water to form HCO_3^- and H^+ ions (Eqs. **3.1**-**3.3**) by sparging CO_2 and air into an aqueous solvent[23]. In the Eqs. **3.1**-**3.3**, $H_2CO_3^*$ includes both concentrations of CO_2(aq) and H_2CO_3. These two species are usually considered together, as they are difficult to distinguish. The value for K_H (defined as aqueous concentration over gaseous concentration) was calculated from Refs.[24,25], and the K_1 and K_2 values were taken from Ref.[26].

$$\mathbf{H_2CO_3^*} = \frac{\mathbf{P_{CO_2}}}{\mathbf{K_H}} \qquad K_H = 29.5 \text{ atm M}^{-1} \qquad 3.1$$

$$\mathbf{H_2CO_3^*} \overset{\mathbf{K_1}}{\leftrightarrow} \mathbf{HCO_3^-} + \mathbf{H^+} \qquad K_1 = 10^{-6.35} \text{ M} \qquad 3.2$$

$$\mathbf{HCO_3^-} \overset{\mathbf{K_2}}{\leftrightarrow} \mathbf{CO_3^{2-}} + \mathbf{H^+} \qquad K_2 = 10^{-10.33} \text{ M} \qquad 3.3$$

Among these technologies, energy from CO_2 gas has been successfully harvested with capacitive electrodes covered by ion exchange membrane[23,28,29], used in a capacitive cell, and selective intercalation electrodes[27], used in a pH-gradient flow cell. Both technologies differ in the combination of the aqueous solution, the type of electrodes, and the technology principle. In the pH-gradient cell[27], an H^+ concentration gradient was obtained by sparging CO_2 and air into 1 M $NaHCO_3$. Both saturated-solutions were pumped into a 2-compartment cell, each containing MnO_2 electrode, generating an open-cell voltage between both electrodes. MnO_2 electrodes have H^+ intercalating through redox reaction properties and can generate an open-cell voltage based on the difference of H^+ concentration on each electrode surface defined by the Nernst equation. In the capacitive cell[23], an H^+ and HCO_3^- concentration difference is obtained by sparging CO_2(g) in deionized water. Both saturated-solutions were then alternatively pumped into a capacitive cell, containing one electrode covered by a cation exchange membrane (CEM), and one electrode covered by an anion exchange membrane (AEM). In such a system, a membrane potential is established across the CEM due to the H^+ concentration ratio across the membrane, whereas a membrane potential is established across the AEM due to the HCO_3^- concentration ratio across the membrane. Fig. 3.1a illustrates the source of the CEM membrane potential in our system, resulting from the ion concentration difference of H^+ obtained by sparging pure CO_2 (100% CO_2) and air (0.04% CO_2) in water. Fig. 3.1b shows the pH of the CO_2-saturated solution for different CO_2 partial pressures according to Eqs. **3**.**1**-**3**.**3**, and the resulting theoretical membrane potential obtained from that solution and air-sparged water. The theoretical membrane potential expected between air-saturated and pure CO_2-saturated water solutions is around ≈102 mV for each membrane, AEM, and CEM (Fig. 3.1b). The relationship between the chemical equilibrium of CO_2 and deionized water, as well as the membrane potential, is extensively described in Refs.[23,29]. Note that a 0.25 M Monoethanolamine (MEA) solution was also used as an aqueous solution in the capacitive cell[23]. Although MEA shows better performance (i.e., a maximum power density of 4.5 mW/m^2, against 0.28 mW/m^2 for deionized water), this solvent is not recommended as the reaction between CO_2 and MEA solution is not isothermally reversible[134,135]. In fact, the amount of energy to regenerate the amine solvent (≈100 kJ/molCO_2)[134] is ten times higher than the mixing energy available between CO_2 and air (≈10.3 kJ/molCO_2)[23].

The pH-gradient flow cell demonstrated 200 times higher power density performance than the capacitive cell[27], mainly due to the higher conductivity of 1 M $NaHCO_3$ solution (≈45 mS cm^{-1}) compared to the CO_2-saturated water (≈45 µS cm^{-1}). Nevertheless, for both technologies, sparging CO_2 into aqueous solutions and pumping the resulting equilibrated solution into the cell are energy-intensive steps. Previous calculations indicated that these two steps (i.e., gas sparging and gas pumping) could either totally cancel out the energy extracted[23] or reduced its amount drastically[27].

Investigating new CO_2 feeding strategies in the cell is of paramount importance to minimize the sparging and pumping energy costs. Therefore, in this study, we investigate the possibility to feed the CO_2 gas and air directly into the capacitive cell. We will refer to this method as "gas-feeding" operation, to distinguish from the above-mentioned "solution-feeding" operation, where the capacitive cell is fed with gas-saturated aqueous solutions. In gas-feeding operation, the chemical equilibrium between CO_2 and water does not occur in a sparging step outside the capacitive cell but directly inside the capacitive cell.

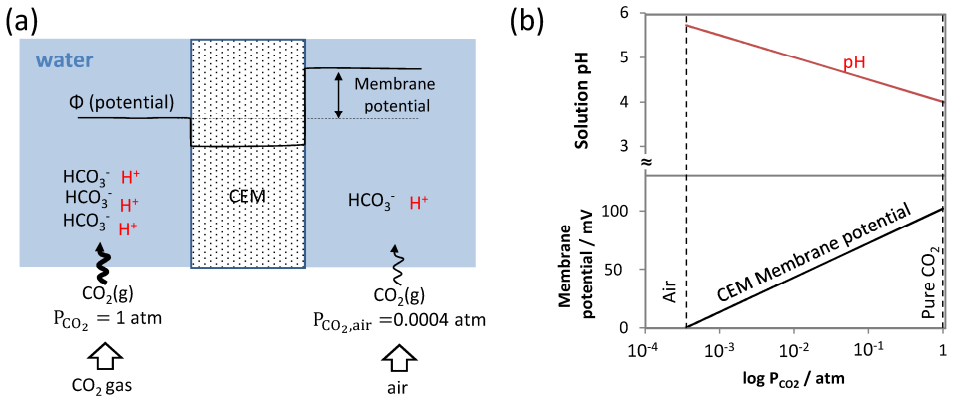

Fig. 3.1:(a) Graphical representation of the CEM membrane potential. Pure CO_2 and air are sparged into water on each CEM side. Due to the difference of CO_2 partial pressure on both the CEM side, a ratio of HCO_3^- and H^+ (or pH) occurs across the CEM. As a result, a potential difference across the membrane arises, referred to as "membrane potential." (b) Calculated pH of the CO_2-saturated water for different CO_2 partial pressures, and theoretical membrane potential (based on Eq. 3.6) obtained between air-saturated water and CO_2-saturated water at different CO_2 partial pressures

In a previous study[23], a flat-shaped conventional capacitive cell (Fig. 3.2a) was used to harvest electrical power. In such a "conventional" design, the solution was fed in a channel between the electrodes (Fig. 3.2a). This flow configuration is not expected to be optimal in the case of gas-feeding operation. Even if the membranes and the channel are pre-wetted, the gas fed into the channel can rapidly dry the membrane surface and the channel, thus causing an increase in the internal electrical resistance. To use a gas-feeding operation and overcome this problem, we modified the gas flow configuration of the cell from "flow-in-between" the electrodes to a "flow-by" configuration, where the gas streams are fed along the electrodes. Besides, two different electrode geometry were investigated, i.e., the "flow-by(wire)" and the "flow-by(flat)" (Fig. 3.2b and c). The flow-by(wire) has been proven to decrease the internal resistance of a capacitive cell for

harvesting energy from seawater and freshwater streams[19,21,22,136,137]. Unlike the conventional design, the membranes and electrodes are in direct contact, giving efficient ionic contact between both electrodes. This design is suitable for gas-feeding operation as the contact between the membranes and electrodes ensure good conductivity between both electrodes while sparging CO_2 and air. The flow-by(flat) design (Fig. 3.2c) was inspired by the Proton Exchange Membrane (PEM) fuel cell technology, e.g., using CO_2 gas for CO_2 reduction[138–143], or H_2 for electrical power generation[144–148]. In this case, both electrodes are in contact with an ion exchange membrane, and the gas flow occurs by the electrodes. In this design, the contact between the electrodes and the ion exchange membrane is beneficial to keep a good ionic conductivity between the electrodes in gas-feeding operation.

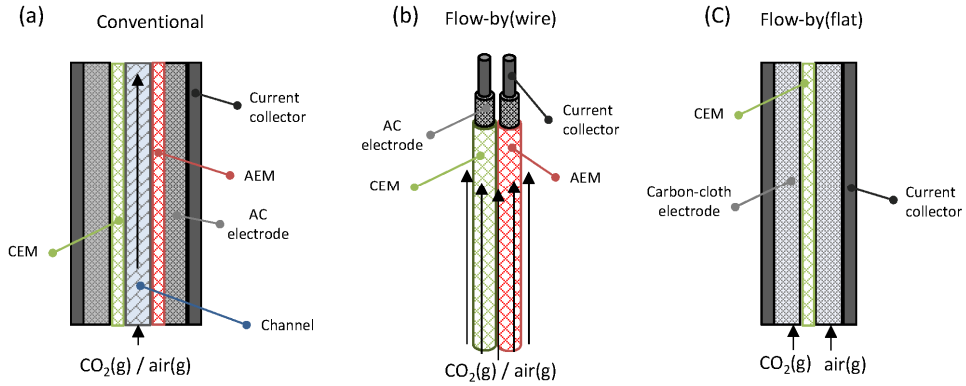

Fig. 3.2: Graphical representation of the investigated cell designs. (a) Conventional (as in Ref.[23]), (b) flow-by(wire), and (c) flow-by(flat).

In this study, we characterized the performance of the three different cell designs shown in Fig. 3.2, using both solution-feeding and direct gas operations. By comparing the performance of the three different designs, we identify the benefits and limitations of each cell design, thus giving future directions to develop new cell design to harvest energy from CO_2 emissions.

3.2. Experimental

3.2.1. Cell and material preparations

Three different capacitive cells were used and compared: the conventional design, the flow-by(wire) design, and the flow-by(flat) design (Fig. 3.2). The conventional cell

configuration was previously described in Refs.[18,23]. This cell consisted of two different homemade capacitive electrodes of activated carbon, coated on a graphite foil current collector. One of the electrodes was covered with a CEM (Ralex CMH, Mega, Czech Republic), and the other electrode was covered by an AEM (Ralex AMH, Mega, Czech Republic). Both membranes were separated by a 200 µm thick polymer spacer (PA 6.6 fabric, Nitex 03-300/51, Sefar, Switzerland) to create a channel between the membranes. The homemade capacitive electrodes were prepared by applying a previously reported method[18,23]. Each capacitive electrode was composed of a layer of 90wt% activated carbon (DLC Super 30, Norit, The Netherlands; BET= 1600 m^2/g) and 10wt% polyvinylidene fluoride (PVDF) binder (KYNAR HSV 900, Arkema Inc., USA). The final electrode weight, thickness, and surface are shown in Table 3.1. Scanning Electron Microscope (SEM) images of the activated carbon electrodes are available in Fig. 3.3.

The flow-by(wire) cell (Fig. 3.2b) consisted of two wire-shaped electrodes, which were made in a 2-step procedure. In the first step, a capacitive layer made of 90wt% activated carbon and 10wt% PVDF was coated onto a current collector made of titanium-coated platinum, following the procedure reported in Refs.[19,22]. The resulting rod was composed of 0.13 g of activated carbon. In the second step, an ion exchange membrane was hot-pressed on each electrode for 10 min at 130°C and 2 bars into a homemade shaped stainless steel mold. Both electrodes were hot-pressed with a CEM and with an AEM (Ralex CMH/AMH, Mega, Czech Republic), respectively. The electrode properties are shown in Table 3.1, and a picture of the final electrodes is shown in Fig. 3.3. More detailed SEM images are shown in supporting information. The resulting final electrodes were treated in CO_2-saturated deionized water for three days, changing the solution at least three times per day. The gas or liquid was fed around the membranes in a “flow-by” gas flow configuration.

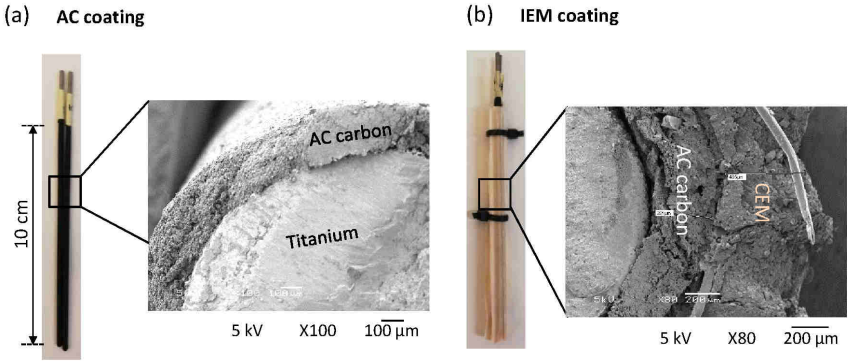

Fig. 3.3: Pictures and SEM images of the flow-by(wire). (a) Wire-shaped electrodes coated with Activated Carbon (AC) layer on the current collector (titanium coated platinum); (b) after hot-pressing the ion exchange membranes (IEM) on the AC layer.

The flow-by(flat) cell consisted of two carbon cloth electrodes (ACC-5092-15, Kynol, Germany) separated by a CEM (Ralex, CMH, Mega, Czech Republic). SEM images of the carbon cloth are available in Fig. 3.3. The solution or gas was fed along the electrodes in a 'flow-by" configuration. The electrode properties are shown in Table 3.1. The electrodes were pre-treated in CO_2-saturated deionized water for three days; the solution was renewed at least three times per day.

Table 3.1: Characterization of the capacitive cells

	Conventional	**flow-by(wire)**	**flow-by(flat)**
Electrode material	Activated carbon	Activated carbon	Carbon cloth
Carbon weight	2 g	0.29 g	0.4 g
Carbon layer thickness	200 µm	40 µm	500 µm
Membrane(s) surface area	100 cm^2	15.2 cm^2	9 cm^2
Gas flow-rate	1 L min^{-1}	1 L min^{-1}	0.25 L min^{-1}
Optimal current for solution-feeding operation	20 mA m^{-2}	33 mA m^{-2}	222 mA m^{-2}
Optimal current for gas-feeding operation	5 mA m^{-2}	16.5 mA.m^{-2}	111 mA m^{-2}

3.2.2. Capacitive cell designs

The main experimental plan was composed of a matrix of 6 different cell designs, shown in Fig. 3.4. Each cell design was characterized both under solution-feeding and gas-feeding operations. In solution-feeding operation (Fig. 3.4a,c,e), CO_2 and air gases were separately sparged into two tanks filled with deionized water. For the conventional and flow-by(flat) designs in solution-feeding operation, the CO_2-saturated and air-saturated water solutions were alternately pumped at 20 mL min^{-1} into the capacitive cell with a peristaltic pump (Cole-Parmer, Masterflex L/S). The outflow solution was discarded and not recirculated into the deionized water tanks to avoid any ion contamination of the deionized water tanks. For the flow-by(wire) design in solution-feeding operation (Fig. 3.4c), the wire-shaped cell was alternatively immersed into the CO_2-saturated water, and the air-saturated water containers by hand.

For the gas-feeding operation experiments (Fig. 3.4b,d,f), pure CO_2 and air were directly fed into the capacitive cell, using mass-flow controllers (mass view, MV-104, Bronkhorst, The Netherlands). Different gas-flow rates were tested during OCV cycles (0.1, 0.25, 0.5, 1 and 2 L min^{-1}). The gas flows used to harvest electrical power during 4-step energy cycles for each cell design are reported in Table 3.1. The flow-by(wire) cell in the gas-feeding condition was placed into a glass container. The gases were humidified by sparging the gas first into water before being feed into the capacitive cell. The gas humidity was measured in-between 80%-90% with a humidity sensor (CO2S-WH-69, CO2Meter.com, USA) for all experiments. All the systems were tested using a galvanostat (Ivium, the Netherlands) connected to the capacitive cell.

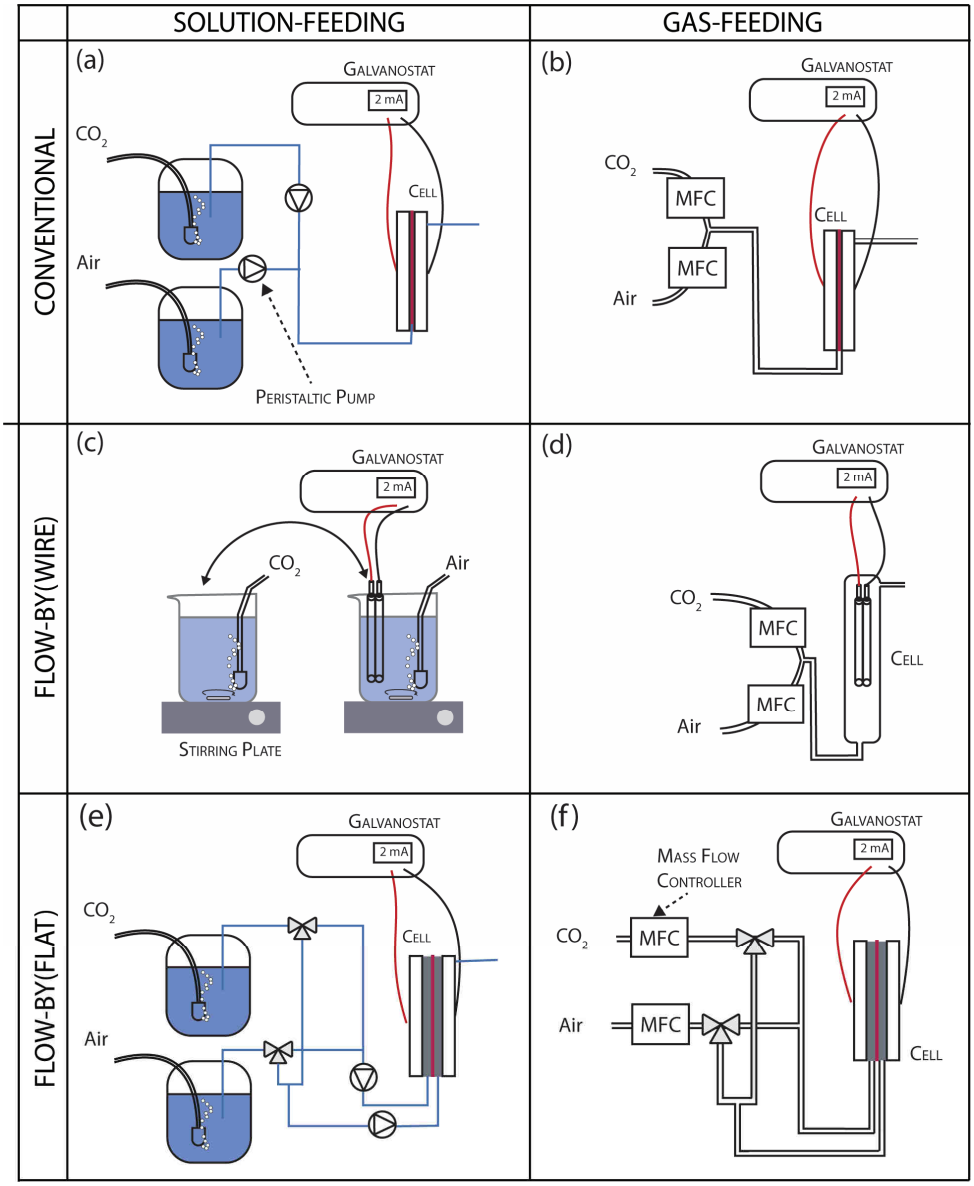

Fig. 3.4: Cell designs in both solution-feeding and gas-feeding operations for the conventional cell (a-b), the flow-by(wire) cell (c-d), and the flow-by(flat) cell (e-f).

3.2.3. Electrochemical measurements

Open Circuit Voltage (OCV) cycles measurement

The membrane potential in the capacitive cell was characterized by measuring the cell voltage difference when CO_2 and air streams were alternatively fed in the cell under open circuit conditions, as described in Ref. [23]. For all cell designs, the CO_2 and air streams, either in solution-feeding or gas-feeding operation, were alternatively fed every 5 minutes inside the capacitive cell. In solution-feeding operation, the CO_2 and air streams are the CO_2-saturated and air-saturated solutions, respectively. In gas-feeding operation, the CO_2 and air streams are the pure CO_2 and air gases being fed into the capacitive cell, respectively.

4-step energy cycle

A four-step operation procedure was used to generate electrical power with the capacitive cell[18,19]. Fig. 3.5 shows the four different steps during the 4-step energy cycle. For each design, the cell is first short-circuited (0V) in the air stream solution. During step 1 (Fig. 3.5), the CO_2 stream is fed into the capacitive cell under open circuit voltage for t=100s. Due to the change of ion concentration of the CO_2 stream, the membrane potential decreases. Consequently, the cell voltage decreases. During step 2, the capacitive cell is charged under constant current (I) during a specific time (t), while the CO_2 stream is fed into the capacitive cell. The charging time during step 2, t, is defined according to the electrode charge tested (Q=I*t). During step 3, the air stream is fed into the capacitive cell under open circuit voltage condition for 100s. Due to the change of ion concentration, the membrane potential decreases. Consequently, the cell voltage decreases in the opposite direction than step 1. During step 4, the capacitive cell is discharged under the opposite current (-I) and time (t) used in step 2. Note that the same amount of electrodes charge is stored in step 2 and released in step 4. A previous study[18] showed that an optimal current density exists for a given charge to obtain a maximum power density. Experiments were done to estimate the optimal current density for each design, shown in supporting information, and reported in Table 3.1. The optimal current density was then chosen to perform every experiment.

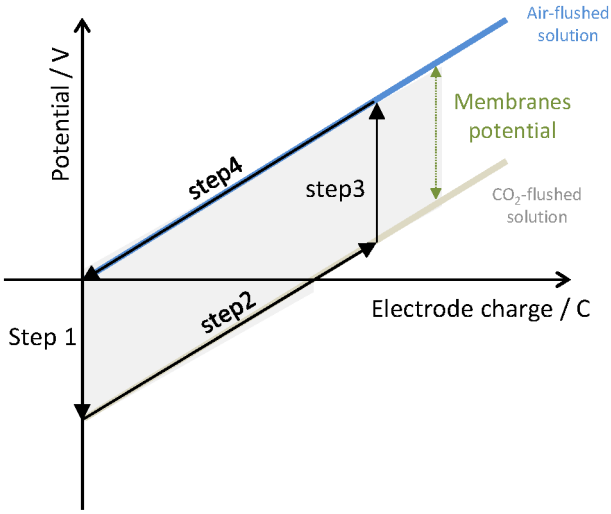

Fig. 3.5: Representation of a 4-step energy cycle. Steps 1 and step 3: open-cell voltage steps related to the establishment of the membrane potential due to the change of streams into the cell. Step 2 (charging): cell voltage under CO_2 stream feeding into the capacitive cell. Step 4 (discharging): cell voltage under airstream feeding.

Additionally, consecutive 4-step cycles were performed for 10 hours for each cell design in gas-feeding operation. Before performing the 10-hours experiment, air-saturated deionized water was fed into the capacitive cell while the cell was short-circuited. After this step, only pure CO_2 and air gas streams were alternatively fed into the cell, according to the 4-step energy cycle procedure.

3.2.4. Power density, membrane potential, and internal resistance calculations

We estimate the internal electrical resistance by following the method used in Ref.[121]. The internal resistance was obtained from the voltage drop measured between open-cell voltage steps (step 1 and step 3) and a charging and discharging steps (step 2 and step 4). In most experiments, the internal resistance was not constant during the four different steps of the energy cycle. In this study, we only reported the internal resistance in the air-saturated solution. We described the calculation procedure in appendix A.

The power density generated was calculated by subtracting the power density invested during the charging step, and the power density harvested during the discharging step.

$$P = \frac{1}{2 * t} * \left(\int_0^Q E_{cell}^{air}\, dQ - \int_0^Q E_{cell}^{CO_2}\, dQ\right) \quad 3.4$$

where P is the generated power density, E_{cell}^{CO2} represents the cell voltage measured during step 2, E_{cell}^{air} represents the cell voltage measured during step 4.

For the conventional and the flow-by(wire) cell designs, the membrane potential (ΔE_m) is defined as the sum of the AEM potential (ΔE_{AEM}) and the CEM potential ((ΔE_{CEM}), $\Delta E_m = \Delta E_{AEM} + \Delta E_{CEM}$, which are defined in Eqs. 3.5-3.6. For the flow-by(flat), only a CEM is used, and the theoretical membrane potential can be calculated as: $\Delta E_m = 2 \cdot \Delta E_{CEM}$.

$$\Delta E_{AEM} = \frac{\alpha \cdot R \cdot T}{n \cdot F} \cdot \ln\left(\frac{a_{HCO_3^-,air}}{a_{HCO_3^-,CO_2}}\right) \quad 3.5$$

$$\Delta E_{CEM} = \frac{\alpha \cdot R \cdot T}{n \cdot F} \cdot \ln\left(\frac{a_{H^+,air}}{a_{H^+,CO_2}}\right) \quad 3.6$$

where *a* represents the activity of either the HCO_3^- or H^+ ions in the CO_2-saturated solution or the air-saturated solution; R, T, n, F are the ideal gas constant, the temperature, the ion valance, and the Faraday constant, respectively. α represents the membrane apparent permselectivity. In CO_2-saturated and air-saturated deionized water, different ions are in solution, i.e., H^+, OH^-, HCO_3^-, CO_3^{2-} and OH^-. In the case of a mixture of multi-valent ions, Eqs. 3.5-3.6 are not valid. However, HCO_3^- and H^+ are the major ions in solution, whereas the other ions can be assumed negligible, which legitimate the use of Eqs. 3.5-3.6. A similar approach was described in Refs.[23,29]. The maximum theoretical membrane potential for each design is estimated at around 205 mV.

3.3. Results and discussion

3.3.1. Cell performance under solution-feeding and gas-feeding operations

We first characterized the performance of the conventional cell under different feeding operations (solution and gas) by comparing the membrane potential (Fig. 3.6), the power density generated (Fig. 3.7a), and the internal resistance (Fig. 3.7b). Fig. 3.6 clearly shows the change of cell voltage when air and CO_2 gases are alternatively fed into the cell in open-cell voltage condition due to the change of membrane potential. The highest

membrane potential obtained was 50 mV, using gas-feeding operation at 2 L min^{-1} (Fig. 3.6). This result shows that a change of H^+ and HCO_3^- concentrations took place in the remaining water phase in the spacer channel, driven by the change of CO_2 concentration in the gas inflow (CO_2 or air) and the chemical reactions shown in Eqs.3.1-3.3. We show here that a membrane potential can be obtained directly from a CO_2 gas concentration ratio, i.e., pure CO_2 and air.

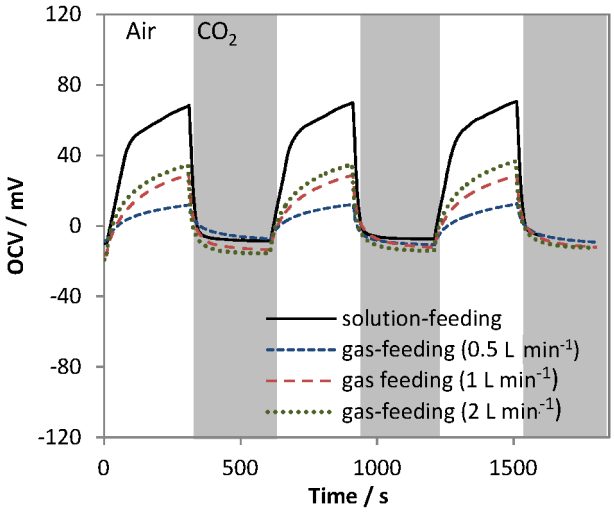

Fig. 3.6: Open Circuit Voltage (OCV) cycles obtained with the conventional cell with solution-feeding and gas-feeding operations for different flow-rates. The grey area in the graph shows the period when pure CO_2 gas was fed into the cell. The white area represents the period when the air gas stream was fed into the cell.

However, the membrane potential was on average two times lower under gas-feeding operation compared to solution-feeding operation (OCV_{sol}=80 mV against OCV_{gas}=20-50 mV). In gas-feeding operation, the ion concentration ratio is achieved by CO_2 absorption/desorption from the gas streams in the water phase inside the spacer channel. The lower membrane potential obtained in gas-feeding operation suggests that a lower ion concentration ratio was achieved in the cell (Eqs. 3.1-3.3), likely due to CO_2 diffusion limitations between the gas and liquid phases. Results at different gas flow-rates show the effect of mass transfer limitation on the membrane potential. In particular, a higher gas flow-rate leads to higher membrane potential due to an improved mixing between the gas and the liquid phases inside the spacer channel. Instead, no gas-liquid diffusion limitation occurs under solution-feeding operation, as the mixing between the water and the gas (CO_2 or air) takes place outside the capacitive cell for a sufficient amount of time.

Moreover, the membrane potential in both gas-feeding and solution-feeding is more than 2.5 times lower than the theoretical values (205 mV). Such performance loss has been previously attributed to physical desorption of CO_2 from plastic tubing [23], and the diffusion of other ions (e.g., OH^-) or carbonic acid through the membrane [29]. All these phenomena are also expected to take place independently of the feeding operation (gas-feeding or solution-feeding), as the flow pattern in the cell is similar in both feeding conditions.

Based on the obtained membrane potential, we harvested electrical power by applying the 4-step energy cycle procedure to compare the electrical power generated (Fig. 3.7a) and the internal electrical resistance (Fig. 3.7b) in both solution and gas-feeding operations. The 4-step energy cycles are shown in supporting information. The maximum power density obtained was five times higher in solution-feeding operation (0.3 mW m^{-2}) compared to the gas-feeding operation (0.05 mW m^{-2}). With capacitive cells, the generated power density increases with higher membrane potentials and lower internal resistance[18]. In solution-feeding operation, the power density generated is higher due to both higher membrane potential (50% higher than direct gas-feeding operation) and lower internal resistance (i.e., ~10 kΩ cm^2 in solution-feeding against ~30 kΩ cm^2 in gas-feeding). The current cell performance is far too low for real applications due to the high internal resistance. Technology harvesting energy from salt streams is capable of generating 1-3 W m^{-2} with similar membranes[121,127,128]. However, technologies based on salt streams are a more mature technology, being developed for more than 20 years. Nevertheless, the performance comparison between different feeding conditions is still relevant to characterize the effect of direct gas feeding in capacitive cells.

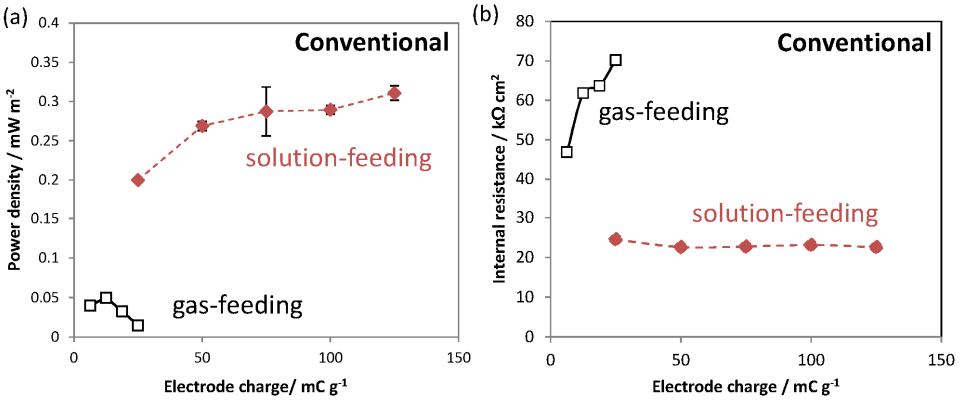

Fig. 3.7: Performance of conventional cell design during the 4-step energy cycle under solution-feeding and gas-feeding operations. (a) Power density; (b) internal electrical resistance.

Constantly feeding the gas through the spacer leads to dryness of the spacer channel over time inside the cell. As a result, the water phase in the spacer channel decreased, leading to a decrease of ionic conductivity between both electrodes, resulting in a higher electrical internal resistance. This observation highlights the fact that the conventional design is not optimized for gas-feeding operation, where the gases are flowing between the electrodes, thus causing a high cell electrical resistance.

In the next sub-section, we introduce and characterize two other cell designs (i.e., "flow-by(wire)" and "flow-by(flat)"). In these designs, the gas flow configuration is not in-between the electrodes but along the electrodes, which could improve the cell conductivity in gas-feeding operation.

3.3.2. Performance comparison between cell designs

As discussed previously, the conventional design is not suitable for a gas-feeding operation due to the non-optimal gas flow configuration of the capacitive cell. Therefore, we proposed to change the gas flow configuration to a gas "flow-by" the electrodes in two other cell designs, i.e., the flow-by(wire) and the flow-by(flat) cell designs (Fig. 3.8b,c). To compare the three designs, we measured the membrane potential (Fig. 3.8) and performed 4-step energy cycles. The cell voltage during 4-step energy cycles is shown in supporting information, whereas the power densities generated for each cycle are shown in Fig. 3.9. Results are compared in terms of power densities (Fig. 3.9a) and internal electrical resistances under gas-feeding operation (Fig. 3.9b).

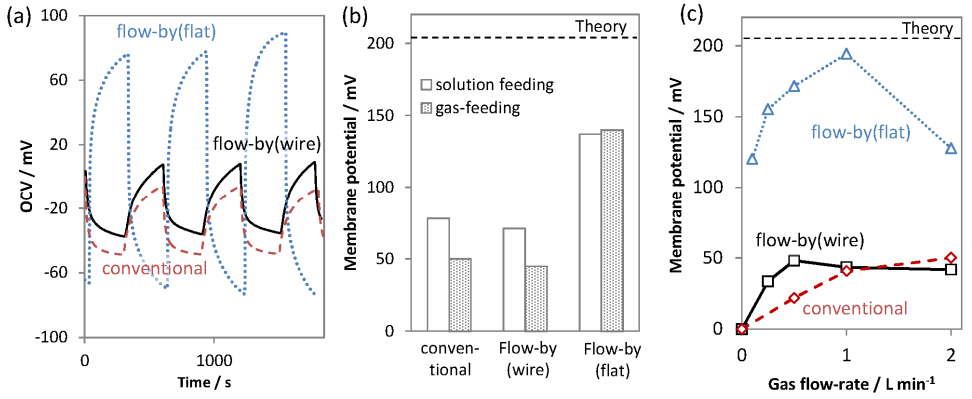

Fig. 3.8: Comparison between conventional, flow-by(wire), flow-by(flat) cell designs in gas-feeding operation. (a) Open circuit cycles (OCV) cycles; (b) the membrane

potential in gas-feeding and solution-feeding operations; (c) membrane potential of the different cell designs in direct-feeding operation for different gas flow rates.

Fig. 3.8a-b shows that the membrane potential in the flow-by(flat) design (~140 mV) at a gas flow-rate of 0.25 L.min^{-1} is the highest among the three designs tested, i.e., ~3 times higher than the conventional cell design (≈50 mV). The same membrane potential was also obtained under solution-feeding condition (Fig. 3.8b), which is 35% higher than membrane potentials previously reported (~140 mV against ~90 mV) [23,29]. The improved membrane performance could be attributed to a better flow configuration in the flow-by(flat) cell. In previous theoretical studies[28,29], the diffusion of $H_2CO_3^*$ through the membrane was identified as the major factor limiting the membrane potential in a conventional cell design in solution-feeding operation. As the solution only flows on one side of the membrane (facing the spacer), $H_2CO_3^*$ diffuses through the membrane and accumulates on one side of the membrane (facing the electrode). As a result, the accumulated $H_2CO_3^*$ can be converted back to HCO_3^- and H^+ (Eqs. 3.1-3.3), decreasing the ion concentration difference across the membranes leading to lower membrane potentials. In contrast, with the flow-by(flat) cell design, feeding simultaneously CO_2 and air gas streams on both membrane sides are beneficial to reduce concentration polarization phenomena and maintain a constant concentration of ions (H^+ and HCO_3^-) and neutral molecule (CO_2 and $H_2CO_3^*$) on each side of the membrane. Therefore, we show that by feeding CO_2 and air gas streams simultaneously in the flow-by(flat) cell design, the membrane performance is higher due to a lower effect of $H_2CO_3^*$ flux through the membrane.

Moreover, Fig. 3.8b shows that the membrane potential obtained in the flow-by(flat) design is similar in both solution-feeding and gas-feeding operations, unlike the other two cell designs (Fig. 3.8b and OCV cycles shown in supporting information). In section 3.1, we explained that a membrane potential difference obtained between the gas-feeding and the solution-feeding operations was likely due to CO_2 mass transfer limitation. Therefore, the results obtained with the flow-by(flat) cell design suggest that CO_2 mass transfer limitation is the smallest among the three cell designs. Fig. 3.8c shows that the CO_2 mass transfer of the flow-by(flat) cell design can be further improved for each design by increasing the gas flow-rate. A maximum of 190 mV was achieved at 1 L min^{-1}. A similar trend can be observed for the two other cell designs to a lesser extent. A maximum of 50 mV at 2 L min^{-1} was achieved in the conventional cell design, whereas a maximum of 45 mV at 2 L min^{-1} was achieved in the flow-by(wire). Apart from cell geometry, the two cell designs were tested under different gas flow velocities (4.8 m s^{-1} for the conventional cell design against 0.05 m s^{-1} for the flow-by(wire) cell design). gas flow velocities calculations are shown in supporting information. Although the same gas flow-rate was

used, the gas flow channel of the conventional and the flow-by(wire) designs were different due to their different cells. Despite the large difference in gas flow velocity, the membrane potential was similar to the conventional and the flow-by(wire) cell designs. For cell designs using two membranes, the wire cell geometry appears to be beneficial for generating a higher membrane potential. Nevertheless, changing the flow configuration using only one membrane (flow-by(flat)) had a higher effect on the membrane performance, as we explained above.

In the flow-by(flat) design, concentration polarization can be further reduced in gas-feeding operation than solution-feeding operation. The membrane potential obtained in the flow-by(flat) is higher in gas-feeding operation than solution-feeding operation (OCV_{sol}=140 mV against OCV_{gas}=190mV at 2 L min^{-1}). We believed that at such high gas flow-rate, the concentration polarization at the membrane surface decreases drastically due to the higher mobility of CO_2 in the gas phase compared to the liquid phase ($D_{CO_2,liquid}$=1.6·10^{-9} m^2 $s^{-1,}$ and $D_{CO_2,gas}$=1.4·10^{-4} m^2 s^{-1}). The same CO_2 mobility property is used in the field of CO_2 reduction, where CO_2 is fed directly as a gas inside the electrochemical cell to improve the CO_2 diffusion on the electrode surface[142]. With lower concentration polarization, $H_2CO_3^*$ flux through the membrane can easily diffuse in/away from the membrane boundary layer, keeping the ion concentration ratio across the membrane close to the ratio expected. However, increasing the gas flow-rate at 2 L min^{-1} decreases the membrane performance due to an expected excessive dryness of the membrane. Therefore, the gas flow-rate is an important parameter to optimize in order to increase the CO_2 mass transfer kinetics between the water and gas phases but also to avoid the excessive dryness of the capacitive cell.

In terms of power density, Fig. 3.9a shows that the power density is more than 20 times higher in the flow-by(flat) cell (~3 mW m^{-2}) compared to the conventional cell (~0.05 mW m^{-2}) and the flow-by(wire) cell (~0.1 mW m^{-2}) under gas-feeding operation. We observed a similar trend under solution-feeding operation (see supporting information). The higher power density obtained in flow-by(flat) is the result of the combined effect of the higher membrane potential and the lower internal resistance compared to the other two designs. Fig. 3.9b shows that the cell internal resistance obtained in flow-by(flat) cell design (1.4 kΩ cm^2) was four times lower than the flow-by(wire) cell design (~6 kΩ cm^2), and more than 20 times lower than the conventional cell design (~30 kΩ cm^2). Both the flow-by(flat) and the flow-by(wire) cell designs highlight the benefits of good contact between the electrodes and membranes to improve the electrical conductivity of the capacitive cell. Moreover, a flat-shaped cell geometry is more suitable to reduce the internal electrical resistance, as the surface contact between the electrodes and the membranes is higher than the wire-shaped electrode geometry. Similar cell designs are

also applied in the field of PEM fuel cell[144–148] to optimize the cell internal resistance and gas diffusion in the cell while using gas for power generation (H_2), or CO_2 reduction[142,143,149].

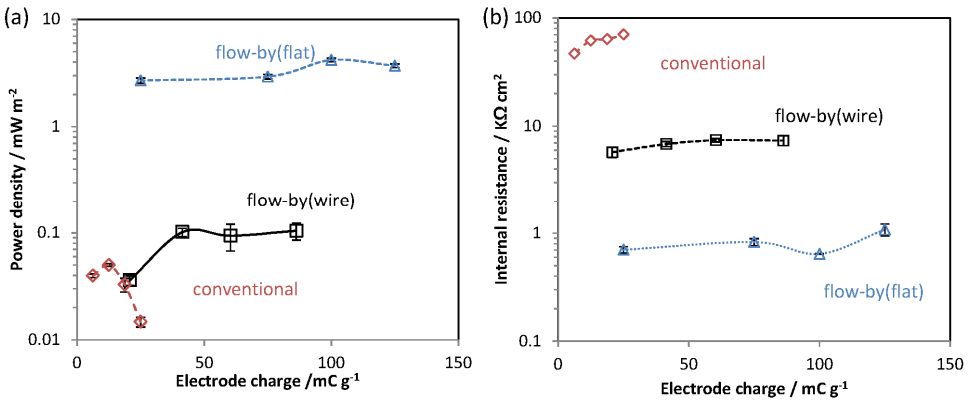

Fig. 3.9: Comparison between conventional, flow-by(wire), and the flow-by(flat) in gas-feeding operation. (a) Power density and (b) cell internal resistance.

Next, we performed consecutive energy cycles for 10 hours under gas-feeding operation to estimate the performance stability of the different cell designs. Fig. 3.10a,b shows that only the flow-by(wire) cell design maintained stable performances for 10 hours (~0.07 µW m^{-2}), unlike for the conventional and the flow-by(flat) cell designs. The generated power decreased until reaching negative values after 5 hours for the conventional cell design and the flow-by(flat) cell design (Fig. 3.10a,b). In this context, reaching negative power density means that higher power was consumed than generated. The performance of each design strongly depends on the internal cell resistance, as shown in Fig. 3.10c. We believe that the increase of internal resistance reflects the drying of the cell over time, as discussed in section 3.1. For instance, the internal resistance of the conventional cell design increases from 20 kΩ cm^2 until 160 kΩ cm^2 after 6 hours, causing a sharp decrease in power density (Fig. 3.10c). Similar behavior can be observed for the flow-by(flat) design. On the contrary, the internal resistance of the flow-by(wire) design remains stable (around ~5 kΩ cm^2), without causing any performance loss over time. As mentioned before, the flow gas velocity with the flow-by(wire) cell design is lower than the two other cell designs. Lower gas velocity avoids the fast drying of the cell, keeping the internal resistance constant. Note that a decrease of membrane potential over time also affects the cell performance to a lesser extent. For instance, the membrane potential of the conventional cell design decreased from 30 mV to 10 mV after 10 hours, and the membrane potential of the flow-by(flat) decreased from 130 mV to 80 mV after 10 hours.

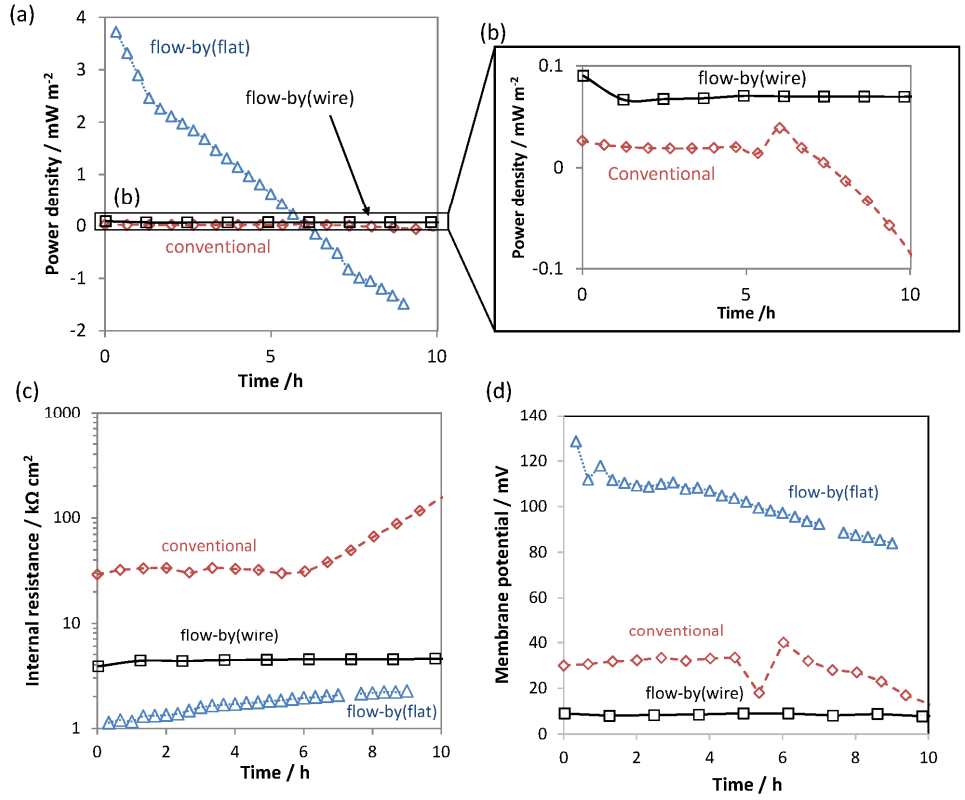

Fig. 3.10: (a) Comparison between, conventional, flow-by(wire) and flow-by(flat) cell designs for consecutive cycles for 10 hours. The conventional cell, the flow-by(wire), and the flow-by(flat) were operated respectively at 5 mA m^{-2}, 16.5 mA $m^{-2,}$ and 111 A m^{-2}. (b) graph inset of the power density for the different cell designs between -0.1 and 0.1 mW m^{-2}. (c) the internal electrical resistance and (d) the membrane potential measured during each energy cycle

The cell humidity can be managed by adding water inside the electrodes compartment. After adding water inside the cell, the power density increases back to the maximum power density (see supporting information). Likewise, in the case of PEM fuel cells, the water content in the electrodes is a key optimization parameter to avoid excessive drying or flooding of the electrodes[142,150]. Several parameters have been used to reach ideal humidification of the electrochemical cell using H_2 or CO_2, e.g., the operating temperature [150], the humidification of the gas [142,150], and the gas flow rate [151]. Note that in most of the studies on CO_2 reduction, the gas streams are humidified before entering the cell, thus highlighting the importance of the gas humidity conditions in the cell. In the case

of H_2 fuel cells and most of the cases in CO_2 reduction, water is produced on the cathode (according to the reaction $O_2 + 4e^- + 4H^+ \rightarrow 2H_2O$), which facilitates the cell humidification. This is not the case in the system described in the present work, where deionized water is used to dissolve CO_2, but water is not produced. Therefore, humidity in the capacitive cell is a crucial parameter to optimize. Good management of the humidity inside the cell is therefore critical to avoid drying the cell and sustain stable power performance.

3.4. Outlook and perspective

In this study, we characterized the performance of three different capacitive cell designs, i.e., conventional, flow-by(wire), and flow-by(flat), under both solution-feeding and gas-feeding operations. The best performance in gas-feeding operation was obtained with the flow-by(flat) cell (3 mW m^{-2}), while the flow-by(wire) cell design showed the most stable performance over time (≈0.07 mW m^{-2} during 10-hour run test). Based on this result, we highlighted the importance of contacting the electrodes with an ion exchange membrane in a flat-shaped cell to reduce the internal resistance of the capacitive cell.

The best gas flow configuration in the cell was reached by sparging the gas along the electrodes (flow-by), instead of in between the electrodes. A similar approach has been extensively applied and demonstrated in fuel cell technology[144–148,150] and CO_2 reduction technology[138,141,143], where gases are used as reactants into electrochemical cells. For the technology reported in this work, the membranes are in direct contact with the electrodes, and the gas flows along the electrodes. In most cases, the electrodes and membrane are pressed together to form a membrane electrode assembly, which improves the ionic contact between the two electrodes. Such a strategy, like the flow-by(flat) design, is also beneficial for a capacitive cell. Moreover, sparging the gas along the electrode improves the gas-liquid mass transfer in the cell, resulting in a faster CO_2 absorption/desorption in the water phase inside the cell. The improved CO_2 diffusion leads to a faster change of ion concentration inside the cell, thus higher membrane potential. By combining higher membrane potential and lower internal resistance, the flow-by(flat) shows the best performance of the three designs tested.

Nevertheless, the high internal resistance caused by the low electrolyte conductivity is a major limitation in such a system. In this study, we chose deionized water for both the CO_2-saturated and air-saturated solutions. Although deionized water has a low conductivity (≈45 μS cm^{-1} when equilibrated with pure CO_2), the addition of a supporting electrolyte (i,e, NaCl) is not feasible, since any other ion in solution will decrease the ions concentration ratio between the CO_2-saturated and air-saturated solutions. The ideal solvent should combine three main criteria, such as (i) a high ion

concentration ratio between the CO_2-saturated and the air-saturated solutions to generate a high membrane potential, (ii) a high ionic conductivity to reduce the internal resistance and (iii) fast adsorption kinetics for CO_2 absorption reversibility (for re-use purposes). For instance, adding salt would reduce the internal resistance by increasing the electrolyte conductivity but would also reduce the membrane potential, which depends on the concentration ratio between the air-saturated and CO_2-saturated solutions. By choosing water as a solvent in this study, a concentration ratio of 60 was obtained between the CO_2-saturated and air-saturated solutions, corresponding to a membrane potential of 206 mV (Eqs. 3.5-3.6). Selecting a solvent 1000 times more conductive than deionized water, such as 1 M $NaHCO_3$ (≈45mS cm^{-1}), would decrease the internal resistance of the cell but would also reduce the ion concentration ratio between the air-saturated and CO_2-saturated solutions (concentration ratio=1.2), resulting into a smaller membrane potential (≈4 mV). To the best of our knowledge, suitable solvents that fit all the criteria mentioned above still need to be identified, and further research efforts are required in this direction to reduce the cell resistance. In this regard, Kim et al. [27] proposed an alternative approach to improve the cell conductivity by changing the cell voltage source from the ion exchange membranes to the electrode potential using intercalation electrodes. Combining intercalation electrodes and 1 M $NaHCO_3$ electrolyte with the flow-by(flat) cell design could be of interest to harvest energy in gas-feeding operation. As a result, higher electrical power density could be achieved due to the improved cell conductivity and the lower sparging and pumping energy costs.

Another important parameter to consider for gas-feeding operation is the water content management inside the cell. We highlight in our results that sparging the gas in the capacitive cell for an extended time period led to a sharp decreasing performance in both conventional and flow-by(flat) designs, mainly due to an increase of the internal resistance. The water management strategy in the cell can be improved by humidifying the gas streams or pumping water in the cell. In practical application, the CO_2 source might already contain a high relative humidity (e.g., in the case of flue gas from coal-fired power plants), which should be sufficient to maintain a good humidity into the cell. If the inlet gas humidity is insufficient, adding water directly in the cell could be sufficient. In addition, water management strategies from PEM fuel cell or CO_2 reduction cells could be applied to optimize the capacitive cell design using a gas-feeding condition. For instance, humidification of the gas or operating the cell at a higher temperature could be adopted. However, these options are energy-intensive, and their techno-economic feasibility should be assessed. Another possibility could be to use a microfluidic cell design[139–141], where both gas and fluid are pumped into the cell and are both in contact with the catalyst through gas diffusion electrodes (GDE). In this case, the catalyst could be a capacitive material such as carbon cloth or activated carbon powder. Thanks to the contact between

the liquid electrolyte, CO_2 gas, and the capacitive material, the electrode will not undergo dryness with time. Nevertheless, the pumping energy costs of the electrolyte should be closely assessed. In general, the use of GDE is of interest to improve the overall contact between the gas and liquid and avoid the fast drying of the cell.

As future applications for this technology, we aim to explore the use of flow-by capacitive cells with direct gas-feeding as a new CO_2 capture strategy. By operating the cell as a membrane capacitive deionization cell, (M)CDI[17,70,117,152,153], electrical energy can be applied on the capacitive cell to absorb CO_2[154]. A conventional cell design under solution-feeding operation has already been applied for CO_2 capture and showed promising low energy requirement to absorb CO_2 (40 kJ $molCO_2^{-1}$)[154]. The internal resistance was identified as the major limiting factor to improve further the cell performance. The flow-by(flat) design would be beneficial to reduce the internal electrical resistance, and the gas-feeding operation would improve the diffusion of CO_2 in the cell. In general, the energy cost for capturing CO_2 has been the main factor limiting the technico-feasibility of CO_2 capture until now[15,155,156].

3.5. Conclusion

In this work, we showed that using CO_2 gas and air directly into a capacitive cell is a feasible option to harvest electrical energy. By comparing three different cell designs, the flow-by(flat) design showed the best performance in terms of power outputs (≈3 mW m^{-2}), leading to power outputs 20 times higher than the other cell designs (conventional and the flow-by(wire) cell designs). We show that contacting both electrodes with one membrane (flow-by(flat) design) improved both the membrane potential established as well as the internal cell resistance. Regarding the membrane potential, we argued that the flow configuration in the flow-by(cell) greatly reduces the concentration polarization across the membrane, limiting the effect of H_2CO_3* on the membrane potential. Regarding the internal cell resistance, using an ion exchange membrane as a separator between both electrodes improve the ionic conductivity between both electrodes. However, the conventional cell design, which has already been used under solution-feeding operation to harvest energy from CO_2 [23,28,29], was not suitable to harvest energy under gas-feeding operation. The gas flow in the spacer separates both electrodes leading to a decrease of ionic conductivity and a sharp increase of the internal resistance. In contrast, only the flow-by(wire) cell design could sustain stable performance during 10-hour run tests. The performance of the conventional and flow-by(flat) designs was not stable over time due to the dryness of the spacer channel (or the electrodes) caused by the gas flow in the cell. We suggest further studies to use GDE instead of carbon cloth electrodes to improve the tri-phase contact (CO_2 gas-water-electrode) and avoid excessive drying. Instead of

sparging the gas directly into the electrodes such as flow-by(flat), using GDEs in combination with a bipolar plate provide a better gas flow distribution outside the electrodes[139,140,142,143,149].

Moreover, the major limiting factor with the design proposed in this study is the low electrolyte conductivity. Therefore, further studies are needed to identify suitable solvents fitting the selection criteria. An interesting alternative could be to combine the knowledge acquired on cell design with gas-feeding operation in this study with the use of intercalation electrodes[27], to decrease further the internal resistance of the cell.

Appendix

Appendix A: Calculation procedure of the internal resistance

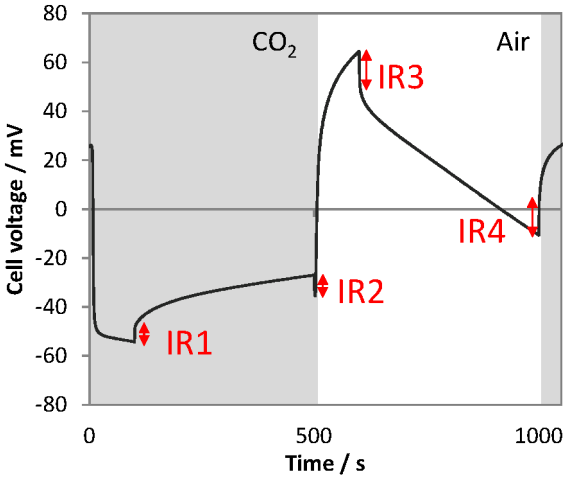

Fig. A3.1: Ohmic drop calculated during the charging step (IR1 and IR2) and the discharging step (IR3 and IR4) during each 4-step energy cycle.

We estimate the internal cell resistance (R_{int}) by measuring the voltage drop (ΔE_{drop}) between an open-cell and a charging/discharging steps at constant current density (I). This method has been widely used for reverse electrodialysis systems[121] and in capacitive deionization[116].

$$R_{int} = \frac{\Delta E_{drop}}{I} \qquad \text{A3.1}$$

As described in the main paper, each 4-step energy cycle is composed of a charging and discharging steps separated by open-cell steps. Fig. A3.2 shows the voltage drop measured (IR_1, IR_2, IR_3, IR_4) for each cycle. The charging and discharging steps occur in two different electrolytes, the CO_2-saturated (R_1, R_2) and the air-saturated solution (R_3, R_4). Since both electrolytes have different conductivity, the internal resistance of the capacitive cell is different between the charging and discharging steps.

A Previous study[18] clearly showed that the resistances measured in the diluted solution (in this case, air-saturated solution) are limiting the most the system performance due to its lower conductivity. Thus, the resistances R_3, R_4 are more representative of the system performance than the resistance R_1 and R_2. Thus, we reported the average resistance in the air-saturated solution (R_3 and R_4).

$$R_{int} = \frac{R_3 + R_4}{2} \qquad \text{A3.2}$$

3.6. Supporting information

Table S3.1**:** Residence time and gas flow velocity calculations

	conventional	**Flow-by(wire)**	**Flow-by(flat)**
Gas flow-rate	1 L min^{-1}	1 L min^{-1}	0.25 L min^{-1}
Gas flow channel di-	Length=250 mm	Length=140 mm	Length=30 mm
mension	Wide=20 mm	Radius= 12.5 mm	Wide=30 mm
	Thickness= 0.25 mm	Porosity=0.5	Thickness=0.5 mm
	Porosity=0.7		
Volume ratio occupied	N/A	N/A	0.33
by the capacitive cell			
Residence time	0.05 s	0.05 s	2.7 s
Gas flow velocity	4.8 m s^{-1}	0.5 m s^{-1}	0.05 m s^{-1}

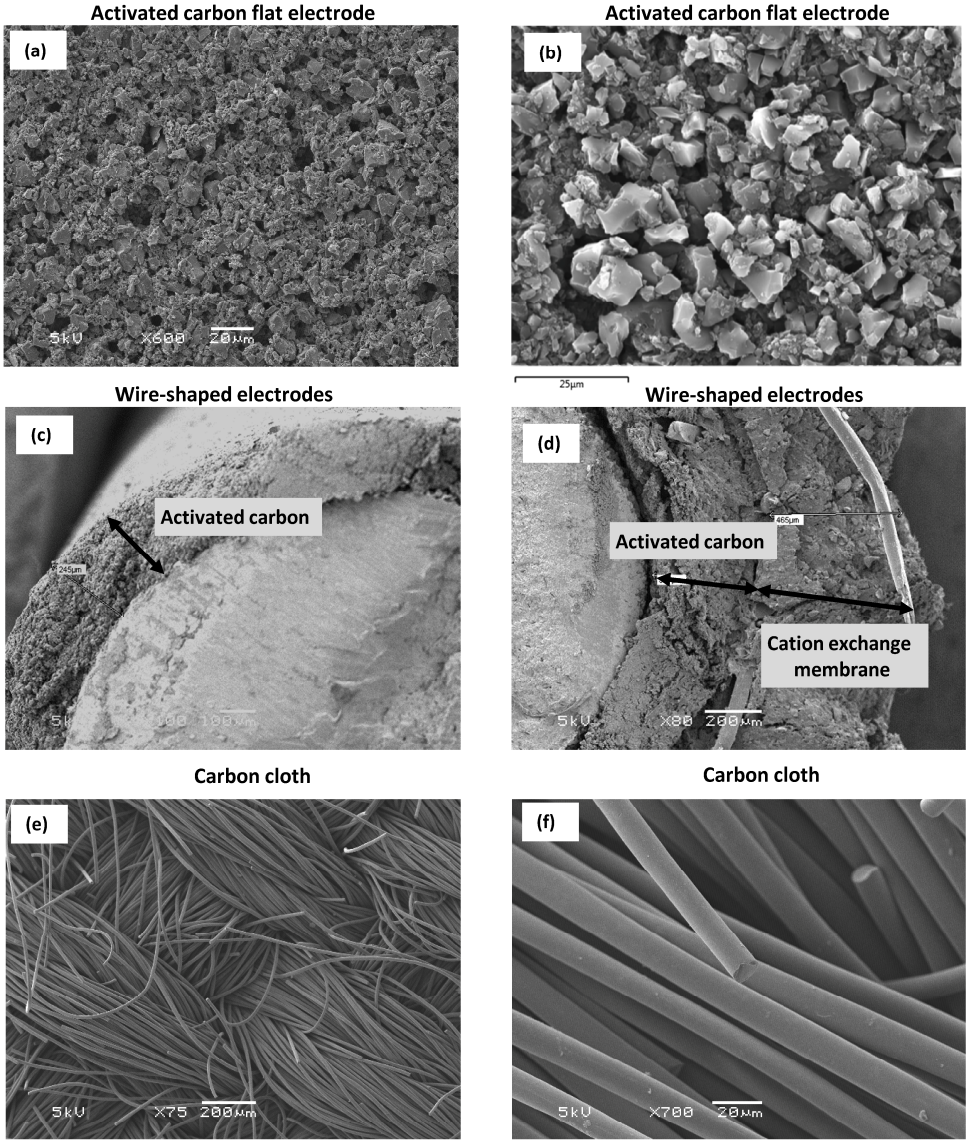

Fig. S3.1: SEM pictures for different electrodes and membrane materials: (a-b) flat-shaped activated carbon electrode, (c) wire-shaped electrode with an activated carbon coating, (d) wire-shaped electrode with activated carbon and membrane coating and (e-f) carbon cloth electrodes.

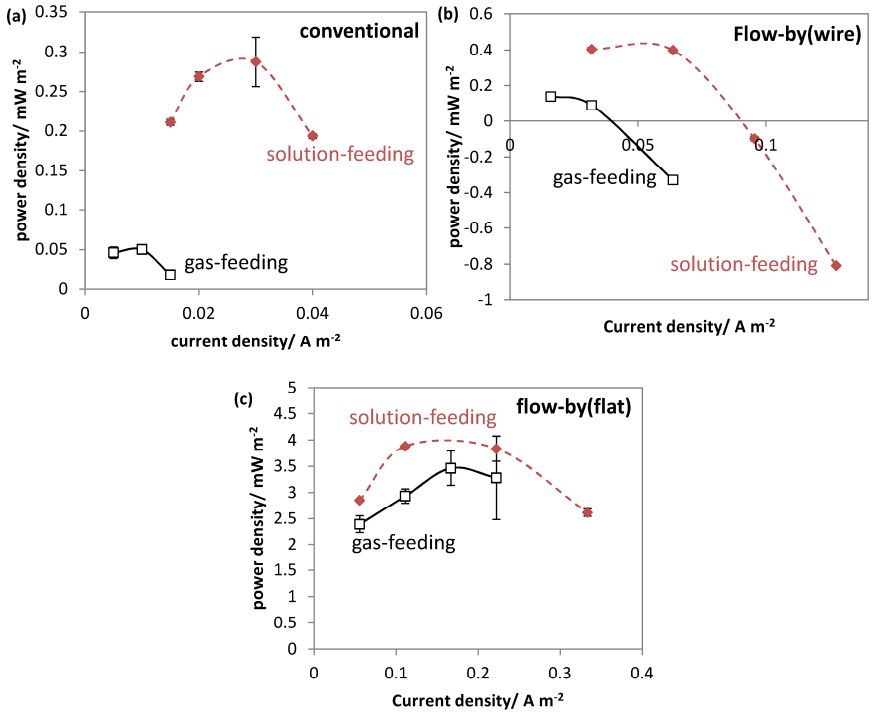

Fig. S3.2: Performance comparison between different cell designs at different current densities: (a) the conventional design; (b) the flow-by(wire), and (c) the flow-by(flat).

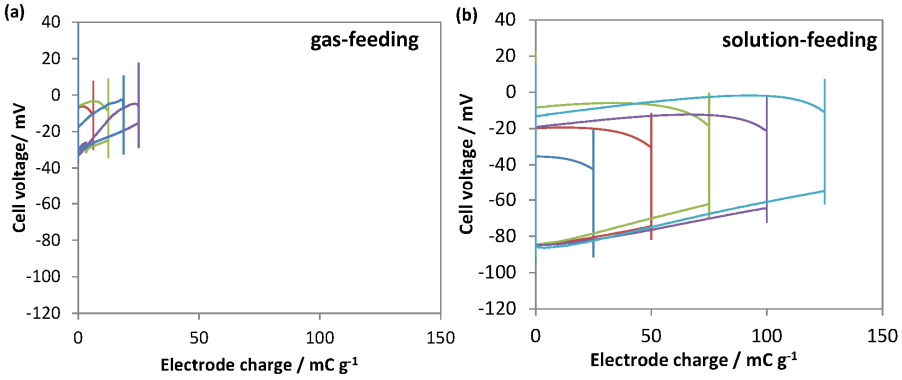

Fig. S3.3: Energy cycles obtained at constant current density with the conventional cell design for both (a) gas-feeding and (b) solution-feeding operations.

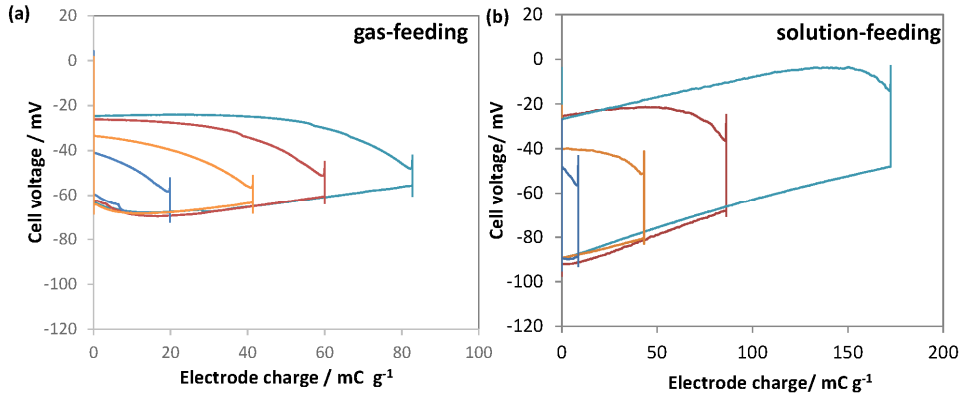

Fig. S3.4: Energy cycles obtained at constant current density with the flow-by(wire) cell design for both (a) gas-feeding and (b) solution-feeding operations.

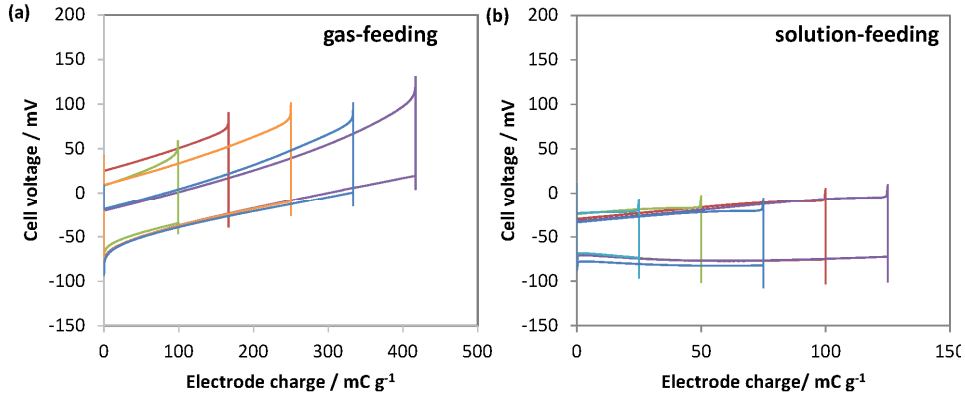

Fig. S3.5: Energy cycles obtained at constant current density with the flow-by(flat) cell design for both (a) gas-feeding and (b) solution-feeding operations.

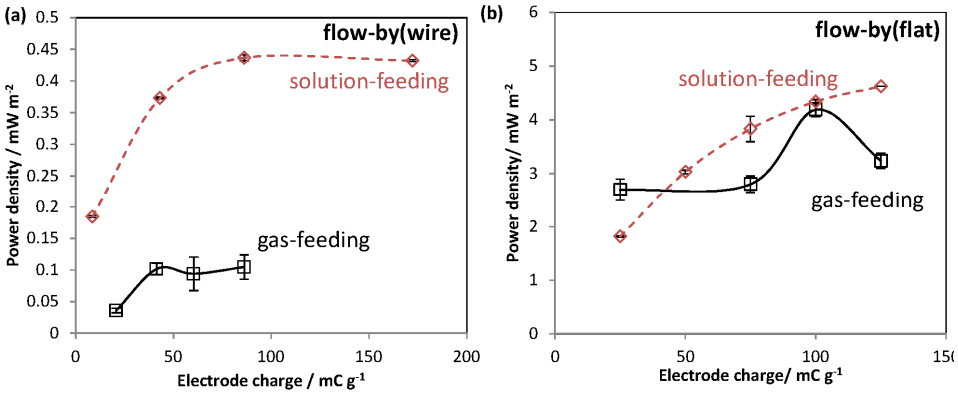

Fig. S3.6: Performance comparison of the three different cell designs under both gas-feeding and solution-feeding operations for (a) the flow-by(wire) and (b) the flow-by(flat) designs.

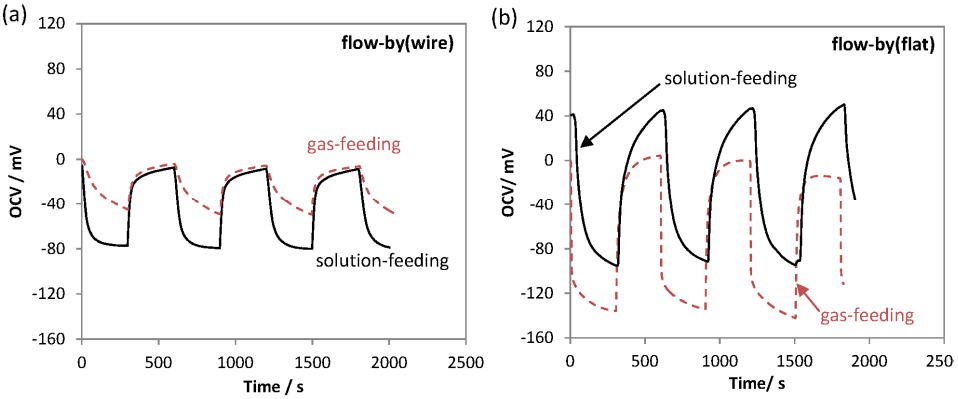

Fig. S3.7: Cell voltage measured during OCV cycles (open circuit conditions) in both solution-feeding and gas-feeding operations for (a) the flow-by(wire) and (b) the flow-by(flat) designs.

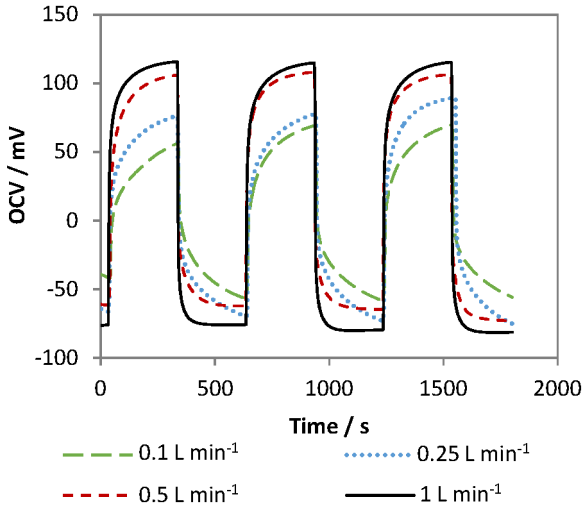

Fig. S3.8: Cell voltage measured during OCV cycles (open circuit conditions) in gas-feeding operations for the flow-by(flat) cell design under different gas flow-rates.

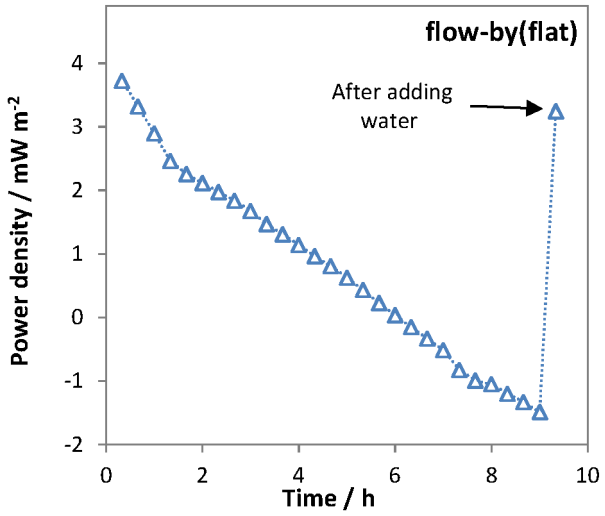

Fig. S3.9: Power density obtained with the flow-by(flat) cell design during a 10-hour run test in gas feeding-operation. Water was added into the cell after 9 hours, as indicated by the arrow.

Chapter 4

Role of ion exchange membranes and capacitive electrodes in Membrane Capacitive Deionization (MCDI) for CO_2 capture

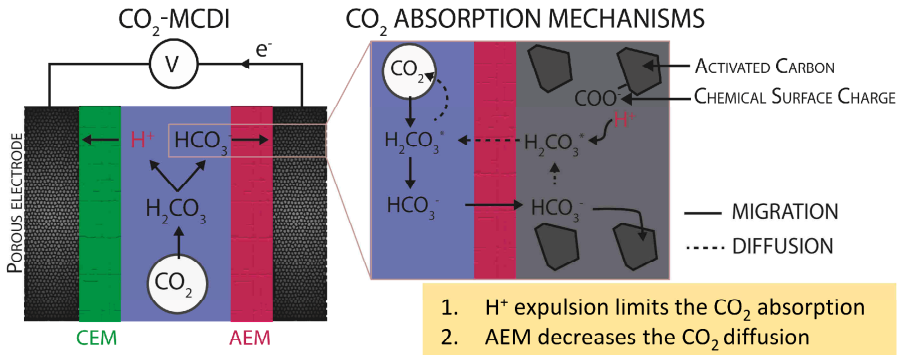

This Chapter has been published as:

L. Legrand, Q. Shu, M. Tedesco, J.E. Dykstra, H.V.M. Hamelers, Role of Ion exchange Membranes and Capacitive electrodes in Membrane Capacitive Deionization (MCDI) for CO_2 capture, J. Colloid. Interface Sci. 564 (**2020**), 478-490. https://doi.org/10.1016/j.jcis.2019.12.039.

Abstract

Recently we showed that membrane capacitive deionization (MCDI) could be used to capture CO_2, but we found that the performance decreases with decreasing current density. In the present study, we investigate the effect of electrodes and ion exchange membranes by performing experiments with two membranes (CO_2-MCDI), with one membrane (cation or anion exchange membrane), and without membranes (CO_2-CDI). We find that the anion exchange membrane is essential to keep high CO_2 absorption efficiencies ($\Lambda_a = n_{CO_2(g)}/n_{charge}$), while the absorption efficiency of the CO_2-CDI cell was lower than expected ($\Lambda_a \approx 0.5$ for CO_2-MCDI against $\Lambda_a \approx 0.18$ for CO_2-CDI). Moreover, we theoretically investigate ion adsorption mechanisms in the electrodes by comparing experimental data of a CO_2-CDI cell with theoretical results of the classic amphoteric-Donnan model developed for conventional CDI. By comparing the experimental results with the amph-D model, we find that the model overestimates the absorption efficiency in CO_2-CDI experiments. To understand this discrepancy, we investigate the effects of other phenomena, i.e., (i) low ion concentration, (ii) passive CO_2 absorption, and (iii) the effect of acid-base reactions on the chemical surface charge.

4.1. Introduction

Climate change mitigation is one of the major and most urgent challenges that society is facing nowadays. In their 2018 report, the Intergovernmental Panel on Climate Change (IPCC) highlighted the importance of achieving zero CO_2 emissions before 2050 to limit the temperature increase [11]. Among the strategies to reduce CO_2 emissions, CO_2 capture technologies have a major role to play[11,157]. Although a large number of technologies have already been proposed for post-combustion CO_2 capture (e.g., amine sorbents[102,158,159], calcium looping[160], gas separation membranes[46,161]), there is still an urgent need of novel technologies to capture CO_2 from flue gas and also directly from the atmosphere[155,162]. Recently a new technology has been proposed to capture CO_2 based on membrane capacitive deionization (MCDI)[154]. MCDI is a well-established process based on Capacitive Deionization (CDI), which has been widely used to desalinate water streams [17,70,72,80,84,163–166]. A CDI cell is composed of two porous electrodes, which can adsorb ions, either through the formation of an electrical double layer (EDL) in the electrodes[84,165,166] or through ion intercalation[167]. The MCDI cell differs from the CDI cell as the porous electrodes are covered by an ion exchange membrane to improve the salt adsorption performance[70].

MCDI can be used to capture CO_2 in the form of HCO_3^- and CO_3^{2-}. Here, we refer to this technology as CO_2-MCDI. CO_2-MCDI is similar to MCDI, except that the electrolyte solution is a CO_2-sparged water solution instead of a saline solution. When CO_2 gas is sparged in water, CO_2 reacts with water to form carbonic acid ($H_2CO_3^*$), which further dissociates to carbonate ions (HCO_3^- and CO_3^{2-}) until reaching a chemical equilibrium, according to the following reaction [25,26]

$$CO_2(g) \overset{H^{cc}}{\longleftrightarrow} H_2CO_3^* \quad 4.1$$

$$H_2CO_3^* \overset{K_1}{\leftrightarrow} HCO_3^- + H^+ \quad 4.2$$

$$HCO_3^- \overset{K_2}{\leftrightarrow} CO_3^{2-} + H^+. \quad 4.3$$

Fig. 4.1a shows the fraction of each carbon species in solution as function of pH. Fig. 4.1b illustrates the principles of the CO_2-MCDI cell. When charging the CO_2-MCDI cell, the carbonate ions (CO_3^{2-} and HCO_3^-) are adsorbed in the electrode EDLs by applying a

charging voltage. The resulting concentration decrease of carbonate ions in solution shifts the chemical equilibrium between CO_2 and carbonic acid (Eqs. 4.1-4.3), leading to the absorption of CO_2 gas. At the end of the charging step, CO_2 is adsorbed in the capacitive electrodes ($n_{CO_2(g)}$) in the form of HCO_3^- and CO_3^{2-}, and as a result, a CO_2-depleted stream is obtained. The electrode regeneration is achieved by short-circuiting the cell or by discharging the CO_2-MCDI cell. During this discharge step, the overall process is reversed: the carbonate ions (HCO_3^- and CO_3^{2-}) are desorbed from the electrodes, leading to CO_2 desorption from the solution to the gas phase.

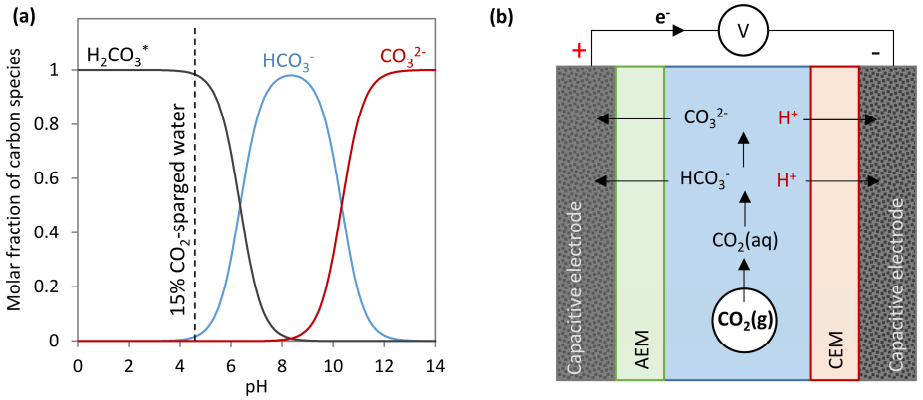

Fig. 4.1: (a) Fraction of chemical species as function of the solution pH (Bjerrum plot) for the H_2O-CO_2 system at 25°C. The curves are calculated according to Eqs. 4.1-4.3 with equilibrium constants H^{cc}=0.83 (Ref. [25]), $K_1=10^{-6.35}$ M (Ref. [26]) and $K_2=10^{-10.33}$ M (Ref. [26]). (b) Schematic representation of CO_2 capture in a CO_2-MCDI cell. During the charging step, a charging voltage is applied.

In conventional MCDI for water desalination, the salt absorption performance is reported by the charge efficiency, Λ, which is for a monovalent salt given by $\Lambda=n_{salt}/n_{charge}$[87], where n_{salt} is the amount of salt adsorbed and n_{charge} is the molar charge stored in the electrodes. Ideally, Λ is equal to 1, which indicates that for every electron transferred, one cation and one anion are adsorbed (in case of a monovalent salt). In CO_2-MCDI, we aim to remove CO_2 gas, and likewise conventional MCDI, the performance of a CO_2-MCDI cell can be measured by the absorption efficiency ($\Lambda_a=n_{CO_2(g)}/n_{charge}$)[154].

In CO_2-MCDI operated at constant current, we found values of Λ_a in the range of 0.6-0.8[154]. Such values of Λ_a are comparable with Λ in conventional MCDI for water desalination[72]. However, we unexpectedly found lower values of Λ_a by charging the CO_2-MCDI cell with lower current densities (from ~0.8 at 0.6 A m^{-2} to ~0.6 at 0.2 A m^{-2}) [154]. A

decrease of Λ in conventional MCDI is mainly caused by co-ion expulsion [70,87,168,169] and by faradaic reactions [73,77,170]. However, both effects are assumed to be negligible in CO_2-MCDI due to (i) the low concentration of ions, (ii) the absence of reactive species in solution (e.g., O_2 and Cl^-)[154], and (iii) the presence of ion exchange membranes [20,28,30]. Therefore, the behavior of a CO_2-MCDI cell seems to be different from a conventional MCDI cell operated for water desalination.

Conventional MCDI and CO_2-MCDI only differ by their electrolyte, i.e., CO_2-sparged water solution for CO_2-MCDI and salt solution for MCDI, which mainly differ by their electrolyte strength. On the one hand, a NaCl solution consists of fully dissociated salt, thus being a strong electrolyte. On the other hand, the CO_2-sparged solution contains amphoteric ions (HCO_3^-), thus being a weak electrolyte. To the best of our knowledge, very few studies describe the performance of an MCDI cell with amphoteric ions[59,60,107,154,171], i.e., HPO_4^{-}[172] and HCO_3^-[59,60,107,154]. Most of these studies describe the performance of an MCDI cell with solutions composed of amphoteric ions in combination with salt ions[59,60,107,172], whereas only one study tested the MCDI cell performance with a solution consisting exclusively of amphoteric ions[154]. A CO_2-sparged water solution can have a significant impact on the MCDI performance. For instance, we previously stressed the importance of the pH inside the electrode EDLs for CO_2-sparged solutions[154]. A higher pH inside the anode EDL could lead to the dissociation of HCO_3^- into CO_3^{2-}, which is not desired as the adsorption of CO_3^{2-} requires twice the number of electrons compared to the adsorption of HCO_3^- (Λ_a=0.5 for 1 CO_3^{2-} removed), and therefore Λ_a decreases. Besides, chemisorption of H_2CO_3* could also take places on the electrode surface. CO_2 gas is known to react with porous electrodes, even when the electrodes are not electrically charged[36,173]. Moreover, recent studies showed that $H_2CO_3^*$ could even be adsorbed in porous electrodes by charging a CDI cell with Na^+ and Cl^- ions, a process which has been referred to supercapacitive swing adsorption (SSA)[59,60,107]. Besides the role of the electrodes, the ion exchange membranes (IEMs) can potentially affect Λ_a. Studies demonstrated the importance of IEMs on the ion selectivity in MCDI cells [71,75], an effect of which was never investigated in CO_2-MCDI with a CO_2-sparged solution.

Compared to a monovalent solution, CO_2-MCDI is a more complex system due to the multitude of physical phenomena (ion adsorption, ion transport in IEMs, gas absorption, and chemical reactions). Therefore, in this work, we separately study the effect of the electrodes and IEMs on the absorption efficiency. In the first part, the role of IEMs on the CO_2-MCDI performance was investigated by performing CO_2 absorption experiments in CO_2-MCDI (i.e., with an AEM and a CEM), in CO_2-AEM-CDI (with only the AEM), in CO_2-CEM-CDI (with only the CEM) and CO_2-CDI (without membranes). In the second part, the HCO_3^-/CO_3^{2-} adsorption mechanisms in the electrodes were theoretically

investigated by comparing experimental data with the amphoteric Donnan model (amph-D model). In conventional MCDI using salt solutions, theoretical models have been widely used to predict the salt adsorption in the capacitive electrodes. Finally, in the last part, different effects on the HCO_3^-/CO_3^{2-} adsorption in the electrodes were investigated, i.e., (i) the passive CO_2 adsorption in the electrodes, (ii) the effect of low ion concentrations, and (iii) the chemical dissociation effect of the chemical surface groups in the electrode micropores.

4.2. Theory

This section describes two theoretical models adopted to predict the performance of a CO_2-CDI cell, operated with a CO_2-sparged solution, and a conventional CDI cell with NaCl solutions. The first model is the so-called amphoteric Donnan (amph-D) model developed by Gao et al. [165] for conventional CDI, while the second model is the multi-equilibria amphoteric Donnan (m-amph-D) model. The m-amph-D model is based on the model proposed by Hemmatifar and Oyarzun et al. [119,174] for conventional CDI. The amph-D model is an extended version of the Donnan model[84], which considers the presence of immobile chemical charge on the carbon surface, the amount of which is assumed to be constant and not dependent on local (electrical) charge and pH. Instead, in the multi-equilibria amph-D model, the amount of chemical surface charge is a function of the local pH at the carbon surface, where the chemical surface charge can vary based on acid-base reactions. Besides the amph-D model, note that other similar models were developed to predict salt adsorption in conventional CDI, namely, the modified Donnan (mD) model [70] and the improved Donnan (i-mD) model [84]. Among these models, the amph-D model describes the physics and chemistry of ion adsorption in EDLs most realistically. The amph-D model can accurately describe adsorption in a wide range of experimental conditions [86] and can predict phenomena observed under specific conditions, including inverted CDI behavior[165,169]. Therefore, we selected the amph-D model in this study.

4.2.1. Amphoteric Donnan (amph-D) model

The amph-D model considers that the micropores are separated into two different regions: an acidic region (region A) and a basic region (region B). The acidic region is covered by negatively chemical surface charged groups, i.e., COO^-, and the basic region is covered by positively chemical surface charged groups, i.e., H^+, as shown in Fig. 4.2. Thus, ion adsorption occurs in 4 different regions (regions A and B in both cathode and anode). For each region, three different types of charge are considered: the electrical charge (σ_{elec}), the ionic charge (σ_{ionic}) and the chemical surface charge (σ_{chem}).

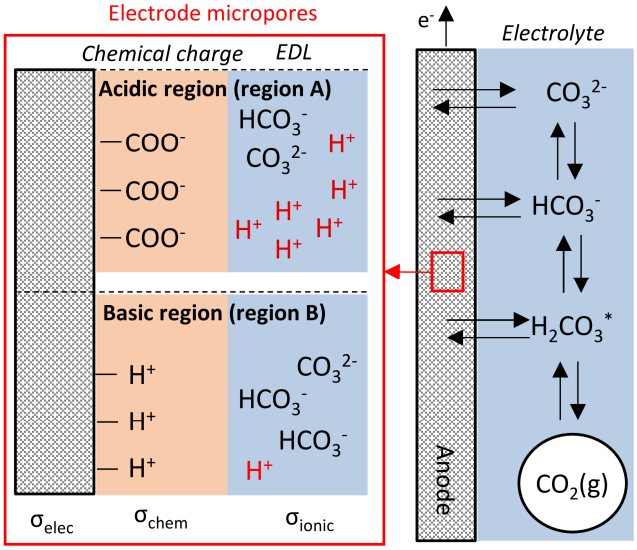

Fig. 4.2: Schematic illustration of the acidic (region A) and basic regions (region B) in the anode micropores.

In each region, the summation of the three different types of charge is equal to zero, as given by

$$\sigma_{\mathrm{chem,r}} + \sigma_{\mathrm{elec,r}} + \sigma_{\mathrm{ionic,r}} = 0 \qquad 4.4$$

where subscript r refers to the region (A or B). The ion adsorption in the micropores is related to the Donnan potential[80,175,176], and therefore, the ion concentration in the micropores is given by the Boltzmann equation

$$c_{\mathrm{i,mi,r}} = c_{\mathrm{i}} \cdot e^{-z_{\mathrm{i}} \cdot \Delta\phi_{\mathrm{D}}} \qquad 4.5$$

where $c_{\mathrm{i,mi,r}}$ refers to the ion concentration in the micropores for each region, c_{i} is the ion concentration in the spacer channel (bulk solution), z_{i} is the ion valence and $\Delta\phi_{\mathrm{D}}$ is the Donnan potential at the interface of the electrode micropore and the solution. In conventional CDI for water desalination, $c_{\mathrm{i,mi,r}}$ usually refers to the concentration of Na^+ or Cl^- [86,118]. Instead, in CO_2-CDI, $c_{\mathrm{i,mi,r}}$ refers to the concentration of HCO_3^-, CO_3^{2-}, H^+, OH^-, $H_2CO_3^*$. The total ionic charge (σ_{ionic}) in each electrode region can be calculated using

$$\sigma_{\mathrm{ionic,r}} = \sum_{\mathrm{i}} z_{\mathrm{i}} \cdot c_{\mathrm{i,mi,r}}. \qquad 4.6$$

The electrode charge (σ_{elec}) is directly related to the Stern potential ($\Delta\phi_{\mathrm{S}}$) and the Stern capacitance (C_{s}), and is given by

$$\sigma_{\mathrm{elec,r}} = \frac{\Delta\phi_{\mathrm{S,r}} \cdot V_{\mathrm{T}} \cdot C_{\mathrm{s}}}{F} \qquad 4.7$$

where V_T is the thermal voltage, and F is the Faraday constant (96485 C mol^{-1}). All potentials are dimensionless, which can be converted to a dimensional voltage by multiplying the dimensional potential with the thermal voltage, $V_{\mathrm{T}} = (R \cdot T)/F$, where R is the ideal gas constant (8.314 J K^{-1} mol^{-1}), and T is the temperature (298 K).

The electrode potential ($\Delta\phi_{\mathrm{elec}}$) is defined as the sum of the Stern and Donnan potentials. Furthermore, the potential of each electrode is equal for the regions A and B and is given by

$$\Delta\phi_{\mathrm{elec}} = [\Delta\phi_{\mathrm{D}} + \Delta\phi_{\mathrm{S}}]_{\mathrm{A}} = [\Delta\phi_{\mathrm{D}} + \Delta\phi_{\mathrm{S}}]_{\mathrm{B}}. \qquad 4.8$$

In equilibrium, there is no potential gradient across the electrodes and the flow channel due to ionic and electronic resistances. Therefore, the (dimensional) cell voltage (V_{cell}) is the difference of the electrode potential between the anode and cathode.

$$V_{\mathrm{cell}} = \left(\Delta\phi_{\mathrm{elec,anode}} - \Delta\phi_{\mathrm{elec,cathode}}\right) \cdot V_{\mathrm{T}}. \qquad 4.9$$

We consider that the mass of both electrode regions (A and B) is the same, and therefore we can calculate the average electrode charge ($\sigma_{\mathrm{elec,av}}$) using

$$\sigma_{\mathrm{elec,av}} = \frac{1}{2} \cdot \left(\sigma_{\mathrm{elec,A}} + \sigma_{\mathrm{elec,B}}\right). \qquad 4.10$$

Assuming a symmetric system with the same mass and dimensions of the anode and cathode sum up to zero ($\sigma_{\mathrm{elec,av,anode}} + \sigma_{\mathrm{elec,av,cathode}} = 0$).

For the CO_2-CDI cell, the chemical dissociation constants of the chemical reactions shown in 4.14.3 must also be included in the amph-D model (see Table 4.1). Note that the constant K_H can be derived from H^{CC} ($K_H = R \cdot T / H^{CC}$).

Table 4.1: Equilibrium dissociation constants between CO_2(g), H_2CO_3*, HCO_3^-, CO_3^{2-}, OH^-, H^+

Equations	Equilibrium Constant	Reference
$H^{cc} = \frac{C_{H_2CO_3^*}}{C_{CO_2(g)}}$	H^{cc}=0.83	25
$K_1 = \frac{C_{HCO_3^-} \cdot C_{H^+}}{C_{H_2CO_3^*}}$	K_1=$10^{-6.35}$	26
$K_2 = \frac{C_{CO_3^{2-}} \cdot C_{H^+}}{C_{HCO_3^-}}$	K_2=$10^{-10.33}$	26
$K_w = C_{OH^-} \cdot C_{H^+}$	K_w=10^{-14}	

The total carbon (n_T) in the system is distributed through the liquid volume and the gas volume and is given by

$$n_T = C_{T,solution} \cdot V_l + m_{elec} \cdot \alpha \cdot V_{mi} \cdot \left(\sum_{r=A,B}^{anode} C_{T,mi,r} + \sum_{r=A,B}^{cathode} C_{T,mi,r} \right) + \frac{P_{CO_2(g)} \cdot V_g}{R \cdot T} \quad 4.11$$

where $C_{T,solution}$ is the concentration of total carbon ($C_{T,solution} = C_{H_2CO_3^*} + C_{HCO_3^-} + C_{CO_3^{2-}}$), $C_{T,mi}$ is the concentration of total carbon in the micropores, V_{mi} is the micropore volume (mL g_{elec}^{-1}), m_{elec} is the mass per electrode (g_{elec}^{-1}), α is the fraction of each micropore region, V_l the volume of the CO_2-sparged solution, and V_g the volume of gas. Note that the volume of micropores was measured by a gas adsorption analyzer, which we will discuss in Section 3.2.

For the CO_2-CDI cell with NaCl solutions, the mass balance for the total amount of Na^+ ($n_{total,Na}$) and Cl^- ($n_{total,Cl}$) in the system is

$$n_{total,Na} = c_{Na} \cdot V_l + m_{elec} \cdot \alpha \cdot V_{mi} \cdot \left(\sum_{r=A,B}^{anode} c_{Na,mi,r} + \sum_{r=A,B}^{cathode} c_{Na,mi,r} \right) \quad 4.12$$

$$n_{total,Cl} = c_{Cl} \cdot V_l + m_{elec} \cdot \alpha \cdot V_{mi} \cdot \left(\sum_{r=A,B}^{anode} c_{Cl,mi,r} + \sum_{r=A,B}^{cathode} c_{Cl,mi,r} \right). \quad 4.13$$

4.2.2. Multi-equilibria Amphoteric-Donnan (m-amph-D) model

In contrast to the amph-D model, the m-amph-D model considers that the chemical surface charge is dependent on the local pH at the carbon surface. Studies showed that the chemical surface charge can change over time, due to the local pH at the carbon surface [119], or due to electrode oxidation reactions [170]. Since the pH is expected to change drastically in both electrodes, as H^+ is the only cation present in solution, we implement a similar approach as developed in Ref.[119] to describe the chemical surface charge as function of pH. We consider the acid-base groups A^-/AH, for the acidic region, and BH^+/B, for the basic region, and their dissociation constants K_A and K_B, respectively. Constants K_A and K_B are given by

$$K_A = \frac{C_{A^-} \cdot C_{H,mi,A}}{C_{AH}} \quad 4.14$$

$$K_B = \frac{C_B \cdot C_{H,mi,B}}{C_{BH^+}}. \quad 4.15$$

Then, we can substitute c_{A^-}=-$\sigma_{chem,A}$ and c_{BH^+}=$\sigma_{chem,B}$. The total concentration of surface groups is then given by $\sigma_{chem,A,tot}$=-(c_{A^-}+c_{AH}) and $\sigma_{chem,B,tot}$=c_{BH^+}+c_B. Consequently, we can express $\sigma_{chem,A}$ and $\sigma_{chem,B}$ in the m-amph-D model as

$$\sigma_{chem,A} = \frac{K_A}{K_A + C_{H,mi,A}} \cdot \sigma_{chem,A,tot} \quad 4.16$$

$$\sigma_{chem,B} = \frac{C_{H,mi,B}}{K_B + C_{H,mi,B}} \cdot \sigma_{chem,B,tot}. \quad 4.17$$

4.3. Material and methods

4.3.1. Electrode and cell preparation

In this work, we selected two types of carbon electrodes, i.e., carbon cloth (CC) and activated carbon (AC) electrodes. The CC electrodes are commercially available (ACC-5092-15, Kynol, Germany), and the AC electrodes were home-made according to a previously reported method[18,23]. In this method, a slurry was prepared from two components: I) activated carbon (DLC, super 30, Norit, the Netherlands, BET=1600 m^2 g^{-1}), II) a solution of N-Methyl-2-pyrrolidone (NMP) and polyvinylidene fluoride (PVDF) (KYNAR HSV 900, Arkema Inc., USA) in a ratio of 30:1 (w/w). The slurry was then cast on a graphite sheet with a 500 µm-thickness casting knife and dried for 24 h. After evaporation of NMP, the fabricated electrodes were then composed of 10 wt% PVDF and 90 wt% AC with a thickness of 200 µm. The electrodes were soaked in deionized water for at least 24 hours. The MCDI cell was composed of several layers, i.e., (i) titanium coated with platinum current collector, (ii) the AC electrode, (iii) a CEM (CMX, Astom (Neosepta), Japan), (iv) a polymeric spacer (PA 6.6 fabric, Nitex 03-300/51, Sefar, Switzerland, 200 µm), (v) an AEM (AMX, Astom (Neosepta), Japan) and (vi) another AC electrode and (vii) a current collector. The CDI cell has a cell structure than the MCDI cell except for the AEM and CEM layers. Moreover, the CDI cell was also tested with the CC electrodes.

4.3.2. Electrode characterization

Porosity analysis, SEM images, and titration were performed on each type of electrode (CC and AC electrodes). Porosity analyses were performed using an automated gas adsorption analyzer (Tristar 3000, micromeritics Instrument Corp., USA). Prior to the analysis, a sample of 0.2 g of electrodes material was dried at 598 K under N_2 atmosphere. Then, an N_2 isotherm was obtained at 77 K using 0.1 g of dry sample of AC electrodes and 0.2 g of dry sample of CC electrodes. The pore-size distribution was then calculated from the N_2 isotherm data using the non-localized density functional theory (NLDFT) model, provided by the built-in software of the instrument (Fig. 4.3c). The volume of micropores was found by integrating the pore volume with a diameter smaller than 2 nm.

Titration was performed with an automated titration station (888 Titrando, Methrom). Before titration, 50 mL of 0.05 M NaOH solution was constantly sparged with N_2 to remove all traces of dissolved CO_2. Then, an electrode sample (0.5 g for the AC electrode and 1 g for the CC electrode) was soaked in the NaOH solution and then titrated by dosing 0.5 mL of acid solution (0.1 M HCl) every 3-5 min. The time for each dosing step was adjusted to reach a stable pH value, which indicates that the electrode reached a

chemical equilibrium with the solution. During the titration period, the NaOH solution was constantly sparged with N_2 to avoid the presence of CO_2 and the effect thereof on the titration results. A blank titration was performed following the same procedure, without the electrode sample. The results of the blank and sample titrations are shown in the supporting information (Fig. S2). For each pH value measured, the concentration of chemical charge on the carbon surface is calculated using

$$\sigma_{\mathrm{chem,pH}} = \frac{(\mathrm{V_{sample}} - \mathrm{V_{blank}}) \cdot \mathrm{C_{titrant}}}{\mathrm{V_{mi}} \cdot \mathrm{m_{electrode}}} \qquad 4.18$$

where $\mathrm{C_{titrant}}$ represents the concentration of the titrant (HCl), $\mathrm{V_{mi}}$ the micropore volume per electrode mass, $\mathrm{m_{electrode}}$ the mass of the electrodes used during titration, $\mathrm{V_{sample}}$ the titrant volume obtained from the sample titration at a given pH value, and $\mathrm{V_{blank}}$ the titrant volume obtained from the blank titration at a given pH value.

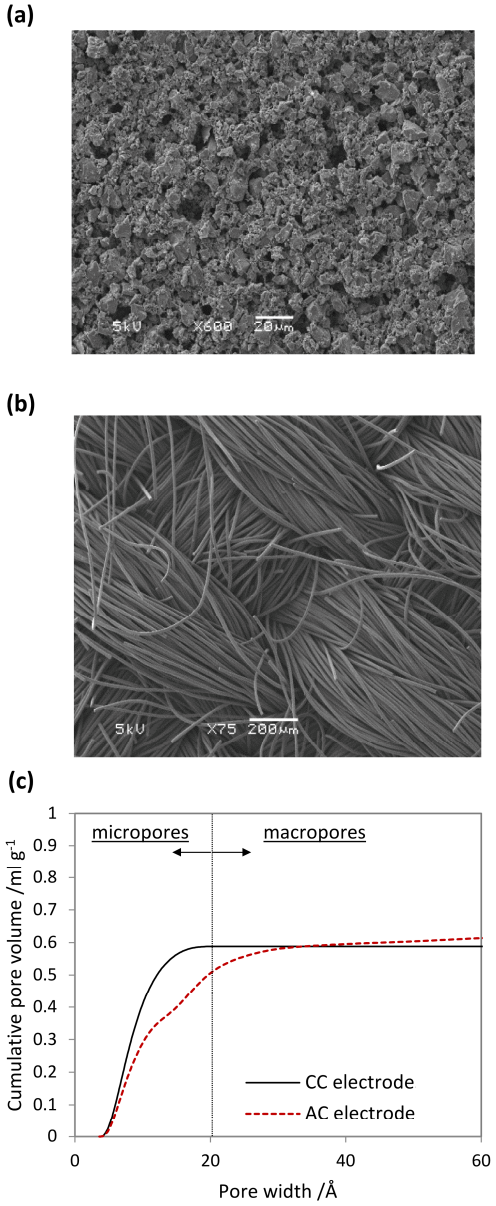

Fig. 4.3: Electrode characterization of the AC and CC electrode materials: SEM image of the (a) AC and (b) CC electrode, and (c) porosity analysis of the AC and CC electrodes. The pores with a diameter smaller than 20 Å (2 nm) are considered as micropores, while the pores with a diameter larger than 20 Å are considered as macropores.

Fig. 4.3a-b shows the microscopic structure of the electrode materials. The AC electrode (Fig. 4.3a) shows a homogeneous porous structure, whereas the CC electrode consists of carbon fibers.

4.3.3. Experimental procedure for passive CO_2 absorption in uncharged electrodes

The CO_2 absorption in the electrodes was characterized in the absence of an electrical field in absorption batch experiments. We refer to this type of experiment as "passive CO_2 absorption". A similar experiment has been previously done with NaCl[84] or with mixtures of salts[177]. The passive CO_2 absorption experiments were performed in batch mode using a home-made reactor. The home-made reactor consisted of a glass flask, which contained a CO_2:N_2 gas mixture (V_g=55 mL) and a CO_2-sparged deionized water solution (V_l=90 mL). Prior to each experiment, the deionized water was equilibrated with a defined CO_2 partial pressure (the same as in the gas phase) by flushing a CO_2:N_2 gas mixture into the reactor. At the same time, the electrode material was pre-treated in two steps. In the first step, the electrode material was soaked into deionized water, and sparged with N_2 for 20 hours. In the second step, the electrode material was dried at room temperature for 4 hours. During the experiment, the pre-treated electrode material was submerged in the reactor (solution phase), while all the gas valves were closed. The amount of carbon species adsorbed in the electrode material was monitored by measuring the gas pressure with a manometer (Cerabar T PMP131, Endress+Hauser). The change of gas pressure is directly related to a change of CO_2 partial pressure, since N_2 is an inert gas, and is not expected to be adsorbed in the electrode. From the change of gas pressure, the total amount of carbon species adsorbed in the electrodes ($C_{total}=CO_2(g)+H_2CO_3^*+HCO_3^-+H^+$) is calculated based on a mass carbon balance and the chemical equilibrium reactions as given by Eqs. 4.1-4.3.

4.3.4. (M)CDI experimental procedure

Charging/discharge cycles were performed with (M)CDI cells using both CO_2-sparged (CO_2 absorption tests) and NaCl solutions (salt adsorption tests). During the charging step, a current (or voltage) was applied between the electrodes to adsorb ions from the solution. During the discharge step, a reversed current or a discharge voltage of 0 V was applied between the electrodes to desorb ions into the solution. The two following sections describe the procedures for the salt adsorption and the CO_2 absorption experiments.

Salt adsorption with NaCl solutions (conventional CDI)

Salt adsorption tests were performed in CDI cells using different NaCl concentrations (0.1, 0.5, 1, 5, and 20 mM) in batch experiments until reaching equilibrium. The research set-up consisted of a CDI cell and a glass bottle stirred with a magnetic stirrer. A peristaltic pump (Masterflex L/S, Cole-Parmer, USA) was used to recirculate a NaCl solution between the CDI cell and the glass bottle at a flow rate of 40 mL min^{-1}. The water volume was different in each experiment to ensure that ion adsorption in the CDI cell did not lead to a complete depletion of NaCl in solution. Charging/discharge cycles were applied to the CDI cell. During the charging step, a constant voltage of 0.3, 0.5, 0.7, or 1V was applied to the CDI cell, while during the discharge step, a constant voltage of 0V was applied. The charging time, which was equal to the discharge time, was long enough to ensure that the CDI cell reached an equilibrium. Since only NaCl was present in solution, the amount of salt removed from the solution was monitored by measuring the conductivity of the solution. The charge efficiency was calculated as

$$\Lambda = \frac{n_{Na^+(ad)} + n_{Cl^-(ad)}}{n_{charge}} = \frac{(C_{NaCl,initial} - C_{NaCl,final}) \cdot F}{Q} \qquad 4.19$$

where Q is the electrical charge stored in the electrode, $c_{NaCl,initial}$ is the NaCl concentration at the beginning of a charging step, and $c_{NaCl,final}$ is the NaCl concentration at the end of a charging step.

CO_2 absorption tests (CO_2-(M)CDI)

Several CO_2-(M)CDI experiments were performed in batch mode using the same procedure, as previously reported in Ref. [154]. Before the experiment, a CO_2-sparged water solution was prepared by flushing a gas mixture of N_2:CO_2 (85%:15% vol/vol) using two mass flow controllers (MASS-STREAM D-6300, Bronkhorst, the Netherlands) in deionized water. A volume of the CO_2-sparged solution (33 mL) was circulated at 30 mL min^{-1} between the (M)CDI cell and a gas-liquid contactor (GLC). Both the (M)CDI cell, and the GLC were contained in a controlled-temperature chamber at 298K. The GLC is a cylinder-shaped glass container, which contains both a gas and a liquid phase, and ensures the exchange of CO_2 between both phases. Note that the recirculated solution and the gas phase in the GLC were sparged with the same gas mixture (15% CO_2) until both phases reach chemical equilibrium. At the same time, the MCDI cell was short-circuited (cell voltage of 0 V) to reach chemical equilibrium between the ion concentrations in the micropores and the CO_2-sparged solution. After the entire system reached equilibrium, gas valves were closed to enclose a defined volume of gas in the GLC. The experiment started by charging the CO_2-(M)CDI cell either in constant current or constant voltage

mode. In constant current mode, a current density (0.2, 0.4, or 0.6 A m^{-2}) was applied between the electrodes, both during galvanostatic charging (positive current) and discharge (negative current). Under constant voltage mode, a cell voltage of 0.3, 0.5, 0.7, or 1 V was applied during charging, and a cell voltage of 0 V was applied during discharge. Different times for charging and discharge were tested (1.1 h, 2h, and 5h). A potentiostat (Ivium, the Netherlands) was used to control the current or the voltage. During the experiment, the relative pressure of the gas in the GLC was monitored with a manometer (Cerabar T PMP131, Endress+Hauser). Based on the change of the partial CO_2 pressure during the experiment (ΔP_{CO_2}), the amount of CO_2 absorbed or desorbed during one cycle was estimated with the ideal gas law as

$$\Lambda_a = \frac{n_{CO_2(g)}}{n_{charge}} = \frac{\Delta P_{CO_2} \cdot F}{Q \cdot R \cdot T}. \quad 4.20$$

Energy consumption (W_{net}^*) was calculated based on the energy consumption of the (M)CDI cell (W_{net}) and the amount of CO_2 gas absorbed

$$W_{net}^* = \frac{W_{net}}{n_{CO_2}} = \frac{\int_0^Q V_{cell}^c dQ - \int_0^Q V_{cell}^D dQ}{n_{CO_2}} \quad 4.21$$

where V_{cell}^c is the cell voltage during charging, V_{cell}^D the voltage during discharge and Q is the electrical charge.

4.4. Results and discussion

4.4.1. Absorption efficiency in CO_2-MCDI

Firstly, we characterized the absorption efficiency in a CO_2-MCDI cell operated in constant current mode under various conditions (different current densities, amount of charge stored, and cycle times). Fig. 4.4a shows the electrical charge and the pressure measured during typical adsorption/desorption cycles in CO_2-MCDI operated in constant current mode Fig. 4.4a shows that the gas pressure in the gas-liquid contactor decreases, when the electrical charge stored in the electrodes increases, and vice-versa. This charge-pressure relationship illustrates the principle of the CO_2-MCDI cell, i.e., by increasing the amount of charge stored in the electrode, carbonate ions (HCO_3^- and CO_3^{2-}) are electro-adsorbed in the anode and removed from the electrolyte solution. Consequently, the carbonate ion concentration decreases in the electrolyte solution, and more CO_2 gas is

spontaneously absorbed in the electrolyte solution (according to equilibrium reactions given by Eqs. 4.1-4.3).

Fig. 4.4b-d show the absorption efficiency (Λ_a) as function of the charge stored in the electrodes (Fig. 4.4b), the current density (Fig. 4.4c), and the charging time (Fig. 4.4d). In our previous study[154], Λ_a was already characterized as function of current density. However, the effect of current density could not be differentiated from other effects (the charge stored in the electrodes and the charging time). Fig. 4.4b-d show that Λ_a tends to decrease with longer charging times (e.g., from Λ_a=0.55 after 1 hour to Λ_a=0.35 after 4.5 hours), while no specific relation is found with the electrode charge and the current density. This observation is in good agreement with our previous study (Λ_a=0.7 for 0.7 hours and Λ_a=0.5 for 3.3 hours) [154]. In Ref.[154], we hypothesized that a decrease of Λ_a with longer cycle time could be related to the selective adsorption of CO_3^{2-} in the electrodes at longer charging times. Time-dependent selective adsorption of divalent ions in capacitive electrodes has been shown in conventional CDI[168]. However, besides the electrode behavior, the IEMs could also influence Λ_a. For instance, the IEMs show a selectivity towards specific ions based on their valence[71,75] or size[71]. The individual effect of the electrodes and the IEMs is challenging to distinguish in CO_2-MCDI experiments. Therefore, we investigate the individual effect of the IEMs and the capacitive electrodes by characterizing Λ_a with (CO_2-MCDI) and without IEMs (CO_2-CDI).

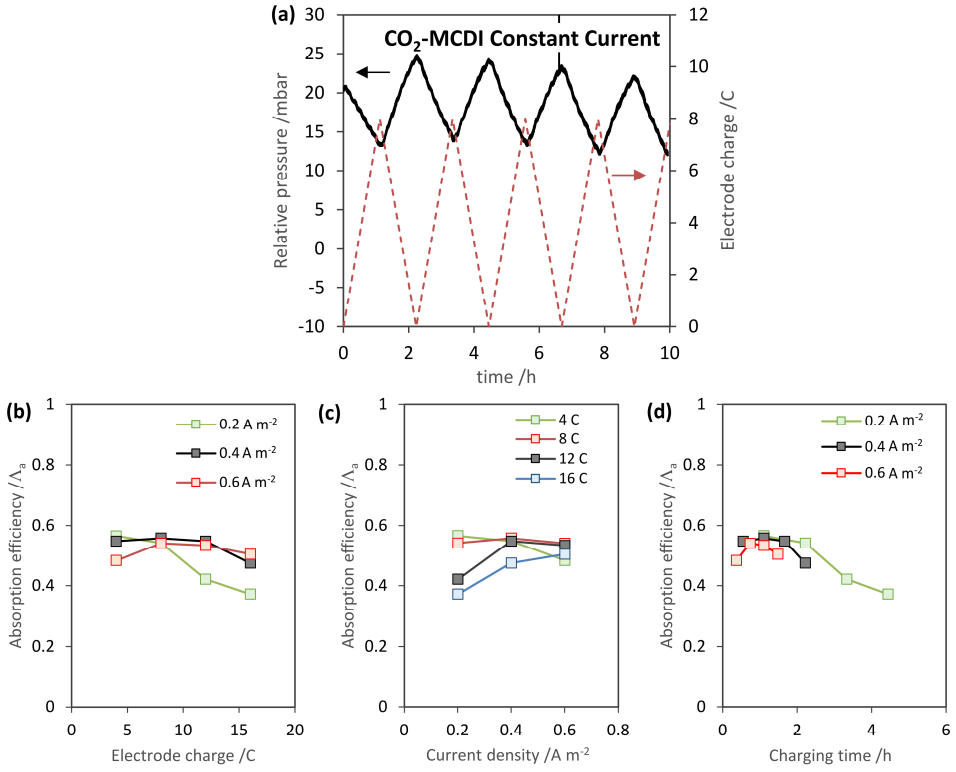

Fig. 4.4: (a) Gas pressure in the gas-liquid contactor (GLC) and the charge stored in the electrode of the CO_2-MCDI cell operated in constant current mode (0.4 A m-2 until 8 C). Absorption efficiency ($\boldsymbol{\Lambda_a}$) as function of the (b) charge, (c) current density, and (d) charging time. Lines are added to guide the eye.

4.4.2. Effect of membranes on CO_2 absorption in CO_2-MCDI

Fig. 4.5 shows the values of Λ_a for CO_2-MCDI and for CO_2-CDI as function of the current density (Fig. 4.5a), cell voltage (Fig. 4.5b), and charging time (charging voltage of 0.5 V) (Fig. 4.5c). Fig. 4.5a shows that values of Λ_a are clearly higher in CO_2-MCDI compared to CO_2-CDI in constant current mode ($\Lambda_a \approx 0.55$ for CO_2-MCDI compared to $\Lambda_a \approx 0$ for CO_2-CDI). These findings are in line with results expected from conventional MCDI for water desalination. In conventional MCDI for water desalination, the IEMs greatly improve the charge efficiency (Λ) by blocking the desorption of co-ions from the electrode macropores[70,72]. Unexpectedly, CO_2-CDI experiments show no significant CO_2 absorption at 0.2 and 0.4 A m^{-2}. While the charge efficiency (Λ) in conventional CDI suffers from co-

ion expulsion [70,87,168,169] and faradaic reactions [73,77,170], we assume that both of these effects are negligible in CO_2-CDI. On the one hand, the effect of co-ion expulsion decreases at lower ion concentrations[72,87]. The concentration of ions in the feed water in CO_2-CDI is very low (≈0.05 mM), more than 400 times lower than ion concentrations usually tested in CDI (i.e., typically 20 mM NaCl). On the other hand, faradaic reactions in conventional CDI are mostly related to the presence of dissolved O_2 gas and of Cl^-, both of which are absent in a CO_2-sparged solution.

To study ion adsorption mechanisms in the electrodes, we performed experiments in constant voltage mode (Fig. 4.5b). In constant voltage mode, a chemical equilibrium in the electrode EDLs is reached when all time-dependent phenomena vanish. In contrast, the current mode controls the flux of ions, which continually drives several time-dependent processes (ionic flux, chemical reaction, ion adsorption). Compared to the results of the constant current mode, Fig. 4.5b shows that values of Λ_a are higher in CO_2-MCDI than CO_2-CDI, independent of the charging voltage. Nevertheless, Fig. 4.5c shows that the values of Λ_a in CO_2-MCDI decrease with charging time (Λ_a≈0.51 at 1 h against Λ_a≈0.35 at 5.5 h), which was not the case for CO_2-CDI. These results demonstrate that the CO_2-MCDI cell did not reach equilibrium even after 5 hours. Fig. 4.5d shows that the CO_2 concentration in CO_2-MCDI experiments never reached a stable value during charging and discharge, which demonstrates that a net CO_2 flux still occurs in the system. Unlike the CO_2-MCDI cell, the CO_2-CDI cell reached equilibrium after 1 hour, as values of Λ_a in CO_2-CDI are stable with time from 1 hour (Fig. 4.5c), and Fig. 4.5d shows that a constant CO_2 concentration is reached in both the charging and discharge steps. Therefore, the decrease in Λ_a observed at a longer charging time in CO_2-MCDI (described in section 4.1) is mostly caused by the presence of IEMs, and not directly from the electrode adsorption behavior. This finding disproves the hypothesis we made in Ref.[154], where we presumed that the loss of Λ_a in CO_2-MCDI with time was related to the electrode behavior.

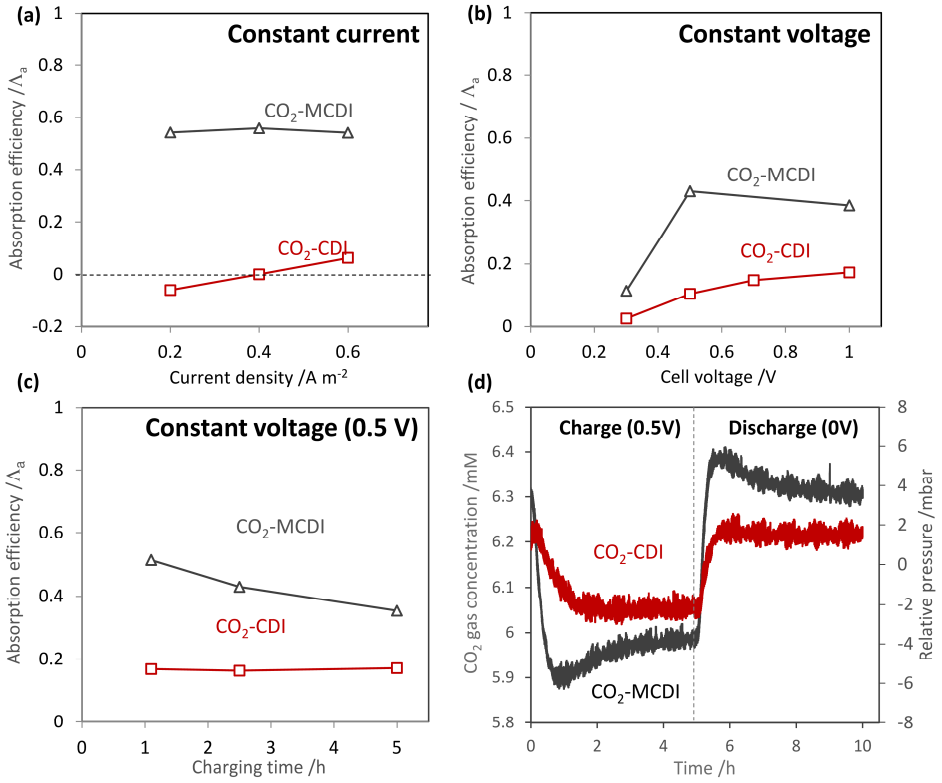

Fig. 4.5: Absorption efficiency of CO_2 in CO_2-MCDI (grey line) and CO_2-CDI configurations (red line) at (a) constant current (0.2-0.6 A m-2 by applying 8 C), (b) at constant voltage (0.3-1 V during 2.2 hours) and (c) at constant voltage with different charging times (0.5 V between 1.1 hours and 5 hours). (d) Gas pressure in CO_2-MCDI (grey line) and CO_2-CDI configurations (red line) at 0.5 V for 5 hours charging.

Since the membrane pair influences the CO_2-MCDI performance, it is not possible to differentiate the individual effect of either the AEM or CEM from the CO_2-CDI and CO_2-MCDI alone. To that end, we performed experiments with a cell by including only an AEM or a CEM, both in constant current and constant voltage mode (Fig. 4.6). Fig. 4.6a shows that higher values of Λ_a were obtained by using only an AEM compared to using only a CEM in both modes ($\Lambda_a \approx 0.49$ with CO_2-AEM-CDI and $\Lambda_a \approx 0.24$ with CO_2-CEM-CDI in constant current operation, see Fig. 4.6). Moreover, using only one AEM gives similar values of Λ_a as in CO_2-MCDI, where both IEMs are used (Λ_a=0.54 with CO_2-MCDI and Λ_a=0.49 with CO_2-AEM-CDI in constant current operation, see Fig. 4.6). Fig. 4.6b also shows similarities between the CO_2-AEM-CDI and CO_2-MCDI cells in terms of CO_2 concentration profile with time (at 0.5V), which suggests that the CO_2-AEM-CDI did not

reach equilibrium either. Instead, the CO_2-CEM-CDI cell shows a similar behavior than CO_2-CDI at constant voltage (Fig. 4.6a-b). Therefore, the higher values of Λ_a from the CO_2-MCDI cell are mainly due to the presence of the AEM. The CO_2 concentration as function of time for the CO_2-AEM-CDI suggests that a concentration gradient builds up across the AEM during charging (and discharge) with time (Fig. 4.6b). For instance, Fig. 4.6b shows that the CO_2 concentration first decreases during the charging step, but then starts to increase after one hour. We believe that, upon charging the cell, more carbonate ions (HCO_3^-/CO_3^{2-}) migrate through the AEM to the macropores of the anode than the amount that is adsorbed in the micropores of the anode. As a result, HCO_3^- and CO_3^{2-} ions accumulate in the anode macropores, increasing the total carbon concentration ($C_T=HCO_3^- +CO_3^{2-}+H_2CO_3^*$) in the macropores of the anode. Driven by the total carbon concentration difference between the anode macropores and the spacer solution, the total carbon diffuses from the macropores to the spacer solution. This total carbon flux can occur through the (i) diffusion of $H_2CO_3^*$ or (ii) the combined transport of HCO_3^- and H^+ due to the co-ion leakage of H^+.

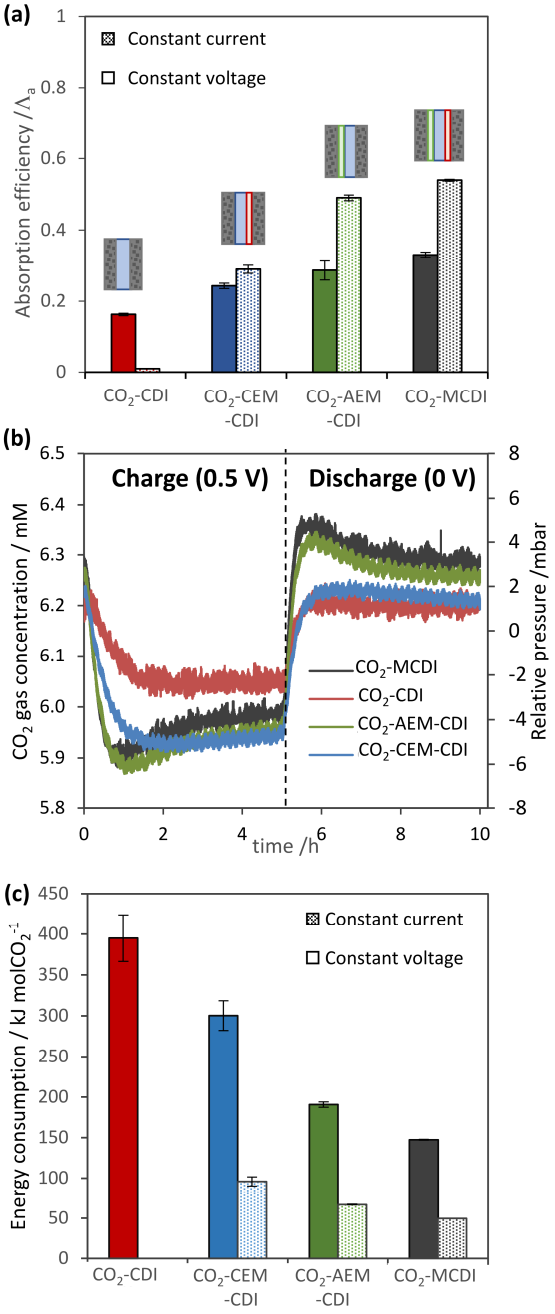

Fig. 4.6: Absorption efficiency of CO_2 in different CDI configurations: CO_2-MCDI, CO_2-AEM-CDI, CO_2-CEM-CDI, and CO_2-CDI (a) at constant voltage (0.5 V at 5 hours charging) and constant current (0.4

A m^{-2}, maximum charge 8 C). (b) Pressure and CO_2 gas concentration at 0.5 V. (c) Energy consumption at 0.5 V and 0.4 A m^{-2}.

As shown in Fig. 4.6a, ion exchange membranes (in particular the AEM) are essential to keep a high absorption efficiency (Λ_a) in CO_2-MCDI. Achieving a high Λ_a is mostly essential to minimize the energy consumption[154]. Fig. 4.6c shows that the lowest energy consumption was achieved with the CO_2-MCDI cell at constant current (W_{net}^*=49 kJ molCO_2^{-1} for CO_2-MCDI), the configuration in which the highest Λ_a was obtained. In contrast, the highest energy consumption was obtained with the CDI cell at constant voltage (W_{net}^*=390 kJ molCO_2^{-1} for CO_2-CDI), the configuration in which the lowest Λ_a was obtained. Covering the electrode with an ion exchange membrane (MCDI) is a suitable strategy to increase Λ_a, and also to decrease the energy consumption. The CDI performance was much lower than expected (compared to conventional CDI), with a maximum absorption efficiency of only 0.18 in constant voltage mode (Fig. 4.6b). As a first step toward developing a theoretical model for CO_2-MCDI, we will theoretically investigate the ion adsorption mechanism in CO_2-CDI at equilibrium condition (time-independent) in the next section. A full MCDI model is more complicated than a CO_2-CDI equilibrium model as an MCDI model includes not only time-independent phenomena (ion adsorption in electrode micropores) but also time-dependent phenomena (ion transport in electrode macropores, membranes and spacer). Thus, developing a reliable model for CO_2-CDI is essential before developing a more complex CO_2-MCDI model.

Studying the system under equilibrium conditions (i.e., constant voltage at long charging time) is essential to understand the system behavior before modeling CO_2-MCDI cells. Besides the equilibrium condition in the micropores, an MCDI model also includes time-dependent phenomena.

4.4.3. CO_2-CDI results compared with theoretical models

Conventional amphoteric-Donnan model

Understanding ion adsorption mechanisms in CO_2-CDI cell is of primary importance in order to optimize the process performance. In this section, we theoretically investigate the adsorption mechanisms by comparing the amphoteric Donnan (amph-D) model[86,165] with experimental data. To the best of our knowledge, the amph-D model has been extensively used for NaCl solutions[79,169,174,177,178], but never for CO_2-sparged solutions. We performed CO_2-CDI experiments with two different carbon materials, i.e., activated carbon (AC) and carbon cloth (CC) electrodes. Prior to our modeling work, we performed a CDI experiment with a NaCl solution (see Fig. S3 in supporting information) to determine

three model parameters, namely, the Stern capacitance (C_s), and the chemical surface charge in the acidic and basic regions ($\sigma_{chem,A}$, $\sigma_{chem,B}$). Finally, the electrode micropore volume was determined by porosity analysis, as shown in Fig. 4.3c. The parameter values for both electrode materials are shown in Table 4.2.

Table 4.2: Parameters used in the amph-D model for both electrode materials

	AC electrode	**CC electrode**
$\mathbf{V_{mi}}$ (mL/g_{elec})	0.5	0.6
$\mathbf{m_{elec}}$ (g_{elec}/electrode)	0.5	0.9
$\boldsymbol{\alpha}$	0.5	0.5
$\mathbf{C_S}$ (F/mL)	170	170
$\boldsymbol{\sigma_{chem,A}}$ (mM)	-620	-710
$\boldsymbol{\sigma_{chem,B}}$ (mM)	400	350

Fig. 4.7 shows the absorption efficiency as function of cell voltage. The model correctly predicts the increase of the adsorption efficiency with increasing voltage but overestimates the value of Λ_a. Fig. 4.8a shows the relative effect of the adsorption of HCO_3^-, the expulsion of H^+ and the adsorption of CO_3^{2-} in/from the micropores of the anode on Λ_a. A non-ideal absorption efficiency (Λ_a<1) can be caused by both (i) the adsorption of CO_3^{2-} and (ii) the expulsion of H^+, which are, in this particular case, underestimated by the amph-D model. Adsorption of CO_3^{2-} is hardly predicted by the amph-D model as the predicted pH in the micropores by the model (maximum of pH≈8) is lower than the pH value where HCO_3^- dissociate into CO_3^{2-} (pH higher than 9 see Fig. 1a). The amph-D model does not describe the CO_2 adsorption accurately with the parameter values reported in Table 4.2, which were found by fitting the theory to experimental data of salt adsorption in desalination experiments.

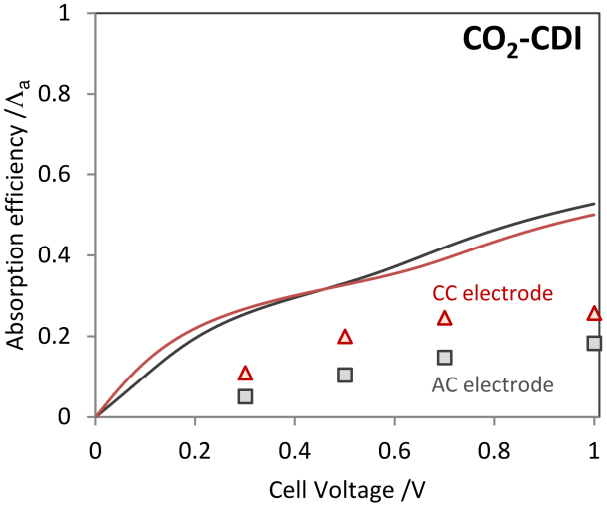

Fig. 4.7: CO_2 absorption efficiency calculated by the amph-D model (line) compared with experimental data (symbols) obtained in CO_2-CDI experiments as function of cell voltage for (a) activated carbon (AC) and (b) carbon-cloth (CC) electrodes

This discrepancy between data and theory can be the result of several factors. Firstly, the ionic strength of CO_2-sparged solutions is lower than of the NaCl solutions used in the CDI experiments. (< 1 mM NaCl). However, the amph-D model describes the data fairly well at low ion concentration, also shown in SI. Secondly, the concentration of the neutral molecule $H_2CO_3^*$ is the highest in the electrolyte. As $H_2CO_3^*$ is a weak acid, and only the dissociated species HCO_3^- and CO_3^{2-} can be electrosorbed, chemical equilibria (Eqs. 4.1-4.3) can have a strong effect on the absorption performance, and these equilibria are dependent on the local pH in the micropores. Thirdly, chemisorption of $H_2CO_3^*$ at the carbon surface can affect the absorption performance.

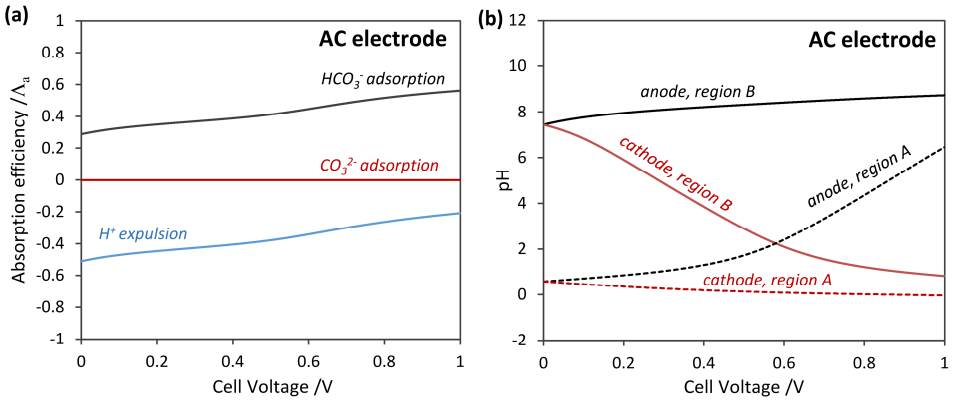

Fig. 4.8: (a) Effect of H^+ expulsion, and HCO_3^- and CO_3^{2-} adsorption in the anode calculated by the amph-D model for the AC electrode. (b) pH calculated in the micropores of the anode and cathode for the acidic (region A) and basic region (region B) for the AC electrode

We investigate the chemisorption of CO_2 at the electrode material by CO_2 absorption experiments with uncharged electrodes in the absence of an electric field. Refs. [174,177] study the effect of chemisorption of specific chemical species (mostly NO_3^-) on ion adsorption and include a new parameter in the amph-D model to describe this effect (intrinsic selectivity coefficient[174] or affinity term[177]). Fig. 4.9 shows the experimental and calculated amount of total carbon (C_{total}=CO_2(g)+$H_2CO_3^*$+HCO_3^-+CO_3^{2-}) adsorbed by uncharged electrodes as a function of the CO_2 partial gas pressure. The amph-D model predicts the CO_2 adsorption in uncharged AC carbon material well, which suggests that no significant CO_2 chemisorption takes place in the AC electrodes. On the other hand, the amph-D model underestimates the amount of CO_2 adsorbed by the CC electrode material. This finding suggests that CO_2 chemisorption seems to occur in the CC electrode material. The CO_2 chemisorption can occur through the chemical affinity between specific chemical surface groups and CO_2, such as amine groups[159].

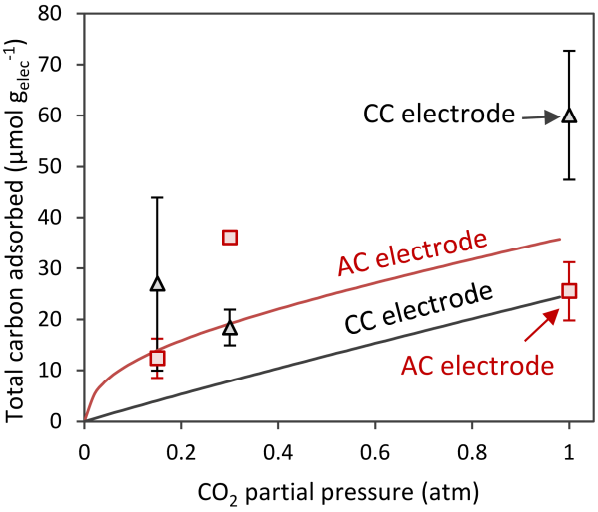

Fig. 4.9: Comparison between model predictions (lines) and experimental data (symbols) for passive adsorption with CC and AC electrodes material at different CO_2 partial pressures. Error bars show standard deviation.

Multi-equilibria amphoteric-Donnan model

In the previous section, we discussed that the amph-D model does not perfectly describe the CO_2 absorption performance of the CDI cell. We will now consider the chemical surface charge at the carbon electrodes as weak acid-base groups, which dissociate according to a dissociation equilibrium constant, especially when strong pH changes occur during charging and discharge. Furthermore, we will run, on both electrode materials, titration experiments in order to determine the amount of chemical surface charge. To include the effect of pH changes in the conventional amph-D model, we adopted the modeling approach from Hemmatifar et al., and we use a "multi-equilibria amphoteric Donnan" (m-amph-D) model[119]. The m-amph-D model requires at least two additional fitting parameters, i.e., a minimum of one dissociation constant for the acidic group (K_A) and one dissociation constant for the basic group (K_B). Moreover, the m-amph-D requires the total amount of surface groups ($\sigma_{chemA,tot}$ and $\sigma_{chemB,tot}$), instead of only the chemical surface charge of the amph-D model (σ_{chemA} and σ_{chemB}). To find parameter values for the m-amph-D model, including the dissociation constants and chemical surface charge parameters, titration experiments were performed (see Supporting information for more details on the fitting procedure) [119]. Fig. 4.10a-b shows the m-amph-D fit with the fitting parameters shown in Table 4.3 to the chemical surface charge obtained from experimental

electrode titrations. Fig. 4.10c-d show the chemical surface charge as function of pH in the regions A and B of the electrodes. Values of the chemical surface charge used for the amph-D (Table 4.2) and m-amph-D models (Table 4.3) are different but are not comparable as the models are different due to the different theoretical models. A similar difference between values of σ_{chem} obtained from electrode titration and the amph-D model was reported by Gao et al. [165].

Table 4.3: parameters used in the titration model

	AC electrode	**CC electrode**
$\sigma_{chemA,tot,1}$ (mM)	-1300	-800
$\sigma_{chemA,tot,2}$ (mM)		-500
$\sigma_{chemB,tot}$ (mM)	400	1300
$pk_{a,1}$ (mM)	2	2
$pk_{a,2}$ (mM)	N/A	9
pk_b (mM)	12	8

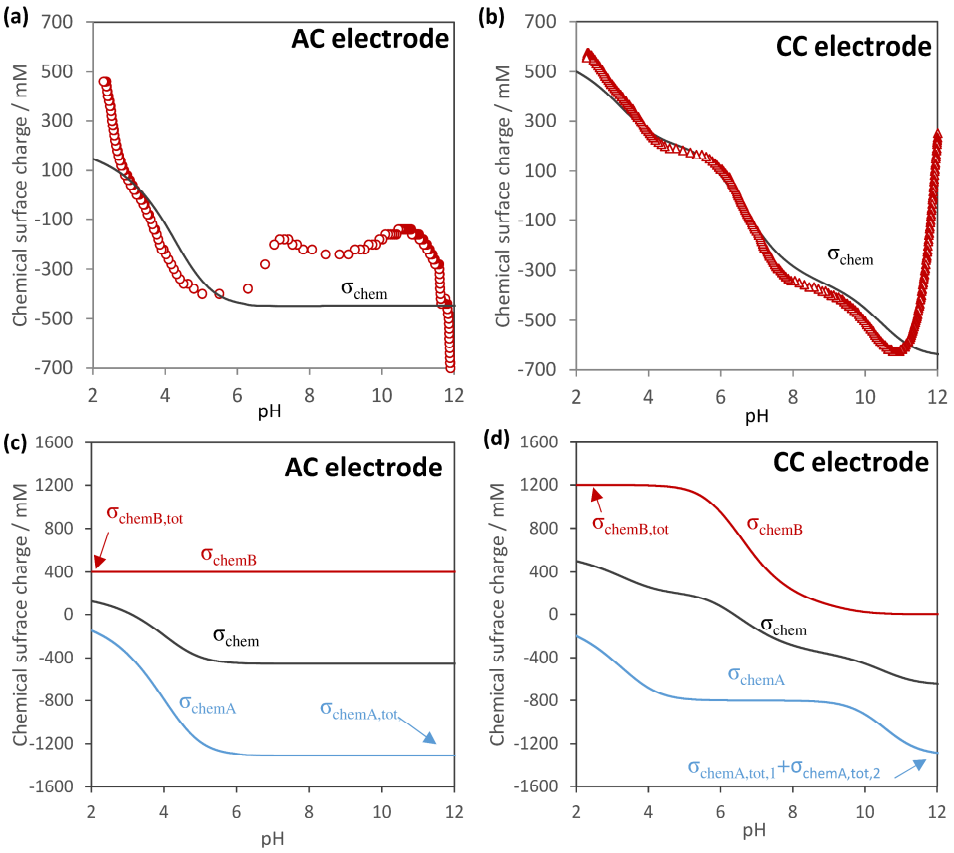

Fig. 4.10: Experimental data fitted with a titration model describing the total chemical surface charge as a function of pH for the (a) AC electrodes and (b) the CC electrodes. The data points are based on electrode titration experiments. Chemical surface charge in region A (σ_{chemA}) and region B (σ_{chemB}) for the (c) AC electrodes and (d) the CC electrodes

Fig. 4.11a-b shows a comparison between the absorption efficiency as function of the cell voltage obtained from both models (amph-D model and the m-amph-D model) and the experimental data. In comparison with the amph-D model, the m-amph-D model shows a better fit with the experimental data obtained from the AC electrodes. Regarding the CC electrodes, the m-amph-D model shows a better fit but underestimates the absorption efficiency at cell voltages below 1 V.

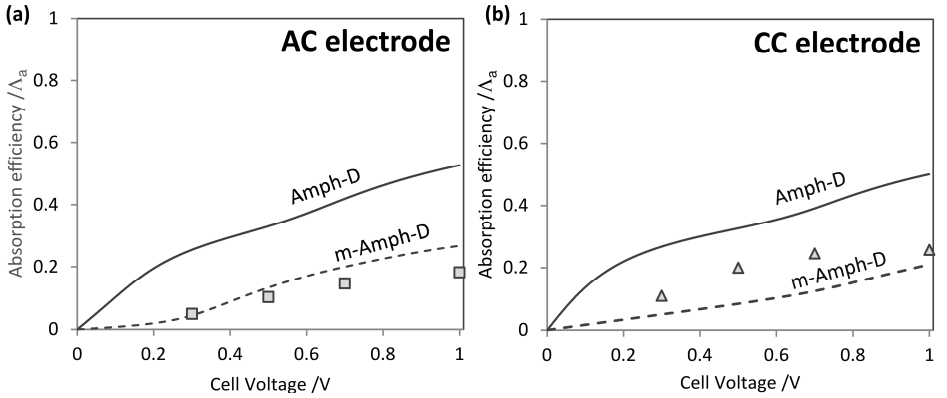

Fig. 4.11: Comparison between the amph-D and m-amph-D models and the experimental data obtained with (a) AC electrodes and (b) CC electrodes.

While the AC and CC electrode materials show similar material properties in terms of pore-size distribution and Stern capacitance (see Table 4.1), the CC electrode differs from the AC electrode in terms of surface chemistry. The AC and CC electrodes also differ in terms of morphology (Fig. 4.3a-b). However, we believe that the electrode morphology has no significant effect on the adsorption performance in equilibrium conditions: the electrode morphology would mainly influence the dynamics of ion transport from the macropores to the micropores of the electrode. Titration results suggest that, on the surface of the CC electrode material, more types of chemical surface groups are present than on the AC electrode material (three pK-values for the CC electrode against one pK value for the AC electrode, see Table 4.3 and Fig. 4.10). Moreover, the results of passive CO_2 absorption experiments suggest that CO_2 chemisorption takes place in the CC electrode micropores (Fig. 4.9), which indicates the presence of specific chemical surface groups with an affinity for the carbon species. For instance, a chemical affinity of CO_2 with amine groups is reported in Refs. [102,159]. We believe that the presence of both types of chemical surface groups can lead to more complex interactions with adsorbed carbonate ions, which are not predicted by the m-amph-D model yet.

Other effects not considered in this study could also influence the absorption efficiency, e.g., (i) the ion size-based selectivity[174] and (ii) the non-ideal dissociation degree in the micropores of the EDL. Regarding size-based selectivity, monovalent ions with lower hydrated radius (i.e., K^+ and Na^+[179]) and a lower ion hydration ratio[180] have shown to be selectively adsorbed in the electrode EDLs from monovalent salt mixtures (e.g., with K^+ and Na^+). However, to the best of our knowledge, no study clearly defines the hydrated radius of HCO_3^-, and therefore, we cannot estimate the effect of size-based selectivity

between HCO_3^- and CO_3^{2-}. Besides the ion-size based selectivity effects, the dissociation constant of carbonate species ($H_2CO_3^*$ and HCO_3^-) in the micropores of the electrode and chemical surface charge could be dependent on the electrical field. According to the dissociation field-effect theory[181,182], the dissociation of acid increases under the presence of an electric field in EDLs, mainly due to a change of permittivity conditions. Thus, we can hypothesize that the dissociation constants of bicarbonate ions (HCO_3^-/CO_3^2) can increase with cell voltage, resulting in a higher amount of CO_3^{2-} adsorbed in the electrode EDLs at a given pH, leading to lower absorption efficiencies. Moreover, the chemical surface charge in the acidic region (region A) can vary similarly according to the same dissociation field-effect theory. In a broader context, a better understanding of chemical interactions in electrode micropores in the presence of an electrical field is of great interest to tune the selectivity of carbon materials towards certain ions in CDI.

4.5. Conclusions

In this work, we investigated the role of the membranes and electrodes on the CO_2-MCDI performance by testing different CDI configurations, i.e., with and without membranes. Moreover, we theoretically investigated ion adsorption in electrodes (CO_2-CDI) by comparing the amph-D model with experimental data. CO_2-MCDI cells show the highest absorption efficiencies and the lowest energy consumption among the investigated CDI configurations. We demonstrated that the improved performance of CO_2-MCDI compared to CO_2-CDI can be mostly attributed to the presence of the AEM in the cell, whereas the CEM contributes to a lower extent. The AEM improves the absorption efficiency by ensuring that only bicarbonate and carbonate ions are transported to the anode during charging, and by hindering the transport of expulsed co-ions (H^+) from the anode to the spacer solution. Although the presence of the AEMs in the CO_2-MCDI cell improves the performance, the absorption efficiency decreases with increasing charging time. At longer charging time, we observe that carbon is transported from the anode back to the spacer channel, which can be explained by (i) co-ion leakage (H^+ and HCO_3^-) due to the high mobility of H^+ and by (ii) the diffusion of neutral molecules ($H_2CO_3^*$). Therefore, to optimize the performance, shorter cycles are preferred in a CO_2-MCDI configuration. Beyond the role of the membranes, we show that the absorption efficiency in CO_2-CDI is lower than predicted by the amph-D model. To explain the discrepancy between theory and data, three different effects were investigated, i.e., (i) chemisorption of CO_2, (ii) the low ion concentrations, and (iii) the acid-base dissociation of the chemical surface groups. A better fit was obtained between the experimental data and a new version of the amph-D model, the so-called multi-equilibria Amphoteric Donnan model, which includes a description of acid-base dissociation reactions of the chemical surface groups. We

demonstrated that these processes affect the performance of the CO_2-CDI system. Future work should focus on investigating and differentiating physical (by employing porous electrodes with no chemical surface charge) and chemical effects (by employing porous electrodes with chemical surface charge) of weak electrolyte solutions in CDI, especially by investigating the effect of the electrical field on the chemical dissociation constant of weak acids, and on the chemical surface charge in the EDLs.

4.6. Supporting information

4.6.1. Titration fitting procedure

The multi-equilibria amphoteric-Donnan (or m-amph-D) model requires the input of several parameters related to the chemical surface charge, i.e., the chemical surface groups of the acidic and basic regions ($\sigma_{sigma,A}$ for the acidic region and $\sigma_{sigma,B}$ for the basic region) and their associated pK values (pK_A for the acidic group and pK_B for the basic group). In the m-amph-D model, surface chemical charges are considered as a weak electrolyte, and therefore an acidic group (i,e., $AH \leftrightarrow A^- + H^+$) can dissociate according to a dissociation constant (pK_A), whereas a basic group (i.e., $BH^+ \leftrightarrow B + H^+$) can dissociate according to a dissociation constant (pK_B). Both constants are shown in Eqs. S4.1-S4.2. These parameters ($\sigma_{sigma,A}$, $\sigma_{sigma,B}$, pK_A and pK_B) can be estimated by fitting the m-amph-D model to the experimental result obtained during electrode titration (shown in Fig. S4.1).

$$K_A = \frac{C_{A^-} \cdot C_{H,mi,A}}{C_{AH}} \quad \text{S4.1}$$

$$K_B = \frac{C_B \cdot C_{H,mi,B}}{C_{BH^+}} \quad \text{S4.2}$$

The m-amph-D model, as shown in section 4.2 of the manuscript article, was used to calculate the pH of the solution during electrode titration. The m-amph-D was used to estimate the pH of the solution with the electrode (sample titration) and without the electrode (blank titration) during the titration experiment. Fig. S4.1a shows the pH calculated by the m-amph-D model.

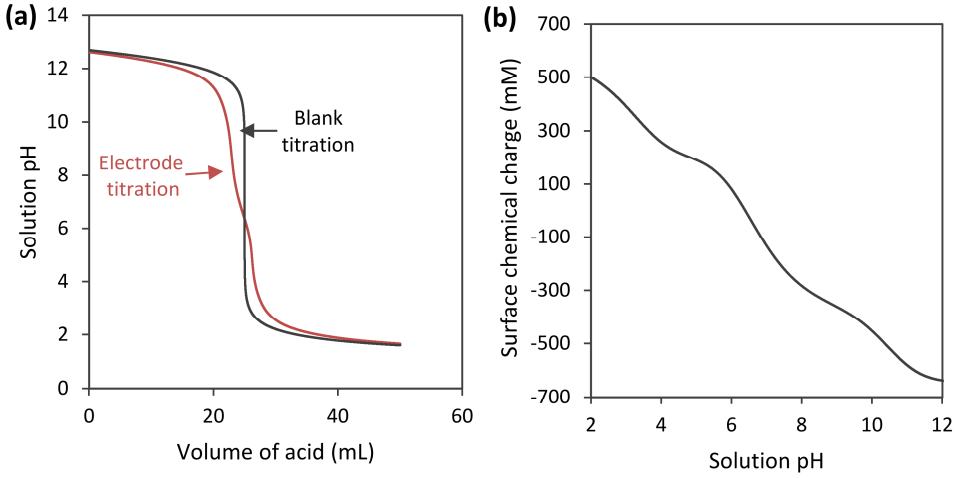

Fig. S4.1: (a) pH of the solution calculated by the m-amph-D model during titration with the electrode sample (electrode titration) and without electrode (blank titration). (b) Surface chemical charge calculated from the simulated result of the m-amph-D model.

Based on the simulated pH, the surface chemical charge was calculated based on the difference in acid volume between the electrode sample titration (V_{sample}) and the blank titration (V_{blank}) to reach the same solution pH (Eq. S4.3). Simulated results are shown in Fig. S4.1b.

$$\sigma_{chem,pH} = \frac{(V_{sample} - V_{blank}) \cdot C_{titrant}}{2 \cdot V_{mi} \cdot m_{electrode}} \qquad S4.3$$

Note that the amount of chemical surface charge is divided by $2V_{mi}$ in Eq. S4.3, while the amount of chemical surface charge was divided by V_{mi} in section 4.2 of the main article manuscript. According to Gao et al. [165], the amount of chemical surface charge found from titration experiments should be divided by the total volume of micropores (V_{mi}). However, the m-amph-D model (based on the amph-D model) assumes that the acidic and basic chemical charges are separated into two different regions (regions A and B), and not into one single region. Therefore the volume for each region is equal to $V_{mi}/2$. Consequently, to obtain any concentration of chemical surface charges ($\sigma_{chem,a}$, $\sigma_{chem,b}$, and $\sigma_{chem,pH}$), the amount of chemical charge should be divided by $V_{mi}/2$.

The concentration of chemical surface charge and their respective pk values were obtained by fitting the m-amph-D mode to the experimental data.

4.6.2. Supporting figures

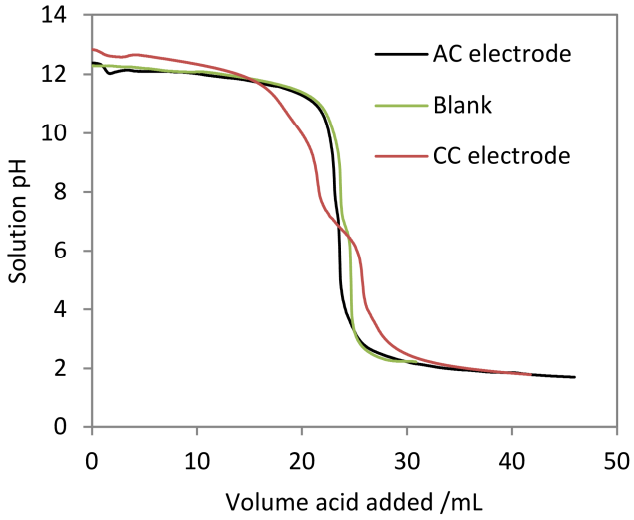

Fig. S4.2: Titration curve obtained without electrodes (blank), with activated electrodes (AC electrodes) and the Carbon-Cloth electrodes (CC electrodes).

Chapter 5

Membrane electrode assembly cell design improves the internal resistance of a CDI cell for CO_2 capture

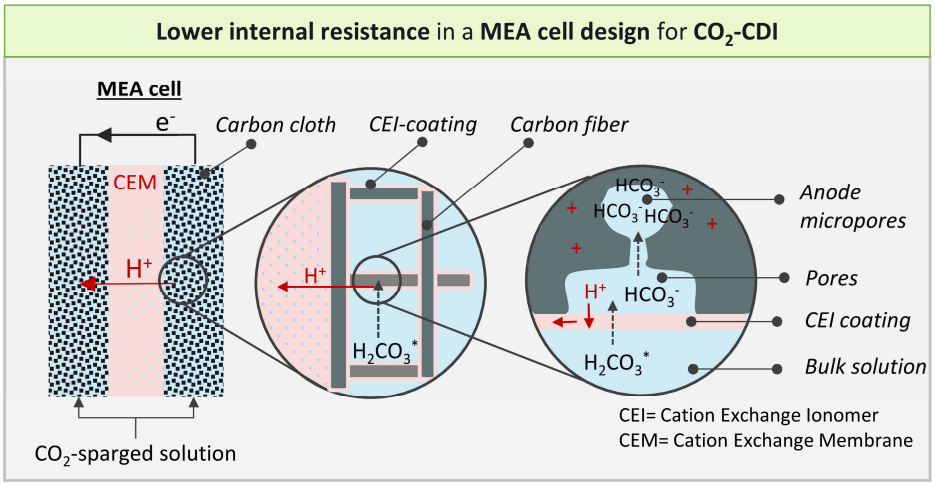

This Chapter has been submitted as:

L. Legrand, M. Tedesco, O. Schaetzle, H.V.M. Hamelers, Membrane-Electrode Assembly cell design improves internal resistance and CO_2 absorption performance in capacitive deionization (CDI) for CO_2 capture. *Environ. Sci. Technol.* **2020**

Abstract

This work demonstrates the use of a novel cell design to reduce the internal resistance of a capacitive deionization cell for CO_2 capture (CO_2-CDI), by introducing a membrane electrode assembly (MEA). In this new cell architecture, instead of using a spacer channel, the CO_2-sparged solution is directly pumped through the electrodes. We compare the MEA design with conventional MCDI design in terms of internal resistance, carbon adsorption efficiency, and energy consumption. We show that the ohmic resistance of the MEA cell design is 20 times smaller than the MCDI cell design, due to the higher electrical conductivity of the CEM compared to the spacer channel. Furthermore, we reached a 10-fold decrease in the non-ohmic resistance by coating both electrodes with a cationic exchange ionomer (CEI). In terms of carbon adsorption efficiency (similar than charge efficiency), the MEA cell design with uncoated electrodes shows the lowest performance ($\Lambda_c \approx 0.16$-0.33), which is 2-3 times smaller compared to the MCDI cell design ($\Lambda_c \approx 0.76$). However, the carbon adsorption efficiency of an MEA cell was improved by coating the electrodes. Despite the decrease of internal resistance, the energy consumption vs. CO_2 absorption rate did not change between an MCDI and MEA coated cell designs, limited by the carbon adsorption efficiency. We believe that the energy consumption could be further increased by improving the carbon adsorption efficiency of the MEA cell with CEI-coated electrodes. Future studies should focus on tuning the ionomer coating in the electrodes (e.g., in terms of ionomer content, loading and thickness) by investigating different coating techniques, as well as on the effect of different ionomers on carbon adsorption efficiency.

5.1. Introduction

Climate change is one of the major challenges our society is facing nowadays. In recent years, the Intergovernmental Panel on Climate Change (IPCC) stressed out the importance of reducing CO_2 emissions to limit the effects of global warming[11]. In its 2018 report, the IPCC recommended various technological solutions to tackle CO_2 emissions, including, e.g., carbon capture and storage (CCS), direct air capture and storage (DACCS), and bioenergy with CCS (BECCS)[11]. Many technologies have been proposed to capture CO_2 based on chemical absorption[101,134,183], physical adsorbents [36,173,184–187], membrane separation[46], cryogenic process[106], calcium looping[41,160,188], and more recently electrochemically based technology[49,53,59,60,107,113,154,189,190]. Chemical adsorption-based technologies are the most widely used and studied. While the technical feasibility of these processes for CO_2 capture has been proven, the large input of thermal energy and amines to capture CO_2 still impairs their application on a full industrial scale. In contrast, electrochemical technologies use only electricity as energy input and do not require chemicals (such as amines). Thus, they represent promising alternatives for the development of environmental-friendly capture processes combined with renewable energy sources.

A number of electrochemical CO_2 capture technologies have been recently proposed, such as: (i) pH swing in bicarbonate solutions (using bipolar membranes[49,53], or molten carbonate fuel cells[50,51]); (ii) electrochemical generation of nucleophiles [113,189]; (iii) electrochemical regeneration of CO_2-loaded amine solvents[190,191]; (iv) electrosorption of CO_2 in carbon materials (supercapacitive swing adsorption[58–60]); (v) electrosorption of HCO_3^- ions in capacitive electrodes (CO_2-CDI) [154]. In particular, the latter technology (CO_2-CDI) is the focus of this study.

CO_2-CDI is based on capacitive deionization (CDI), i.e., a technology widely developed in the last decade for water desalination[17,70–73,75,77,178]. An MCDI cell is composed of two capacitive electrodes, both covered by an ion exchange membrane, i.e., an anion exchange membrane (AEM) for the anode, and a cation exchange membrane (CEM) for the cathode. During operation, an electrolyte solution is fed into a compartment between the electrodes, where ions in solution can be transported and adsorbed into the capacitive electrodes under the effect of an applied electric field. In CO_2-MCDI, CO_2 gas is continuously absorbed in solution while the electrosorption of carbonate ions (i.e., HCO_3^- and CO_3^{2-}) and protons takes place at the electrodes (Fig. 5.1a). In particular, the following chemical reactions occur in solution[26]:

$$CO_2(g) \overset{H^{cc}}{\leftrightarrow} H_2CO_3^* \quad 5.1$$

$$H_2CO_3^* \overset{K_1}{\leftrightarrow} HCO_3^- + H^+ \quad 5.2$$

$$HCO_3^- \overset{K_2}{\leftrightarrow} CO_3^{2-} + H^+ \quad 5.3$$

where H^{cc} is the Henry's constant, expressed in $\mathrm{mol}_{H_2CO_3^*}/\mathrm{mol}_{CO_2(g)}$ (H^{cc}=0.83[24,25]), and K_1 and K_2 are the chemical dissociation constants ($K_1=10^{-6.33}$ and $K_2=10^{-10.33}$ [26]). The CO_2-MCDI system showed promising low values of energy consumption to capture CO_2 (as low as ≈50 kJ mol^{-1} when the system was fed with 15% CO_2 at a current density of 0.6 A m^{-2})[154]. However, in our previous work[154], the CO_2 absorption rate was limited by the low current density used. Operating the cell at higher current density would lead to higher CO_2 absorption rates, but also higher energy consumption due to the electrical resistance of the MCDI cell. Therefore, decreasing the electrical resistance of the CO_2-CDI is essential to reduce the energy consumption of the CO_2-CDI cell at higher current density.

In Ref.[154], we showed that the internal cell resistance was especially dominated by the resistivity of the CO_2-sparged solution in the spacer channel (see Fig. 5.1c). In a previous study[192], we proposed a spacerless Membrane Electrode Assembly (MEA) cell design to minimize the internal cell resistance for a related application (i.e., harvesting energy from CO_2 emissions). In the MEA cell design, the solution flow occurs through the electrodes instead of a spacer, and both electrodes are separated by a CEM (see Fig. 5.1b). Thanks to the higher conductivity of the CEM than the spacer, the cell internal resistance could be substantially decreased with an MEA cell design for harvesting energy from CO_2 emissions (from 60 kΩ cm^2 to 1 kΩ cm^2 using air-sparged deionized water[192]). Moreover, for fuel cell applications, an ionomer is usually added to the electrodes in MEA to decrease the internal cell resistance further (a process referred to as ionomer impregnation[146,193,194]). This approach is of interest to reduce the ionic resistance in the electrode macropores[195] in CDI systems and is also expected to decrease resistances related to stagnant boundary layers between the electrode macropores and the CEM. Overall, we expected that an MEA cell design with ionomer impregnated electrodes (Fig. 5.1b) would result in lower resistance due to less resistive elements in the cell (no spacer) and a lower number of interfaces (see Fig. 5.1c-d).

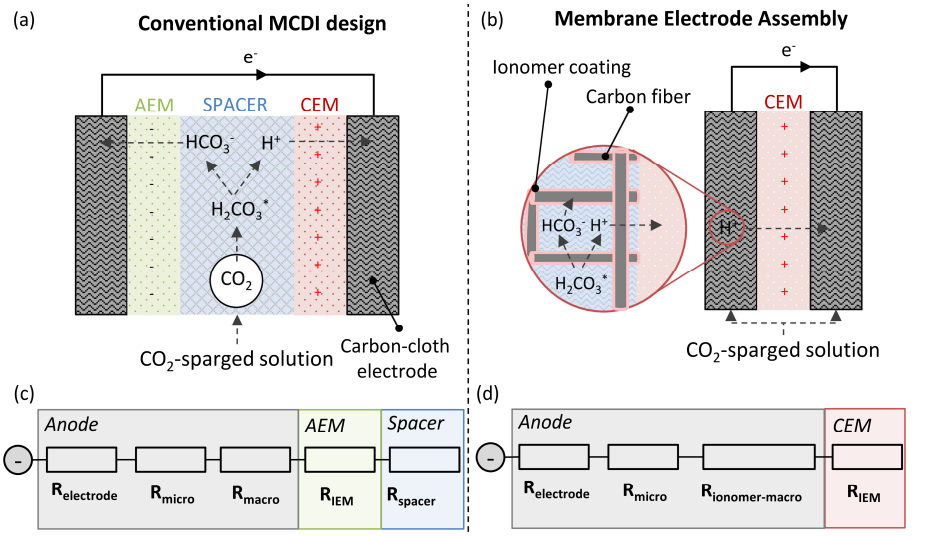

Fig. 5.1: Scheme of (a) a conventional (flow-by) MCDI cell and (b) an Membrane Electrode Assembly (MEA) cell design. The contribution of different resistive elements is illustrated in the form of an equivalent circuit for (c) half-cell MCDI cell design and (d) half-cell MEA cell design.

In this study, we first investigate the effect of (i) cell designs (MCDI and MEA) and (ii) ionomer coating in MEA cells on the internal resistance. Then, we characterize the CO_2 absorption performance of each cell configurations in terms of (i) carbon adsorption efficiency, (ii) internal resistance, and (iii) energy consumption.

5.2. Material and methods

5.2.1. Electrode material and imaging

We first used commercially available carbon cloth as reference material for "uncoated" capacitive electrodes (ACC-5092-15, Kynol, Germany). Next, we modified the electrode by coating with an ion exchange ionomer, i.e., either an anion exchange ionomer (AEI) (Fumion FAS-solution, Fumatech, Germany) or a cation exchange ionomer (CEI) (Fumion FKS-solution, Fumatech, Germany). The electrode coating took place through a two-step procedure. In the first step, the carbon-cloth substrate was dip-coated into a mixture of ionomer and N-Methyl-2-pyrrolidone (NMP), the latter used as a solvent. In the second step, the resulting coated electrodes were first dried at 100 °C for one hour on a heating plate and then dried for twelve hours at room temperature (to evaporate the

solvent). Both AEI-coated and CEI-coated electrodes were obtained in this way, using different solvent:ionomer ratio (4:1 (w/w) for AEI, and 6:1 (w/w) and 18:1 (w/w) for CEI). The electrodes coated with a 6:1 ratio is referred to as "CEI-coated electrode," whereas the electrodes coated with an 18:1 ratio are referred to as "diluted CEI-coated electrode" (Table 5.1). SEM images of the electrode are shown in Fig. 5.2.

Table 5.1: Thickness, ionomer:substrate ratio and ionomer content for each electrode coated

Electrodes	**Total thickness (mm)**	**Ionomer:substrate ratio**	**Ionomer content (%)**
Uncoated electrode	0.52 mm	N/A	N/A
Diluted CEI-coated	0.57 mm	0.8:1	44%
CEI-coated	0.69 mm	2.2:1	68%
AEI-coated	0.73 mm	1.9:1	66%

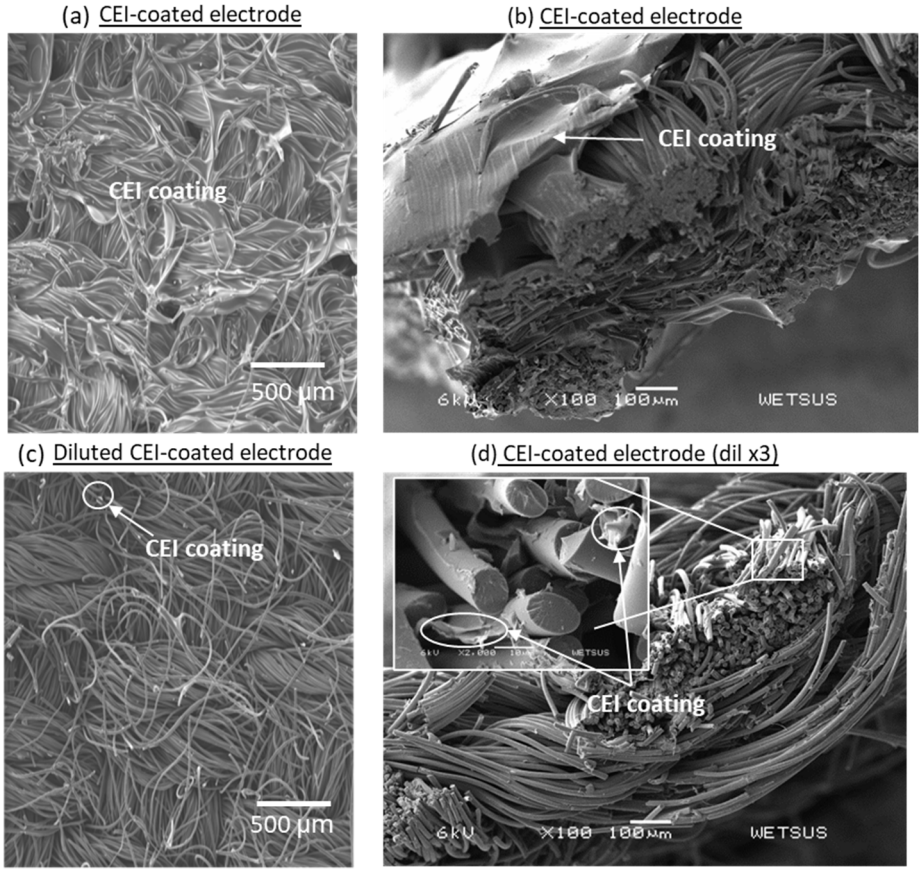

Fig. 5.2: SEM images of the hand-coated electrodes. (a) CEI-coated electrodes (top view); (b): CEI-coated electrodes (cross section); (c) diluted CEI-coated electrodes (cross section); (d) diluted CEI-coated electrodes (cross section).

5.2.2. Cell resistance and capacitance characterization

An electrochemical cell was built to characterize the internal resistance and the capacitance of the MEA and MCDI cell design, see supporting information (SI). The MEA characterization cell consisted of (i) two PMMA end-plates, (ii) graphite foil as current collectors, (iii) two capacitive electrodes (30 x 30 x 0.5 mm, 9 cm^2) enclosed in a silicon gasket (300 µm) and one cation exchange membrane. Instead, for the MCDI characterization cell, two membranes, i.e., an anion exchange membrane (AMX, ASTOM Corporation, Japan) and a cation exchange membrane (CMX, ASTOM Corporation, Japan), and one spacer (PA 6.6 fabric, Nitex 03-300/51, 121 Sefar, Switzerland, 200 µm thick) were

also included. Table 5.2 shows all the electrode materials tested in the MEA configuration. The internal cell resistance and capacitance were characterized with NaCl solutions at different salt concentrations (0.1, 0.5, 1.0, and 5.0 mM NaCl), and with CO_2-sparged solutions at different CO_2 partial pressures (0.1, 0.15, 0.3, and 1.0 atm CO_2). CO_2-sparged solutions were prepared by sparging a CO_2:N_2 mixture into deionized water, as described in Refs.[154,192]. The solution was pumped into the cell with a peristaltic pump (Cole-Parmer, Masterflex L/S) at 20 mL min^{-1}.

Table 5.2: Configurations of the MEA cell design tested

Cell configuration	**Anode**	**membrane**	**Cathode**
1	Uncoated electrode	CEM	Uncoated electrode
2	Uncoated electrode	CEM	CEI-coated electrode
3	Uncoated electrode	CEM	Uncoated electrode (0.1 M HCl)
4	AEI-coated electrode	CEM	CEI-coated electrode
5	CEI-coated electrode	CEM	CEI-coated electrode
6	Diluted CEI-coated electrode	CEM	CEI-coated electrode
7	AEI-coated electrode	AEM	AEI-coated electrode

We estimate the total internal resistance (R_{total}) by extending the method in Ref.[192]. The total internal resistance was obtained during galvanostatic charge and discharge from the voltage drop measured between an open cell and a charging step. The total cell resistance was further separated into two contributions, i.e., the ohmic resistance (R_{ohmic}) and the non-ohmic resistance ($R_{non-ohmic}$), i.e.:

$$R_{total} = R_{ohmic} + R_{non-ohmic} \quad 5.4$$

The ohmic resistance (R_{ohmic}) represents the internal resistance related to the electrical resistivity of each material in the cell, e.g., electrodes, membranes, and spacer. The ohmic resistance is time-independent and is typically measured by electrochemical impedance spectroscopy (EIS) at high frequencies[116]. Qu et al. refer to the ohmic resistance as setup resistance[116]. We measure the ohmic resistance with EIS at 10 MHz

and 0 V with an amplitude of 10 mV. All EIS scans can be found in SI. Unlike the ohmic resistance, the non-ohmic resistance includes all time-dependent resistances inside the cell. Non-ohmic resistance mostly includes concentration polarization effect on stagnant boundary layers in interfaces (interfaces shown in Fig. 5.1c-d). More details about the resistance measurement can be found in SI.

The specific electrode capacitance (C_s) was estimated from the galvanostatic discharge as

$$C_s = \frac{|I_{discharge}| \cdot t_{discharge}}{m_{electrode} \cdot \Delta_{voltage}} \quad 5.5$$

where $m_{electrode}$ is the mass of each electrode, $\Delta_{voltage}$ the voltage window, $I_{discharge}$ the electrical current applied during the discharge step, $t_{discharge}$ the time of the discharging step. Note that the contribution of the ohmic drop is removed from $\Delta_{voltage}$. Due to the low ionic conductivity of the solution electrolyte, the establishment of the complete ohmic drop could take several seconds. The methodology to correct for the ohmic drop is shown in supporting information.

5.2.3. CO_2 absorption experiments

The CO_2 absorption performance was investigated through the experimental procedure previously reported in Ref.[154]. For the absorption experiments, a larger cell (absorption cell) was needed to measure a significant and measurable variation of CO_2 gas absorbed and desorbed. The absorption cell and the characterization cell differ in (i) electrode size, (ii) current collector material, and (iii) thickness of gaskets on the electrodes. The size of the electrode was 250x20x0.5 mm, with a surface area of 50 cm^2. The current collector was made of titanium coated with platinum. Finally, the thickness of the gaskets was ~500 µm. Such thicker gaskets were necessary to avoid any solution and gas leakages during experiments.

A schematic representation of the research setup is shown in Fig. 5.3. During the absorption experiment, a volume of CO_2-sparged solution equilibrated with a CO_2:N_2 mixture (with a v/v ratio of 15:85) was recirculated between the cell and the gas-liquid contactor (GLC) at 30 mL min^{-1} using a peristaltic pump (Cole-Parmer, Masterflex L/S). The gas composition has been selected to mimic flue gas from thermal power plants. The volume of water (V_w) was ~30 mL for MCDI and ~60 mL for MEA cell designs. The GLC encloses a volume of CO_2:N_2 gas mixture (V_g=~120 mL) and ensure the CO_2 exchange

between the gas and liquid phases until reaching. The gas pressure was measured with a manometer (Cerabar T PMP131, Endress+Hauser, Switzerland). The measured pressure was directly correlated with the CO_2 concentration using the ideal gas law (since N_2 behaves as inert in the system). Experiments were carried out under constant current mode using a galvanostat (Ivium, the Netherlands) by performing charge and discharge cycles. Current densities in the range of 0.6-3.0 A m^{-2} were applied for both cells and using different electrode materials. The charging and discharging times were controlled by two operation conditions, i.e., (i) by storing an electrical charge of 20 C in the electrodes, and (ii) by charging/discharging the cell in the range E_{cell}=0–1 V to avoid faradaic reactions. Before performing each experiment, the system was first equilibrated through a two-step procedure. Firstly, the cell was equilibrated by pumping the CO_2-sparged solution (through valves V-1 and V-2 in Fig. 5.3) under short-circuit conditions (E_{cell}=0V). Next, the CO_2-sparged solution was recirculated between the cell and the GLC under open cell voltage condition, while a CO_2:N_2 gas mixture was continuously fed through the GLC (valves V-3 and V-4 in Fig. 5.3) for at least 30 min. This step ensures that the gas and liquid phases in the GLC are in equilibrium before starting the experiment.

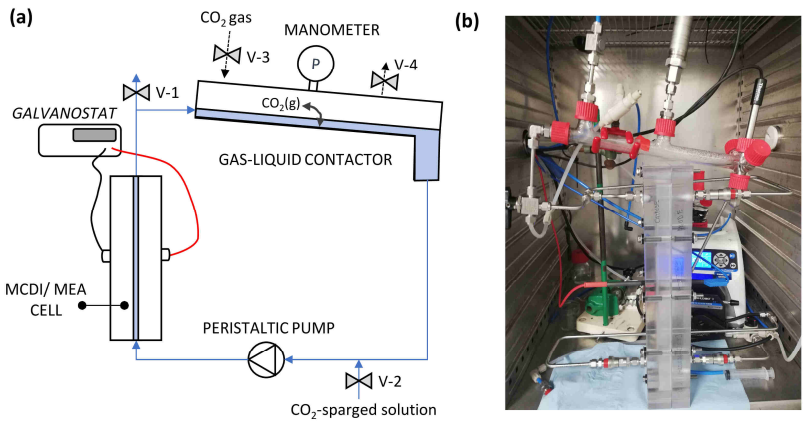

Fig. 5.3: (a) Schematic illustration and (b) picture of the experimental setup used for CO_2 absorption tests.

The system performance was quantified in terms of carbon adsorption efficiency (Λ_c) and net energy consumption per mol of CO_2 (W^*_{net}). Carbon adsorption efficiency has been defined in Ref.[154] and represents the amount of carbon adsorbed per electrical charged defined as

$$\Lambda_c = \frac{n_{HCO_3^-(ad)} + n_{CO_3^{2-}(ad)}}{n_{charge}} \quad 5.6$$

Note that Λ_c is equal to the charge efficiency (Λ) if the electrical charge is compensated by the adsorption of bicarbonate ions. Values of Λ_c are derived from experimental measurement of absorption efficiency ($\Lambda_a = n_{CO_2,(g)}/n_{charge}$) as

$$\Lambda_c = \frac{\Lambda_a}{(1-f_w)} = \frac{n_{CO_2,(g)}}{(1-f_w)\cdot n_{charge}} \quad \text{with} \quad f_w = \frac{V_w \cdot H^{cc}}{V_g + V_w \cdot H^{cc}} \quad 5.7$$

where f_w is the water fraction, $n_{CO_2(g)}$ the amount of CO_2 gas adsorbed, n_{charge} is the amount of electrical charge stored. The relationship between Λ, Λ_c and Λ_a are extensively described in Ref.[154]. Values of $n_{CO_2(g)}$ were calculated from the ideal gas law and the pressure difference obtained between a charge and discharge steps (see pressure data in Fig. 5.7).

The net energy consumption per mol of CO_2 (W^*_{net}) can be calculated from the energy difference between the charging and discharging (W_{net})[154], as shown in Eq. 5.8.

$$W^*_{net} = \frac{W_{net}}{n_{CO_2(g)}} = \frac{\int_0^Q E^c_{cell} dQ - \int_0^Q E^D_{cell} dQ}{n_{CO_2(g)}} \quad 5.8$$

5.3. Results and discussion

5.3.1. Effect of cell design on the internal resistance

We first investigate the performance of the MEA cell by comparing the internal resistance against the (conventional) MCDI cell. Fig. 5.4 shows the internal resistance (divided into ohmic and non-ohmic contributions) for both cells, as a function of the CO_2 partial pressure. Both cells were tested by using the same flow rate, and at constant current density (1.6 A m^{-2}). A cell voltage comparison between both cell designs is shown in SI.

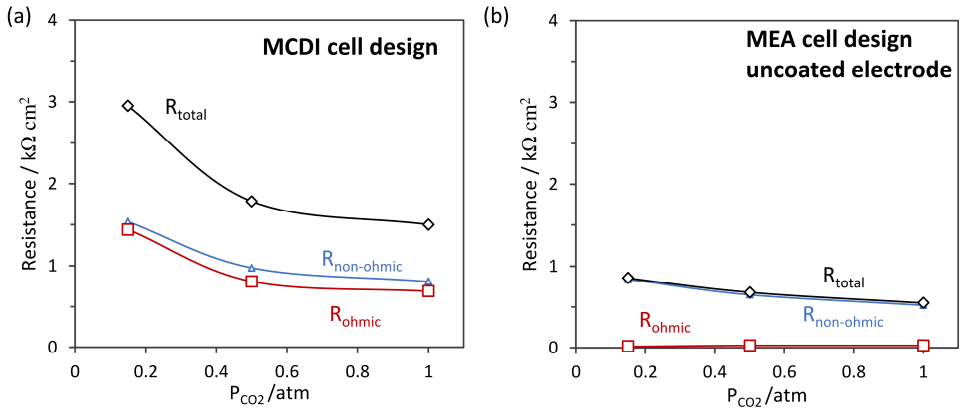

Fig. 5.4: Comparison of electrical resistance (R_{total}, R_{ohmic}, $R_{non-ohmic}$) between (a) conventional MCDI cell and (b) MEA cell at different CO_2 partial pressure and current density (1.6 A m^{-2}). Lines are added to guide the eye.

Fig. 5.4 shows that the total internal resistance of the MEA cell is three times smaller compared to the MCDI cell (R_{total}~850 Ω cm^2 for the MEA cell against R_{total}~3000 Ω cm^2 for the MCDI cell at P_{CO_2}=0.15 atm). Such improved internal resistance mainly results from a significant decrease of the ohmic resistance, which is almost 100 times lower for the MEA cell (e.g., R_{ohmic}~18 Ω cm^2 for the MEA cell, compared to R_{ohmic}~1410 Ω cm^2 for the MCDI cell at 0.15 atm). In the MCDI cell, the conductivity of the spacer channel is limited by the low ionic conductivity of the CO_2-sparged solution (in the range of 17-40 µS cm^{-1} for CO_2-sparged solution), which increase the ohmic resistance[154]. Instead of a spacer, the electrodes in the MEA cell are separated by a CEM, which is more conductive, thus reducing the ohmic resistance. Moreover, in the MEA cell design, the ohmic resistance is little dependent on the CO_2 partial pressure (Fig. 5.4b). The ohmic resistance of IEMs is not or little dependent on the ion concentration due to its fixed charge density[196,197]. This is not the case in the MCDI design as the resistance of the spacer is directly dependent on the ion concentration given by the CO_2 partial pressure. Therefore, an MEA cell design is thus favorable to limit R_{ohmic}, especially with low ionic conductive solutions, such as CO_2-CDI.

Furthermore, Fig. 5.4 shows that the non-ohmic resistance of the MEA design decreases by almost two times compared to the conventional MCDI cell (e.g., 1535 Ω cm^2 in the MCDI cell, compared to 840.5 Ω cm^2 in the MEA cell). Non-ohmic resistances are related to time-dependent resistances in the cell[121,127,196,198,199], most of which are related to concentration polarization in diffusion boundary layers (DBLs) at different interfaces

(e.g., membrane/electrode macropores, membrane/spacer, see Fig. 5.1). We believe that non-ohmic resistance decrease in the MEA cell due to fewer interfaces compared to the MCDI cell (see Fig. 5.1). The non-ohmic resistance increases with lower CO_2 partial pressure as the non-ohmic resistance of IEMs tend to increase at lower molar concentration[200].

Overall, the MEA cell is a suitable cell design to reduce the ohmic resistance, which is the most significant resistance contribution in the conventional CO_2-MCDI cell[154]. As a result of reducing the ohmic resistance, the non-ohmic resistance becomes now the dominant resistance in the MEA cell design. Therefore, new strategies should be investigated to decrease the non-ohmic resistance.

5.3.2. Effect of electrode coating on MEA cell resistance

To reduce the non-ohmic resistance, we propose to coat the electrodes with ion exchange ionomer. A similar strategy is used in Proton Exchange Membrane (PEM) fuel cells[201–203] for optimizing the ionic conductivity of electrodes. In PEM fuel cells, both electrodes are coated with a single ionomer (symmetric configuration) to optimize the ion transport of cation (H^+). This approach has not been investigated with MCDI as the transport of both anions (anode adsorption), and cations (cathode adsorption) need to be optimized in the cell. Instead, an asymmetric configuration has been investigated in conventional CDI by using, i.e., AEI-coated anode and CEI-coated cathode. Fig. 5.5 shows the total internal resistance ($\mathrm{R_{total}}$) obtained for asymmetric configuration (Fig. 5.5a) and symmetric configuration (Fig. 5.5b) using a CO_2 partial pressure of $\mathrm{P_{CO_2}}$=0.15. A comparison of cell voltage obtained between the different electrode coating is available in SI.

Fig. 5.5a shows that the combination of AEI-coated anode and CEI-coated cathode separated by a CEM generates the highest internal resistance among the cell design tested, two times higher than uncoated electrodes (1820 Ω cm^2 against 909 Ω cm^2 for uncoated cathode at 3 A m^{-2}). We believe that the AEI-coating on the anode causes this increase in resistance. Although the AEI-coating favors the transport and adsorption of anions in the electrode pores, the AEI-coating also decreases the conductivity of cations from the anode macropores to the CEM, hence a significant increase of resistance. In contrast, the CEI-coated cathode does not impair the internal resistance as both the transport and adsorption of H^+ is optimized with the CEI coating. For instance, tests with only CEI-coated cathode show lower internal resistance than uncoated cathode (563 Ω cm^2 for CEI-coated cathode against 858 Ω cm^2 for uncoated cathode at 3 A m^{-2}). A CEI-coated cathode used with low H^+ concentrated solution (i.e., in the case of CO_2-sparged

solution) shows similar resistance than a cathode soaked in a high H^+ concentrated solution (0.1 M HCl) (563 Ω cm^2 for CEI-coated cathode against 558 Ω cm^2 for the uncoated cathode in 0.1M HCl at 1.6 A m^{-2}, see Fig. 5.5a).

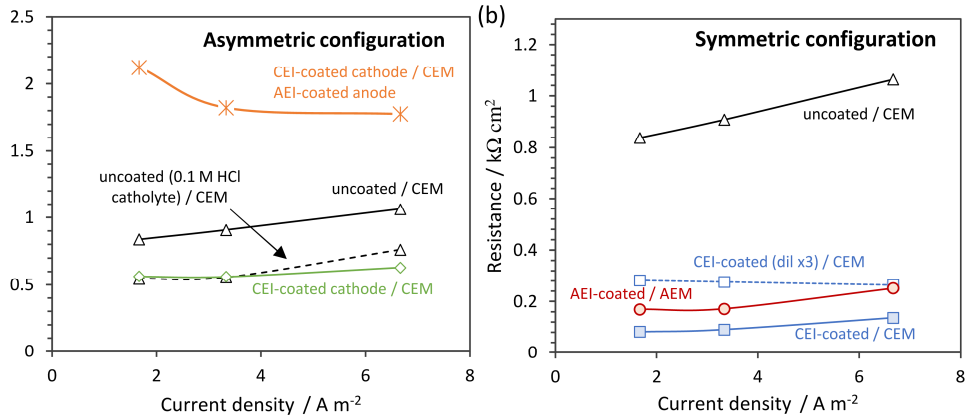

Fig. 5.5: Effect of electrode coating and type of membrane on the cell resistance in a membrane electrode assembly (MEA) cell at 0.15 atm CO_2 partial pressure for (a) asymmetric configurations and (b) symmetric configurations.

To improve the H^+ transport through the complete cell, we adapted the same approach to fuel cell by coating both electrodes with a single ionomer. Fig. 5.5b shows that coating both electrodes with a single ionomer decrease the internal resistance up to 10 times (giving a resistance of 909 Ω cm^2 for uncoated electrodes and 90 Ω cm^2 for CEI-coated electrodes at 3 A m^{-2}). This decrease in resistance is due to a decrease in non-ohmic resistance (see SI). This observation holds for both cationic and anionic charge. For instance, an MEA configuration with anion exchange ionomer (AEI) coated electrodes (with an AEM) shows similar performances than the CEI-coated electrodes (with a CEM) configuration. Moreover, the internal resistance depends on the ionomer content on the electrodes, which again demonstrates the beneficial effect of coating the electrodes with a single ionomer (see Fig. 5.5b).

The beneficial effect of coating both electrodes with a single ionomer was not expected. Instead, we expected that coating both electrodes with a single ionomer would lead to ions shielding of the electrode pores in CDI application, preventing ion adsorption. For instance, the CEI coating on the anode is expected to favor the expulsion of anions, and therefore, prevent anion adsorption in the anode (i.e., anions are repelled as co-ions [17,70,84,85,87,165]). To investigate this effect, we perform tests with a monovalent and non-

amphoteric electrolyte, i.e., NaCl solutions (Fig. 5.6). Experiments with NaCl solutions suggest that a shielding effect occurs when both electrodes are coated with a single ionomer, demonstrated by an increase of internal resistance at low solution resistivities (Fig. 5.6a) and a 2-fold decrease of electrode capacitance (Fig. 5.6b). In contrast, no sign of shielding effect is observed with CO_2-sparged solutions as the electrode capacitance is comparable with an without the presence of electrode coating (see. Fig. 5.6a). We hypothesize that HCO_3^- can still be transported in the form of H_2CO_3* into the anode micropores, where H_2CO_3* can dissociate into HCO_3^- and H^+. The diffusion of H_2CO_3* is possible as the CEI coating is not selective toward neutral molecules. After dissociation, HCO_3^- can be adsorbed in the anode, while H^+ can be transported to the cathode through the CEI coating.

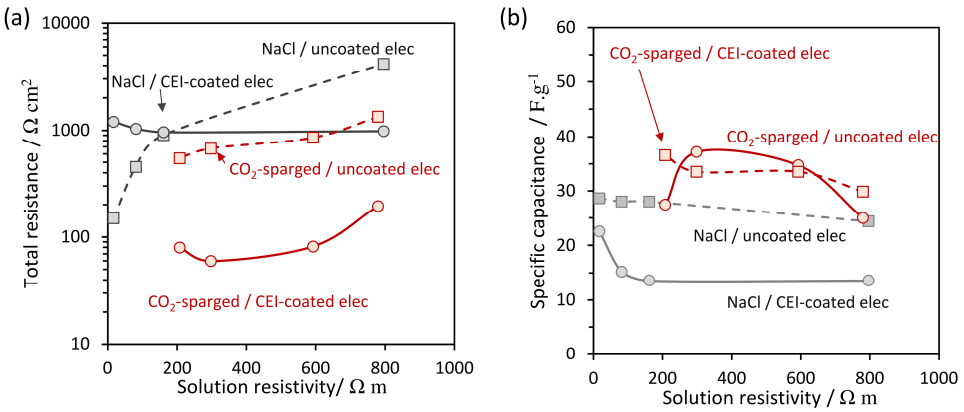

Fig. 5.6: (a) Total resistance and (b) specific capacitance measured in different NaCl (from 5 mM to 0.1 mM) and CO_2-sparged solutions (10% to 100% partial CO_2 pressure). Data are plotted against the solution resistivity.

Overall, coating the electrode with a single ionomer (symmetric configuration) is more favorable to reduce the internal resistance of the MEA cell in CO_2-CDI. As a next step, we propose to compare the CO_2 absorption performance between different cell designs and electrode coatings.

5.3.3. Effect of cell design and electrode coating on CO_2 absorption

Fig. 5.7a shows an example of CO_2 absorption tests performed with CEI-coated electrodes at 0.6 A m^{-2}. Charging and discharging the capacitive cell results into the absorption (charging step) and desorption (discharging step) of CO_2 gas, measured though

pressure change. Fig. 5.7b shows the pressure measured for different cell designs (Fig. 5.7b). Pressure and cell voltage data for all cell designs are shown in SI. We compare the performance between each cell design in terms of carbon adsorption efficiencies (Λ_c) (Fig. 5.8a), total internal resistance (Fig. 5.8b), and energy consumption (Fig. 5.9).

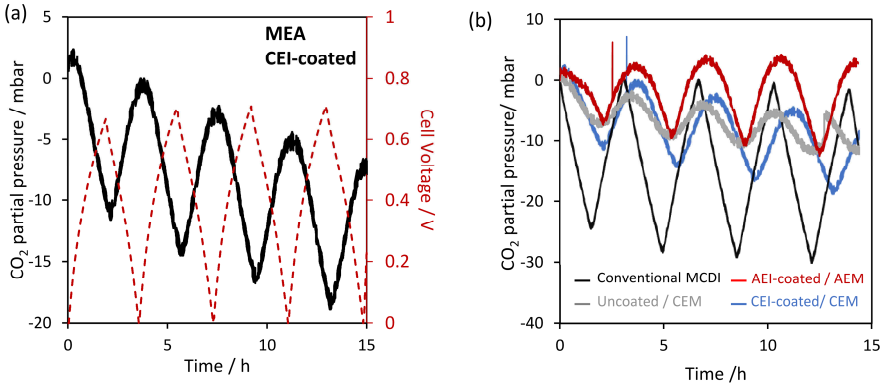

Fig. 5.7: (a) CO_2 absorption cycle and cell voltage obtained with an MEA cell design with CEI-coated electrodes at 0.6 A m^{-2}, (b) CO_2 absorption cycles obtained for different cell designs at 0.6 A m^{-2}.

Fig. 5.8a shows that the MCDI cell configuration shows the highest values of Λ_c, 2.5 times higher than the MEA cell with uncoated electrodes (Λ_c=0.73-0.76 for the conventional MCDI cell compared to Λ_c=0.16-0.33 for the MEA cell design with uncoated electrodes). This result is in line with our previous study[204], where bare carbon electrodes (flat CO_2-CDI) showed lower carbon adsorption efficiencies than electrode covered by an IEM (flat CO_2-MCDI). Like a CO_2-CDI cell design, the feed solution is in direct contact with the electrodes in the MEA cell design, where co-ion expulsion occurs, thus resulting in a decrease of Λ_c. In contrast, covering the electrodes with IEM (CO_2-MCDI design) improve Λ_c by reducing the diffusion of $H_2CO_3^*$ and the effect of co-ion expulsion[29,204]. For the same reasons, coating the electrodes increases Λ_c as the ionomer coating act as a thin layered IEM. Among the two types of investigated coatings, the AEI coating shows the highest values of Λ_c, i.e., around two times higher than uncoated electrodes (Λ_c=0.34-0.53 with AEI-coated electrodes against Λ_c=0.16-0.33 with uncoated electrodes, see Fig. 5.8a). These results are in line with our previous study[204] where we demonstrated that the AEM had a higher contribution than the CEM on Λ_c in a MCDI cell designs. Future work should focus on improving the ionomer coatin to further improve values of on Λ_c.

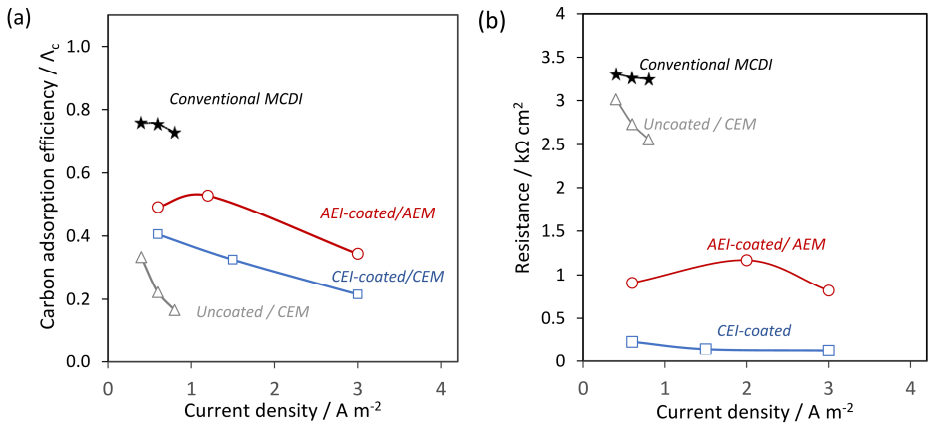

Fig. 5.8: (a) Carbon adsorption efficiencies and (b) internal resistance measured during CO_2 absorption experiments.

In this study, we compare the energy consumption both as a function of current densities (Fig. 5.9a) and CO_2 absorption rates (Fig. 5.9b). Fig. 5.9a shows that the energy consumption of MEA coated designs is lower than MCDI design at comparable current densities (34 kJ molCO_2^{-1} and 65 kJ molCO_2^{-1} at 0.6 A m^{-2} for the MEA CEI-coated and MCDI designs, respectively). In a previous study, we show and explain that the energy consumption of a CO_2-CDI cell decreases with lower values of R_{total} and higher values of Λ_c [154]. MEA CEI-coated cell design reach a compromise between those two governing parameters. Thanks to an improved R_{total} from MCDI to MEA coated cell designs, the energy consumption decreases. Moreover, lower R_{total} enable the use of higher current density, three times higher in MEA coated cell design (3 A m^{-2} compared to 0.8 A m^{-2} in MCDI). Nevertheless, the energy consumption improved is also impacted by the lower values of Λ_c in MEA cell designs (see Fig. 5.8b). The highest energy consumption was obtained in an MEA design with uncoated electrodes where values of Λ_c decrease by more than five times compared to MCDI, while the internal resistance barely improves by 15% (see Fig. 5.8b). Note that the total resistances reported in Fig. 5.8b and Fig. 5.4 show the same trend but differ in values. Both sets of data were obtained with different cells, i.e., characterization cell in section 3.2 and the CO_2 absorption cell in section 3. Such differences could be explained by the different geometrical features of the testing cells (i.e., electrode aspect ratio and gasket thickness), causing different fluid dynamic conditions, and therefore, different non-ohmic resistances (see EIS with different gasket thickness in supporting information).

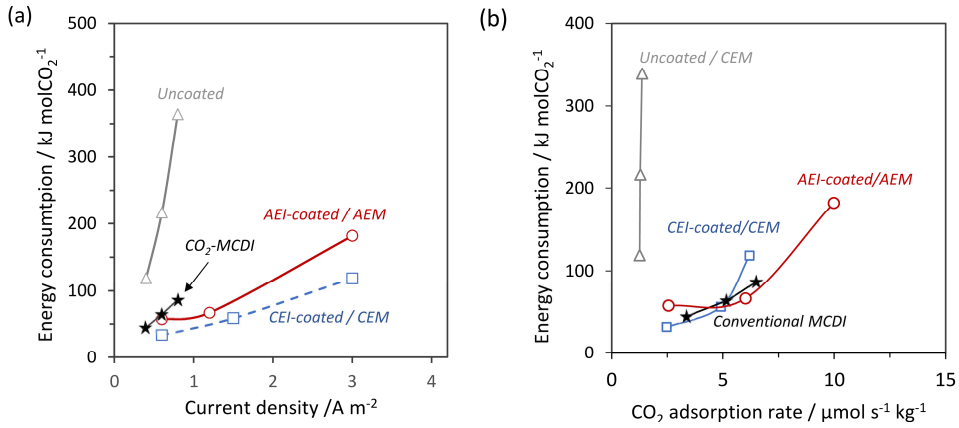

Fig. 5.9**:** Energy consumption for different cell designs plotted against (i) current densities and (b) CO_2 adsorption rates

From a technology development point of view, we believe that comparing energy consumptions at the same CO_2 absorption rates (CAR) is fairer rather than current densities. Comparing with CO_2 absorption rates is more representative as the effect of Λ_c on both energy consumption and CAR is taken into account. Overall, Fig. 5.9b shows that no major energy improvement is obtained between MEA coated and MCDI cell designs at comparable CO_2 absorption rates (34-65 kJ $molCO_2^{-1}$ for CO_2 absorption rates of 2.5-5 $\mu molCO_2\ s^{-1}\ kg^{-1}$, see Fig. 5.9b). These results highlight the importance of improving Λ_c of MEA cell design for both improving the energy consumption and adsorption rate. Future work should focus on testing more selective material (electrodes and ionomer) toward bicarbonate ions and aqueous CO_2.

5.4. Perspective and outlook

Based on the results shown in this study, we believe that the MEA cell performance can be further improved by optimizing the ionomer coating in terms of (i) ionomer homogeneity, (ii) ionomer loading, (iii) ionomer content, and (iv) ionomer material. In this study, we adopted a simple coating method, where the homogeneity and ionomer loading of the coating could not be easily tuned. The thickness of the coating was not homogeneous in the electrode, as more ionomer material tends to cover the carbon fiber on the electrode surface (Fig. 5.2). In contrast, little ionomer material penetrates inside the electrodes. As a result, the carbon fibers inside the electrode matrix were covered by a thinner layer of ionomer (or even not covered). The non-homogenous ionomer coating leads to a non-homogenous ion selectivity through the electrodes. Thinner ionomer layers

(e.g., IEM) are prone to higher co-ion expulsion[205], which reduces the ion selectivity of the ionomer layer. In this regard, future studies should be focused on testing different coating methods (e.g., slurry casting[18,23], electrospinning[206,207], electrospraying[208], or spraying with a spray gun[209,210]) to better tune the coating homogeneity, loading, and content.

Furthermore, identifying suitable ionomer material is essential to improve both the internal cell resistance and the carbon adsorption efficiency. However, a trade-off seems to exist between these two properties. On the one hand, a CEI coating with low selectivity toward H_2CO_3* would lower the cell resistance. We explain in section 3.2 that HCO_3^- is transported in the form of $H_2CO_3^*$ into the micropores of the anode. On the other hand, a CEI coating with high selectivity toward HCO_3^- and $H_2CO_3^*$ is essential to improve the carbon adsorption efficiency (Λ_c). We believe that developing ionomer material with low selectivity is preferable to decrease further the cell resistance. The carbon adsorption efficiency can be improved by other means, for instance, by using more suitable electrode materials (such as chemically modified carbon[178]).

5.5. Supporting information

5.5.1. CALCULATION PROCEDURE

Total internal resistance calculations

In this study, we assume the MEA or MCDI cell designs like a simple RC circuit consisting of one total resistance (R_{total}) and one capacitance (C_{total}). The total resistance includes the contribution of many elements, such as the electrode micropores, the electrode macropores, the ion exchange membrane (IEM), the spacer, and the electrode matrix.

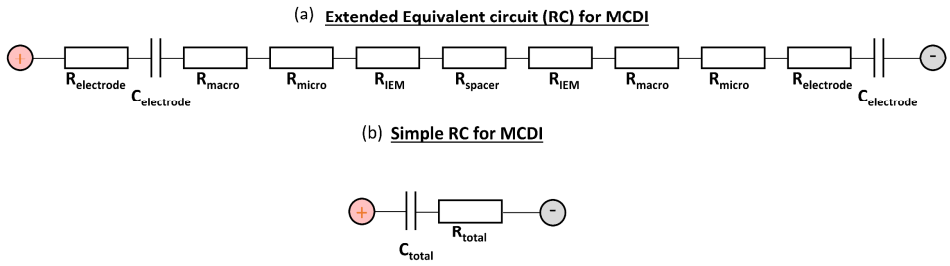

Fig. S5.1: (a) an extended equivalent circuit for a complete MCDI cell and (a) its representation as a simple RC circuit. The terms macro stands for macropores, micro for micropores, and IEM for ion exchange membrane.

The total internal resistance (R_{total}) can be estimated from the voltage drop between an open-cell voltage step and a charging step using ohm's law[192,199,200]. The voltage drop is usually measured in a 1 second time step [116,192]. However, in this study, the establishment of the voltage drop can take up to 100s in the most resistive electrolyte solution tested. The ionic conductivity of the electrolyte solutions used ($\sim$10-50 $\mu S\ cm^{-1}$) is lower than the usual solutions tested. Therefore, we measure the total internal resistance from the voltage drop by adjusting the time step of the measurement to ensure that the cell reaches a steady state. The contribution of the capacitance within the time step was removed from the voltage drop measurement as:

$$R_{total} = \frac{E_{cell,t} - E_{cell,0}}{I} - \frac{t_{step}}{C} \quad \text{S5.1}$$

where $E_{cell,0}$ is the cell voltage at the start of a charge step at t=0 and $E_{cell,t}$ is the cell voltage measured after the time step (t_{step}), C is the electrode capacitance. As an example, Fig. S5.2 shows the total resistance measured at different time steps with 5 mM NaCl solution. The total resistance was found around 140 Ωcm^{-2} at 130s.

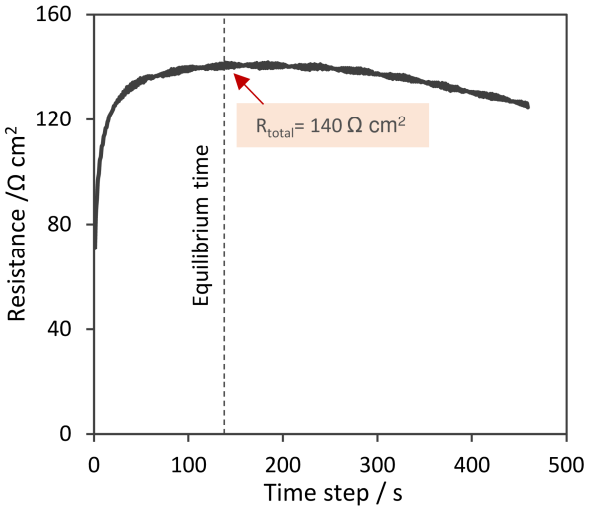

Fig. S5.2: Total resistance calculated for different time steps (calculated from Eq. S5.1).

Ohmic resistance calculations

In this study, the total internal resistance of the capacitive cell (R_{total}) is divided into two categories, the ohmic resistance (R_{ohmic}) and the non-ohmic resistance ($R_{non-ohmic}$). The ohmic resistance is typically time-independent resistance, which represents the electrical conductivity of the different material inside the cell (electrodes, membranes, solution conductivity). The ohmic resistance can either be determined by direct current (DC) method [18,19,121] or by an Alternative current (AC) method [116,196,200]. In the DC method, R_{ohmic} is found from the voltage drop (V_{drop}), measured at a small-time step (1 ms to 1s), between an open-cell voltage step and a constant current (I) step by using ohm's law (R_{ohmic}=V_{drop}/I). The AC method consists of measuring the real part of the impedance measured through Electrical Impedance Spectroscopy (EIS) at high frequencies (>1000 Hz) when the imaginary part of the EIS measurement is minimum

(close to zero). Fig. S5.3 shows that an EIS measurement at different frequencies in the form of a Nyquist Plot. In Fig. S5.3, the ohmic resistance can be found at the highest frequency tested (10 kHz), where the imaginary part (Z_{Im}) of the impedance is close to zero. We believed that the AC method is more suitable than the DC method since the DC method is limited in frequency (max 500 Hz), which is not the case with the AC method. The ohmic resistance was estimated through EIS at 10 kHz, at a cell voltage of 0V, and an amplitude of 10 mV.

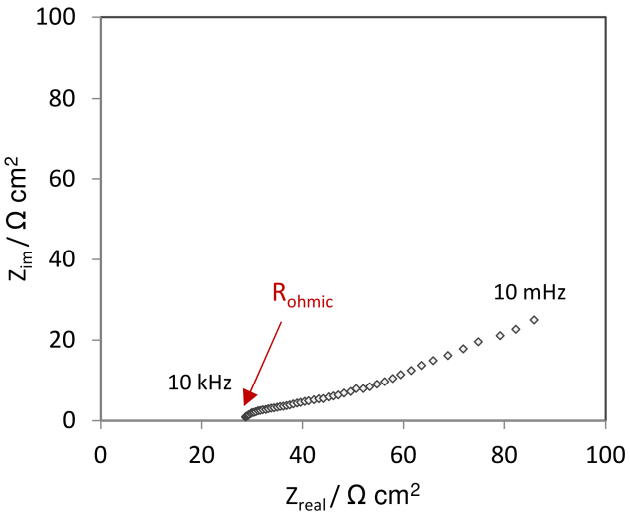

Fig. S5.3: Nyquist plot obtained with the MEA cell design at 0V (amplitude 10 mV) from 10 kHz to 10 mHz for 5 mM NaCl.

Non-ohmic resistance calculations

Next to the ohmic resistance, we refer to all remaining resistances as non-ohmic resistance ($R_{non-ohmic}$). The non-ohmic resistance can simply be found by subtracting the ohmic resistance to the total internal resistance of the cell as

$$R_{non-ohmic}=R_{total}-R_{ohmic}. \quad \text{S5.2}$$

5.5.2. FIGURES

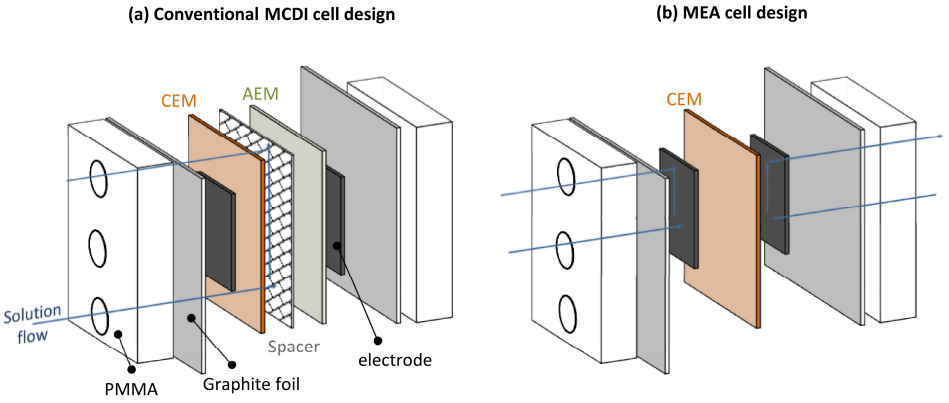

Fig. S5.4: Scheme of the cell assembly for the resistance characterization of (a) conventional MCDI and (b) MEA cell.

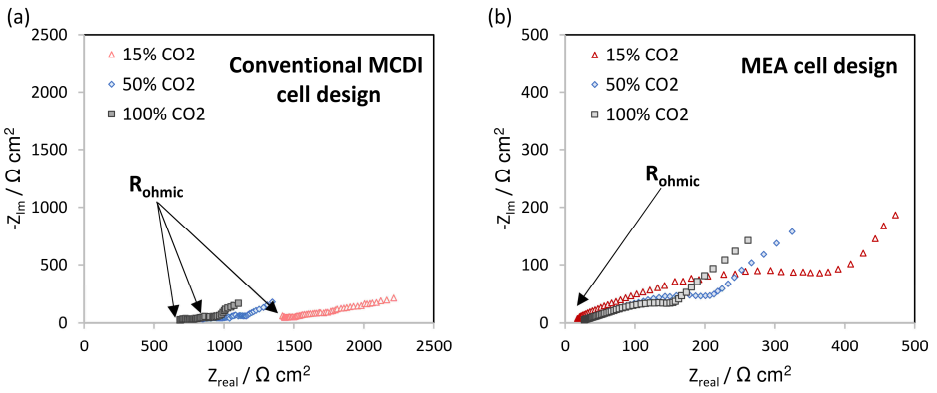

Fig. S5.5: Electrical Impedance Spectroscopy scan performed with (a) conventional MCDI design and (b) membrane electrode assembly (MEA) cell design with uncoated electrodes using CO_2-sparged electrolyte at different CO_2 partial pressure. The impedance spectroscopy scans were performed at 0V from 10 MHz to 0.01 Hz with an amplitude of 10 mV.

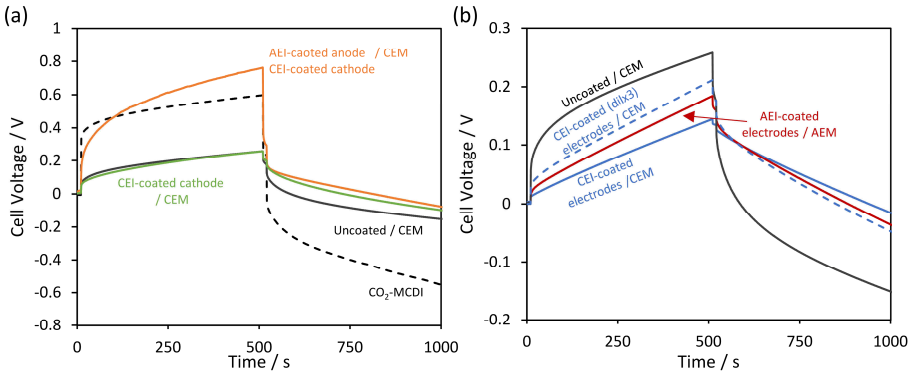

Fig. S5.6: Galvanostatic charge and discharge (GCD) with different cell designs at 3 A m^{-2} and 15% CO_2-sparged solution, i.e. (a) CO_2-MCDI and MEA designs with uncoated electrodes and asymmetric ionomer coating and (b) MEA cell designs with symmetric ionomer coating. The electrode coating and the membrane used are shown on the graph.

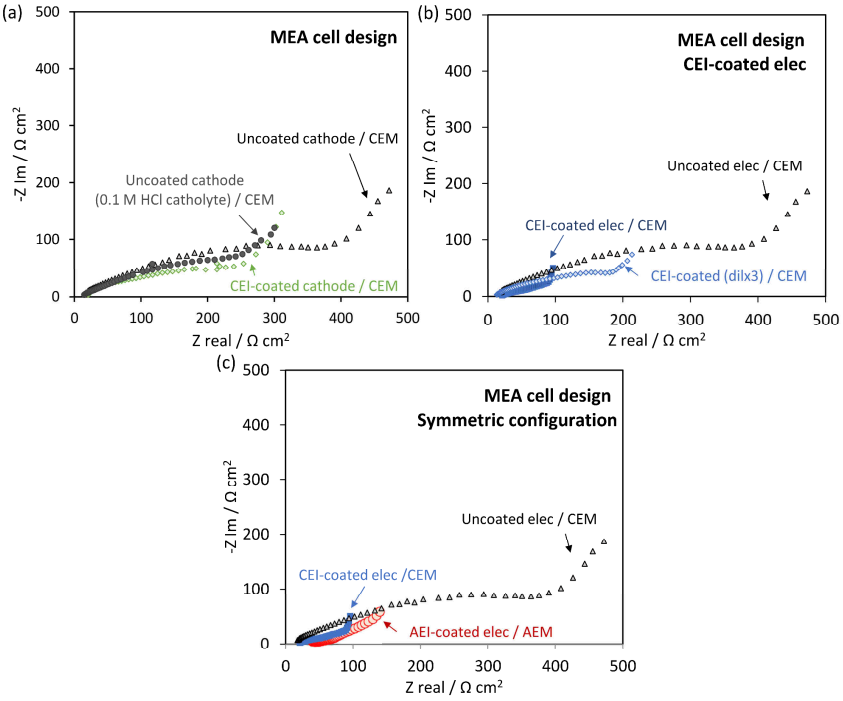

Fig. S5.7: Electrical Impedance Spectroscopy scan performed with an MEA cell with (a) different cathode material and catholyte, (b) different CEI-coated concentration, and (c) different symmetric

coating. The impedance spectroscopy scans were performed at 0V from 10 MHz to 0.01 Hz with an amplitude of 10 mV.

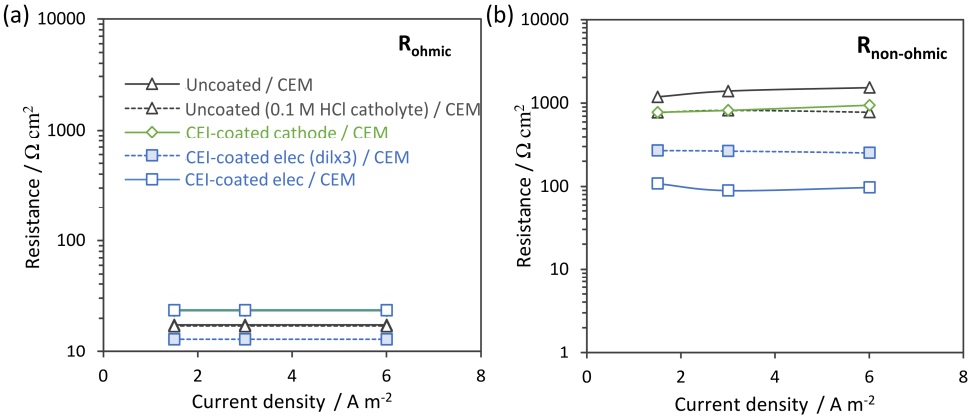

Fig. S5.8: (a) Ohmic resistance (R_{ohmic}) and (b) non-ohmic resistance ($R_{non-ohmic}$) obtained for the MEA cell design with different electrode coating.

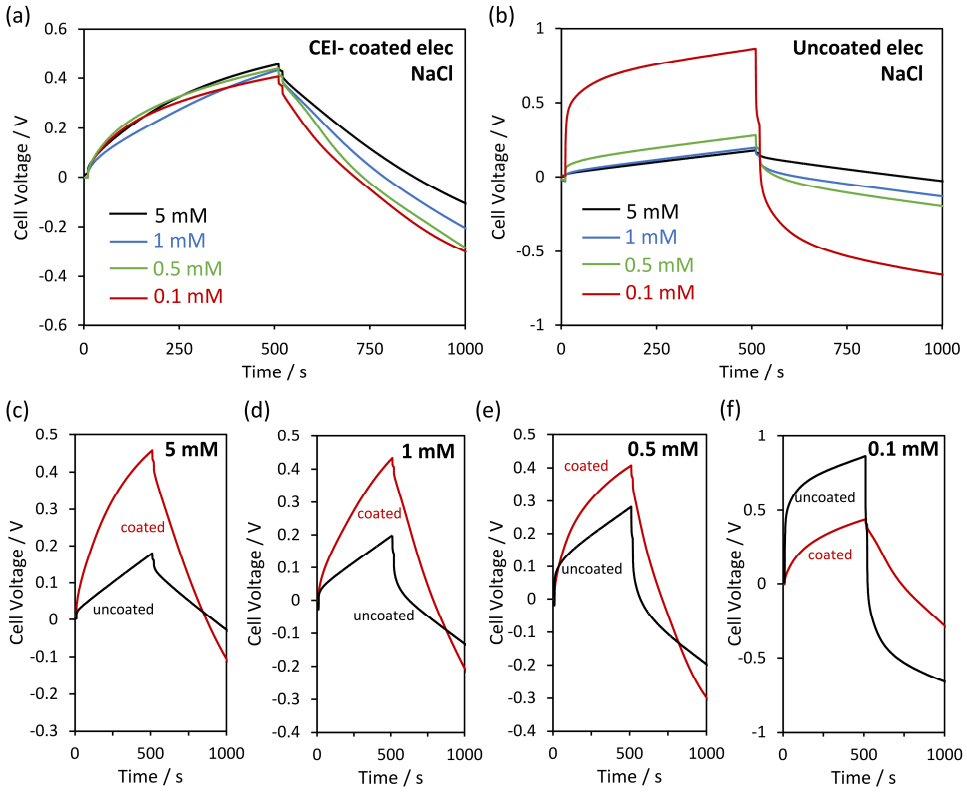

Fig. S5.9: Galvanostatic charge and discharge (GCD) with (a) CEI-coated and (b) uncoated electrodes with different NaCl salt concentration at 1.5 A m^{-2}. Comparison of galvanostatic charge and discharge between CEI-coated and uncoated electrodes for (c) 5 mM NaCl solution, (d) 1 mM NaCl solution, (e) 0.5 mM NaCl solution and (f) 0.1 mM NaCl solution.

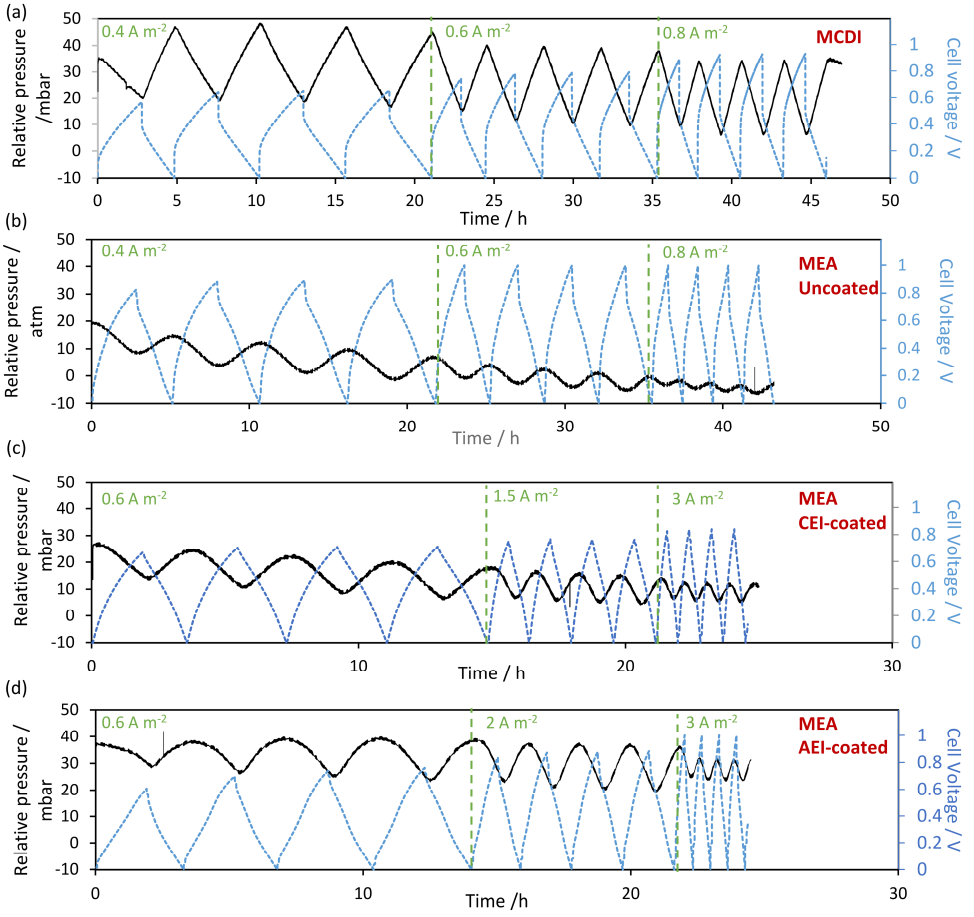

Fig. S5.10: Pressure and cell voltage measurement data obtained for different electrode materials during CO_2 absorption performance: (a) MCDI cell design, (b) MEA cell design with uncoated electrodes, (c) MEA with CEI-coated electrodes and (d) MEA cell design with AEI-coated electrodes.

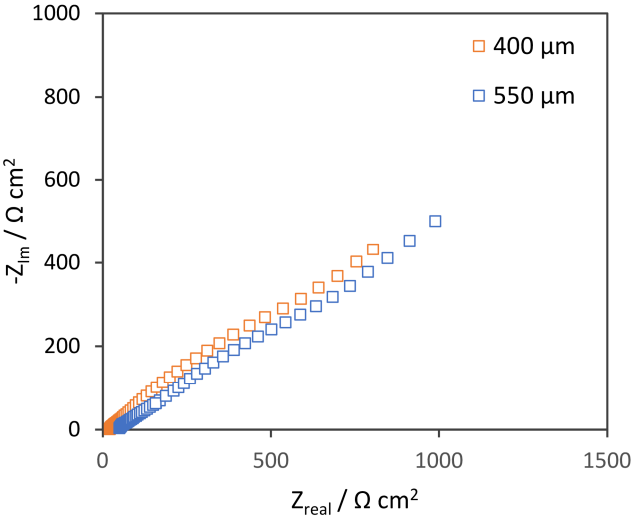

Fig. S5.11: EIS scan performed with the cell used for CO_2 absorption tests with different gasket thickness. The EIS scan was performed from 10 MHz to 10 mHz at 0 V with an amplitude of 10 mV.

Chapter 6

Effect of ionomer coating in capacitive mixing cell (CAPMIX) for harvesting energy from CO_2 emissions.

Cation exchange ionomer (CEI) coating improves the power density generated of a CO_2-CAPMIX cell

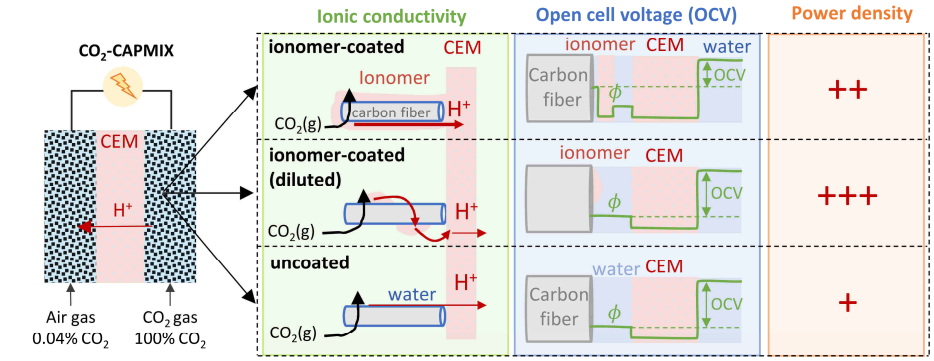

Abstract

Harvesting electrical energy from CO_2 emissions is an interesting concept to improve the energy efficiency of thermal power plants, ultimately reducing CO_2 emissions in the atmosphere. Capacitive cells (CAPMIX cells) show promising results to harvest this source of energy, but their performance is still too low and, therefore, uneconomical for upscaling. The performances are mainly limited by the high energy losses related to the high internal resistance of the cell. In this study, we propose to improve the performance of a CAPMIX cell by coating the capacitive electrodes with ionomer materials. Our results show that the power density generated improved by five times with coated electrodes compared to uncoated electrodes (50 mW m^{-2} compared to 6 mW m^{-2}). The power density performance increases with the presence of ionomer coating thanks to a significant decrease of the internal resistance (2245 Ω cm^2 against 55 Ω cm^2) but is limited by a decrease in membrane potential. We believe that both the membrane potential and internal resistance can be further optimized by optimizing the ionomer loading and structure.

6.1. Introduction

Reducing CO_2 emissions is the major concern of this century to limit the effect of global warming[211]. To achieve this objective, the IEA suggested in 2017 a panel of strategies to efficiently reduce CO_2 emissions, i.e., (i) developing renewable strategies, (ii) increasing CO_2 capture and storage facilities, and (iii) improving the efficiency of existing thermal plant facilities[14]. To improve the energy efficiency of power plants, a number of strategies and new processes have been proposed in the past years. In this regard, capacitive technologies were introduced to harvest electrical energy from CO_2 emissions in 2014[23]. The concept consists of harvesting the chemical mixing energy available (or entropy of mixing) when two gas streams of different CO_2 concentrations are mixed, e.g., flue gas (≈5-15% CO_2) and air (0.04% CO_2). Potentially, harvesting such mixing energy can result in an increase in the energy efficiency of power plants by 5-10%, depending on the flue gas composition[23].

In general, mixing energy has been mostly harvested from natural saline streams (i.e., river and seawater), a process that is referred to as "blue energy." For this process, several technologies have been developed based on, e.g., semi-permeable membrane in pressure reverse osmosis (PRO)[123–125], ion-exchange membranes (RED)[88,121,126–128], or capacitive electrodes[18–20,129–132]. Except for the PRO technology, all these technologies are electrochemical technologies, which rely on the transport of ions (e.g., Na^+ and Cl^-) inside an electrochemical cell to generate electrical power.

Up to now, the recovery of chemical mixing from CO_2 gas streams has been proposed using two different technologies, both based on capacitive electrodes, i.e., (i) porous electrodes (CO_2-CAPMIX)[23,192] and (ii) intercalation electrodes (or pH gradient flow cell)[27]. Since CO_2 is a neutral molecule, these technologies do not harvest electric energy directly from CO_2 gas but rely on the formation of ion by sparging CO_2 gas in water, where CO_2 reacts and is converted into bicarbonate and proton ions (see Eqs. 6.1-6.3).

$$CO_2(g) + H_20 \overset{H^{cc}}{\longleftrightarrow} H_2CO_3^* \quad 6.1$$

$$H_2CO_3^* \overset{K_1}{\leftrightarrow} HCO_3^- + H^+ \quad 6.2$$

$$HCO_3^- \overset{K_2}{\leftrightarrow} CO_3^{2-} + H^+. \quad 6.3$$

These two capacitive technologies show a similar cell architecture but differ in their working principle. In CO_2-CAPMIX, a cell voltage is generated from the establishment of a

membrane potential, while driven by the membrane potential, an electrical current is generated by adsorbing ions in porous electrodes. Fig. 6.1 shows the principle of a CO_2-CAPMIX cell. The membrane potential results from the difference of the cation concentration across the cation exchange membrane (CEM), which is obtained by sparging flue gas and air gas streams across the membrane. In contrast, in the pH gradient flow cell, both the cell voltage and the electrical current originate from the electrodes. The cell voltage is generated from the difference between the pH of the solution in the anode and the cathode compartment. The pH difference is obtained by sparging the flue gas and air streams into a 1 M $NaHCO_3$ solution: driven by the cell voltage, the electrical current occurs through the intercalation of Na^+ and H^+ into the electrodes [27].

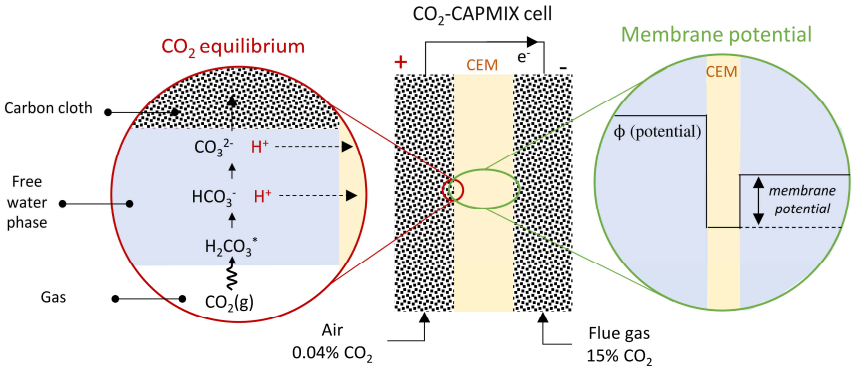

Fig. 6.1: Scheme of a CO_2-CAPMIX, including an illustration of the CO_2 chemical equilibrium and the membrane potential.

The major limitation of both technologies is the energy-intensive gas sparging step, which represents the major source of energy losses in the process[23,27]. To avoid this energy-intensive step, we demonstrated in a previous work that the gas-sparging step could be avoided by flushing the gas directly inside a CO_2-CAPMIX cell[192]. We referred to this feeding operation as "gas feeding." Fig. 6.1 shows the CO_2-CAPMIX cell operated under gas feeding conditions. Despite the improved process, the power density generated by the CO_2-CAPMIX cell is still too low to make the process upscaling economically feasible. The CO_2-CAPMIX cell performance is mainly limited by energy losses related to the high internal resistance, which is caused by the low ion conductivity of the CO_2-sparged deionized water (e.g., 45 µS cm^{-1} at 1 atm CO_2). Therefore, finding new strategies to improve the electrical conductivity of a CO_2-CAPMIX cell is a critical step to develop the technology further.

A possible solution to improve the electrical conductivity of the CO_2-CAPMIX is to add ionomer material in the electrode matrix. For instance, in fuel cell applications, ionomer materials are usually added to the electrode composition to improve the ionic conductivity [146,193,194]. The ionomer material is ionically conductive, thus facilitating the flux of protons through the entire fuel cell. In this study, we propose to adopt the same approach to increase the ionic conductivity of the CO_2-CAPMIX cell. In particular, we tested and compared the performance of a CO_2-CAPMIX with ionomer coated and uncoated electrodes. Finally, the performances between different electrode materials were compared in terms of (i) membrane potential, (ii) generated electrical power, and (iii) internal resistance.

6.2. Material and methods

6.2.1. Cell and material preparation

We use a commercially available carbon cloth material (ACC-5092-15, Kynol, Germany) as a pristine reference electrode ("uncoated electrodes"). Next, the carbon cloth material was coated with a cation exchange ionomer (Fumion FKS-solution, Fumatech, Germany) through a 2-step procedure. In the first step, pristine carbon cloth material was dip-coated into a mixture of ionomer and N-Methyl-2-pyrrolidone (NMP). In the second step, the coated electrodes were dried at 373 K for one hour in a heating plate and then dried for a minimum of 12 hours at room temperature. Two sets of coated electrodes were prepared with solutions of different ionomer:NMP ratio (1:4 and 1:18 w/w). Coated electrodes prepared from 1:4 and 1:18 mixture solutions are referred to as CEI-coated-50 and CEI-coated-15, respectively. Note that the code of the electrodes has been given according to their ionomer content (see Table 6.1).

Table 6.1: Electrode thickness and ionomer content of uncoated and CEI-coated electrodes

Electrode material	Thickness (μm)	Ionomer content
Uncoated	624	N/A
CEI-coated-15	671	15%
CEI-coated-50	765	51%

The cell design tested in this study is a membrane electrode assembly (MEA), shown in Fig. 6.1. The cell consisted of two electrodes separated by a cation exchange membrane (CEM) (Ralex, CMH, Mega, Czech Republic). CO_2 and air gas streams were fed separately along each electrode.

6.2.2. Experimental set-up

The experimental set-up has been described in Ref.[192] and is shown in Fig. 6.2. Two mass flow controllers (mass view, MV-104, Bronkhorst, The Netherlands) were used to control the flow rates of both gas streams (pure CO_2 and air) at 0.5 L min^{-1}. Before entering the cell, the gas streams were separately humidified into humidifiers. The humidified gas streams were then fed into each electrode compartment in the CO_2-capmix cell. Two 3-ways valves were added between the humidifier and CO_2-CAPMIX cell to switch each gas outlet from anode and cathode compartments and vice-versa. A galvanostat (Ivium, the Netherlands) was connected to the CO_2-CAPMIX cell and used to control the current during the tests.

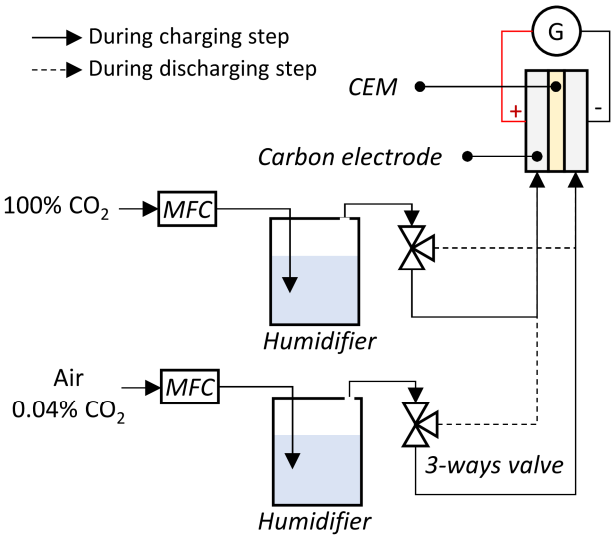

Fig. 6.2: Graphical representation of the research set-up. MFC stands for Mass Flow Controller and CEM for cation exchange ionomer.

6.2.3. Electrochemical measurements

Open circuit voltage (OCV) measurements

The procedure for measuring the maximum open-circuit voltage (OCV) values is reported in Refs. [23,192]. The maximum open-circuit voltage (OCV) values are obtained by measuring the biggest difference of cell voltage when switching the air and CO_2 gas streams between compartments in the MEA cell under no current condition. During the

OCV measurement tests, air and CO_2 gas streams were alternatively switched between the electrode compartments every 5 minutes at a flow rate of 0.5 L min^{-1}. Note that in Ref. [192], the maximum OCV values have been referred to as membrane potentials. It is possible to refer to OCV values as membrane potentials when only an IEM separates the two electrodes. Although this is the case in an MEA cell design with uncoated electrodes, it was not the case in MEA cell design with CEI-coated electrodes.

4-step energy cycle procedure

Electrical power was generated through a 4 step energy procedure reported in Refs. [18,19,192]. Fig. 6.3 shows a Q-V plot of a 4-step energy cycle. Prior to the experiment, the cell was short-circuited while the air gas stream was fed into the anode compartment, and the CO_2 gas stream was fed into the cathode compartment. During the first step, the membrane potential develops by switching the gas streams compartment in the cell under open-cell voltage for 100s. During the second step, the CO_2-CAPMIX cell is charged by applying a positive current (I). During the third step, both gas streams are switched compartments, which generate a membrane potential (reverse direction than the first step). During the fourth and last step, the CO_2-CAPMIX cell is discharged by applying a negative current (-I). The cell was charged and discharged using the same time (t). 4-step energy cycles were performed at different current densities (0.05-3.3 A m^{-2}) under the same amount of electrical charge stored (30 mC for uncoated electrodes and 300 mC for CEI-coated-15 and CEI-coater-50 electrodes) for each electrode material.

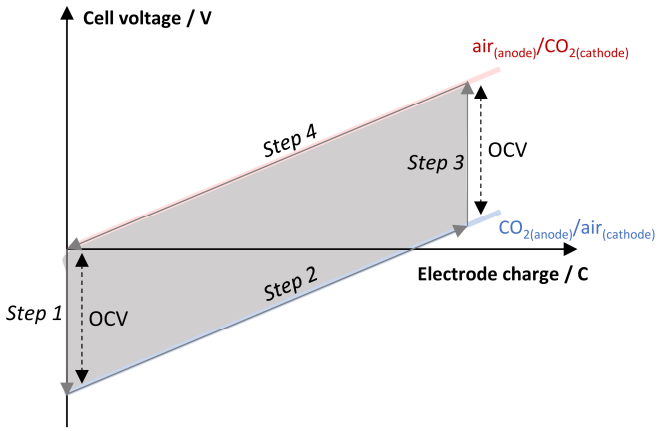

Fig. 6.3: Cell voltage vs. electrode charge plot of a 4-step energy cycle. Each step is shown in the graph as well as the gas stream inflow in each cell compartment. OCV stands for the open-circuit

voltage measurement in steps 1 and 3. Finally, the grey area is a measurement of the net energy generated during the operation of a 4-step energy cycle.

The average power density (P) obtained during each 4-step energy cycle was calculated as

$$P = \frac{1}{2 \cdot (t + t_{OCV})} \cdot \left(\int_0^Q E_{cell}^{charging} \, dQ - \int_0^Q E_{cell}^{discharging} \, dQ \right) \quad 6.4$$

where, $E_{cell}^{charging}$ is the cell voltage during the charge step, $E_{cell}^{discharging}$ is the cell voltage during the discharge step, t is the charging and discharging times, t_{OCV} is the time during the open cell steps (1st and 3rd steps) during the discharge step, and Q is the amount of electrical charge stored.

Internal resistance measurement

The total internal electrical resistance (R_{total}) was measured by an extended version of the method reported in Ref.[192]. The total internal resistance is derived from the voltage drop (E_{drop}) between an open-cell voltage step and a charge/discharge step using ohm's law ($R_{total}=E_{drop}/I$) when the cell reaches a steady-state ($d_E/d_t=0$) [121]. However, the cell reaches a steady-state after several seconds in cell design with high internal resistance. Therefore, for this case, we corrected the voltage drop by removing the capacitive current as

$$R_{total} = \frac{E_{drop}}{I} - \frac{t_{steady-state}}{m \cdot C_s} \quad 6.5$$

where $t_{steady-state}$ is the time when the cell reaches steady-state, m the electrode mass and C_s the specific capacitance. The specific capacitance was measured from the slope of Q-E plots during galvanostatic discharge. During charge, the equilibrium time was estimated when the derivative of cell voltage wit time is a constant ($d_E/d_t=I/C_s$).

Moreover, we analyze the resistance by distinguishing the ohmic resistance (R_{ohmic}) and the non-ohmic resistance ($R_{non-ohmic}$). The ohmic resistance represents the time-independent part of the total cell resistance, which is related to the electronic and ionic conductivity of the different materials inside the cell (electrode, membrane). R_{ohmic} was determined during Electrical Impedance Spectroscopy (EIS) at a frequency of 10 kHz. A similar method was used in Refs.[116,154]. EIS scans were performed from 10 kHz to 10 mHz

at 0V with an amplitude of 10 mV. The non-ohmic resistance represents the time-dependent part of the total cell resistance related to ions transport in boundary layers, usually refer to as concentration polarization[198,200]. The non-ohmic resistance was determined by subtracting the ohmic resistance to the total internal resistance ($R_{non-ohmic}$=R_{total}-R_{ohmic}).

Power density model

Liu et al. proposed a simple power density model.[18] for CAPMIX systems based on a simple RC equivalent circuit. In this circuit, each electrode is model as a capacitor and a resistor in series, while the CEM is modeled as a voltage generator and a resistor in series. Finally, the spacer is modeled as a resistor. To simplify the system, all resistors are sum-up into on resistors, which represent the total internal cell resistance. The cell voltage can then be defined as:

$$E_{cell} = \Delta E_{CEM} + E_c - IR_{int} \quad 6.6$$

$$E_c = E_c^0 + \frac{I}{m \cdot C_s} t \quad 6.7$$

where E_c is the cell voltage that relates to the amount of electrical charge stored, E_c^0 is the initial cell voltage at the beginning of the charge and discharge step, R_{int} is the total internal resistance, m the electrode mass, and C_s the electrode capacitance. The membrane potential can be defined as:

$$\Delta E_{CEM} = \frac{\alpha \cdot R \cdot T}{n \cdot F} \cdot \ln\left(\frac{a_{H^+,CO_2}}{a_{H^+,air}}\right) \quad 6.8$$

where a_{H^+,CO_2} is the activity of the ion of protons in pure CO_2 sparged-water, $a_{H^+,air}$ the ion activity of proton in air sparged-water, α the membrane apparent permselectivity; R, T, n, F, are the ideal gas constant, the temperature, the ion valence, and the Faraday constant (96485 C mol^{-1}), respectively. In this study, we prefer to refer to ΔE_{CEM} as Open circuit voltage (OCV= ΔE_{CEM}) as ΔE_{CEM} takes into account the potential generated by the CEM but not the potential generated by the ionomer coating.

By integrating Eqs. 6.4-6.6, we can express the power density as:

$$P = \frac{(OCV - 2 \cdot I \cdot R_{int}) \cdot Q}{2 \cdot (t_{OCV} + t)} \quad 6.9$$

6.3. Results and discussion

6.3.1. Electrode imaging

Fig. 6.4 shows top and cross-section SEM images of the electrodes without CEI coating (uncoated electrode) and with CEI coating with different ionomer loadings (CEI-coated-15 and CEI-coated-50 electrodes). The electrode coating structure is different between CEI-coated-15 and CEI-coated-50. In CEI-coated-50, the CEI-coating takes the shape of a layer on the surface of the carbon cloth. The difference is visible by comparing uncoated electrodes (Fig. 6.4a-d) and CEI-coated-50 electrodes (Fig. 6.4c-f). In contrast, the CEI coating is more dispersed in CEI-coated-15 electrodes. At first sight, the CEI-coating is not particularly visible by comparing the top view images of uncoated (Fig. 6.4a) and CEI-coated-15 electrodes (Fig. 6.4b). Paying closer attention, we can see ionomer clusters dispersed between the carbon fiber (Fig. 6.4e), which are not visible in uncoated electrodes (Fig. 6.4d).

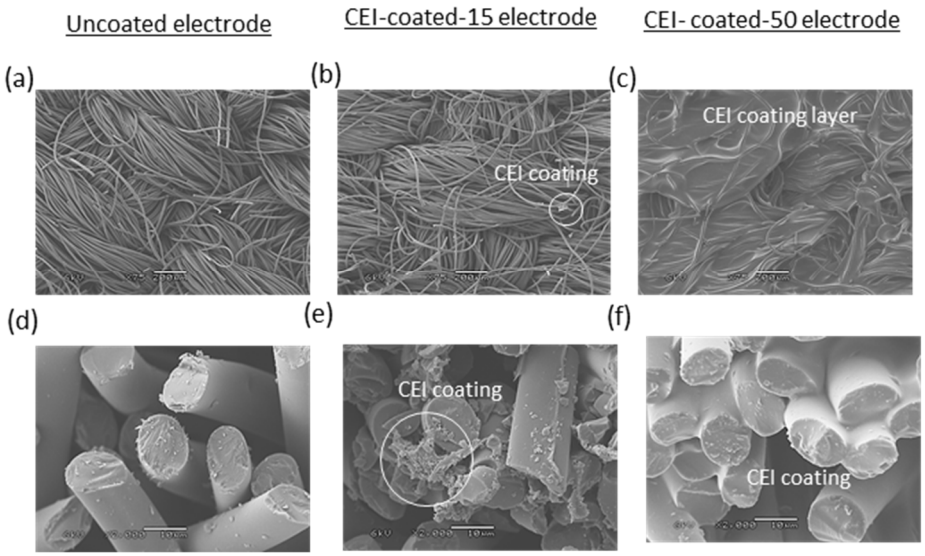

Fig. 6.4: Top-view SEM imaging (x75) of (a) uncoated electrode, (b) CEI-coated-15 electrodes and (c) CEI-coated-50 electrodes. Cross-section SEM imaging (x2000) of (d) uncoated electrode, (e) CEI-coated-15 and (f) CEI-coated-50 electrodes.

6.3.2. Open circuit voltage (OCV) measurement

Generating an open circuit voltage (OCV) by alternatively switching the CO_2-sparged and air-sparged solutions (OCV cycle) in the capacitive cell is essential to harvest electrical energy. Fig. 6.5a shows the cell voltage measured during OCV cycles and Fig. 6.5b shows the resulting OCV values for different cell designs. The highest OCV value was obtained with the uncoated electrodes ($OCV_{uncoated}$=~225 mV), which is 3.5 times higher than the membrane potential measured with CEI-coated-50 electrodes ($OCV_{CEI\text{-}coated\text{-}50}$ = ~65 mV). With uncoated electrode, OCV values are a direct measurement of the CEM potential. Fig. 6.6a shows an illustration of the OCV measured with uncoated electrodes. By switching gas stream across the CEM, the free water phase in the cell equilibrates with the CO_2 partial pressure in the gas inflow, leading to a change of ion concentration. The change of ion concentration on both the side of the CEM leads to a change of ion concentration ratio across the CEM, resulting in the establishment of a CEM potential. Consequently, continuously switching gas streams in each electrode compartment results in a change of OCV values due to the establishment of the CEM potential. In fact, the OCV values obtained with uncoated electrodes (~225 mV) is similar to the estimated theoretical CEM potential (~200-210 mV [23,29]). Note that the OCV values should not be higher than the theoretical CEM potential as we assume that the electrodes do not generate any potential under no current condition. Nevertheless, studies have shown that charged chemical groups exist on the carbon surface [85,86,204], which may generate an electrical potential.

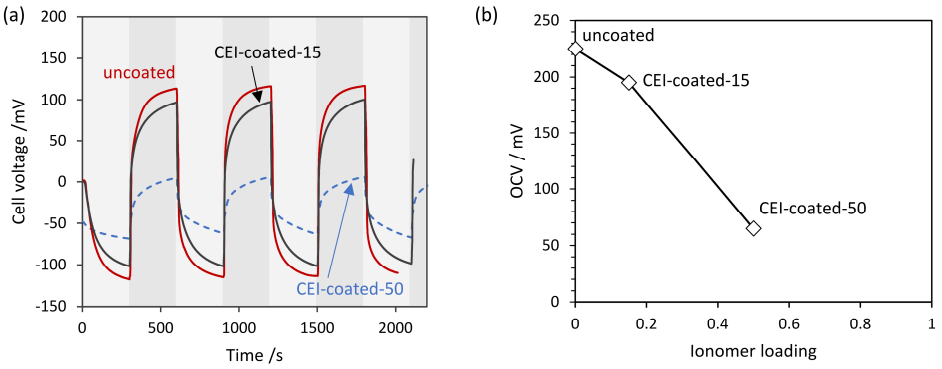

Fig. 6.5: (a) OCV cycles measured in a CO_2-CAPMIX cell with different electrode materials, i.e., uncoated electrodes, CEI-coated-15 electrodes, and CEI-coated-50 electrodes. (b) maximum OCV values measured as function of the ionomer loading of the electrode material tested

In contrast, the OCV values in CEI-coated-50 is not only related to the CEM potential, but also to the Donnan potential arising at the CEI-coating. As the CEI-coating and CEM are both ionomer-based layer, they can both generate a cell potential during OCV cycles. Similar ionomer coating has been used to generate membrane potential in conventional CAPMIX systems[19,22]. We believe that the lower OCV values obtained in CEI-coated-50 electrodes likely comes from the potential generated by the ionomer coating itself. Fig. 6.6c shows an illustration of the OCV measured with CEI-coated-50 electrodes. Unlike uncoated electrodes, the gas stream inflows are physically separated from the electrode pores by the ionomer coating. Therefore, the water phase in the electrode pores is not directly equilibrated by the inflow of CO_2 gas streams. Instead, CO_2 must diffuse through the ionomer coating in the form of CO_2 gas or $H_2CO_3^*$ (see Fig. 6.6c). As the diffusion of chemical species is slower in ionomer materials compared to the free aqueous solution, a higher amount of time is required for the electrode pores to reach equilibrium with the CO_2 partial pressure of the gas inflow. Thus, for a given time, a lower ion concentration ratio is obtained between the electrode pores with CEI-coating, resulting in lower membrane potential.

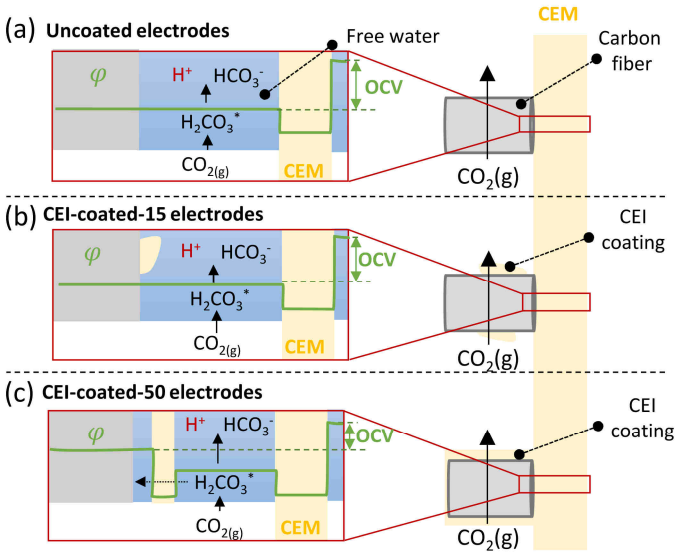

Fig. 6.6: Illustration of the membrane potential with (a) uncoated electrodes, (b) CEI-coated-15 electrodes and (c) CEI-coated-50 electrodes. Only one side of the CEM is illustrated. The same principle applied to the other side of the CEM.

Despite the effect of the electrode coating, the CEI-coated-15 electrodes show similar values of membrane potential ($OCV_{CEI\text{-}coated\text{-}15}$ = ~195 mV) comparable to uncoated electrodes ($OCV_{uncoated}$= ~225 mV), i.e., three times higher than CEI-coated-50 electrodes. Rather than the ionomer content, we attribute the significant difference of membrane potential between CEI-coated-15 and CEI-coated-50 to the ionomer coating morphology. As discussed in section 3.1, instead of forming a layer, the ionomer coating is more dispersed in CEI-coated-15 electrodes. As a result, the ionomer coating does not entirely cover the electrode, thus allowing a flow of CO_2 and air gas streams in the electrode pores. Therefore, CO_2 diffusion can still occur through the free water phase to the electrode pores. Fig. 6.6b illustrates the OCV measured with CEI-coated-15 electrodes.

6.3.3. Power densities generated in 4 step energy cycles

The 4-step energy cycles were performed to compare the generated power density with different electrode materials at different current densities (Fig. 6.7a-b). Besides, we also compare the OCV values (measured in step 3) and the internal resistance for the different electrode materials obtained during the 4-step energy cycles (Fig. 6.7c).

Compared to uncoated electrodes, Fig. 6.7a-b shows that the power density generated increases by coating the electrodes. The highest power density was obtained with CEI-coated-15 electrodes (~50 mW m^{-2} at 1 A m^{-2}), which is more than five times higher than uncoated electrodes (~7 mW m^{-2} at 0.15 A m^{-2}). Nevertheless, Fig. 6.7b shows that the higher ionomer loading does not yield the highest power density. The power density obtained is twice higher with CEI-coated-15 electrodes than CEI-coated-50 electrodes (~50 mW m^{-2} against ~21 mW m^{-2} at 1 A m^{-2}).

The effect of ionomer on power density can be explained by the compromise achieved between internal resistance and membrane potential performance with ionomer loading. As shown in Eq. 6.9, the power density in CAPMIX increases by both increasing the power density and reducing the internal resistance. On the one hand, higher ionomer loadings lead to lower membrane potential (Fig. 6.7c), hence an expected decrease of power density. On the other hand, lower values of internal resistance were obtained with higher ionomer loading (55 Ω cm^2 for CEI-coated electrodes against 2240 Ω cm^2 for uncoated electrodes), hence an expected increase of power density.

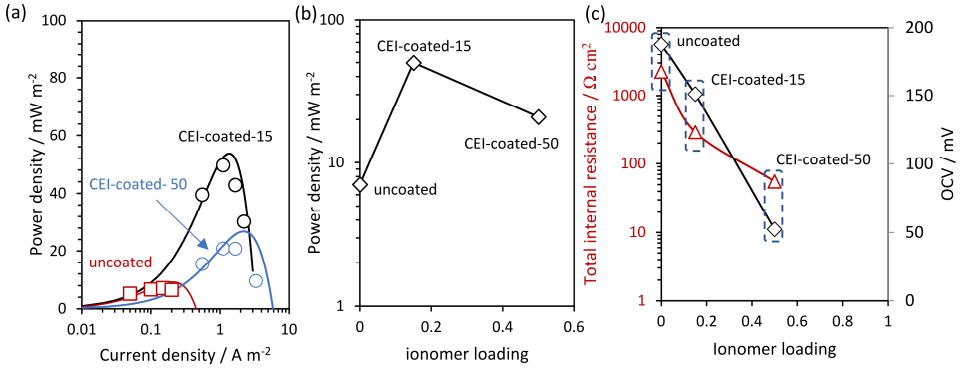

Fig. 6.7: Power density generated for different electrode materials as a function of (a) current densities and (b) ionomer loading (average values). The lines in (a) show calculated values with the power density model, while the symbols show the data values. (c) Measured internal resistance and membrane potential during 4-step energy cycles.

We can conclude that the CEI coating is beneficial to increase the power densities generated by a CO_2-CAPMIX by decreasing the internal resistance. Nevertheless, power densities achieved in a CO_2-CAPMIX cell is still 30 times lower than the processes using intercalation electrodes [27]. Further strategies should be implemented to (i) decrease the internal resistance, and (ii) increase the OCV. Before implementing new strategies, we propose to gain more insight into the cell internal resistance behavior by distinguishing the relative contribution of the ohmic and non-ohmic resistances.

6.3.4. Internal resistance analysis

The ohmic resistance (R_{ohmic}) was obtained for different electrode materials from EIS scans (Fig. 6.8a), while the non-ohmic resistance ($R_{non\text{-}ohmic}$) represents the remaining part of the total internal resistance. All resistances (ohmic, non-ohmic, and total resistances) are summarized in Fig. 6.8b.

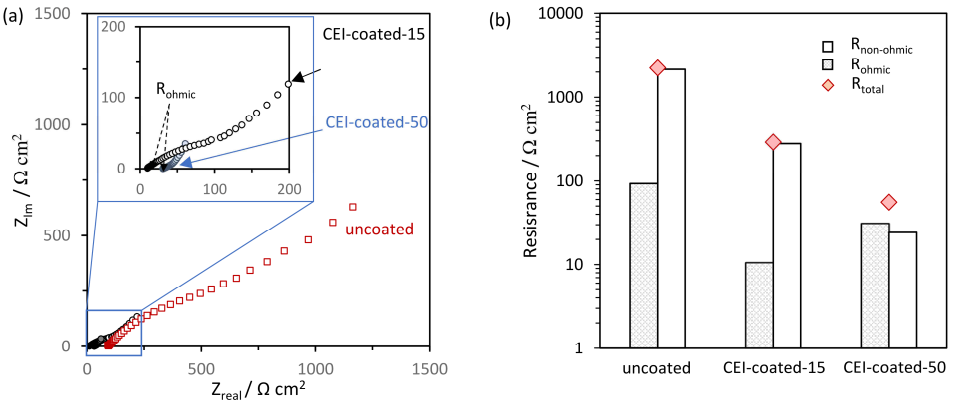

Fig. 6.8: (a) Electrical Impedance Scan obtained for different electrode materials. (b) total internal resistance, ohmic and non-ohmic resistances measured for each material tested.

Values of R_{ohmic} do not show a clear relationship with the amount of ionomer coating. The ohmic resistance of the different electrode material varies between 10-100 Ω cm² (92.61 Ω cm², 10.62 Ω cm², 31.23 Ω cm² for uncoated, CEI-coated-15 and CEI-coated-50 electrodes, respectively). All electrodes materials have been tested in the same cell architecture where both electrodes were separated by the same cation exchange membrane, which should lead to similar ohmic resistance. The CEM resistance has been characterized around ~11-20 Ω cm² [212,213] (in a 0.5 M NaCl solution), which is in line with the R_{ohmic} obtained with CEI-coated-15 and CEI-coated-50 electrodes. The ohmic resistance is somewhat bigger with uncoated electrodes. We believe that the difference can originate from the difference of force applied to the electrodes by the current collector. All electrodes were tested with the same cell and the same enclosing gasket. Nevertheless, the thickness of the coated electrodes is thicker than the uncoated electrodes, which could result in a higher pressure applied between the coated electrode and the current collector. Therefore, R_{ohmic} can be further improved by increasing the ionic conductivity of the CEM (e.g., decreasing thickness [205,214]) but also by adapting the force applied to the electrodes (cell construction design).

Fig. 6.8b shows that $R_{non-ohmic}$ decreases with ionomer loadings. Values of $R_{non-ohmic}$ are 80 times smaller in CEI-coated electrodes compared to uncoated electrodes (~25 Ω cm² for CEI-coated electrode against ~2146 Ω cm² for uncoated electrodes). Firstly, the CEI-coating increases the overall ionic conductivity of the electrode macropores. Secondly, the CEI-coating improves the contact area between the electrode and the CEM, resulting in a more integrated interface between both materials. As a result, concentration polarization in the electrodes and membrane interfaces is reduced, hence a decrease of

non-ohmic resistance. A similar effect has been observed in fuel cells with electrodes impregnated with ionomer materials[146,193,194].

6.4. Conclusions

This work has aimed to investigate the effect of CEI coating on the CO_2-CAPMIX performance. In particular, we observed that coating the ionomer with a cation exchange ionomer (CEI) is beneficial to increase the power densities generated by a CO_2-CAPMIX cell due to a significant improvement of the internal resistance. However, the improvement of the internal resistance was achieved at the cost of the OCV values, thus limiting the generated power density generated. We discussed that the ionomer coating structure, rather than the ionomer loading, likely lead to a decrease of OCV. In this study, a simple coating procedure was used by simply deep coating the electrodes into the ionomer solutions. Thus, for future work, we recommend investigating different coating procedures (slurry casting[18,23], electrospinning[206,207], electrospraying[208], or spraying with a spray gun[209,210]) to better tune the ionomer loading and final content in the electrode. Furthermore, identifying ionomer material with lower selectivity toward $H_2CO_3^*$ is also of interest to improve the OCV values. As explained in section 6.3.2, improved $H_2CO_3^*$ permeability through the ionomer layer could increase the OCV values. MEA cell designs have been optimized for many years in fuel cells, for instance, by selecting suitable ionomer material[215,216], optimizing the electrodes and membrane thickness[205,214], as well as optimizing the loading and structure of the coating in the electrodes.

Chapter 7

General discussion and outlook

7.1. Introduction

In this thesis, we explored the use of capacitive processes (CDI and CAPMIX) for carbon capture (CO_2-CDI) and energy recovery from CO_2 emissions. Conventionally, capacitive technologies have been developed for water technologies, i.e., water desalination (CDI) and blue energy (CAPMIX). Therefore, the focus of the work presented in this thesis was to adapt these water technologies into gas technologies.

Our research work investigated the use of capacitive cell for CO_2-CDI and CO_2-CAPMIX through three different steps, i.e. (i) proof of concept (**Chapters 2 and 3**), (ii) in-depth understanding (**Chapter 4**), and (iii) cell design exploration (**Chapters 5 and 6**). CO_2-CDI is investigated in Chapters 2,4,5 and CO_2-CAPMIX in Chapters 3 and 6. In this thesis, CO_2-CDI and CO_2-CAPMIX were investigated together, which is not usually the case of conventional CDI and CAPMIX. Although both applications are based on the same principles, the technologies have been studied separately, leading to different research directions, as well as different figures of merit and indicators. Nevertheless, at this development stage, CO_2-CDI and CO_2-CAPMIX should not be separated by application but rather investigating together to give more insight into the capacitive cell behavior with CO_2-sparged electrolyte solutions.

Three aspects show to be important in our finding, i.e., (i) importance of water in CO_2 reactive electrosorption, (ii) the effect of CO_2-sparged solution on ion selectivity, and (iii) the effect of cell designs on cell resistance and ion selectivity. First, CO_2 reactive electrosorption is the key element on which CO_2-CDI and CO_2-CAPMIX are based. We identified in Chapters 2 and 3 that the internal resistance and ion selectivity are two major factors limiting the performance of the capacitive cell. Ion selectivity was characterized for both systems in terms of ion adsorption in electrodes in CO_2-CDI (absorption efficiency, Λ_a) and membrane apparent permselectivity (α) in CO_2-CAPMIX. At last, different cell designs were tested to reduce the internal resistance.

In this final chapter, we connect our findings from different chapters and discuss the three aspects we found the more important. After that, we discuss the potential of capacitive technology with CO_2 gas and give future research directions.

7.2. Importance of water in CO_2 reactive electrosorption performance

The novelty in this Ph.D. thesis is to investigate capacitive cells with CO_2 gas and not with conventional salt solutions. Salt solutions and CO_2 gas are radically different as they do not share the same physical state. Unlike true electrolyte (e.g., NaCl), CO_2 reacts with water to generate ions via a multi-step and pH-dependent mechanism, which involves the generation of amphoteric ions. We refer to this complete mechanism as CO_2 reactive electrosorption principle. Through this mechanism, CO_2 gas can be adsorbed in porous electrodes in the form of bicarbonate ions in CO_2-CDI (see Fig. 7.1 and Chapter 2). Moreover, a membrane potential can be obtained by alternatively feeding a capacitive cell (CO_2-CAPMIX) with two CO_2-sparged solutions at different CO_2 concentrations to produce electrical power (Chapter 3).

Besides demonstrating the underlying mechanisms, we also demonstrated the concept of direct gas feeding. Instead of pumping CO_2-sparged solution in the cell (solution feeding operation), the CO_2 gas is directly fed into the capacitive cell where the CO_2 reaction and the electrosorption co-occur (Chapters 3 and 6). The reactive process occurs then in the water fraction remaining in the capacitive cell. Fig. 7.1 illustrates a CO_2-CDI cell under gas-feeding operation.

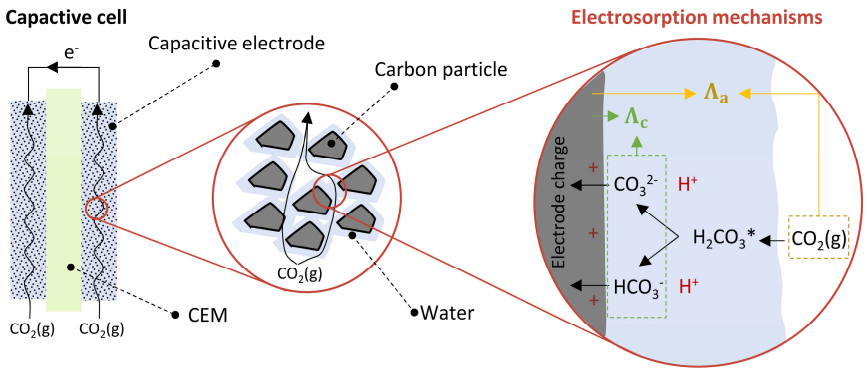

Fig. 7.1: Illustration of the CO_2 reactive electrosorption mechanisms in a capacitive cell in gas feed operation. Λ_a refers to absorption efficiency, which is defined as the amount of CO_2 gas absorbed per electrical charge. Λ_c refers to the carbon adsorption efficiency, which is defined as the amount of carbon adsorbed in the electrodes (HCO_3^- and CO_3^{2-}) per electrical charge.

In direct gas feeding, the water fraction in the capacitive cell plays an essential role, and therefore, its management is crucial. During short-time operation (up to 10 hours), operating the capacitive cell is suitable as enough water volume remains in the cell to generate ions (from CO_2) and transport them between electrodes. However, during longer operation time (>10 hours), our finding showed that the cell would slowly dry (i.e., the water fraction inside the electrodes decrease), thus resulting in an increase of internal resistance (shown in **Chapter 3**). The drying of the cell likely depends on the humidity of the inflow gas streams. In thermal power plants, the humidity in flue gas is relatively high, which is not expected to cause significant drying of the cell. On the other hand, in direct air capture (DAC) application, the relative humidity in the air is lower than flue gas. Thus, for each targeted application, strategies should be investigated to ensure a sufficient level of humidity in the cell by, for instance, humidifying the gas [142,150] and controlling the gas flow rates[217].

The water fraction also influences the CO_2 gas absorption efficiency (introduced in **Chapter 2**), which is defined as the amount of CO_2 gas absorbed per electrical charge ($\Lambda_a = n_{CO_2(g)}/n_{charge}$). We explained in **Chapter 2** that at higher water fraction, the lower is the absorption efficiency due to the CO_2 solubility in water. This means that for an equal carbon adsorption efficiency, $\Lambda_c = (n_{HCO_3^-} + n_{CO_3^{2-}})/n_{charge}$, a higher amount of CO_2 gas will be absorbed with lower water fractions. In this regard, operating the capacitive cell under direct gas feeding is of interest to minimize the water fraction and maximize the absorption efficiency. The concepts of Λ_a and Λ_c are both illustrated in Fig. 7.1.

7.3. From salt to CO_2-sparged electrolyte solutions: what effect on ion selectivity?

Understanding the ion electrosorption mechanisms in the electrodes and ion transport through ion exchange membranes is essential to optimize both CO_2-CDI and CO_2-CAPMIX. Such mechanisms have been extensively studied with salt solutions in the last 20 years[17,69,152,218–220]. An extensive range of theoretical models has been developed to predict salt electrosorption in CDI cells[70,84,86,152,221] over the years. Besides, salt ion transport through ion exchange membranes has been investigated not only for Membrane-CDI (MCDI) but also for other technologies, e.g., capacitive mixing (CAPMIX)[21,22,132,137], electrodialysis (ED) [205,222–224] and reverse electrodialysis (RED)[88,225]. However, understanding CO_2-sparged solutions require the incorporation of additional physical phenomena (e.g., gas absorption, dissociation of amphoteric ions), which is not the case for salt solutions.

7.3.1. Electrosorption in porous electrodes

In **Chapter 4,** we theoretically investigated the electrosorption in CO_2-CDI by including acid-base reactions in the amphoteric Donnan (amph-D) model. The amph-D model is a theoretical model that has been successfully used for the prediction of ion adsorption with salt solutions [79,86,165,177,226]. Despite its proven accuracy with salt solutions, the amph-D model showed poor prediction capability in the case of CO_2-CDI experimental results. In a second step, we improved the fit between CO_2-CDI experimental results and the model by integrating the effect of the surface group on the carbon electrode surface (m-amph-D model in Chapter 4). To further improve the electrosorption prediction, we strongly believe that other effects need to be further investigated, such as preferential adsorption of divalent ion[71,75,120] (CO_3^{2-} in the case of CO_2-sparged solutions), and size-based ion selectivity[179,180,227] (which could reduce the carbon adsorption efficiency). Another intriguing possibility could be the dissociation of weak acids in the electrical double layers. Some studies suggested that the dissociation constants of weak acids tend to decrease inside electrical double layers (EDL) by charging the electrodes [181,182] (dissociation field effect). In a broader context, the understanding gained in CO_2-CDI can also profit conventional CDI. For instance, considering the surface chemical groups as reactive species is of great importance for reactive species (e.g., NH_3, H_3PO4). Moreover, CDI systems relying on the surface chemical charge to adsorb ions must consider the reactivity of surface chemical charges as a function of cell voltage.

7.3.2. Role and permselectivity of ion exchange membranes in CO_2-CDI

Through this Ph.D. thesis, we found that using ion exchange membranes (IEMs) is a suitable strategy to increase the absorption efficiency using an MCDI cell design despite the low electrode selectivity (Chapter 4). In fact, a CO_2-MCDI cell reached similar charge efficiency than conventional MCDI, clearly showing the beneficial effect of IEMs (Chapter 2). Among the CEM and AEM, we demonstrated in Chapter 4 that the AEM has a higher contribution to the increased charge efficiency than the CEM. From this result, the ion-selective property of AEM with CO_2-sparged has been utilized to improve the absorption efficiency of new cell designs. For instance, we coated the electrodes of a membrane electrodes assembly (MEA) with anionic exchange ionomer (AEI) in Chapter 5 to improve the absorption efficiency (≈50% increase compared to uncoated electrodes). Thus, we showed that using ionomers or ion exchange membranes is a suitable strategy to improve the absorption efficiency (and charge efficiency) in CO_2-CDI systems.

However, the beneficial effect of IEMs in CO_2-CDI is time-dependent, as the absorption efficiency decreases with longer charging time (≈hour) (chapter 4). In the Chapters 2,4,5 and 6, we attributed the loss of membrane performance to the CO_2-sparged electrolyte solution. In CO_2-CAPMIX, we showed that the apparent permselectivity of IEMs is significantly lower in CO_2-sparged solution compared to NaCl solutions. For instance, we demonstrated in chapter 3 that a CO_2-CAPMIX cell with flat-MCDI design shows membrane apparent permselectivity around $\alpha \approx 0.3$, which is three times lower than values expected from NaCl solutions ($\alpha > 0.95$)[88,127,228]. Note that membrane apparent permselectivity values were derived from membrane potential experiments in open-cell voltage [88,90,229]. This lower membrane apparent permselectivity was attributed to the diffusion of neutral carbonic acid through the IEMs (Chapters 3 and 4), a hypothesis that is supported by another theoretical study[29]. Therefore, selecting IEMs and ionomer material less permeable to $H_2CO_3^*$ could be a reasonable approach to improve the membrane apparent permselectivity and the performance of CO_2-CDI and CO_2-CAPMIX.

Against all expectations, we instead propose to develop IEMs and ionomer more permeable to $H_2CO_3^*$. Surprisingly, our work on cell designs (**Chapters 5 and 6**) showed that the low membrane apparent permselectivity can be advantageous to decrease the internal resistance of a CO_2-CDI system. In our attempt to reduce the internal resistance of a CO_2-MCDI, we designed an MEA where both electrodes were coated with the same ionomer (see MEA(coated) in Fig. 7.2). Selecting MEA(coated) cell designs is counter-intuitive as coating the anode with cationic exchange ionomer (CEI) is expected to increase the internal resistance due to the shielding effect. However, this was not the case with CO_2-sparged solution. We explained in chapter 5 that we believe that HCO_3- is first transported in the form of $H_2CO_3^*$ through the CEI coating anode, before being adsorbed in the anode micropores. Instead of focusing on increasing the ionomer selectivity, we propose to focus on increasing the selectivity of the electrode and develop permeable ionomer for CO_2 to improve further the internal resistance. In this regard, pseudocapacitive material selective to CO_2[57] is an interesting alternative to investigate.

7.4. Exploring cell designs: a compromise between internal resistance and ion selectivity

Reducing the internal resistance in CO_2-CDI and CO_2-CAPMIX have been the major challenge of this Ph.D. project. The performance of the CO_2-CDI and CO_2-CAPMIX greatly suffers from the high energy losses caused by the internal resistance of the capacitive cell. High internal resistance was obtained in conventional MCDI cell designs due to the poor

ionic conductivity of CO_2-sparged electrolyte solutions (e.g., 17 µS cm^{-1} for 15% CO_2-sparged solution). Therefore, the work presented in this Ph.D. thesis mainly focused on developing novel cell designs to reduce the internal cell resistance of capacitive cells with poorly conductive solutions. All cell designs tested are shown in Fig. 7.2.

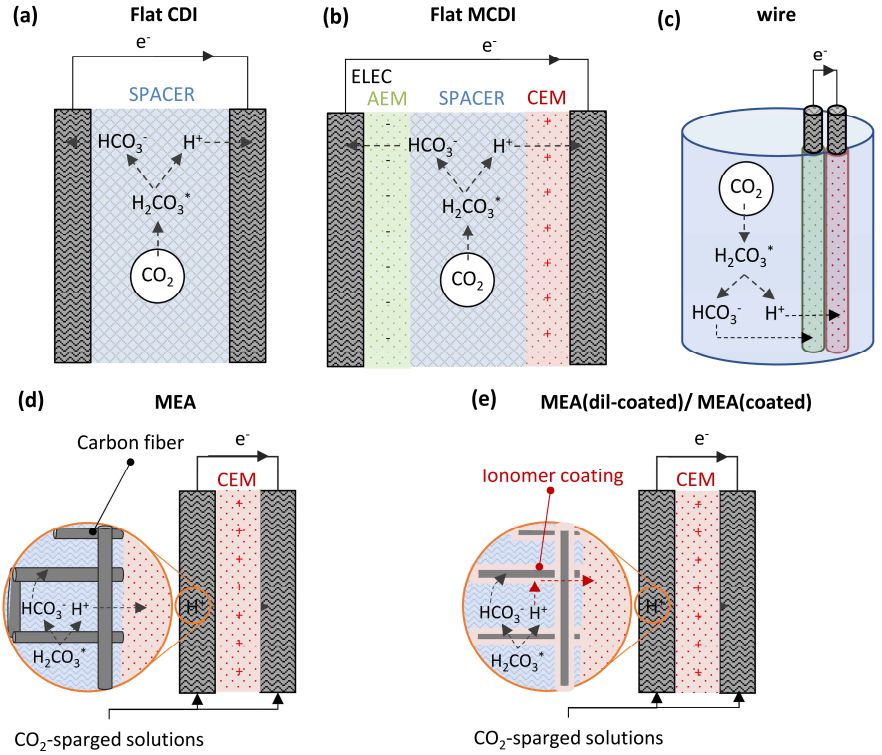

Fig. 7.2: Cell designs tested through this Ph.D. thesis.

7.4.1. Lower internal resistance obtained with membrane electrode assembly (MEA) cell design

In this thesis, the internal cell resistance has been investigated by separating two contributions, i.e., the ohmic resistance and the non-ohmic resistance (Chapters 2, 5, and 6). As a reminder, the ohmic resistance is the time-independent part of the internal resistance, mostly relating to the ionic conductivity of the cell. In contrast, the non-ohmic resistance is the time-dependent part of the internal resistance, which is mostly attributed to ion depletion in the diffusive boundary layers (concentration polarization)[121,127,200,230].

Fig. 7.3 shows the ohmic and non-ohmic resistance measured for all cell designs tested for both CO_2-CAPMIX and CO_2-CDI.

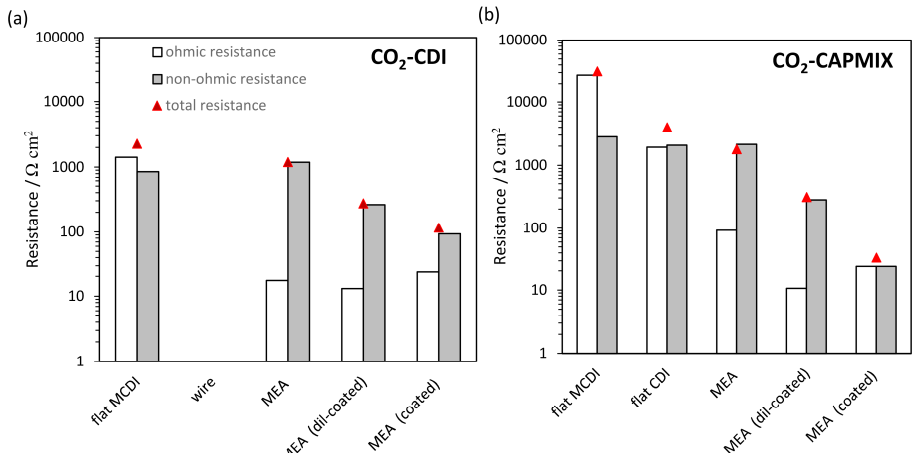

Fig. 7.3: Ohmic, non-ohmic, and total internal resistance obtained with different cell designs for (a) CO_2-CDI and (b) CO_2-CAPMIX.

Ohmic resistance

The ohmic resistance is the dominating resistance in the MCDI cell design for CO_2-CDI and CO_2-CAPMIX (Chapter 2). This cell design is not suitable as the CO_2-sparged solution is fed in between the electrodes, decreasing the ionic conductivity between the electrodes. Instead, we show that the membrane electrode assembly (MEA) design is more suitable as the electrodes are separated by an IEM, which is more conductive than the CO_2-sparged solution. To further reduce the ohmic resistance, we recommend future studies to (i) select more ionic conductive membrane and (ii) reduce the membrane thickness.

Non-ohmic resistance

As the ohmic resistance decreases from MCDI to MEA cell designs, the non-ohmic resistance became the dominant resistance in the capacitive cell (see Fig. 7.3). For instance, the non-ohmic resistance represents more than 90% of the resistance measured in the MEA cell design with uncoated electrodes. In Chapters 5 and 6, we demonstrated that the non-ohmic resistance could be reduced by coating both electrodes with the same ionomer. A similar strategy has also been used in fuel cells [145,146,203,209] and electrochemical

CO_2 reduction[141,142] technology to improve the ionic contact between membranes and electrodes.

As explained in section 7.3, we did not expect such a significant decrease in internal resistance by coating the electrodes with a single ionomer. Therefore, we believe that the non-ohmic resistance of the MEA-coated cell design could decrease further by improving our understanding of the ion transport mechanisms. MEA(coated) cell design has been first used and optimized for PEM fuel cell applications for many years [145,146,194,203,209], where internal resistance as low as 0.032 Ω cm^2 was achieved (3000 times lower than CO_2-CAPMIX/CO_2-MCDI). However, PEM fuel cells and CO_2-CDI (capacitive systems) differ in many aspects (reaction, transport mechanisms). It is interesting what we can learn from PEM fuel cells to reduce the resistance, as the ohmic resistance and non-ohmic resistance are related to the H+ transport in both cases.

7.4.2. Energy performance with different cell designs: a compromise between ion selectivity and internal resistance

Internal resistance and ion selectivity together determine the energy consumption in CDI and the power density in CAPMIX. Table 7.1 shows the relationship between those two parameters and their respective energetic performance. In CO_2-CDI, the ion selectivity is expressed by the absorption efficiency (Λ_a) or carbon adsorption efficiency (Λ_c). In CO_2-CAPMIX, the ion selectivity is expressed by the apparent membrane selectivity (α).

Table 7.1: Figure of merit related to electrical energy for CO_2-CDI and CO_2-CAPMIX

Process	Figure of merits	Equations
CO_2-CDI	Energy consumption, W_{net} / kJ molCO_2^{-1}	$W_{net} = \frac{2 \cdot I \cdot \mathbf{R_{int}} \cdot F_a}{(1 - f_w) \cdot \mathbf{\Lambda_c}}$
CO_2-CAPMIX	Power density generated (P) / W m^{-2}	$P = \frac{1}{2}(\boldsymbol{\alpha} \cdot \Delta E_{m,th} - 2 \cdot I \cdot \mathbf{R_{int}})$

I: current density, F_a : Faraday constant, f_w : water fraction in the cell, $\Delta E_{m,th}$: theoretical membrane potential.

Overall, the energy consumption between a flat MCDI and an MEA(coated) cell designs barely improved (Fig. 7.4b). The decrease of cell resistance by using an

MEA(coated) cell design is obtained at the cost of a decrease in carbon adsorption efficiency (Fig. 7.4a), resulting in lower energy consumption. The loss of carbon adsorption efficiency is related to the absence of IEM or ionomer coating covering the electrodes (explained in section 7.3). Related to our conclusion in section 7.3, we believe that improving the ion selectivity of the electrodes is the future strategy to follow. While the ionomer coating reduces the internal resistance, higher ion selectivity must be sort.

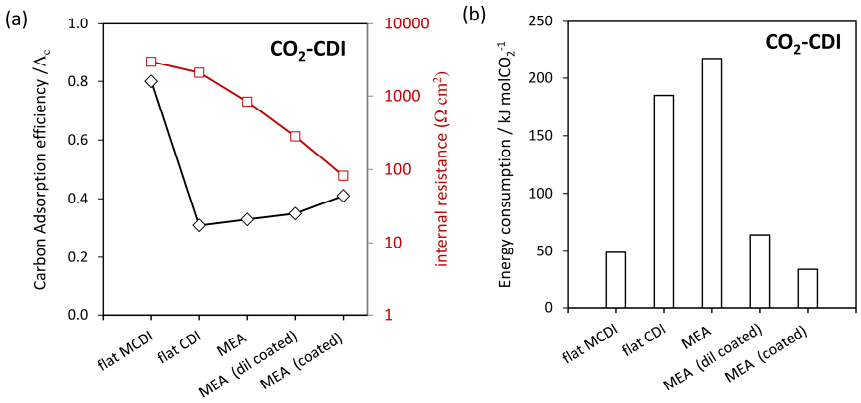

Fig. 7.4: (a) Carbon adsorption efficiency (Λ_c), total internal resistance and (b) energy consumption for different cell designs in CO_2-CDI. Experimental results from Chapters 4,5, except for the data obtained with the CDI cell design. Data obtained with the flat CDI cell design were obtained by charging the cell under constant current (0.6 A m^{-2}) between 0 and 1 V.

A compromise between membrane apparent permselectivity and internal resistance on the generated power is also observed in CO_2-CAPMIX (Fig. 7.5). However, the trend of membrane apparent permselectivity as a function of cell designs is wholly reversed to CO_2-CDI. In CO_2-CAPMIX, MEA cell design with uncoated electrodes results in the highest membrane apparent permselectivity. In Chapter 3, we explained that higher membrane apparent permselectivities are obtained when both gas streams are fed across the membrane between the electrodes. Moreover, when covered by an ionomer coating or an IEM, $H_2CO_3^*$ diffusion occurs through the IEM/coating to the electrode pores, where no mixing occurs, thus reducing the concentration ratio of ions and therefore the membrane potential. Interestingly, we found that the MEA(dil-coated) cell design did not suffer from a significant loss of membrane apparent permselectivity. With a dispersed ionomer coating, sufficient gas mixing can occur in the pores of the electrodes, limiting the effect of $H_2CO_3^*$ diffusion. We propose to optimize the ionomer dispersion coating in

future work to decrease the internal resistance further while keeping high membrane potentials.

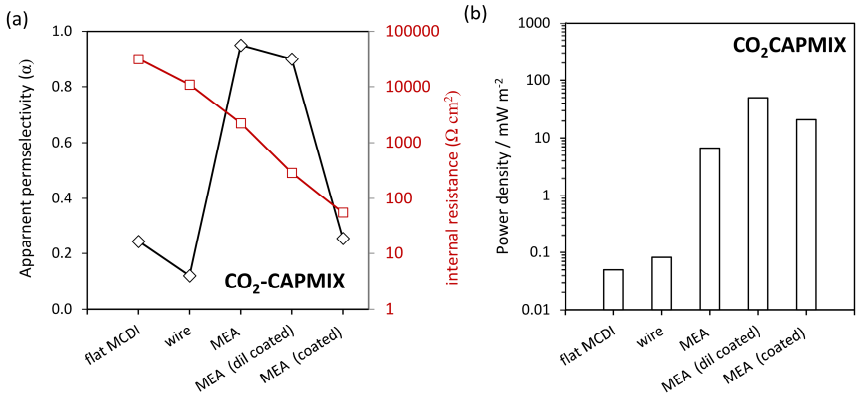

Fig. 7.5: (a) membrane apparent permselectivity, internal resistance, and (b) power density for different cell designs in CO_2-CAPMIX under direct gas operation. Experimental results are obtained from Chapters 3 and 6.

To conclude, the MEA(coated) design can improve the energy consumption in both CO_2-CDI and CO_2-CAPMIX if the ion selectivity increases for both systems (in terms of Λ_c or Λ_a and α). Future research should focus on optimizing electrode materials and ionomer coating methods. Furthermore, efforts in understanding the ion electrosorption in the electrodes, and ion transport through the cell is essential to improve the cell designs.

7.5. Perspective on technology development

In this section, CO_2-CDI and CO_2-CAPMIX are discussed separately as their development depends on their application.

7.5.1. Development of CO_2-CAPMIX

Throughout this Ph.D. thesis, we improved the CO_2-CAPMIX cell performance from 0.2 mW m^{-2} ([23]) until reaching 50 mW m^{-2} by optimizing cell design and material. The power generated could be increased by further improving the cell design. For instance, reverse electrodialysis, i.e., another salinity gradient energy technology, has seen continuous improvements in the generated power density by optimizing membrane and cell designs, until reaching power densities up to 3 W m^{-2} ([121,231]). However, on a practical level,

implementing CO_2-CAPMIX as a technology for power plants does not seem feasible for the coming years. On the one hand, the practical energy recovery in power plants is limiting. At 100% thermodynamic efficiency, CO_2-CAPMIX could improve the energy efficiency of power plants up to 5%. However, reaching thermodynamic efficiency higher than 10% is challenging. A recent study on capacitive technologies showed that the thermodynamic efficiencies reported for such systems are far below 1% [232,233]. Moreover, a trade-off exists between power generated and thermodynamic efficiency. For instance, an optimal power density was obtained at thermodynamic efficiency of ~30% for blue energy in reverse electrodialysis (RED)[126,234]. Therefore, assuming a thermodynamic efficiency of 10%, the electrical efficiency of power plants gained would still be too small for implementation.

On the other hand, governments aim at reducing the CO_2 emissions of power plants to tackle global warming. Thus, political and technical efforts are mostly focused on CO_2 capture for thermal power plants instead of promoting technologies based on CO_2 emissions. In this regard, operating a capacitive cell as a CO_2-CDI unit for CO_2 capture is more promising than as a CO_2-CAPMIX device.

Nonetheless, we propose to look at alternative applications for CO_2-CAPMIX, where available energy exists from CO_2 concentration gradient. In any case, studying CO_2-CAPMIX is still worth investigating from a scientific point of view to gain knowledge on capacitive systems with CO_2 gas and saline solutions.

7.5.2. Development of CO_2-CDI

Toward the development of a complete CO_2 capture cycle

A crucial development step in CO_2-CDI is to operate the cell in a complete CO_2 capture cycle, including the adsorption step (CO_2 capture) and the CO_2 concentration step at high purity (see Table 7.2). While cleaning the flue gas from CO_2, generating a high purity of CO_2 gas is crucial to process CO_2 in further utilization routes, e.g., CO_2 gas storage [15,235,236] or CO_2 chemical conversion[140,142,237]. In this Ph.D. thesis, we separately focused on the performance of the adsorption step and the CO_2 concentration step (Chapter 2). In this chapter, we proposed a simple calculation framework to estimate the effect of combining both the adsorption and concentration steps in CO_2-CDI (see Appendix). Fig. 7.6 shows the cell voltage and CO_2 partial pressure measured during a 4-step CO_2 capture cycle. Fig. 7.7a shows an example of a CO_2 pressure cycle obtained at different electrode charge during a complete CO_2 capture cycle.

Table 7.2: Step description of a 4-step cycle for CO_2 capture cycle in CO_2-CDI

Step	Description	Current	Gas
1	Switching from concentrated to dilute gas in the channel	Open-cell voltage	15% CO_2 gas
2	Charging step	Positive current	15% CO_2 gas
3	Switching from diluted to concentrated gas in the channel	Open-cell voltage	100% CO_2 gas
4	Discharging step	Negative current	100% CO_2 gas

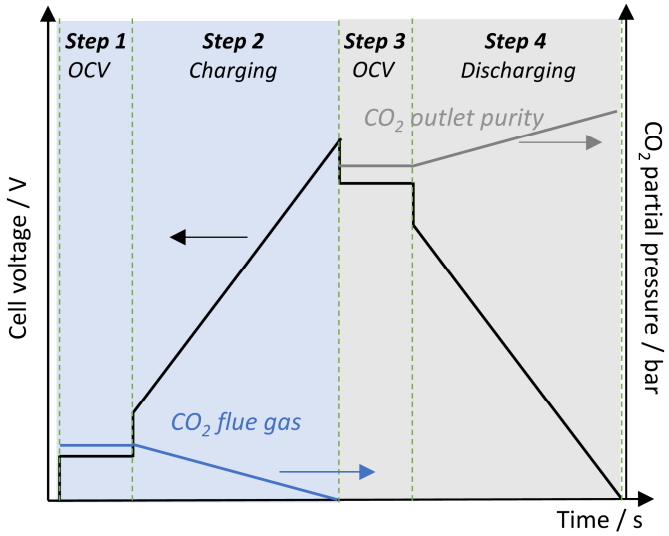

Fig. 7.6: The cell voltage and the CO_2 partial pressure described by the 4-step CO_2 capture model.

In this chapter, we propose to estimate the effect of water fraction (f_w), the CO_2 purity, the electrode capacitance, and the internal resistance. Fig. 7.7a-b shows that the water fraction (f_w) in the system has a significant impact on energy consumption when increasing the CO_2 purities. When desorbing CO_2 from the electrodes, part of the CO_2 remains is dissolved in the water phase (due to the solubility of CO_2 in water). This effect can even result in negative CO_2 absorption and desorption. For instance, in the case of f_w=11% (i.e., water fraction tested in Chapter 2), more CO_2 gas is absorbed in the water fraction during the desorption than desorbed into the CO_2 gas, resulting into no net CO_2 gas desorption at CO_2 purities above 30%. Our calculation shows that water fraction values

below 1.2% are necessary to operate the CO_2-CDI cell (see Fig. 7.7c). In this regard, a direct gas approach is more suitable to minimize the water fraction. Other strategies to reduce the effect of water fraction could include the optimization of gas flow rates (both diluted and concentrated gas).

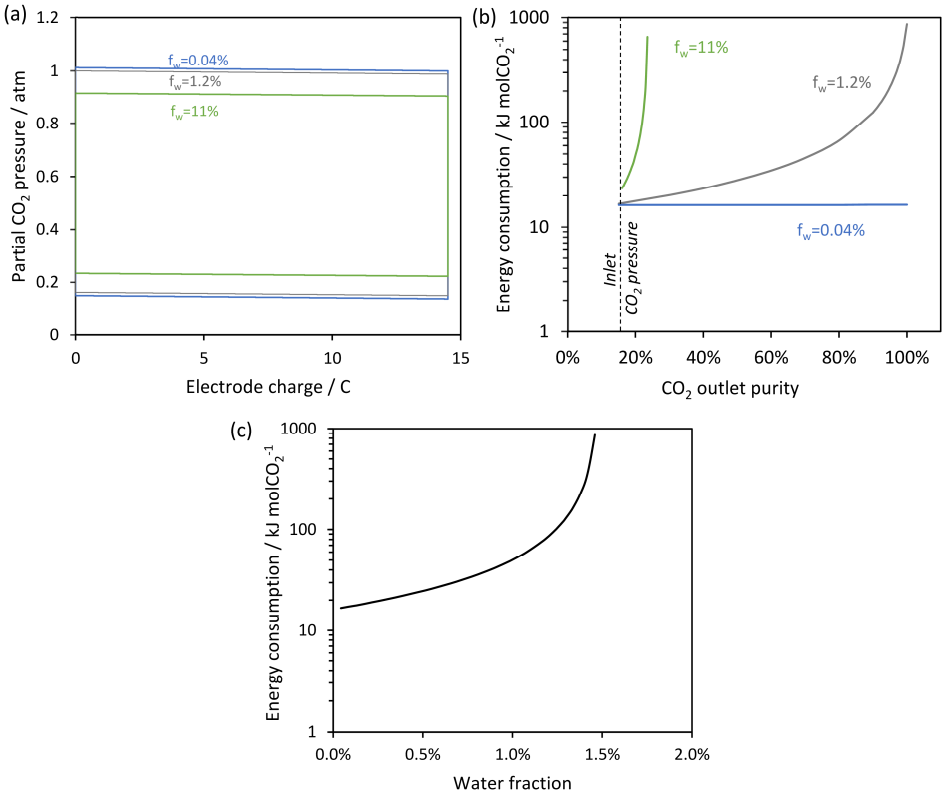

Fig. 7.7: (a) CO_2 pressure modeled during a 4-step cycle for different water fraction. (b) Energy consumption calculated at different water fractions as a function of CO_2 concentration purities. (c) Energy consumption as a function of water fraction at 100% CO_2 outlet stream.

Comparison with conventional technology

Different output parameters should be considered to assess the potential of CO_2-CDI as a technology for CO_2 capture i.e., (i) energy consumption, (ii) CO_2 absorption rate (CAR), and (iii) CO_2 adsorption capacity (CAC). Table 7.3 shows a comparison between conventional thermal adsorption (using zeolites), and CO_2-CDI with two different cell designs.

Table 7.3: Performance comparison between different technologies

System	Energy consumption / kJ molCO_2^{-1}	CO_2 absorption rate (CAR) / µmol s^{-1} kg_{ad}^{-1}	CO_2 absorption Capacity (CAC) / mmol kg_{ad}^{-1}	Source
Conventional adsorption (zeolites)	88-200	250	700	38,238, 239
CO_2-CDI / MDI	65	5.09	67	Chapter 2
CO_2-CDI / MEA(coated)	34	2.47	34	Chapter 5

Table 7.3 shows that CO_2-CDI has lower CO_2 adsorption rates (CAR) and capacities (CAC) than conventional adsorption processes. Compared to conventional adsorption, the CAC is ten times lower in CO_2-CDI. Nevertheless, CAC in CO_2-CDI could increase by selecting electrode materials with higher capacitance while keeping the water fraction as low as possible. Fig. 7.8 shows that similar CAC than zeolites can be potentially obtained with electrode capacitance as high as 80 F g^{-1} for low water fraction values. This value is not unrealistic since capacitive materials with capacitance in the range of 100 F.g^{-1} has been reported with activated carbon material[240] and up to 1000 F.g^{-1} for intercalation material[167]. Intercalation materials are of interest to investigate, thanks to their high charge efficiency and capacitance values in conventional CDI[167,241]. Moreover, this capacitance value can also be lowered by increasing the charge efficiency.

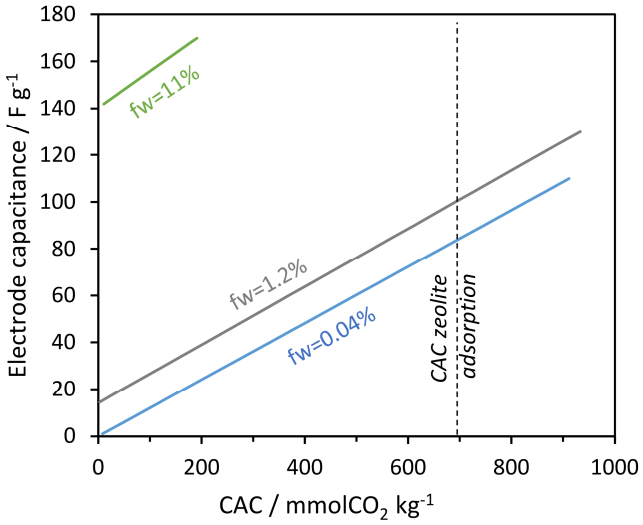

Fig. 7.8: Calculated CO_2 adsorption capacity (CAC) as a function of electrode capacitance for different water fractions in a CO_2-CDI cell.

In terms of energy consumption, CO_2-CDI shows values two times lower than conventional adsorption zeolites (50 kJ mol^{-1}. Nevertheless, the low energy consumption in CO_2-CDI is obtained at the cost of CAR, which is significantly higher in conventional adsorption systems (50 times higher). Values of CAR from conventional adsorption processes can currently not be achieved in CO_2-CDI due to the high internal cell resistance (see Fig. 7.9). Decreasing the internal resistance is essential to increase the current density and the CAR. Fig. 7.9 shows that achieving cell resistance values below 50 Ω cm^{-2} while keeping high charge efficiency value is essential to match values of CAR similar to conventional adsorption systems. Our work on cell designs shows that reaching internal resistance of 50 Ω cm^2 is possible as we demonstrate that an MEA cell design could reach resistance value in the range of 100-200 Ω cm^2 (Chapter 5). Nevertheless, implementing an MEA cell design also leads to a loss of absorption efficiency. A combination of an MEA cell design with more selective electrode material is of great interest to improve both the energy consumption and CAR. In a broader context, future strategies could be implemented from different fields, i.e., fuel cell (cell designs and material), CDI (capacitive materials), and other electrochemical CO_2 capture systems (CO_2 selective electroactive material).

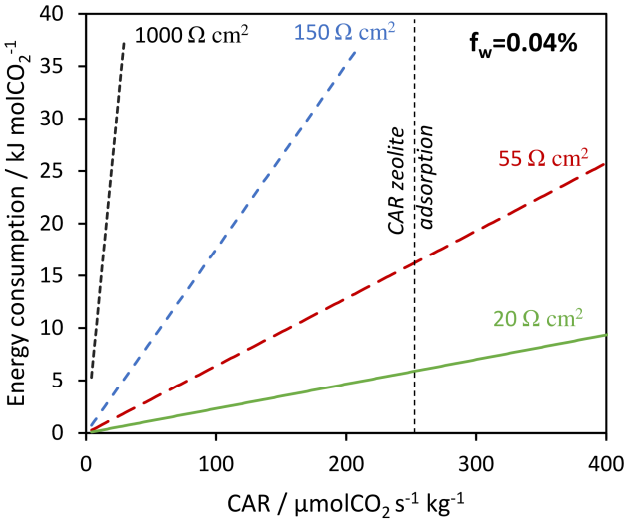

Fig. 7.9: CO_2 adsorption rate obtained as a function of energy for CO_2-CDI at different average internal resistance under constant current operation. Theoretical data were obtained at different current densities in a cell voltage range between 0 and 1V.

Compared to conventional adsorption systems, reaching low energy consumption is the main advantage of CO_2-CDI. Unlike conventional adsorption systems, reaching low energy consumption is possible as (i) the energy invested during the CO_2 absorption can be partially recovered during desorption, as suggested for CDI[74,242,243], and (ii) the electrical current can be controlled to optimize the energy consumption. Nevertheless, low energy consumptions in CO_2-CDI are obtained to the cost of CAR. Therefore, either CO_2-CDI should be applied to CO_2 capture application with low CAR unless future research steps focus on improving the internal resistance and absorption efficiency.

Exploring specific applications for CO_2-CDI

We believe that identifying specific applications for CO_2-CDI is essential, as the technical requirement differs according to the chosen application. For instance, gas mixtures from power plants are humidified, which is favorable to operate a CO_2-CDI cell. This is not the case in direct air capture (DAC), which can lead to the drying of the cell. On the other hand, the volumetric flow and gas mixture is strongly dependent on the application. For instance, a large volume of flue gas needs to be treated in power plants, which can be less the case in DAC. Moreover, the destination of the captured CO_2 is also important to consider as high CO_2 purity are essential in CO_2 capture and storage (CCS), which is not always necessary for certain carbon and capture and utilization (CCU)

application. As a reminder, CCU is the process where CO_2 is first captured and then used for further application, e.g., CO_2 conversion into chemicals.

Upon the urgency of implementing CCS for tackling global warming[15], CO_2-CDI does not appear as a suitable technology for short-term applications (10 years) in thermal power plants. The IEA and IPPC recommend implementing large CCS plants as soon as possible, which requires mature technology (amine, conventional adsorption). A similar observation seems to apply for other electrochemical systems. Although these systems were first tested with artificial flue gas from thermal plants (15% CO_2), their application is now developing toward direct air capture (DAC) (bipolar membrane[55], faradaic-electro swing[57]). Nevertheless, we believe that electrochemical CO_2 capture technology can play a future role in CCS in combination with other technologies. As renewable energies developed, electrification of various industries and energy sectors developed simultaneously, which is expected to increase in the coming years. Since electrochemical technologies are powered by only electrical energy, they represent a great opportunity to develop future CO_2 capture technology in 15-20 years.

In terms of integration, It would be of interest to invest CO_2-CDI for DAC and investigate its possible integration with electrochemical CO_2 conversion technologies. This development routes could be investigated by adding electroactive materials (catalysts) in the CO_2-CDI cell. We believe that electrochemical systems for CO_2 capture are foreseen to play a major role in our future chemical industry. On the one hand, the continued electrification of the energy sector favors the development of technology powered by electrical power alone. On the other hand, captured CO_2 (from DAC [237]or flue gas) is expected to be utilized by the chemical industry as a carbon source to produce fuel and chemicals.

Last but not least, CO_2-CDI could be developed to store energy and capture CO_2 gas simultaneously. This dual functionality could be an interesting asset for designing future integrated technology for the energy and chemical industries. In principle, CO_2-CDI cells function as supercapacitors, which can store electrical energy. Within a society relying on a large amount of renewable energy, energy storage devices become essential to balance the electrical power through the electrical grid[244–246].

7.6. Future research direction and recommendation

Overall, CO_2-CDI can be defined as a hybrid technology between fuel cell and CDI cell. While fuel cell is a mature technology, which has been actively developed for many years, CDI is still a young technology with untapped potential. CDI technology is

developing fast and is finding continually more applications along with its development (e.g., in water desalination, selective ions removal[174,177], sterilization[117], ammonia recovery[247]). CO_2-CDI is now a new member of the CDI technology family, which contributes to the scientific understanding of CDI cells. CO_2-CDI is still a proof-of-principle concept and requires many steps before being implementing on a larger scale. We propose to focus on the following steps:

1. Develop a continuous CO_2-CDI process

In this thesis, we perform batch experiments in which only the CO_2 adsorption takes place, but not the CO_2 concentration step. Therefore, a continuous CO_2 capture process must be demonstrated to develop the CO_2-CDI technology further. Box 2 shows an example of a cell design in which the CO_2 adsorption and desorption steps co-occur.

Box 2: Example of a continuous process for CO_2-CDI

Fig. 7.10 shows a concept idea of a cell configuration (based on Refs. [226]) where only one single cell composed of an MEA is needed to adsorb and desorb CO_2 simultaneously. In this approach, a chemically modified anode adsorbs anions in the anolyte compartment, while a chemically modified cathode desorbs an anion in the catholyte compartment. This results then into the accumulation of a concentrated CO_2 gas in the cathode compartment and a dilute CO_2 gas in the anode compartment.

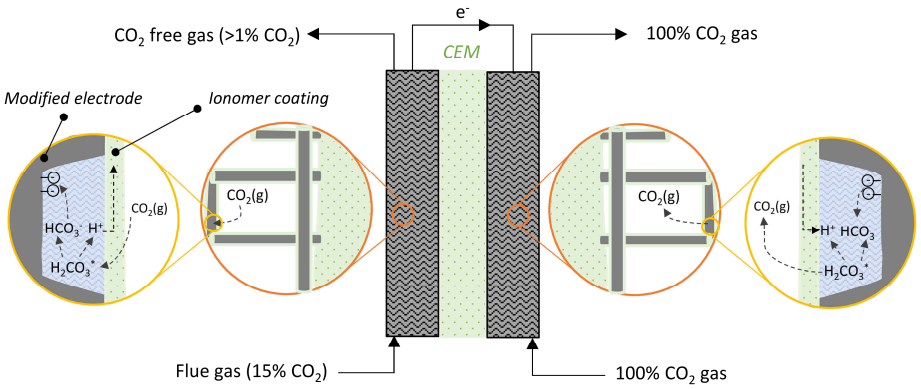

Fig. 7.10: Scheme of a continuous process for CO_2 capture.

2. Improve the MEA cell design

In order to improve the cell resistance and ion selectivity, I recommend optimizing the MEA cell design with coated electrodes by improving the ionomer coating method, introducing highly selective and conductive ionomer materials, and by decreasing the thickness of the electrodes and membranes.

3. Physicochemical investigation of electrosorption mechanisms coupled with material development

Activated carbon electrode showed low ion selectivity toward CO_2-sparged solution (Chapter 4). We investigate to some extent, the possible mechanisms leading to such low selectivity. The electrosorption mechanisms can be better understood by investigating the physicochemical interaction of the electrode material with CO_2, and thereafter, leading to the identification of material properties more selective toward CO_2. Theoretical modeling

can also be a useful tool to gain more scientific insight into the system on a micro- and nanoscale.

4. Explore other alternatives in terms of cell design and electrosorption mechanisms

Exploring other cell architectures and concepts is an alternative approach for CO_2-CDI. For instance, flow-through CDI[76,248], flow-electrode CDI[77,78], desalination battery[133] or intercalation electrodes[167,249,250] could be tested. The latter shows great promises in terms of capacity and energy efficiency, and therefore we recommend investigating first the use of intercalation electrodes for CO_2-CDI. As a matter of fact, novel concepts start to emerge on such systems, e.g., the proton-driven concentration process with intercalation electrodes[64], the faradaic electro-swing adsorption process[57], and supercapacitive swing adsorption[61,107]. Overall, these different technologies share similar principles (all using capacitive or pseudocapacitive electrodes) and show promises for the future of CO_2 capture.

To conclude, our finding shows the proof of principle and first optimization study of CO_2-CDI as a first milestone for the technology. Future developments should focus on interdisciplinary research by combining knowledge in the field of PEM fuel cell, CDI, and electrochemical CO_2 capture (see Fig. 7.11).

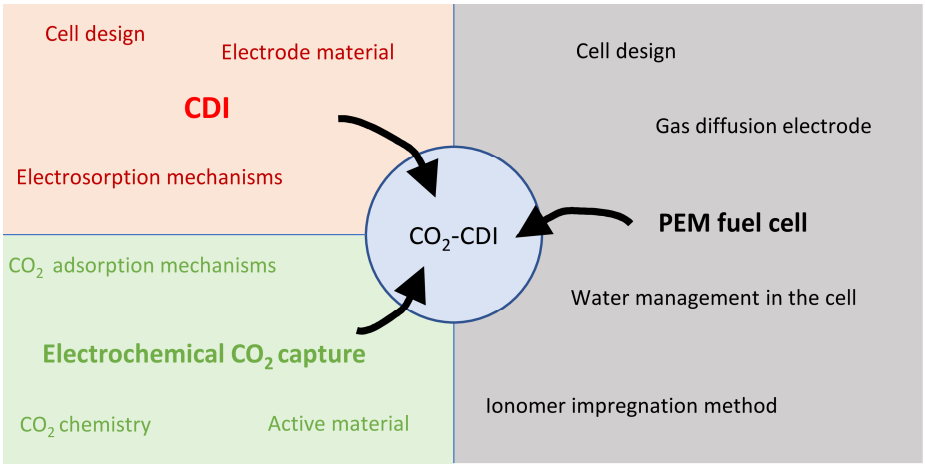

Fig. 7.11: Illustration of interdisciplinary research needed to develop the CO_2-CDI further technology.

Appendix: 4-step CO_2 capture cycle model

In CO_2-CDI, a complete CO_2 capture cycle is composed of 4 different steps (see Table 7.2) in which CO_2 gas is absorbed from flue gas and desorbed in a concentrated gas stream. In practice, a CO_2-CDI cell should be operated in a continuous process. For simplicity reason, we propose to model the CO_2-CDI performance cell in a semi-continuous operation (see Fig. A7.1).

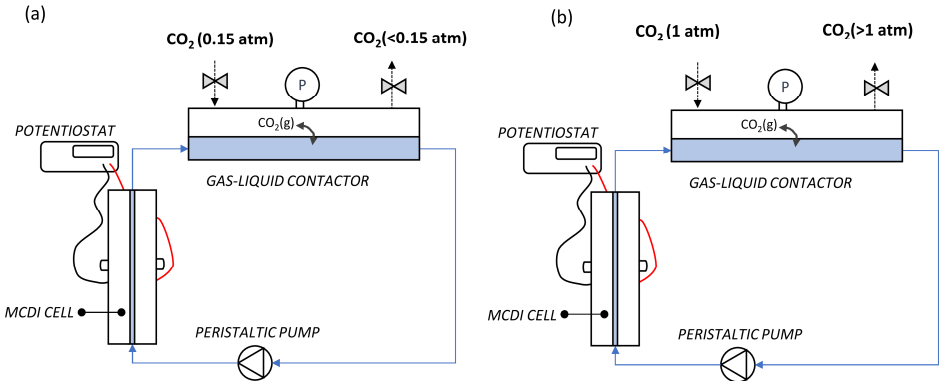

Fig. A7.1: (a) Scheme of the set-up during the charging step and (b) during the discharging step. (a) steps 1 and 2; (b) steps 3 and 4.

The CO_2-CDI cell was modeled as a simple RC circuit in which the cell voltage is calculated as

$$E_{cell} = Q \cdot \left(\frac{1}{m \cdot C} + I \cdot R_{int}\right) \qquad \text{A7.1}$$

where C is the capacitance, I the current density and R_{int} the average internal resistance (normalized per electrode area), Q the amount of electrical charge stored, and m the mass of electrodes. In this model, we used experimental data obtained in Chapter 2 as input parameters for capacitance, the amount of electrical charge stored, and internal resistance. We assumed the same values of electrode capacitance for the charging and discharging steps. Moreover, the internal resistance is defined as a function of the P_{CO_2} according to the following empirical correlation:

$$R_{int} = -1128.4 \cdot P_{CO_2} + 1682 \qquad \text{A7.2}$$

where Rint is the internal resistance (Ω cm^2) and P_{CO_2} the CO_2 partial pressure (in atm). This empirical correlation was obtained by fitting experimental data of internal resistance under different CO_2 partial pressure in CO_2-MCDI (Chapter 2).

The chemical dissociation constant must be included to calculate the concentration of each carbon species in the water and gas phases (see Table A7.1).

Table A7.1: Dissociation constants of chemical equilibria between CO_2 and water

Equation	Equilibrium Constant	Reference
$\mathbf{K_H} = \frac{\mathbf{P_{CO_2(g)}}}{\mathbf{C_{H_2CO_3^*}}}$	$\mathbf{K_H}$=29	25
$\mathbf{K_1} = \frac{\mathbf{C_{HCO_3^-}} \cdot \mathbf{C_{H^+}}}{\mathbf{C_{H_2CO_3^*}}}$	$\mathbf{K_1}$=$10^{-6.35}$	26
$\mathbf{K_2} = \frac{\mathbf{C_{CO_3^{2-}}} \cdot \mathbf{C_{H^+}}}{\mathbf{C_{HCO_3^-}}}$	$\mathbf{K_2}$=$10^{-10.33}$	26
$\mathbf{K_w} = \mathbf{C_{OH^-}} \cdot \mathbf{C_{H^+}}$	$\mathbf{K_w}$=10^{-14}	

The electroneutrality condition holds in the bulk solution ($\sum_i z_i \cdot C_i = 0$). Since CO_2-sparged solution is acidic, HCO_3^- and H^+ are the two dominant ions in solution. Therefore, we can relate the amount of electrode charge stored to the amount of carbon adsorbed as

$$Q = \frac{F}{2} \cdot \Lambda_c \left(n_{HCO_3^-,ad} + n_{H^+,ad}\right) = F \cdot \Lambda_c \left(n_{H_2CO_3,ad}\right) \qquad \text{A7.3}$$

where F is the Faraday constant (96485 C mol^{-1}), $n_{HCO_3^-,ad}$ the amount of bicarbonate adsorbed, $n_{H^+,ad}$ the amount of protons adsorbed, Λ_c the carbon adsorption efficiency (defined in chapter 2). Overall, a mass carbon balance can be set during charging and discharging steps as

$$n_T = \frac{P_{CO_2} \cdot V_g}{R.T} + V_w \cdot (C_{H_2CO_3^*} + C_{HCO_3^-} + C_{CO_3^{2-}}) - \frac{Q}{\Lambda_c \cdot F} \quad \text{A7.4}$$

where n_T is the total amount of carbon in the bulk solution and gas phase, V_g is the gas volume, V_w is the bulk volume, R is the ideal gas constant and T the temperature.

A number of figures of merit are introduced to describe the CO_2-CDI cell performance, i.e., (i) the energy consumption (W^*_{net}), (ii) the CO_2 capture rate (CAR), and (iii) the CO_2 capture capacity (CAC).

$$W^*_{net} = \frac{(R_{int,charge} + R_{int,discharge}) \cdot I \cdot Q}{n_{CO_2,recovered}} \quad \text{A7.5}$$

$$CAR = \frac{n_{CO_2(ad)}}{t_{cycle}} = \frac{n_{CO_2,recovered} \cdot I}{2 \cdot (Q + \frac{t_{OCV}}{I})} \quad \text{A7.6}$$

$$CAC = \frac{n_{CO_2,recovered}}{m} \quad \text{A7.7}$$

where $n_{CO_2,recovered}$ is the amount of CO_2 gas recovered during the discharging step, t_{cycle} the total cycle time, t_{OCV} the time of each open cell voltage step (steps 1-3). Finally, $n_{CO_2,recovered}$ can be calculated as

$$n_{CO_2,recovered} = \frac{(P_{CO_2,discharge} - P_{CO_2,purity}) \cdot V_g}{R * T} \quad \text{A7.8}$$

where $P_{CO_2,discharge}$ is the CO_2 partial pressure obtained at the end of the discharging step, $P_{CO_2,purity}$ is the CO_2 partial pressure of the concentrated gas fed in the cell in step 3, and V_g the gas volume. The change of CO_2 partial pressure was estimated through chemical equilibrium calculations (as shown in Chapters 2 and 4). Several cycles were modeled until reaching an equilibrium cycle. Cycles are shown in Fig. 7.7. Note that if $P_{CO_2,discharge} < P_{CO_2,purity}$, no net CO_2 gas desorption occurs during the discharge step, and therefore no performance calculations are possible. The input values for each parameter are taken from Chapter 2 and are summarized in Table A7.2.

Table A7.2: Input parameters used in the 4-cycles model (obtained from Chapter 2)

Parameter	**Value**	**Units**
Specific capacitance	10.5	F g-1
Electrical charge stored	14.5	C
Current density	0.6	A m-2
Water fraction	0.11	-
Electrode mass	1	g. electrode^{-1}
Gas Volume	0.23	L
Liquid Volume	0.03	L

The water fraction was defined in Chapter 2 as

$$f_w = \frac{V_w \cdot H^{cc}}{V_g + V_w \cdot H^{cc}}. \qquad \text{A7.8}$$

where H^{cc} is the CO_2 solubility constant in water. Note that the CO_2 solubility constant and the Henry's constant (K_H) are related as $H^{cc}=R \cdot T/K_H$.

Summary

Introduction: CO_2-CDI and CO_2-CAPMIX

This Ph.D. thesis explores the use of capacitive processes for two novel applications, i.e., CO_2 capture (CO_2-CDI) and energy recovery from CO_2 emissions (CO_2-CAPMIX). Conventionally, capacitive processes have been applied for water technologies, either to desalinate water streams (Capacitive deionization, CDI) or to harvest electrical energy from salinity gradients (capacitive mixing, CAPMIX). Both CDI and CAPMIX are electrochemical technologies, which operated based on the presence of ions in water. CDI cells adsorb ions from an aqueous solution by alternatively charging and discharging two porous electrodes (electrosorption). CAPMIX cells harvest electrical energy based on the establishment of a membrane potential due to ion electrosorption in porous electrodes.

The major goal of this Ph.D. thesis is to shape CDI and CAPMIX processes from water-based toward CO_2 gas-based technologies. Previous works lead the way toward this transition by demonstrating a proof of concept of CO_2-CAPMIX, and the possibility to form ions from CO_2 gas through reaction with deionized water. Nevertheless, the electrical power generated was strongly limited by the high internal resistance of the CO_2-CAPMIX cell, caused by the low ionic conductivity of CO_2-sparged deionized water. From that starting point, this Ph.D. thesis aims at developing CO_2-CAPMIX further and demonstrating the concept of CO_2-CDI through three different steps, i.e., (i) proof of CO_2 reactive electrosorption and direct gas feeding concepts, (ii) in-depth understanding and (iii) exploration of cell designs to reduce the internal resistance.

Proof-of-principles of CO_2 reactive electrosorption and direct gas feeding (Chapter 2 and 3)

In Chapter 2, we demonstrate for the first time that CO_2 gas can be adsorbed in a membrane capacitive deionization (MCDI) cell through CO_2 reactive electrosorption. The term “reactive” refers to the hydration reaction of CO_2 gas necessary to form bicarbonate ions, and the term “electrosorption” refers to the adsorption of HCO_3^- ions in the porous electrodes. Besides, we characterize the different mechanisms of CO_2 reactive electrosorption through a calculation framework in which we relate the charge efficiency (Λ), conventionally used in CDI, to a new figure of merit, the absorption efficiency (Λ_a). While the charge efficiency is the amount of ions adsorbed to the electrical charge, the absorption efficiency is the amount of CO_2 gas absorbed per electrical charge. Our results show a promising value of $\Lambda_a \approx$ 0.7 (corresponding to $\Lambda \approx$ 0.8), which is close to values expected from conventional MCDI. Furthermore, we report energy consumption values as low as 40-50 $\mathrm{kJ/mol_{CO_2}}$ (at 0.2-0.6 A m^{-2}), which is comparable to other electrochemical CO_2 capture systems. Nevertheless, the CO_2 absorption rate was rather low due to the low

current density applied, which was limited by the internal resistance. Two limiting factors on the energy consumption were then identified, i.e., (i) the high ohmic internal resistance caused by the low ionic conductivity of the CO_2-sparged solution and (ii) the loss of absorption efficiency observed at long charging times.

In **Chapter 3**, we demonstrate that the CO_2 gas can be directly fed into a capacitive cell operated as CO_2-CAPMIX. We refer to this feeding mode as "direct gas feeding" as opposed to "solution feeding," where CO_2 gas is first sparged into deionized water outside the capacitive cell. By feeding the gas directly into the cell, the reactive and electrosorption process directly co-occurs in the capacitive cell, thus avoiding the energy-intensive CO_2-sparging step. The direct gas feeding mode was tested with three different cell designs, i.e., flat MCDI, wire-shaped MCDI, and a membrane electrode assembly (MEA) cell designs. Among the cell design tested, the MEA design, inspired from PEM fuel cells, shows the lowest internal resistance and the higher apparent membrane permselectivity (≈0.9), resulting in power output 100 times higher than conventional MCDI cells (0.05 against 4 mW m^{-2}). Overall, we conclude that an MEA is an interesting alternative to MCDI cell design for capacitive cell design operated for the energy recovery from CO_2 emissions. Moreover, to further improve the power density, other strategies to decrease the internal resistance should still be investigated.

Understanding the role of membranes and electrodes during CO_2 reactive electrosorption (Chapter 4)

To understand the loss of absorption efficiency (Λ_a) with time, we investigate in **Chapter 4** the individual role of the electrodes and ion exchange membranes in CO_2-(M)CDI. The role of membranes was characterized by testing different CDI configurations with and without membranes. Moreover, the role of the electrodes was theoretically investigated by adopting the amphoteric Donnan (amph-D) model for CO_2-CDI. Our result shows that the presence of membranes is essential to keep high values of Λ_a, which has been found two times higher in flat CO_2-MCDI compared to flat CO_2-CDI cell. Besides, between both membranes, we show that the presence of the anion exchange membrane largely contributes to a larger extent to increase Λ_a compared to the cation exchange membrane.

Concerning the behavior of the electrodes, a discrepancy between data and theoretical results was observed, suggesting that other physicochemical mechanisms not included in the amph-D could influence the CO_2 reactive electrosorption process. By including the effect of ionization of surface chemical charge, a better fit was obtained between the model and the data, thus showing the importance of the surface chemical

charge on the CO_2-CDI performance. We suggest investigating other properties, such as ion-size selectivity, ion-valence selectivity, as well as the field dissociation effect. Investigating such properties is also of interest for conventional CDI in mixture solutions or acidic solutions.

Cell designs exploration to reduce the internal resistance (Chapter 3 5 and 6)

Reducing the internal resistance is a crucial challenge to tackle for developing CO_2-CDI and CO_2-CAPMIX. Therefore, **Chapters 3,5** and **6** focus on exploring different cell designs to reduce the internal resistance. In this regard, the internal resistance was separated into two contributions, i.e., ohmic (time-independent) and non-ohmic (time-dependent) resistances.

In Chapter 3 (CO_2-CAPMIX) and Chapter 5 (CO_2-CDI), the internal resistance of a flat MCDI and MEA cell designs are compared. Our main results show that the MEA cell design improves the internal resistance, to a certain extent. In Chapter 5, we demonstrate that the MEA cell design significantly reduces the ohmic contribution of the internal resistance (more than 100 times). Moreover, in chapters 5 and 6, we show that the internal resistance of an MEA cell further decreases (more than five times) by coating the anode and cathode with the same ionomer (more than five times). The reduced internal resistance by coating the electrodes was attributed to a decrease of non-ohmic resistance. Compared to a flat MCDI cell design, power densities 100 times higher were obtained with an MEA cell with coated electrodes, and energy consumption decreased by more than 2.5 times in CO_2-CDI. Nevertheless, the energy performance was lower than expected as the reduced resistance occurs at the cost of lower ion selectivities in the MEA cell design. We recommend investigating the ion selectivity mechanisms in MEA cell design to find suitable strategies to improve the ion selectivity.

Discussion on CO_2-CDI and CO_2-CAPMIX (Chapter 7)

In **Chapter 7,** all the main results from previous chapters are summarized and further discussed. The discussion is mostly focused on internal resistance and ion selectivity (i.e., absorption efficiency in CO_2-CDI and membrane potential in CO_2-CAPMIX), and possible strategies to improve them. Furthermore, we share and discuss our long-term perspective for both technologies.

Bibliography

(1) Etheridge, D. M.; Steele, L. P.; Langenfelds, R. L.; Francey, R. J.; Barnola, J. M.; Morgan, V. I. In Atmospheric the Last 1000 Years from Air in Antarctic Ice and Firn. *J. Geophys. Res.* **1996**, *101* (D2), 4115–4128. https://doi.org/10.1029/95JD03410.

(2) Brohan, P.; Kennedy, J. J.; Harris, I.; Tett, S. F. B.; Jones, P. D. Uncertainty Estimates in Regional and Global Observed Temperature Changes: A New Data Set from 1850. *J. Geophys. Res. Atmos.* **2006**, *111* (12). https://doi.org/10.1029/2005JD006548.

(3) Lenssen, N. J. L.; Schmidt, G. A.; Hansen, J. E.; Menne, M. J.; Persin, A.; Ruedy, R.; Zyss, D. Improvements in the GISTEMP Uncertainty Model. *J. Geophys. Res. Atmos.* **2019**, *124* (12), 6307–6326. https://doi.org/10.1029/2018JD029522.

(4) Ruedy, R.; Schmidt, G.; Persin, A.; Sato, M.; Lo, K. NASA GISS Surface Temperature (GISTEMP) Analysis.

(5) Crippa, M.; Oreggioni, G.; Guizzardi, D.; Muntean, M.; Schaaf, E.; Lo Vullo, E.; Solazzo, E.; Monforti-Ferrario, F.; Olivier, J. G. J.; Vignati, E. *Fossil CO2 and GHG Emissions of All World Countries-2019 Report*; Luxembourg, 2019.

(6) Noaa. https://www.esrl.noaa.gov/gmd/dv/data/.

(7) Root, T. L.; Price, J. T.; Hall, K. R.; Schneider, S. H.; Rosenzweigk, C.; Pounds, J. A. Fingerprints of Global Warming on Wild Animals and Plants Terry. *Nature* **2003**, *421*, 57–60. https://doi.org/10.1142/9781848162044_0011.

(8) Mousavi, M. E.; Irish, J. L.; Frey, A. E.; Olivera, F.; Edge, B. L. Global Warming and Hurricanes: The Potential Impact of Hurricane Intensification and Sea Level Rise on Coastal Flooding. *Clim. Change* **2011**, *104* (3–4), 575–597. https://doi.org/10.1007/s10584-009-9790-0.

(9) Jevrejeva, S.; Moore, J. C.; Grinsted, A. How Will Sea Level Respond to Changes in Natural and Anthropogenic Forcings by 2100? *Geophys. Res. Lett.* **2010**, *37* (7), 0–1. https://doi.org/10.1029/2010GL042947.

(10) Zhang, K.; Douglas, B. C.; Leatherman, S. P. Global Warming and Coastal Erosion. *Clim. Change* **2004**, *64* (1–2), 41–58. https://doi.org/10.1023/B:CLIM.0000024690.32682.48.

(11) Masson-Delmotte, V., P. Zhai, H.-O. Pörtner, D. Roberts, J. Skea, P. R. S.; A. Pirani, W. Moufouma-Okia, C. Péan, R. Pidcock, S. Connors, J.B.R. Matthews, Y. Chen, X. Zhou, M. I. G.; E. Lonnoy, T. Maycock, M. Tignor, and T. W. *ICCP Report (Summary for Policymarkers)*; 2018.

(12) United Nations. *Report of the Conference of the Parties on Its Twenty-First Session, Held in Paris from 30 November to 13 December 2015 Addendum Contents Part Two: Action Taken by the Conference of the Parties at Its Twenty-First Session Decisions*; 2016; Vol. 10.

(13) International, I. E. A.; Agency, E. Energy Technology Perspectives 2016. **2017**. https://doi.org/10.1787/energy_tech-2017-en.

(14) International Energy Agency. Energy Technology Perspectives 2017: Catalysing Energy Technology Transformations. *Int. Energy Agency Publ.* **2017**, 371. https://doi.org/10.1787/energy_tech-2014-en.

(15) Bui, M.; Adjiman, C. S.; Bardow, A.; Anthony, E. J.; Boston, A.; Brown, S.; Fennell, P. S.; Fuss, S.; Galindo, A.; Hackett, L. A.; Hallett, J. P.; Herzog, H. J.; Jackson, G.; Kemper, J.; Krevor, S.; Maitland, G. C.; Matuszewski, M.; Metcalfe, I. S.; Petit, C.; Puxty, G.; Reimer, J.; Reiner, D. M.; Rubin, E. S.; Scott, S. A.; Shah, N.; Smit, B.; Trusler, J. P. M.; Webley, P.; Wilcox, J.; Mac Dowell, N. Carbon Capture and Storage (CCS): The Way Forward. *Energy Environ. Sci.* **2018**, *11* (5), 1062–1176. https://doi.org/10.1039/c7ee02342a.

(16) Suss, M. E.; Porada, S.; Sun, X.; Biesheuvel, P. M.; Yoon, J.; Presser, V. Water Desalination via Capacitive Deionization: What Is It and What Can We Expect from It? *Energy Environ. Sci.* **2015**, *8* (8), 2296–2319. https://doi.org/10.1039/c5ee00519a.

(17) Porada, S.; Zhao, R.; Van Der Wal, A.; Presser, V.; Biesheuvel, P. M. Review on the Science and Technology of Water Desalination by Capacitive Deionization. *Prog. Mater. Sci.* **2013**,

58 (8), 1388–1442. https://doi.org/10.1016/j.pmatsci.2013.03.005.

(18) Liu, F.; Schaetzle, O.; Sales, B. B.; Saakes, M.; Buisman, C. J. N.; Hamelers, H. V. M. Effect of Additional Charging and Current Density on the Performance of Capacitive Energy Extraction Based on Donnan Potential. *Energy Environ. Sci.* **2012**, *5* (9), 8642–8650. https://doi.org/10.1039/c2ee21548a.

(19) Liu, F.; Donkers, T. F. W.; Wagterveld, R. M.; Schaetzle, O.; Saakes, M.; Buisman, C. J. N.; Hamelers, H. V. M. Parallel Up-Scaling of Capacitive Mixing (CapMix) System Enhances the Specific Performance. *Electrochim. Acta* **2016**, *187*, 104–112. https://doi.org/10.1016/j.electacta.2015.10.196.

(20) Fernández, M. M.; Wagterveld, R. M.; Ahualli, S.; Liu, F.; Delgado, A. V.; Hamelers, H. V. M. Polyelectrolyte-versus Membrane-Coated Electrodes for Energy Production by Capmix Salinity Exchange Methods. *J. Power Sources* **2016**, *302*, 387–393. https://doi.org/10.1016/j.jpowsour.2015.10.076.

(21) Marino, M.; Misuri, L.; Jiménez, M. L.; Ahualli, S.; Kozynchenko, O.; Tennison, S.; Bryjak, M.; Brogioli, D. Modification of the Surface of Activated Carbon Electrodes for Capacitive Mixing Energy Extraction from Salinity Differences. *J. Colloid Interface Sci.* **2014**, *436*, 146–153. https://doi.org/10.1016/j.jcis.2014.08.070.

(22) Burheim, O. S.; Liu, F.; Sales, B. B.; Schaetzle, O.; Buisman, C. J. N.; Hamelers, H. V. M. Faster Time Response by the Use of Wire Electrodes in Capacitive Salinity Gradient Energy Systems. *J. Phys. Chem. C* **2012**, *116* (36), 19203–19210. https://doi.org/10.1021/jp306522g.

(23) Hamelers, H. V. M.; Schaetzle, O.; Paz-García, J. M.; Biesheuvel, P. M.; Buisman, C. J. N. Harvesting Energy from CO_2 Emissions. *Environ. Sci. Technol. Lett.* **2014**, *1* (1), 31–35. https://doi.org/10.1021/ez4000059.

(24) Wilhelm, E.; Battino, R.; Wilcock, R. J. Low-Pressure Solubility of Gases in Liquid Water. *Chem. Rev.* **1977**, *77* (2), 219–262. https://doi.org/10.1021/cr60306a003.

(25) Sander, R. Compilation of Henry's Law Constants (Version 4.0) for Water as Solvent. *Atmos. Chem. Phys.* **2015**, *15* (8), 4399–4981. https://doi.org/10.5194/acp-15-4399-2015.

(26) Wang, X.; Conway, W.; Burns, R.; McCann, N.; Maeder, M. Comprehensive Study of the Hydration and Dehydration Reactions of Carbon Dioxide in Aqueous Solution. *J. Phys. Chem. A* **2010**, *114* (4), 1734–1740. https://doi.org/10.1021/jp909019u.

(27) Kim, T.; Logan, B. E.; Gorski, C. A. A PH-Gradient Flow Cell for Converting Waste CO2into Electricity. *Environ. Sci. Technol. Lett.* **2017**, *4* (2), 49–53. https://doi.org/10.1021/acs.estlett.6b00467.

(28) Paz-Garcia, J. M.; Dykstra, J. E.; Biesheuvel, P. M.; Hamelers, H. V. M. Energy from CO2using Capacitive Electrodes - A Model for Energy Extraction Cycles. *J. Colloid Interface Sci.* **2015**, *442*, 103–109. https://doi.org/10.1016/j.jcis.2014.11.045.

(29) Paz-Garcia, J. M.; Schaetzle, O.; Biesheuvel, P. M.; Hamelers, H. V. M. Energy from CO2using Capacitive Electrodes - Theoretical Outline and Calculation of Open Circuit Voltage. *J. Colloid Interface Sci.* **2014**, *418*, 200–207. https://doi.org/10.1016/j.jcis.2013.11.081.

(30) Laboratory, N. E. T. Carbon capture and storage projects (Laboratory, National Energy Technology) https://www.netl.doe.gov/coal/carbon-storage/worldwide-ccs-database.

(31) Wagner, E. D.; Hsu, K. M.; Lagunas, A.; Mitch, W. A.; Plewa, M. J. Comparative Genotoxicity of Nitrosamine Drinking Water Disinfection Byproducts in Salmonella and Mammalian Cells. *Mutat. Res. - Genet. Toxicol. Environ. Mutagen.* **2012**, *741* (1–2), 109–115. https://doi.org/10.1016/j.mrgentox.2011.11.006.

(32) Lepaumier, H.; Picq, D.; Carrette, P. L. New Amines for CO2 Capture. II. Oxidative Degradation Mechanisms. *Ind. Eng. Chem. Res.* **2009**, *48* (20), 9068–9075. https://doi.org/10.1021/ie9004749.W

(33) Martin, S.; Lepaumier, H.; Picq, D.; Kittel, J.; De Bruin, T.; Faraj, A.; Carrette, P. L. New Amines for CO 2 Capture. IV. Degradation, Corrosion, and Quantitative Structure Property Relationship Model. *Ind. Eng. Chem. Res.* **2012**, *51* (18), 6283–6289. https://doi.org/10.1021/ie2029877.

(34) Da Silva, E. F.; Lepaumier, H.; Grimstvedt, A.; Vevelstad, S. J.; Einbu, A.; Vernstad, K.; Svendsen, H. F.; Zahlsen, K. Understanding 2-Ethanolamine Degradation in Postcombustion CO 2 Capture. *Ind. Eng. Chem. Res.* **2012**, *51* (41), 13329–13338. https://doi.org/10.1021/ie300718a.

(35) Bui, M.; Adjiman, C. S.; Bardow, A.; Anthony, E. J.; Boston, A.; Brown, S.; Fennell, P. S.; Fuss, S.; Galindo, A.; Hackett, L. A.; Hallett, J. P.; Herzog, H. J.; Jackson, G.; Kemper, J.; Krevor, S.; Maitland, G. C.; Matuszewski, M.; Metcalfe, I. S.; Petit, C.; Puxty, G.; Reimer, J.; Reiner, D. M.; Rubin, E. S.; Scott, S. A.; Shah, N.; Smit, B.; Trusler, J. P. M.; Webley, P.; Wilcox, J.; Mac Dowell, N. Carbon Capture and Storage (CCS): The Way Forward. *Energy Environ. Sci.* **2018**, *11* (5), 1062–1176. https://doi.org/10.1039/c7ee02342a.

(36) Younas, M.; Sohail, M.; Leong, L. K.; Bashir, M. J.; Sumathi, S. Feasibility of CO2 Adsorption by Solid Adsorbents: A Review on Low-Temperature Systems. *Int. J. Environ. Sci. Technol.* **2016**, *13* (7), 1839–1860. https://doi.org/10.1007/s13762-016-1008-1.

(37) Creamer, A. E.; Gao, B. Carbon-Based Adsorbents for Postcombustion CO2 Capture: A Critical Review. *Environ. Sci. Technol.* **2016**, *50* (14), 7276–7289. https://doi.org/10.1021/acs.est.6b00627.

(38) Yu, C. H.; Huang, C. H.; Tan, C. S. A Review of CO2 Capture by Absorption and Adsorption. *Aerosol Air Qual. Res.* **2012**, *12* (5), 745–769. https://doi.org/10.4209/aaqr.2012.05.0132.

(39) Grande, C. A.; Rodrigues, A. E. Electric Swing Adsorption for CO2 Removal from Flue Gases. *Int. J. Greenh. Gas Control* **2008**, *2* (2), 194–202. https://doi.org/10.1016/S1750-5836(07)00116-8.

(40) Kremer, J.; Galloy, A.; Ströhle, J.; Epple, B. Continuous CO2 Capture in a 1-MWth Carbonate Looping Pilot Plant. *Chem. Eng. Technol.* **2013**, *36* (9), 1518–1524. https://doi.org/10.1002/ceat.201300084.

(41) Arias, B.; Diego, M. E.; Abanades, J. C.; Lorenzo, M.; Diaz, L.; Martínez, D.; Alvarez, J.; Sánchez-Biezma, A. Demonstration of Steady State CO2 Capture in a 1.7MWth Calcium Looping Pilot. *Int. J. Greenh. Gas Control* **2013**, *18*, 237–245. https://doi.org/10.1016/j.ijggc.2013.07.014.

(42) Hanak, D. P.; Biliyok, C.; Anthony, E. J.; Manovic, V. Modelling and Comparison of Calcium Looping and Chemical Solvent Scrubbing Retrofits for CO2 Capture from Coal-Fired Power Plant. *Int. J. Greenh. Gas Control* **2015**, *42*, 226–236. https://doi.org/10.1016/j.ijggc.2015.08.003.

(43) Hills, T.; Leeson, D.; Florin, N.; Fennell, P. Carbon Capture in the Cement Industry: Technologies, Progress, and Retrofitting. *Environ. Sci. Technol.* **2016**, *50* (1), 368–377. https://doi.org/10.1021/acs.est.5b03508.

(44) Du, N.; Park, H. B.; Dal-Cin, M. M.; Guiver, M. D. Advances in High Permeability Polymeric Membrane Materials for CO 2 Separations. *Energy Environ. Sci.* **2012**, *5* (6), 7306–7322. https://doi.org/10.1039/c1ee02668b.

(45) Robeson, L. M. The Upper Bound Revisited. *J. Memb. Sci.* **2008**, *320* (1–2), 390–400. https://doi.org/10.1016/j.memsci.2008.04.030.

(46) Rafiq, S.; Deng, L.; Ha, M. Role of Facilitated Transport Membranes and Composite Membranes for Efficient CO 2 Capture – A Review. **2016**, No. 2, 68–85. https://doi.org/10.1002/cben.201500013.

(47) Khalilpour, R.; Mumford, K.; Zhai, H.; Abbas, A.; Stevens, G.; Rubin, E. S. Membrane-Based Carbon Capture from Fl Ue Gas : A Review. *J. Clean. Prod.* **2015**, *103*, 286–300.

https://doi.org/10.1016/j.jclepro.2014.10.050.

(48) Rheinhardt, J. H.; Singh, P.; Tarakeshwar, P.; Buttry, D. A. Electrochemical Capture and Release of Carbon Dioxide. **2017**. https://doi.org/10.1021/acsenergylett.6b00608.

(49) Eisaman, M. D.; Alvarado, L.; Larner, D.; Wang, P.; Garg, B.; Littau, K. A. Environmental Science. **2011**, *4* (4). https://doi.org/10.1039/c0ee00303d.

(50) HUEBSCHER RG; BABINSKY AD. Electrochemical Concentration and Separation of Carbon Dioxide for Advanced Life Support Systems. Carbonation Cell System. *SAE-Paper 690640* **1969**, 2164–2170.

(51) Mastropasqua, L.; Pierangelo, L.; Spinelli, M.; Romano, M. C.; Campanari, S.; Consonni, S. Molten Carbonate Fuel Cells Retrofits for CO2 Capture and Enhanced Energy Production in the Steel Industry. *Int. J. Greenh. Gas Control* **2019**, *88* (October 2018), 195–208. https://doi.org/10.1016/j.ijggc.2019.05.033.

(52) Campanari, S.; Chiesa, P.; Manzolini, G. CO2 Capture from Combined Cycles Integrated with Molten Carbonate Fuel Cells. *Int. J. Greenh. Gas Control* **2010**, *4* (3), 441–451. https://doi.org/10.1016/j.ijggc.2009.11.007.

(53) Datta, S.; Henry, M. P.; Lin, Y. J.; Fracaro, A. T.; Millard, C. S.; Snyder, S. W.; Stiles, R. L.; Shah, J.; Yuan, J.; Wesoloski, L.; Dorner, R. W.; Carlson, W. M. Electrochemical CO 2 Capture Using Resin-Wafer Electrodeionization. **2013**.

(54) Eisaman, M. D.; Alvarado, L.; Larner, D.; Wang, P.; Littau, K. A. CO 2 Desorption Using High-Pressure Bipolar Membrane Electrodialysis. *Energy Environ. Sci.* **2011**, *4* (10), 4031–4037. https://doi.org/10.1039/c1ee01336j.

(55) Sabatino, F.; Mehta, M.; Grimm, A.; Gazzani, M.; Gallucci, F.; Kramer, G. J.; van Sint Annaland, M. Evaluation of a Direct Air Capture Process Combining Wet Scrubbing and Bipolar Membrane Electrodialysis. *Ind. Eng. Chem. Res.* **2020**. https://doi.org/10.1021/acs.iecr.9b05641.

(56) Xie, H.; Wu, Y.; Liu, T.; Wang, F.; Chen, B.; Liang, B. Low-Energy-Consumption Electrochemical CO2 Capture Driven by Biomimetic Phenazine Derivatives Redox Medium. *Appl. Energy* **2020**, *259* (August), 114119. https://doi.org/10.1016/j.apenergy.2019.114119.

(57) Voskian, S.; Hatton, T. A. Faradaic Electro-Swing Reactive Adsorption for CO 2 Capture . *Energy Environ. Sci.* **2019**, 3530–3547. https://doi.org/10.1039/c9ee02412c.

(58) Kokoszka, B.; Jarrah, N. K.; Liu, C.; Moore, D. T.; Landskron, K. Supercapacitive Swing Adsorption of Carbon Dioxide. *Angew. Chemie - Int. Ed.* **2014**, *53* (14), 3772–3775. https://doi.org/10.1002/ange.201310308.

(59) Liu, C.; Landskron, K. Design, Construction, and Testing of a Supercapacitive Swing Adsorption Module for CO_2 Separation. *Chem. Commun.* **2017**, *53* (26), 3661–3664. https://doi.org/10.1039/C7CC01055A.

(60) Zhu, S.; Ma, K.; Landskron, K. M. Relationships between the Charge-Discharge Methods and the Performance of a Supercapacitive Swing Adsorption Module for CO2Separation. *J. Phys. Chem. C* **2018**, No. July. https://doi.org/10.1021/acs.jpcc.8b03968.

(61) Zhu, S.; Li, J.; Toth, A.; Landskron, K. Relationships between Electrolyte Concentration and the Supercapacitive Swing Adsorption of CO2. *ACS Appl. Mater. Interfaces* **2019**, *11*, 21489–21495. https://doi.org/10.1021/acsami.9b03598.

(62) Taniguchi, I.; Yamada, T. Low Energy CO2 Capture by Electrodialysis. *Energy Procedia* **2017**, *114* (November 2016), 1615–1620. https://doi.org/10.1016/j.egypro.2017.03.1902.

(63) Kim, S.; Choi, M.; Kang, J. S.; Joo, H.; Park, B. H.; Sung, Y. E.; Yoon, J. Electrochemical Recovery of LiOH from Used CO2 Adsorbents. *Catal. Today* **2019**, No. June, 1–7. https://doi.org/10.1016/j.cattod.2019.06.056.

(64) Rahimi, M.; Wang, M.; Hatton, T. A.; Rahimi, M.; Catalini, G.; Hariharan, S.; Wang, M.;

Puccini, M. Carbon Dioxide Capture Using an Electrochemically Driven Proton Concentration Process Carbon Dioxide Capture Using an Electrochemically Driven Proton Concentration Process. *Cell Reports Phys. Sci.* **2020**, 100033. https://doi.org/10.1016/j.xcrp.2020.100033.

(65) Watkins, J. D.; Siefert, N. S.; Zhou, X.; Myers, C. R.; Kitchin, J. R.; Hopkinson, D. P.; Nulwala, H. B. Redox-Mediated Separation of Carbon Dioxide from Flue Gas. *Energy and Fuels* **2015**, *29* (11), 7508–7515. https://doi.org/10.1021/acs.energyfuels.5b01807.

(66) Gurkan, B.; Simeon, F.; Hatton, T. A. Quinone Reduction in Ionic Liquids for Electrochemical CO2 Separation. *ACS Sustain. Chem. Eng.* **2015**, *3* (7), 1394–1405. https://doi.org/10.1021/acssuschemeng.5b00116.

(67) Ishida, H.; Ohba, T.; Yamaguchi, T.; Ohkubo, K. Interaction between CO 2 and Electrochemically Reduced Species of N-Propyl-4,4′-Bipyridinium Cation . *Chemistry Letters*. 1994, pp 905–908. https://doi.org/10.1246/cl.1994.905.

(68) Ranjan, R.; Olson, J.; Singh, P.; Lorance, E. D.; Buttry, D. A.; Gould, I. R. Reversible Electrochemical Trapping of Carbon Dioxide Using 4,4′-Bipyridine That Does Not Require Thermal Activation. *J. Phys. Chem. Lett.* **2015**, *6* (24), 4943–4946. https://doi.org/10.1021/acs.jpclett.5b02220.

(69) Lee, J. B.; Park, K. K.; Eum, H. M.; Lee, C. W. Desalination of a Thermal Power Plant Wastewater by Membrane Capacitive Deionization. *Desalination* **2006**, *196* (1–3), 125–134. https://doi.org/10.1016/j.desal.2006.01.011.

(70) Biesheuvel, P. M.; Zhao, R.; Porada, S.; van der Wal, A. Theory of Membrane Capacitive Deionization Including the Effect of the Electrode Pore Space. *J. Colloid Interface Sci.* **2011**, *360* (1), 239–248. https://doi.org/10.1016/j.jcis.2011.04.049.

(71) Hassanvand, A.; Chen, G. Q.; Webley, P. A.; Kentish, S. E. A Comparison of Multicomponent Electrosorption in Capacitive Deionization and Membrane Capacitive Deionization. *Water Res.* **2018**, *131*, 100–109. https://doi.org/10.1016/j.watres.2017.12.015.

(72) Zhao, R.; Biesheuvel, P. M.; Van Der Wal, A. Energy Consumption and Constant Current Operation in Membrane Capacitive Deionization. *Energy Environ. Sci.* **2012**, *5* (11), 9520–9527. https://doi.org/10.1039/c2ee21737f.

(73) Tang, W.; He, D.; Zhang, C.; Kovalsky, P.; Waite, T. D. Comparison of Faradaic Reactions in Capacitive Deionization (CDI) and Membrane Capacitive Deionization (MCDI) Water Treatment Processes. *Water Res.* **2017**, *120*, 229–237. https://doi.org/10.1016/j.watres.2017.05.009.

(74) Długołecki, P.; Van Der Wal, A. Energy Recovery in Membrane Capacitive Deionization. *Environ. Sci. Technol.* **2013**, *47* (9), 4904–4910. https://doi.org/10.1021/es3053202.

(75) Wang, L.; Lin, S. Mechanism of Selective Ion Removal in Membrane Capacitive Deionization for Water Softening. *Environ. Sci. Technol.* **2019**. https://doi.org/10.1021/acs.est.9b00655.

(76) Suss, M. E.; Baumann, T. F.; Bourcier, W. L.; Spadaccini, C. M.; Rose, K. A.; Santiago, J. G.; Stadermann, M. Capacitive Desalination with Flow-through Electrodes. *Energy Environ. Sci.* **2012**, *5*, 9511–9519. https://doi.org/10.1039/c2ee21498a.

(77) Nativ, P.; Badash, Y.; Gendel, Y. New Insights into the Mechanism of Flow-Electrode Capacitive Deionization. *Electrochem. commun.* **2017**, *76*, 24–28. https://doi.org/10.1016/j.elecom.2017.01.008.

(78) He, C.; Ma, J.; Zhang, C.; Song, J.; Waite, T. D. Short-Circuited Closed-Cycle Operation of Flow-Electrode CDI for Brackish Water Softening. *Environ. Sci. Technol.* **2018**, *52* (16), 9350–9360. https://doi.org/10.1021/acs.est.8b02807.

(79) Mubita, T. M.; Porada, S.; Biesheuvel, P. M.; van der Wal, A.; Dykstra, J. E. Capacitive Deionization with Wire-Shaped Electrodes. *Electrochim. Acta* **2018**, *270*, 165–173. https://doi.org/10.1016/j.electacta.2018.03.082.

(80) Wal, V. Der. 2011_J.Colloid.Int.Sci._Theory of Membrane Capacitive Deionization Including the Effect of the Electrode Pore Space.Pdf. **2011**, *360* (2011).

(81) Yang, K. L.; Ying, T. Y.; Yiacoumi, S.; Tsouris, C.; Vittoratos, E. S. Electrosorption of Ions from Aqueous Solutions by Carbon Aerogel: An Electrical Double-Layer Model. *Langmuir* **2001**, *17* (6), 1961–1969. https://doi.org/10.1021/la001527s.

(82) Ying, T. Y.; Yang, K. L.; Yiacoumi, S.; Tsouris, C. Electrosorption of Ions from Aqueous Solutions by Nanostructured Carbon Aerogel. *J. Colloid Interface Sci.* **2002**, *250* (1), 18–27. https://doi.org/10.1006/jcis.2002.8314.

(83) Porada, S.; Weinstein, L.; Dash, R.; Van Der Wal, A.; Bryjak, M.; Gogotsi, Y.; Biesheuvel, P. M. Water Desalination Using Capacitive Deionization with Microporous Carbon Electrodes. *ACS Appl. Mater. Interfaces* **2012**, *4* (3), 1194–1199. https://doi.org/10.1021/am201683j.

(84) Biesheuvel, P. M.; Porada, S.; Levi, M.; Bazant, M. Z. Attractive Forces in Microporous Carbon Electrodes for Capacitive Deionization. *J. Solid State Electrochem.* **2014**, *18* (5), 1365–1376. https://doi.org/10.1007/s10008-014-2383-5.

(85) Biesheuvel, P. M.; Hamelers, H. V. M.; Suss, M. E. Theory of Water Desalination by Porous Electrodes with Immobile Chemical Charge. *Colloids Interface Sci. Commun.* **2015**, *9*, 1–5. https://doi.org/10.1016/j.colcom.2015.12.001.

(86) Biesheuvel, P. M. Activated Carbon Is an Electron-Conducting Amphoteric Ion Adsorbent. *arXiv* **2015**, No. October, 1–9.

(87) Zhao, R.; Biesheuvel, P. M.; Miedema, H.; Bruning, H.; van der Wal, A. Charge Efficiency: A Functional Tool to Probe the Double-Layer Structure inside of Porous Electrodes and Application in the Modeling of Capacitive Deionization. *J. Phys. Chem. Lett.* **2010**, *1* (1), 205–210. https://doi.org/10.1021/jz900154h.

(88) Güler, E.; Elizen, R.; Vermaas, D. A.; Saakes, M.; Nijmeijer, K. Performance-Determining Membrane Properties in Reverse Electrodialysis. *J. Memb. Sci.* **2013**, *446*, 266–276. https://doi.org/10.1016/j.memsci.2013.06.045.

(89) Długołecki, P.; Anet, B.; Metz, S. J.; Nijmeijer, K.; Wessling, M. Transport Limitations in Ion Exchange Membranes at Low Salt Concentrations. *J. Memb. Sci.* **2010**, *346* (1), 163–171. https://doi.org/10.1016/j.memsci.2009.09.033.

(90) Kingsbury, R. S.; Flotron, S.; Zhu, S.; Call, D. F.; Coronell, O. Junction Potentials Bias Measurements of Ion Exchange Membrane Permselectivity. *Environ. Sci. Technol.* **2018**, *52* (8), 4929–4936. https://doi.org/10.1021/acs.est.7b05317.

(91) Nikonenko, V.; Lebedev, K.; Manzanares, J. A.; Pourcelly, G. Modelling the Transport of Carbonic Acid Anions through Anion-Exchange Membranes. *Electrochim. Acta* **2003**, *48* (24), 3639–3650. https://doi.org/10.1016/S0013-4686(03)00485-7.

(92) Alias, N.; Mohamad, A. A. Advances of Aqueous Rechargeable Lithium-Ion Battery: A Review. *J. Power Sources* **2015**, *274*, 237–251. https://doi.org/10.1016/j.jpowsour.2014.10.009.

(93) Tornow, C. E.; Thorson, M. R.; Ma, S.; Gewirth, A. A.; Kenis, P. J. A. Nitrogen-Based Catalysts for the Electrochemical Reduction of CO2 to CO. *J. Am. Chem. Soc.* **2012**, No. 134, 19520–19523.

(94) Kas, R.; Kortlever, R.; Yilmaz, H.; Koper, M. T. M.; Mul, G. Manipulating the Hydrocarbon Selectivity of Copper Nanoparticles in CO2 Electroreduction by Process Conditions. *ChemElectroChem* **2015**, *2* (3), 354–358. https://doi.org/10.1002/celc.201402373.

(95) Ma, S.; Sadakiyo, M.; Luo, R.; Heima, M.; Yamauchi, M.; Kenis, P. J. A. One-Step Electrosynthesis of Ethylene and Ethanol from CO2 in an Alkaline Electrolyzer. *J. Power Sources* **2016**, *301*, 219–228. https://doi.org/10.1016/j.jpowsour.2015.09.124.

(96) Bansode, A.; Urakawa, A. Towards Full One-Pass Conversion of Carbon Dioxide to Methanol and Methanol-Derived Products. *J. Catal.* **2014**, *309*, 66–70.

https://doi.org/10.1016/j.jcat.2013.09.005.

(97) Zander, S.; Kunkes, E. L.; Schuster, M. E.; Schumann, J.; Weinberg, G.; Teschner, D.; Jacobsen, N.; Schlögl, R.; Behrens, M. The Role of the Oxide Component in the Development of Copper Composite Catalysts for Methanol Synthesis. *Angew. Chemie - Int. Ed.* **2013**, *52* (25), 6536–6540. https://doi.org/10.1002/anie.201301419.

(98) Liu, Z.; Wang, L.; Kong, X.; Li, P.; Yu, J.; Rodrigues, A. E. Onsite CO 2 Capture from Flue Gas by an Adsorption Process in a Coal-Fired Power Plant. *Ind. Eng. Chem. Res.* **2012**, *51* (21), 7355–7363. https://doi.org/10.1021/ie3005308.

(99) Ho, M. T.; Allinson, G. W.; Wiley, D. E. Reducing the Cost of CO2 Capture from Flue Gases Using Pressure Swing Adsorption. *Ind. Eng. Chem. Res.* **2008**, *47* (14), 4883–4890. https://doi.org/10.1021/ie070831e.

(100) Lu, C.; Bai, H.; Wu, B.; Su, F.; Hwang, J. F. Comparative Study of CO2 Capture by Carbon Nanotubes, Activated Carbons, and Zeolites. *Energy and Fuels* **2008**, *22* (5), 3050–3056. https://doi.org/10.1021/ef8000086.

(101) Conway, W.; Wang, X.; Fernandes, D.; Burns, R.; Puxty, G.; Maeder, M. Comprehensive Kinetic and Thermodynamic Study of the Reactions of CO 2 (Aq) and HCO 3 À with Monoethanolamine (MEA) in Aqueous Solution. **2011**, *2*, 14340–14349.

(102) Dugas, R.; Rochelle, G. Absorption and Desorption Rates of Carbon Dioxide with Monoethanolamine and Piperazine. *Energy Procedia* **2009**, *1* (1), 1163–1169. https://doi.org/10.1016/j.egypro.2009.01.153.

(103) Rochelle, G. T. Amine Scrubbing for CO2 Capture. *Science (80-.).* **2009**, *325* (5948), 1652–1654. https://doi.org/10.1126/science.1176731.

(104) Ramasubramanian, K.; Verweij, H.; Winston Ho, W. S. Membrane Processes for Carbon Capture from Coal-Fired Power Plant Flue Gas: A Modeling and Cost Study. *J. Memb. Sci.* **2012**, *421–422*, 299–310. https://doi.org/10.1016/j.memsci.2012.07.029.

(105) Pera-Titus, M. Porous Inorganic Membranes for CO2 Capture: Present and Prospects. *Chem. Rev.* **2014**, *114* (2), 1413–1492. https://doi.org/10.1021/cr400237k.

(106) Tuinier, M. J.; Annaland, M. V. S.; Kramer, G. J.; Kuipers, J. A. M. Cryogenic CO 2 Capture Using Dynamically Operated Packed Beds. *Chem. Eng. Sci.* **2010**, *65* (1), 114–119. https://doi.org/10.1016/j.ces.2009.01.055.

(107) Kokoszka, B.; Jarrah, N. K.; Liu, C.; Moore, D. T.; Landskron, K. Supercapacitive Swing Adsorption of Carbon Dioxide. *Angew. Chemie - Int. Ed.* **2014**, *53* (14), 3698–3701. https://doi.org/10.1002/anie.201310308.

(108) Yadav, R.; Wanjari, S.; Prabhu, C.; Kumar, V.; Labhsetwar, N.; Satyanarayanan, T.; Kotwal, S.; Rayalu, S. Immobilized Carbonic Anhydrase for the Biomimetic Carbonation Reaction. *Energy and Fuels* **2010**, *24* (11), 6198–6207. https://doi.org/10.1021/ef100750y.

(109) Ozdemir, E. Biomimetic CO2 Sequestration: 1. Immobilization of Carbonic Anhydrase within Polyurethane Foam. *Energy and Fuels* **2009**, *23* (11), 5725–5730. https://doi.org/10.1021/ef9005725.

(110) Lepaumier, H.; Da Silva, E. F.; Einbu, A.; Grimstvedt, A.; Knudsen, J. N.; Zahlsen, K.; Svendsen, H. F. Comparison of MEA Degradation in Pilot-Scale with Lab-Scale Experiments. *Energy Procedia* **2011**, *4*, 1652–1659. https://doi.org/10.1016/j.egypro.2011.02.037.

(111) Dai, N.; Shah, A. D.; Hu, L.; Plewa, M. J.; McKague, B.; Mitch, W. A. Measurement of Nitrosamine and Nitramine Formation from NOx Reactions with Amines during Amine-Based Carbon Dioxide Capture for Postcombustion Carbon Sequestration. *Environ. Sci. Technol.* **2012**, *46* (17), 9793–9801. https://doi.org/10.1021/es301867b.

(112) Li, K.; Li, N. Removal of Carbon Dioxide from Breathing Gas Mixtures Using an Electrochemical Membrane Cell. *Sep. Sci. Technol.* **1993**, *28* (4), 1085–1090. https://doi.org/10.1080/01496399308029240.

(113) Apaydin, D. H.; Głowacki, E. D.; Portenkirchner, E.; Sariciftci, N. S. Direct Electrochemical Capture and Release of Carbon Dioxide Using an Industrial Organic Pigment: Quinacridone. *Angew. Chemie - Int. Ed.* **2014**, *53* (26), 6819–6822. https://doi.org/10.1002/anie.201403618.

(114) Mizen, M. B.; Wrighton, M. S. Reductive Addition of C02 to 9 ,10-Phenanthrenequinone. *J. Electrochem. Soc.* **1989**, *136* (4), 941–946.

(115) Dykstra, J. E.; Zhao, R.; Biesheuvel, P. M.; Van der Wal, A. Resistance Identification and Rational Process Design in Capacitive Deionization. *Water Res.* **2016**, *88*, 358–370. https://doi.org/10.1016/j.watres.2015.10.006.

(116) Qu, Y.; Baumann, T. F.; Santiago, J. G.; Stadermann, M. Characterization of Internal Resistance of a Capacitive Deionization System. *Environ. Sci. Technol.* **2015**, 1–15.

(117) He, D.; Wong, C. E.; Tang, W.; Kovalsky, P.; David Waite, T. Faradaic Reactions in Water Desalination by Batch-Mode Capacitive Deionization. *Environ. Sci. Technol. Lett.* **2016**, *3* (5), 222–226. https://doi.org/10.1021/acs.estlett.6b00124.

(118) Dykstra, J. E.; Keesman, K. J.; Biesheuvel, P. M.; van der Wal, A. Theory of PH Changes in Water Desalination by Capacitive Deionization. *Water Res.* **2017**, *119*, 178–186. https://doi.org/10.1016/j.watres.2017.04.039.

(119) Hemmatifar, A.; Oyarzun, D. I.; Palko, J. W.; Hawks, S. A.; Stadermann, M.; Santiago, J. G. Equilibria Model for PH Variations and Ion Adsorption in Capacitive Deionization Electrodes. *Water Res.* **2017**, *122*, 387–397. https://doi.org/10.1016/j.watres.2017.05.036.

(120) Zhao, R.; Soestbergen, M. Van; Rijnaarts, H. H. M.; Wal, A. Van Der; Bazant, M. Z.; Biesheuvel, P. M. Journal of Colloid and Interface Science Time-Dependent Ion Selectivity in Capacitive Charging of Porous Electrodes. *J. Colloid Interface Sci.* **2012**, *384* (1), 38–44. https://doi.org/10.1016/j.jcis.2012.06.022.

(121) Vermaas, D. A.; Saakes, M.; Nijmeijer, K. Doubled Power Density from Salinity Gradients at Reduced Intermembrane Distance. *Environ. Sci. Technol.* **2011**, *45* (16), 7089–7095. https://doi.org/10.1021/es2012758.

(122) Merel, J.; Clausse, M.; Meunier, F. Experimental Investigation on CO2 Post-Combustion Capture by Indirect Thermal Swing Adsorption Using 13X and 5A Zeolites. *Ind. Eng. Chem. Res.* **2008**, *47* (1), 209–215. https://doi.org/10.1021/ie071012x.

(123) Loeb, S. Production of Energy from Concentrated Brines by Pressure-Retarded Osmosis. *J. Memb. Sci.* **1976**, *1*, 49–63. https://doi.org/10.1016/S0376-7388(00)82257-7.

(124) She, Q.; Jin, X.; Tang, C. Y. Osmotic Power Production from Salinity Gradient Resource by Pressure Retarded Osmosis: Effects of Operating Conditions and Reverse Solute Diffusion. *J. Memb. Sci.* **2012**, *401–402*, 262–273. https://doi.org/10.1016/j.memsci.2012.02.014.

(125) Helfer, F.; Lemckert, C.; Anissimov, Y. G. Osmotic Power with Pressure Retarded Osmosis: Theory, Performance and Trends - A Review. *J. Memb. Sci.* **2014**, *453*, 337–358. https://doi.org/10.1016/j.memsci.2013.10.053.

(126) Post, J. W.; Hamelers, H. V. M.; Buisman, C. J. N. Energy Recovery from Controlled Mixing Salt and Fresh Water with a Reverse Electrodialysis System. *Environ. Sci. Technol.* **2008**, *42* (15), 5785–5790. https://doi.org/10.1021/es8004317.

(127) Vermaas, D. A.; Saakes, M.; Nijmeijer, K. Power Generation Using Profiled Membranes in Reverse Electrodialysis. *J. Memb. Sci.* **2011**, *385–386* (1), 234–242. https://doi.org/10.1016/j.memsci.2011.09.043.

(128) Moreno, J.; Slouwerhof, E.; Vermaas, D. A.; Saakes, M.; Nijmeijer, K. The Breathing Cell: Cyclic Intermembrane Distance Variation in Reverse Electrodialysis. *Environ. Sci. Technol.* **2016**, *50* (20), 11386–11393. https://doi.org/10.1021/acs.est.6b02668.

(129) Brogioli, D. Extracting Renewable Energy from a Salinity Difference Using a Capacitor. *Phys. Rev. Lett.* **2009**, *103* (5), 31–34. https://doi.org/10.1103/PhysRevLett.103.058501.

(130) Brogioli, D.; Zhao, R.; Biesheuvel, P. M. A Prototype Cell for Extracting Energy from a Water Salinity Difference by Means of Double Layer Expansion in Nanoporous Carbon Electrodes. *Energy Environ. Sci.* **2011**, *4* (3), 772–777. https://doi.org/10.1039/c0ee00524j.

(131) Sales, B. B.; Saakes, M.; Post, J. W.; Buisman, C. J. N.; Biesheuvel, P. M.; Hamelers, H. V. M. Direct Power Production from a Water Salinity Difference in a Membrane-Modified Supercapacitor Flow Cell. *Environ. Sci. Technol.* **2010**, *44* (14), 5661–5665. https://doi.org/10.1021/es100852a.

(132) Ahualli, S.; Jiménez, M. L.; Fernández, M. M.; Iglesias, G.; Brogioli, D.; Delgado, V. Polyelectrolyte-Coated Carbons Used in the Generation of Blue Energy from Salinity Differences. *Phys. Chem. Chem. Phys.* **2014**, *16* (46), 25241–25246. https://doi.org/10.1039/c4cp03527e.

(133) La Mantia, F.; Pasta, M.; Deshazer, H. D.; Logan, B. E.; Cui, Y. Batteries for Efficient Energy Extraction from a Water Salinity Difference. *Nano* **2011**, *11*, 1810–1813. https://doi.org/10.1021/nl200500s.

(134) Kim, I.; Svendsen, H. F. Heat of Absorption of Carbon Dioxide (CO2) in Monoethanolamine (MEA) and 2-(Aminoethyl)Ethanolamine (AEEA) Solutions. *Ind. Eng. Chem. Res.* **2007**, *46* (17), 5803–5809. https://doi.org/10.1021/ie0616489.

(135) Dugas, R.; Rochelle, G. Absorption and Desorption Rates of Carbon Dioxide with Monoethanolamine and Piperazine. *Energy Procedia* **2009**, *1* (1), 1163–1169. https://doi.org/10.1016/j.egypro.2009.01.153.

(136) Sales, B. B.; Burheim, O. S.; Porada, S.; Presser, V.; Buisman, C. J. N.; Hamelers, H. V. M. Extraction of Energy from Small Thermal Differences near Room Temperature Using Capacitive Membrane Technology. *Environ. Sci. Technol. Lett.* **2014**, *1* (9), 356–360. https://doi.org/10.1021/ez5002402.

(137) Liu, F.; Wagterveld, R. M.; Gebben, B.; Otto, M. J.; Biesheuvel, P. M.; Hamelers, H. V. M. Carbon Nanotube Yarns as Strong Flexible Conductive Capacitive Electrodes. *Colloids Interface Sci. Commun.* **2014**, *3*, 9–12. https://doi.org/10.1016/j.colcom.2015.02.001.

(138) Endrődi, B.; Bencsik, G.; Darvas, F.; Jones, R.; Rajeshwar, K.; Janáky, C. Continuous-Flow Electroreduction of Carbon Dioxide. *Prog. Energy Combust. Sci.* **2017**, *62*, 133–154. https://doi.org/10.1016/j.pecs.2017.05.005.

(139) Jhong, H. R. Q.; Brushett, F. R.; Kenis, P. J. A. The Effects of Catalyst Layer Deposition Methodology on Electrode Performance. *Adv. Energy Mater.* **2013**, *3* (5), 589–599. https://doi.org/10.1002/aenm.201200759.

(140) Kim, B.; Hillman, F.; Ariyoshi, M.; Fujikawa, S.; Kenis, P. J. A. Effects of Composition of the Micro Porous Layer and the Substrate on Performance in the Electrochemical Reduction of CO2to CO. *J. Power Sources* **2016**, *312*, 192–198. https://doi.org/10.1016/j.jpowsour.2016.02.043.

(141) Weekes, D. M.; Salvatore, D. A.; Reyes, A.; Huang, A.; Berlinguette, C. P. Electrolytic CO_2 Reduction in a Flow Cell. *Acc. Chem. Res.* **2018**, acs.accounts.8b00010. https://doi.org/10.1021/acs.accounts.8b00010.

(142) Salvatore, D. A.; Weekes, D. M.; He, J.; Dettelbach, K. E.; Li, Y. C.; Mallouk, T. E.; Berlinguette, C. P. Electrolysis of Gaseous CO_2 to CO in a Flow Cell with a Bipolar Membrane. *ACS Energy Lett.* **2017**, 149–154. https://doi.org/10.1021/acsenergylett.7b01017.

(143) Delacourt, C.; Ridgway, P. L.; Kerr, J. B.; Newman, J. Design of an Electrochemical Cell Making Syngas (CO+H[Sub 2]) from CO[Sub 2] and H[Sub 2]O Reduction at Room Temperature. *J. Electrochem. Soc.* **2008**, *155* (1), B42. https://doi.org/10.1149/1.2801871.

(144) Costamagna, P.; Srinivasan, S. Quantum Jumps in the PEMFC Science and Technology from the 1960s to the Year 2000: Part II. Engineering, Technology Development and Application Aspects. *J. Power Sources* **2001**, *102* (1–2), 253–269. https://doi.org/10.1016/S0378-

7753(01)00808-4.

(145) Park, S.; Lee, J. W.; Popov, B. N. A Review of Gas Diffusion Layer in PEM Fuel Cells: Materials and Designs. *Int. J. Hydrogen Energy* **2012**, *37* (7), 5850–5865. https://doi.org/10.1016/j.ijhydene.2011.12.148.

(146) Mehta, V.; Cooper, J. S. Review and Analysis of PEM Fuel Cell Design and Manufacturing. *J. Power Sources* **2003**, *114* (1), 32–53. https://doi.org/10.1016/S0378-7753(02)00542-6.

(147) Gamburzev, S.; Appleby, A. J. Recent Progress in Performance Improvement of the Proton Exchange Membrane Fuel Cell (PEMFC). *J. Power Sources* **2002**, *107* (1), 5–12. https://doi.org/10.1016/S0378-7753(01)00970-3.

(148) Litster, S.; McLean, G. PEM Fuel Cell Electrodes. *J. Power Sources* **2004**, *130* (1–2), 61–76. https://doi.org/10.1016/j.jpowsour.2003.12.055.

(149) Yang, H.; Kaczur, J. J.; Sajjad, S. D.; Masel, R. I. Electrochemical Conversion of CO2to Formic Acid Utilizing Sustainion™ Membranes. *J. CO2 Util.* **2017**, *20* (April), 208–217. https://doi.org/10.1016/j.jcou.2017.04.011.

(150) Williams, M. V.; Kunz, H. R.; Fenton, J. M. Operation of Nafion®-Based PEM Fuel Cells with No External Humidification: Influence of Operating Conditions and Gas Diffusion Layers. *J. Power Sources* **2004**, *135* (1–2), 122–134. https://doi.org/10.1016/j.jpowsour.2004.04.010.

(151) Sharaf, O. Z.; Orhan, M. F. An Overview of Fuel Cell Technology: Fundamentals and Applications. *Renew. Sustain. Energy Rev.* **2014**, *32*, 810–853. https://doi.org/10.1016/j.rser.2014.01.012.

(152) He, F.; Biesheuvel, P. M.; Bazant, M. Z.; Hatton, T. A. Theory of Water Treatment by Capacitive Deionization with Redox Active Porous Electrodes. *Water Res.* **2018**, *132*, 282–291. https://doi.org/10.1016/j.watres.2017.12.073.

(153) Bao, W.; Tang, X.; Guo, X.; Choi, S.; Wang, C.; Gogotsi, Y.; Wang, G. Porous Cryo-Dried MXene for Efficient Capacitive Deionization. *Joule* **2018**, *2* (4), 778–787. https://doi.org/10.1016/j.joule.2018.02.018.

(154) Legrand, L.; Schaetzle, O.; De Kler, R. C. F.; Hamelers, H. V. M. Solvent-Free CO2Capture Using Membrane Capacitive Deionization. *Environ. Sci. Technol.* **2018**, *52* (16), 9478–9485. https://doi.org/10.1021/acs.est.8b00980.

(155) Sanz-Pérez, E. S.; Murdock, C. R.; Didas, S. A.; Jones, C. W. Direct Capture of CO2from Ambient Air. *Chem. Rev.* **2016**, *116* (19), 11840–11876. https://doi.org/10.1021/acs.chemrev.6b00173.

(156) Keith, D. W.; Holmes, G.; Angelo, D. S.; Heidel, K. A Process for Capturing CO2 from the Atmosphere. *Joule* **2017**, *54* (4), 32–37. https://doi.org/10.1016/j.joule.2018.05.006.

(157) International, I. E. A.; Agency, E. Energy Technology Perspectives 2017. **2017**. https://doi.org/10.1787/energy_tech-2017-en.

(158) Dutcher, B.; Fan, M.; Russell, A. G. Amine-Based CO 2 Capture Technology Development from the Beginning of 2013 ? A Review. **2015**. https://doi.org/10.1021/am507465f.

(159) Parvazinia, M.; Garcia, S.; Maroto-valer, M. CO2 Capture by Ion Exchange Resins as Amine Functionalised Adsorbents. *Chem. Eng. J.* **2018**, *331* (August 2017), 335–342. https://doi.org/10.1016/j.cej.2017.08.087.

(160) Dean, C. C.; Blamey, J.; Florin, N. H.; Al-Jeboori, M. J.; Fennell, P. S. The Calcium Looping Cycle for CO2 Capture from Power Generation, Cement Manufacture and Hydrogen Production. *Chem. Eng. Res. Des.* **2011**, *89* (6), 836–855. https://doi.org/10.1016/j.cherd.2010.10.013.

(161) Khalilpour, R.; Mumford, K.; Zhai, H.; Abbas, A.; Stevens, G.; Rubin, E. S. Membrane-Based Carbon Capture from Fl Ue Gas : A Review. *J. Clean. Prod.* **2015**, *103*, 286–300. https://doi.org/10.1016/j.jclepro.2014.10.050.

(162) Keith, D. W.; Holmes, G.; Angelo, D. S.; Heidel, K. A Process for Capturing CO2 from the

Atmosphere. *Joule* **2017**, *54* (4), 32–37. https://doi.org/10.1016/j.joule.2018.05.006.

(163) Dykstra, J. E.; Biesheuvel, P. M.; Bruning, H.; Ter Heijne, A. Theory of Ion Transport with Fast Acid-Base Equilibrations in Bioelectrochemical Systems. *Phys. Rev. E - Stat. Nonlinear, Soft Matter Phys.* **2014**, *90* (1), 1–10. https://doi.org/10.1103/PhysRevE.90.013302.

(164) Gao, X.; Omosebi, A.; Holubowitch, N.; Landon, J.; Liu, K. Capacitive Deionization Using Alternating Polarization: Effect of Surface Charge on Salt Removal. *Electrochim. Acta* **2017**, *233*, 249–255. https://doi.org/10.1016/j.electacta.2017.03.021.

(165) Gao, X.; Porada, S.; Omosebi, A.; Liu, K. L.; Biesheuvel, P. M.; Landon, J. Complementary Surface Charge for Enhanced Capacitive Deionization. *Water Res.* **2016**, *92*, 275–282. https://doi.org/10.1016/j.watres.2016.01.048.

(166) Dykstra, J. E.; Porada, S.; Wal, A. Van Der; Biesheuvel, P. M. Energy Consumption in Capacitive Deionization – Constant Current versus Constant Voltage Operation. *Water Res.* **2018**, No. Cdi, 1–12. https://doi.org/10.1016/j.watres.2018.06.034.

(167) Porada, S.; Bukowska, P.; Shrivastava, A.; Biesheuvel, P. M.; Smith, K. C. Nickel Hexacyanoferrate Electrodes for Cation Intercalation Desalination. *Arxiv: 1612.08293* **2017**, 1–16. https://doi.org/10.1016/j.electacta.2017.09.137.

(168) Zhao, R.; Soestbergen, M. Van; Rijnaarts, H. H. M.; Wal, A. Van Der; Bazant, M. Z.; Biesheuvel, P. M. Journal of Colloid and Interface Science Time-Dependent Ion Selectivity in Capacitive Charging of Porous Electrodes. *J. Colloid Interface Sci.* **2012**, *384* (1), 38–44. https://doi.org/10.1016/j.jcis.2012.06.022.

(169) Biesheuvel, P. M.; Hamelers, H. V. M.; Suss, M. E. Theory of Water Desalination by Porous Electrodes with Immobile Chemical Charge. *Colloids Interface Sci. Commun.* **2015**, *9*, 1–5. https://doi.org/10.1016/j.colcom.2015.12.001.

(170) Yu, J.; Jo, K.; Kim, T.; Lee, J.; Yoon, J. Temporal and Spatial Distribution of PH in Fl Ow-Mode Capacitive Deionization and Membrane Capacitive Deionization. *Desalination* **2018**, *439* (December 2017), 188–195. https://doi.org/10.1016/j.desal.2018.04.011.

(171) Huang, X.; He, D.; Tang, W.; Kovalsky, P.; Waite, T. D. Environmental Science Investigation of PH-Dependent Phosphate Removal from Wastewaters by Membrane Capacitive. **2017**, 875–882. https://doi.org/10.1039/c7ew00138j.

(172) Huang, X.; He, D.; Tang, W.; Kovalsky, P.; Waite, T. D. Environmental Science Investigation of PH-Dependent Phosphate Removal from Wastewaters by Membrane Capacitive. *Environ. Sci. Water Res. Technol.* **2017**, *3* (5), 875–882. https://doi.org/10.1039/c7ew00138j.

(173) Plaza, M. G.; García, S.; Rubiera, F.; Pis, J. J.; Pevida, C. Post-Combustion CO2capture with a Commercial Activated Carbon: Comparison of Different Regeneration Strategies. *Chem. Eng. J.* **2010**, *163* (1–2), 41–47. https://doi.org/10.1016/j.cej.2010.07.030.

(174) Oyarzun, D. I.; Hemmatifar, A.; Palko, J. W.; Stadermann, M.; Santiago, J. G. Ion Selectivity in Capacitive Deionization with Functionalized Electrode : Theory and Experimental Validation. *Water Res. X* **2018**, *1*, 100008. https://doi.org/10.1016/j.wroa.2018.100008.

(175) Ohshima, H.; Ohki, S. Donnan Potential and Surface Potential of a Charged Membrane. *Biophys. J.* **1985**, *47* (5), 673–678. https://doi.org/10.1016/S0006-3495(85)83963-1.

(176) Galama, A. H.; Post, J. W.; Cohen Stuart, M. A.; Biesheuvel, P. M. Validity of the Boltzmann Equation to Describe Donnan Equilibrium at the Membrane-Solution Interface. *J. Memb. Sci.* **2013**, *442*, 131–139. https://doi.org/10.1016/j.memsci.2013.04.022.

(177) Mubita, T. M.; Dykstra, J. E.; Biesheuvel, P. M.; Wal, A. Van Der; Porada, S. Selective Adsorption of Nitrate over Chloride in Microporous Carbons. *Water Res.* **2019**, *164*, 114885. https://doi.org/10.1016/j.watres.2019.114885.

(178) Gao, X.; Omosebi, A.; Landon, J.; Liu, K. Enhanced Salt Removal in an Inverted Capacitive Deionization Cell Using Amine Modified Microporous Carbon Cathodes. *Environ. Sci.*

Technol. **2015**, *49* (18), 10920–10926. https://doi.org/10.1021/acs.est.5b02320.

(179) Suss, M. E. Size-Based Ion Selectivity of Micropore Electric Double Layers in Capacitive Deionization Electrodes. **2017**, *164* (9), 270–275. https://doi.org/10.1149/2.1201709jes.

(180) Li, Y.; Zhang, C.; Jiang, Y.; Wang, T.; Wang, H. Effects of the Hydration Ratio on the Electrosorption Selectivity of Ions during Capacitive Deionization. *DES* **2016**, *399*, 171–177. https://doi.org/10.1016/j.desal.2016.09.011.

(181) Onsager, L. Deviations from Ohm's Law in Weak Electrolytes. *J. Chem. Phys.* **1934**, *2* (9), 599–615. https://doi.org/10.1063/1.1749541.

(182) H.W. Nurnberg, G. W. Influences on Homogeneous Chemical Reactions in the Diffuse Double Layer. *J. Electroanal.Chem.* **1969**, *21*, 99–122.

(183) Dutcher, B.; Fan, M.; Russell, A. G. Amine-Based CO2 Capture Technology Development from the Beginning of 2013 : A Review. *ACS Appl. Mater. Interfaces* **2015**, *7* (4), 2137–2148. https://doi.org/10.1021/am507465f.

(184) Tan, X.; Kou, L.; Tahini, H. A.; Smith, S. C. Conductive Graphitic Carbon Nitride as an Ideal Material for Electrocatalytically Switchable CO2Capture. *Sci. Rep.* **2015**, *5* (November), 1–8. https://doi.org/10.1038/srep17636.

(185) Frantz, T. S.; Ruiz, W. A.; Augusto, C.; Mortola, V. B. Microporous and Mesoporous Materials Synthesis of ZSM-5 with High Sodium Content for CO 2 Adsorption. *Microporous Mesoporous Mater.* **2016**, *222*, 209–217. https://doi.org/10.1016/j.micromeso.2015.10.022.

(186) Oschatz, M.; Antonietti, M. A Search for Selectivity to Enable CO2capture with Porous Adsorbents. *Energy Environ. Sci.* **2018**, *11* (1), 57–70. https://doi.org/10.1039/c7ee02110k.

(187) Zhao, Y.; Liu, X.; Yao, K. X.; Zhao, L.; Han, Y. Superior Capture of CO2achieved by Introducing Extra-Framework Cations into N-Doped Microporous Carbon. *Chem. Mater.* **2012**, *24* (24), 4725–4734. https://doi.org/10.1021/cm303072n.

(188) Qin, C.; He, D.; Zhang, Z.; Tan, L.; Ran, J. The Consecutive Calcination/Sulfation in Calcium Looping for CO2 Capture: Particle Modeling and Behaviour Investigation. *Chem. Eng. J.* **2018**, *334* (November 2017), 2238–2249. https://doi.org/10.1016/j.cej.2017.11.169.

(189) Rheinhardt, J. H.; Singh, P.; Tarakeshwar, P.; Buttry, D. A. Electrochemical Capture and Release of Carbon Dioxide. *ACS Energy Lett.* **2017**, *2* (2), 454–461. https://doi.org/10.1021/acsenergylett.6b00608.

(190) Stern, M. C.; Simeon, F.; Herzog, H.; Hatton, T. A. Post-Combustion Carbon Dioxide Capture Using Electrochemically Mediated Amine Regeneration. *Energy Environ. Sci.* **2013**, *6* (8), 2505–2517. https://doi.org/10.1039/c3ee41165f.

(191) Wang, M.; Rahimi, M.; Kumar, A.; Hariharan, S.; Choi, W.; Hatton, T. A. Flue Gas CO 2 Capture via Electrochemically Mediated Amine Regeneration : System Design and Performance. *Appl. Energy* **2019**, *255* (September), 113879. https://doi.org/10.1016/j.apenergy.2019.113879.

(192) Legrand, L.; Schaetzle, O.; Tedesco, M.; Hamelers, H. V. M. Electrical Energy from CO2 Emissions by Direct Gas Feeding in Capacitive Cells. *Electrochim. Acta* **2019**, *319*, 264–276. https://doi.org/10.1016/j.electacta.2019.06.126.

(193) Gottesfled, S.; Zawodzinski, T. A. . Polymer Electrolyte Fuel Cells. **2008**, 301–311. https://doi.org/10.1007/978-4-431-56042-5_22.

(194) Ticianelli, E. A.; Derouin, C. R.; Redondo, A.; Srinivasan, S. Methods to Advance Technology of Proton Exchange Membrane Fuel Cells. *J. Electrochem. Soc.* **1988**, *135* (9), 2209–2214. https://doi.org/10.1149/1.2096240.

(195) Wang, L.; Liang, Y.; Zhang, L. Enhancing Performance of Capacitive Deionization with Polyelectrolyte-Infiltrated Electrodes: Theory and Experimental Validation. *Environ. Sci. Technol.* **2020**. https://doi.org/10.1021/acs.est.9b07692.

(196) Kamcev, J.; Sujanani, R.; Jang, E. S.; Yan, N.; Moe, N.; Paul, D. R.; Freeman, B. D. Salt Concentration Dependence of Ionic Conductivity in Ion Exchange Membranes. *J. Memb. Sci.* **2018**, *547* (October 2017), 123–133. https://doi.org/10.1016/j.memsci.2017.10.024.

(197) Galama, A. H.; Hoog, N. A.; Yntema, D. R. Method for Determining Ion Exchange Membrane Resistance for Electrodialysis Systems. *Desalination* **2016**, *380*, 1–11. https://doi.org/10.1016/j.desal.2015.11.018.

(198) Długołecki, P.; Ogonowski, P.; Metz, S. J.; Saakes, M.; Nijmeijer, K.; Wessling, M. On the Resistances of Membrane, Diffusion Boundary Layer and Double Layer in Ion Exchange Membrane Transport. *J. Memb. Sci.* **2010**, *349* (1–2), 369–379. https://doi.org/10.1016/j.memsci.2009.11.069.

(199) Rijnaarts, T.; Huerta, E.; Van Baak, W.; Nijmeijer, K. Effect of Divalent Cations on RED Performance and Cation Exchange Membrane Selection to Enhance Power Densities. *Environ. Sci. Technol.* **2017**, *51* (21), 13028–13035. https://doi.org/10.1021/acs.est.7b03858.

(200) Galama, A. H.; Vermaas, D. A.; Veerman, J.; Saakes, M.; Rijnaarts, H. H. M.; Post, J. W.; Nijmeijer, K. Membrane Resistance: The Effect of Salinity Gradients over a Cation Exchange Membrane. *J. Memb. Sci.* **2014**, *467*, 279–291. https://doi.org/10.1016/j.memsci.2014.05.046.

(201) Xu, W.; Scott, K. The Effects of Ionomer Content on PEM Water Electrolyser Membrane Electrode Assembly Performance. *Int. J. Hydrogen Energy* **2010**, *35* (21), 12029–12037. https://doi.org/10.1016/j.ijhydene.2010.08.055.

(202) Du, S.; Millington, B.; Pollet, B. G. The Effect of Nafion Ionomer Loading Coated on Gas Diffusion Electrodes with In-Situ Grown Pt Nanowires and Their Durability in Proton Exchange Membrane Fuel Cells. *Int. J. Hydrogen Energy* **2011**, *36* (7), 4386–4393. https://doi.org/10.1016/j.ijhydene.2011.01.014.

(203) Jeon, S.; Lee, J.; Rios, G. M.; Kim, H. J.; Lee, S. Y.; Cho, E.; Lim, T. H.; Hyun Jang, J. Effect of Ionomer Content and Relative Humidity on Polymer Electrolyte Membrane Fuel Cell (PEMFC) Performance of Membrane-Electrode Assemblies (MEAs) Prepared by Decal Transfer Method. *Int. J. Hydrogen Energy* **2010**, *35* (18), 9678–9686. https://doi.org/10.1016/j.ijhydene.2010.06.044.

(204) Legrand, L.; Shu, Q.; Tedesco, M.; Dykstra, J.; Hamelers, H. V. M. Role of Ion Exchange Membrane and Capacitive Electrodes in Membrane Capacitive Deionization for CO2 Capture. 2019.

(205) Tedesco, M.; Hamelers, H. V. M.; Biesheuvel, P. M. Nernst-Planck Transport Theory for (Reverse) Electrodialysis: III. Optimal Membrane Thickness for Enhanced Process Performance. *J. Memb. Sci.* **2018**, *565*, 480–487. https://doi.org/10.1016/j.memsci.2018.07.090.

(206) Li, J.; Liu, E. hui; Li, W.; Meng, X. yun; Tan, S. ting. Nickel/Carbon Nanofibers Composite Electrodes as Supercapacitors Prepared by Electrospinning. *J. Alloys Compd.* **2009**, *478* (1–2), 371–374. https://doi.org/10.1016/j.jallcom.2008.11.024.

(207) Pan, J.; Hou, L.; Wang, Q.; He, Y.; Wu, L.; Mondal, A. N.; Xu, T. Preparation of Bipolar Membranes by Electrospinning. *Mater. Chem. Phys.* **2017**, *186*, 484–491. https://doi.org/10.1016/j.matchemphys.2016.11.023.

(208) Chaparro, A. M.; Gallardo, B.; Folgado, M. A.; Martín, A. J.; Daza, L. PEMFC Electrode Preparation by Electrospray: Optimization of Catalyst Load and Ionomer Content. *Catal. Today* **2009**, *143* (3–4), 237–241. https://doi.org/10.1016/j.cattod.2008.12.003.

(209) Kim, K. H.; Lee, K. Y.; Kim, H. J.; Cho, E. A.; Lee, S. Y.; Lim, T. H.; Yoon, S. P.; Hwang, I. C.; Jang, J. H. The Effects of Nafion® Ionomer Content in PEMFC MEAs Prepared by a Catalyst-Coated Membrane (CCM) Spraying Method. *Int. J. Hydrogen Energy* **2010**, *35* (5), 2119–2126.

https://doi.org/10.1016/j.ijhydene.2009.11.058.

(210) Breitwieser, M.; Bayer, T.; Büchler, A.; Zengerle, R.; Lyth, S. M.; Thiele, S. A Fully Spray-Coated Fuel Cell Membrane Electrode Assembly Using Aquivion Ionomer with a Graphene Oxide/Cerium Oxide Interlayer. *J. Power Sources* **2017**, *351*, 145–150. https://doi.org/10.1016/j.jpowsour.2017.03.085.

(211) asson-Delmotte, V., P. Zhai, H.-O. Pörtner, D. Roberts, J. Skea, P. R. S.; A. Pirani, W. Moufouma-Okia, C. Péan, R. Pidcock, S. Connors, J.B.R. Matthews, Y. Chen, X. Zhou, M. I. G.; E. Lonnoy, T. Maycock, M. Tignor, and T. W. ICCP Report (Summary for Policymarkers). 1–21.

(212) Długołecki, P.; Nymeijer, K.; Metz, S.; Wessling, M. Current Status of Ion Exchange Membranes for Power Generation from Salinity Gradients. *J. Memb. Sci.* **2008**, *319* (1–2), 214–222. https://doi.org/10.1016/j.memsci.2008.03.037.

(213) Sheet, P. D. RALEX Membrane ® CM-PP. **2005**, No. 1907.

(214) Chen, D.; Hickner, M. A.; Agar, E.; Kumbur, E. C. Optimizing Membrane Thickness for Vanadium Redox Flow Batteries. *J. Memb. Sci.* **2013**, *437*, 108–113. https://doi.org/10.1016/j.memsci.2013.02.007.

(215) Savett, S. C.; Atkins, J. R.; Sides, C. R.; Harris, J. L.; Thomas, B. H.; Creager, S. E.; Pennington, W. T.; DesMarteau, D. D. A Comparison of Bis[(Perfluoroalkyl)Sulfonyl]Imide Ionomers and Perfluorosulfonic Acid Ionomers for Applications in PEM Fuel-Cell Technology. *J. Electrochem. Soc.* **2002**, *149* (12), A1527. https://doi.org/10.1149/1.1516218.

(216) Karlsson, L. E.; Jannasch, P. Polysulfone Ionomers for Proton-Conducting Fuel Cell Membranes: Sulfoalkylated Polysulfones. *J. Memb. Sci.* **2004**, *230* (1–2), 61–70. https://doi.org/10.1016/j.memsci.2003.10.033.

(217) Sharaf, O. Z.; Orhan, M. F. An Overview of Fuel Cell Technology: Fundamentals and Applications. *Renew. Sustain. Energy Rev.* **2014**, *32*, 810–853. https://doi.org/10.1016/j.rser.2014.01.012.

(218) Farmer, J. C.; Fix, D. V.; Mack, G. V.; Pekala, R. W.; Poco, J. F. Capacitive Deionization of NH4ClO4 Solutions with Carbon Aerogel Electrodes. *J. Appl. Electrochem.* **1996**, *26* (10), 1007–1018. https://doi.org/10.1007/BF00242195.

(219) Ryoo, M. W.; Kim, J. H.; Seo, G. Role of Titania Incorporated on Activated Carbon Cloth for Capacitive Deionization of NaCl Solution. *J. Colloid Interface Sci.* **2003**, *264* (2), 414–419. https://doi.org/10.1016/S0021-9797(03)00375-8.

(220) Cheng, Y.; Hao, Z.; Hao, C.; Deng, Y.; Li, X.; Li, K.; Zhao, Y. A Review of Modification of Carbon Electrode Material in Capacitive Deionization. *RSC Adv.* **2019**, *9* (42), 24401–24419. https://doi.org/10.1039/c9ra04426d.

(221) Porada, S.; Borchardt, L.; Oschatz, M.; Bryjak, M.; Atchison, J. S.; Keesman, K. J.; Kaskel, S.; Biesheuvel, P. M.; Presser, V. Direct Prediction of the Desalination Performance of Porous Carbon Electrodes for Capacitive Deionization. *Energy Environ. Sci.* **2013**, *6* (12), 3700–3712. https://doi.org/10.1039/c3ee42209g.

(222) Al-Amshawee, S.; Yunus, M. Y. B. M.; Azoddein, A. A. M.; Hassell, D. G.; Dakhil, I. H.; Hasan, H. A. Electrodialysis Desalination for Water and Wastewater: A Review. *Chem. Eng. J.* **2020**, *380* (July 2019). https://doi.org/10.1016/j.cej.2019.122231.

(223) Galama, A. H.; Daubaras, G.; Burheim, O. S.; Rijnaarts, H. H. M.; Post, J. W. Seawater Electrodialysis with Preferential Removal of Divalent Ions. *J. Memb. Sci.* **2014**, *452*, 219–228. https://doi.org/10.1016/j.memsci.2013.10.050.

(224) Sosa-Fernandez, P. A.; Post, J. W.; Leermakers, F. A. M.; Rijnaarts, H. H. M.; Bruning, H. Removal of Divalent Ions from Viscous Polymer-Flooding Produced Water and Seawater via Electrodialysis. *J. Memb. Sci.* **2019**, *589* (July), 117251. https://doi.org/10.1016/j.memsci.2019.117251.

(225) Vermaas, D. A.; Veerman, J.; Nijmeijer, K. Environmental Science In Fl Uence of Multivalent Ions on Renewable Energy Generation in Reverse Electrodialysis †. **2014**, 1434–1445. https://doi.org/10.1039/c3ee43501f.

(226) Arulrajan, A. C.; Ramasamy, D. L.; Sillanpää, M.; van der Wal, A.; Biesheuvel, P. M.; Porada, S.; Dykstra, J. E. Exceptional Water Desalination Performance with Anion-Selective Electrodes. *Adv. Mater.* **2019**, *31* (10), 1–5. https://doi.org/10.1002/adma.201806937.

(227) Dykstra, J. E.; Dijkstra, J.; Van der Wal, A.; Hamelers, H. V. M.; Porada, S. On-Line Method to Study Dynamics of Ion Adsorption from Mixtures of Salts in Capacitive Deionization. *Desalination* **2016**, *390*, 47–52. https://doi.org/10.1016/j.desal.2016.04.001.

(228) Moreno, J.; Díez, V.; Saakes, M.; Nijmeijer, K. Mitigation of the Effects of Multivalent Ion Transport in Reverse Electrodialysis. *J. Memb. Sci.* **2018**, *550* (December 2017), 155–162. https://doi.org/10.1016/j.memsci.2017.12.069.

(229) Geise, G. M.; Cassady, H. J.; Paul, D. R.; Logan, E.; Hickner, M. A. Specific Ion Effects on Membrane Potential and the Permselectivity of Ion Exchange Membranes. *Phys. Chem. Chem. Phys.* **2014**, *16*, 21673–21681. https://doi.org/10.1039/C4CP03076A.

(230) Sistat, P.; Pourcelly, G. Chronopotentiometric Response of an Ion-Exchange Membrane in the Underlimiting Current-Range. Transport Phenomena within the Diffusion Layers. *J. Memb. Sci.* **1997**, *123* (1), 121–131. https://doi.org/10.1016/S0376-7388(96)00210-4.

(231) Kang, B.; Kim, H. J.; Kim, D. K. Membrane Electrode Assembly for Energy Harvesting from Salinity Gradient by Reverse Electrodialysis. *J. Memb. Sci.* **2018**, *550* (December 2017), 286–295. https://doi.org/10.1016/j.memsci.2018.01.006.

(232) Wang, L.; Dykstra, J. E.; Lin, S. Energy Efficiency of Capacitive Deionization. *Environ. Sci. Technol.* **2019**, *53* (7), 3366–3378. https://doi.org/10.1021/acs.est.8b04858.

(233) Hemmatifar, A.; Ramachandran, A.; Liu, K.; Oyarzun, D. I.; Bazant, M. Z.; Santiago, J. G. Thermodynamics of Ion Separation by Electrosorption. *Environ. Sci. Technol.* **2018**, *52* (17), 10196–10204. https://doi.org/10.1021/acs.est.8b02959.

(234) Vermaas, D. A. *Energy Generation from Mixing Salt Water and Fresh Water*; 2014. https://doi.org/10.3990/1.9789036535731.

(235) Lu, J.; Cook, P. J.; Hosseini, S. A.; Yang, C.; Romanak, K. D.; Zhang, T.; Freifeld, B. M.; Smyth, R. C.; Zeng, H.; Hovorka, S. D. Complex Fluid Flow Revealed by Monitoring CO2 Injection in a Fluvial Formation. *J. Geophys. Res. Solid Earth* **2012**, *117* (3), 1–13. https://doi.org/10.1029/2011JB008939.

(236) Chadwick, R. A.; Noy, D. J. History-Matching Flow Simulations and Timelapse Seismic Data from the Sleipner CO2 Plume. *7th Pet. Geol. Conf. [FROM Matur. BASINS to NEW Front. (London, 3/30/2009-4/2/2009) Proc.* **2010**, *2*, 1171–1182.

(237) Smith, W. A.; Burdyny, T.; Vermaas, D. A.; Geerlings, H. Pathways to Industrial-Scale Fuel Out of Thin Air from CO2 Electrolysis. *Joule* **2019**, *3* (8), 1822–1834. https://doi.org/10.1016/j.joule.2019.07.009.

(238) Megías-Sayago, C.; Bingre, R.; Huang, L.; Lutzweiler, G.; Wang, Q.; Louis, B. CO2 Adsorption Capacities in Zeolites and Layered Double Hydroxide Materials. *Front. Chem.* **2019**, *7* (August), 1–10. https://doi.org/10.3389/fchem.2019.00551.

(239) Clausse, M.; Merel, J.; Meunier, F. Numerical Parametric Study on CO2 Capture by Indirect Thermal Swing Adsorption. *Int. J. Greenh. Gas Control* **2011**, *5* (5), 1206–1213. https://doi.org/10.1016/j.ijggc.2011.05.036.

(240) Park, B. H.; Choi, J. H. Improvement in the Capacitance of a Carbon Electrode Prepared Using Water-Soluble Polymer Binder for a Capacitive Deionization Application. *Electrochim. Acta* **2010**, *55* (8), 2888–2893. https://doi.org/10.1016/j.electacta.2009.12.084.

(241) Vafakhah, S.; Guo, L.; Sriramulu, D.; Huang, S.; Saeedikhani, M.; Yang, H. Y. Efficient Sodium-Ion Intercalation into the Freestanding Prussian Blue/Graphene Aerogel Anode in a Hybrid

Capacitive Deionization System. *ACS Appl. Mater. Interfaces* **2019**, *11*, 5989–5998. https://doi.org/10.1021/acsami.8b18746.

(242) Rommerskirchen, A.; Linnartz, C. J.; Müller, D.; Willenberg, L. K.; Wessling, M. Energy Recovery and Process Design in Continuous Flow-Electrode Capacitive Deionization Processes. *ACS Sustain. Chem. Eng.* **2018**, *6* (10), 13007–13015. https://doi.org/10.1021/acssuschemeng.8b02466.

(243) Ma, J.; Liang, P.; Sun, X.; Zhang, H.; Bian, Y.; Yang, F.; Bai, J.; Gong, Q.; Huang, X. Energy Recovery from the Flow-Electrode Capacitive Deionization. *J. Power Sources* **2019**, *421* (January), 50–55. https://doi.org/10.1016/j.jpowsour.2019.02.082.

(244) Gür, T. M. Review of Electrical Energy Storage Technologies, Materials and Systems: Challenges and Prospects for Large-Scale Grid Storage. *Energy Environ. Sci.* **2018**, *11* (10), 2696–2767. https://doi.org/10.1039/c8ee01419a.

(245) Ould Amrouche, S.; Rekioua, D.; Rekioua, T.; Bacha, S. Overview of Energy Storage in Renewable Energy Systems. *Int. J. Hydrogen Energy* **2016**, *41* (45), 20914–20927. https://doi.org/10.1016/j.ijhydene.2016.06.243.

(246) Yang, Y.; Bremner, S.; Menictas, C.; Kay, M. Battery Energy Storage System Size Determination in Renewable Energy Systems: A Review. *Renew. Sustain. Energy Rev.* **2018**, *91* (April), 109–125. https://doi.org/10.1016/j.rser.2018.03.047.

(247) Zhang, C.; Ma, J.; Song, J.; He, C.; Waite, T. D. Continuous Ammonia Recovery from Wastewaters Using an Integrated Capacitive Flow Electrode Membrane Stripping System Continuous Ammonia Recovery from Wastewaters Using an Integrated Capacitive Flow Electrode Membrane Stripping System. **2018**, No. November. https://doi.org/10.1021/acs.est.8b02743.

(248) Tang, W.; Liang, J.; He, D.; Gong, J.; Tang, L.; Liu, Z. Various Cell Architectures of Capacitive Deionization : Recent Advances and Future Trends. **2019**, *150*. https://doi.org/10.1016/j.watres.2018.11.064.

(249) Srimuk, P.; Lee, J.; Fleischmann, S.; Choudhury, S.; Jäckel, N.; Zeiger, M.; Kim, C.; Aslan, M.; Presser, V. Faradaic Deionization of Brackish and Sea Water via Pseudocapacitive Cation and Anion Intercalation into Few-Layered Molybdenum Disulfide. *J. Mater. Chem. A* **2017**, *5* (30), 15640–15649. https://doi.org/10.1039/c7ta03120c.

(250) Singh, K.; Porada, S.; de Gier, H. D.; Biesheuvel, P. M.; de Smet, L. C. P. M. Timeline on the Application of Intercalation Materials in Capacitive Deionization. *Desalination* **2019**, *455* (October 2018), 115–134. https://doi.org/10.1016/j.desal.2018.12.015.

List of publications

In relation to this thesis:

Legrand, L.; Schaetzle, O.; De Kler, R. C. F.; Hamelers, H. V. M. Solvent-Free CO2Capture Using Membrane Capacitive Deionization. *Environ. Sci. Technol.* **2018**, *52 (16)*, 9478–9485. https://doi.org/10.1021/acs.est.8b00980.

Legrand, L.; Schaetzle, O.; Tedesco, M.; Hamelers, H. V. M. Electrical Energy from CO2 Emissions by Direct Gas Feeding in Capacitive Cells. *Electrochim. Acta* **2019**, *319*, 264–276. https://doi.org/10.1016/j.electacta.2019.06.126.

Legrand, L.; Shu, Q.; Tedesco, M.; Dykstra, J. E.; Hamelers, H. V. M. Role of Ion Exchange Membranes and Capacitive Electrodes in Membrane Capacitive Deionization (MCDI) for CO2 Capture. *J. Colloid Interface Sci.* **2020**, *564*, 478–490. https://doi.org/10.1016/j.jcis.2019.12.039.

Other publication:

Shu, Q.; **Legrand, L.**; Kuntke, P.; Tedesco, M.; Hamelers, H. V. M. Electrochemical Regeneration of Spent Alkaline Absorbent from Direct Air Capture. *Environ. Sci. Technol.* **2020**, *54 (14)*, 8990–8998. https://doi.org/10.1021/acs.est.0c01977.

Acknowledgments

Almost 5 year to finish my Ph.D. project… What a road it was. This would have not been possible without the help of so many people.

After completing my master thesis, **Olivier Schaetzle** and **Bert Hamelers** invited me to continue my scientific work as a Ph.D. candidate. First, I would like to thank Olivier for his great support as a supervisor during my master's and Ph.D. thesis. I might have been a stubborn student at the time, but I cannot thank you enough for the trust and the time you spend on supporting me. You are a great defender of science, which is definitely needed. I would also like to thank Bert Hamelers for his trust and support as a co-promotor in my project. Although we might sometimes have tumultuous meetings on research directions, I admire your sharp vision on scientific data. Working with you has been a great opportunity to learn more about myself, my own talent, and also hidden talents I could still discover. Furthermore, I would like to thank **Cees Buisman**, the promotor of my project, and **Johannes Boonstra** for accepting me working in Wetsus.

Next, I would like to thank **Michele Tedesco**, the second co-promotor of my project. As a matter of fact, you only joined my project for the last two years. I would have to admit that your supervision style was quite different from what I was used to, which has been challenging for me at first. Nevertheless, I learned a great deal from you on how to organize tasks and priorities, organize collaborations, write efficiently scientific papers. Until the end of my Ph.D. project, your reliable support has been priceless to finalize my thesis. I am very grateful for that.

My project was part of the CO_2 energy theme in Wetsus, a research group in which Alliander, Engie, and Shell was part of. I would like to thank **Michiel Geurds, Elise Nanini-Maury, and Joost Smits** for their cooperation in my projects. Your inputs have always been relevant and essential to my project.

One of the big challenges in my project was to solve many engineering problems related to my set-up. Working with gas is not something common in a water technology research institute. Assisting me in this task, I would like to thank the **technical and analytical team of Wetsus**. In particular, I would like to thank **Jan JurJen Salverda** and **Jan Tuinstra**. Jan JurJen, I am a big fan of your positive energy and passion for solving issues and designing systems. When nothing seems to work, it is great to have somebody like you around for support. Jan, I cannot count how many times I popped up in the workshop, asking you just “a very fast question.” Even if you had no time, you always find time to help me, a big thank for that.

This Ph.D. thesis leads to the publication of three articles and the submission of another one. This would not have been possible without the contributions of all co-authors. I would like to thank Dr. Olivier Schaetlze, Dr. Michele Tedesco, **Jouke Dykstra**, **Robert de Kler**, **Qingidan Shu,** and Dr. Bert Hamelers. Your inputs have been valuable to improve the quality of our work. I owe a big thank to Jouke for kindly introducing me to mathematical modeling. Finally, I acknowledge the students who perform their master thesis and internship in my project: Qingdian Shu, **Yuerui Ma,** and **Veronica Paglialunga**. I learned as much from you that you did from me. I am proud to have supervised you, and I wish you the best in your future career. In particular, I would like to thank Qingdian Shu for his help during my thesis. At the end of my project, you even joined our team as a new Ph.D. candidate and greatly helped us to develop new innovative CO_2 capture systems. It was a great pleasure to work together with you. I am sure you will succeed in our research group.

Wetsus has been a unique place to work in, where I met a lot of nice colleagues, some of whom became good friends. To start my Ph.D., I first needed to find a house, and that how I met my first flatmate, **Philipp Wilfert**. Although cooking was not our main strength, late discussions around a nice beer was an activity I enjoyed a lot. Thinking about it, you gave me great advice, which took me two years to fully understand. You are a wise man in your way, which I can still learn a lot from. **To Paulina Sosa and Goncalo Macedo**, I am so glad that I had you as great comrades. You guys are awesome. Paulina, our morning coffees have been a game-changer to force us to be on time in the morning. Moreover, few people I met have so much positive energy to share than you. Goncalo, it was great to hang out with you. You and I are both idealists and share common passions. I could not dream of a better colleague for my Ph.D. and team partner in our volleyball team and music band.

Speaking of which, I want to thank my colleagues with whom I could share my sport and music hobbies. To my excellent volleyball team, **Goncalo Macedo**, **Thomas Prot**, **Ricardo Cunha, Hector Hernandez, Laura Carcelli**, it was such a pleasure playing with you. To the table tennis Wetsus non-official club, I had so much fun challenging Qingdian and **Chris Schott**. Our rivalry made us better players and good friends (looking forward to challenging you again). Besides, a big thanks to the Wetsus band, **Jorrit Hillebrand, Sofia Semitsoglou-Tsiapou, Fabian Ruhnau, Prashanth Kumar, Stan Willems,** and Goncalo.

I would also like to thank my office mate: Sofia Semitsoglou-Tsiapou, **Ilse Verburg**, **Casper Borsje**, **Yin Ye**, **Enas Othman**, Jorrit Hillebrand, **Antoine Karengera**, **Zexin Qian**, **Suyash Gupta, Tania Mubita**. Casper, thank you a lot for the great technical and scientific discussion. Jorrit, you are a great and kind person, thanks for all the help (asked

and unasked). What an inspiration and a model you were Yin, I will never forget the “panda style”: perform with no stress.

Finalement, je voudrais aussi remercier ma famille, en particulier ma mère et ma sœur. On dit qu’on ne choisit pas sa famille et je n’aurais pas pu rêver mieux que vous. De même, je suis extrêmement reconnaissant à ma partenaire, **Vasiliki Aspasiou**. Ces années de thèse n’ont pas toujours été facile. Malgré ma frustration et mauvaise humeur, tu as toujours su rester à mes côtés et à m’encourager. L’amour inconditionnel n’existe peut-être pas, mais parfois je doute en te regardant. Je ne pouvais pas être plus heureux que d’avoir notre petite fille avec toi, **Agnès Legrand**. A Agnès, tu es maintenant une nouvelle source d’inspiration sans fin dans ma vie. En tant que parent, Je ne souhaite de toi que d’être la meilleure version de toi-même et la plus heureuse. Je serais ravi de te montrer l’exemple en actant également comme la meilleure version de moi-même, commençant par finir cette thèse.

About the author

Louis Legrand was born on the 20th of May 1990, in Bèthune (France). In 2013, he completed his master degree in Food industry and agriculture at ISA Lille (France). In 2014, he completed his other master degree with cum laude in Environmental Science specialized in Environmental technology at Wageningen (the Netherlands). During its master studies, he wrote a thesis about generating electrical power from CO_2 emissions with an electrochemical cell. He also performs his master internship in a consultancy company where he wrote a technical and financial feasibility to combine a power-to-gas station to a wastewater treatment plant. After completed his master studies, he started his PhD research on capacitive systems for energy recovery and CO_2 capture from CO_2 emissions at Wageningen University. The research was carried out at Wetsus, European centre of excellence for sustainable water technology.

Netherlands Research School for the
Socio-Economic and Natural Sciences of the Environment

D I P L O M A

for specialised PhD training

The Netherlands research school for the
Socio-Economic and Natural Sciences of the Environment
(SENSE) declares that

Louis Jean Philippe Legrand

born on 20 May 1990 in Béthune, France

has successfully fulfilled all requirements of the
educational PhD programme of SENSE.

Wageningen, 11 September 2020

Chair of the SENSE board

Prof. dr. Martin Wassen

The SENSE Director

Prof. dr. Philipp Pattberg

The SENSE Research School has been accredited by the Royal Netherlands Academy of Arts and Sciences (KNAW)

K O N I N K L I J K E N E D E R L A N D S E
A K A D E M I E V A N W E T E N S C H A P P E N

The SENSE Research School declares that **Louis Jean Philippe Legrand** has successfully fulfilled all requirements of the educational PhD programme of SENSE with a work load of 35.0 EC, including the following activities:

SENSE PhD Courses

- Environmental research in context (2016)
- Research in context activity: 'Organizer and chair of Wetsus workshop on "Direct air-capture "Direct air capture: Building a chemical industry while cleaning the air"'(2020)

Other PhD and Advanced MSc Courses

- Presentation skills, VanZelf (2015)
- International Summer School on CO2 conversion, University of Bern/ETH Zürich (2016)
- Supervision of thesis students by PhD students, VanZelf (2016)
- Image Editing and Graphical Abstract, Somersault (2016)
- Communication Styles, How Company b.v. (2017)
- Scientific writing, Wageningen Graduate Schools (2019)
- Electrochemical theory and practical applications, University of Bath (2019)

Management and Didactic Skills Training

- Supervising three MSc student with thesis titled: 'Characterization of an innovative chemical free CO2 capture process using Membrane Capacitive Deionization (MCDI)', 'Modelling and Experimental investigation of a capacitive deionization (CDI) cell for CO2 capture application' & 'Design and optimization of novel electrochemical CO2 capture systems' (2017-2019)

Oral Presentations

- *Reactive Gas Electrosorption: novel, clean and energy CO2 capture concept*. Trondheim CO2 capture, Transport, Storage9 , 12-14 June 2017, Trondheim, Norway
- *Reactive Gas Electrosorption: Innovative CO2 capture concept*. Wetsus congress 2017, 9-10 September 2017, Leeuwarden, Netherlands
- *CO2 capture using capacitive electrodes*. KNCV symposium, 8 June 2017, Ghent, Belgium
- *Novel application for (M)CDI: CO2 capture*. CDI&E 2019, 20-23 May 2019, Beijing, China

SENSE coordinator PhD education

Dr. ir. Peter Vermeulen

This work was performed in the cooperation framework of Wetsus, European Centre of Excellence for Sustainable Water Technology (www.wetsus.nl). Wetsus is co-funded by the Dutch Ministry of Economic Affairs and Climate Policy and Ministry of Infrastructure and Water Management, the province of Frysln, and the Northern Netherlands Provinces. The author likes to thank the participants of the research theme “Sustainable carbon cycle” for the fruitful discussions and their financial support.